Gravitational Microlensing

Elspeth M. Minty

Doctor of Philosophy
The University of Edinburgh
2001

This thesis is my own composition except where indicated in the text.

July 17, 2001

Acknowledgements

While it is standard practice in theses for students to thank their supervisors for their help and support, in this case it seems even more appropriate. The combination of a part-time PhD and a demanding job have made my study patterns somewhat erratic to say the least. Both my supervisors, Alan Heavens and Mike Hawkins, have given me constant support and encouragement, even though at times all three of us must of wondered if this thesis was ever going to be finished. Thank you!

I'd also like to thank my former colleagues at EPCC. Alan Simpson and Arthur Trew both supported my original application for a PhD place and allowed me to adapt my working time to make it possible to complete. My former office mates Mario Antonioletti, Gavin Pringle and Paul Graham kindly avoided telling me too often I was insane to be doing this.

The computer simulations which form the basis of the work described in this thesis were carried out on the Hitachi SR2201 belonging to the High Performance Computer Group of Hitachi Europe Ltd. Having virtually unlimited access to an HPC platform is, I suspect, not an experience I'm likely to get to repeat. In particular, I'd like to thank Ben Edgington and his colleagues for their prompt response to the surprisingly few problems I had using their system.

The hierarchical tree implementation used in the computer simulation was based on software made available by Joshua Barnes on his web site
`http://www.ifa.hawaii.edu/ barnes/software.html`.

This thesis would not have been possible without the support my parents have given me over the frightening large number of years of my education – this is going to be the last degree, honest! I'm fairly sure I haven't told them enough times how much I appreciate it. Finally, a big thank you must go to my soon to be husband Michael McCormack, who has alternately encouraged, nagged and

laughed at me for the last 6 1/2 years. Without his support I would never have completed this degree.

Abstract

The formulation of the Theory of General Relativity and the observational evidence for the expansion of the universe provided the basis for much of the work carried out in the field of cosmology over the past hundred years. Huge volumes of research have been conducted to find reliable values for cosmological parameters and to describe the amount and nature of the matter in the universe. Chapter 1 of this thesis attempts to summarise current theoretical and observational thinking on these matters and, in particular, examines the wide-ranging application of gravitational lensing to the search for so-called dark matter. The use of gravitational microlensing to investigate a cosmological population of compact objects, their effects on the long term variability of the apparent luminosity of quasars and on the results of the on-going observations of high redshift supernovae is discussed. Such investigation forms the basis for this thesis.

The main tool for this investigation is a computer model which simulates the gravitational lensing effect of a population of compact object over a period of time. Chapter 2 sets out the theoretical background for this simulation. In particular, the methods used to set the physical parameters of the simulation, such as its volume, the redshifts of the lenses and their masses, are outlined.

Chapter 3 presents the implementation of the computer model. Modelling techniques used by other researchers are discussed, as are alternative approaches considered for the implementation of this model. In order to simulate the evolving distribution of the lensing objects over time, the simulation was designed to run on high performance parallel supercomputers. The method by which the simulation was designed to take advantage of this type of computing platform is also discussed.

In order to examine the effects of a cosmological distribution of compact objects on high redshift sources properly, it is necessary to have observational data. For

this thesis, the observational data consists of a set of lightcurves from high redshift quasars observed over a 25 year period. This data set is outlined in Chapter 4. The results from the computer simulation are then presented, including both example light curves and power spectra for a variety of cosmological models, source sizes, source redshifts and lens masses. This observational data is compared with the simulation data and is found to have comparable levels of power for a number of simulation models.

Chapter 5 examines the effect of a cosmological population of compact objects on the ongoing high redshift supernovae searches. The effects of such objects are modelled for a number of cosmological models for the range of redshifts proposed for the SNAP and VISTA searches. It is found that the proposed number counts for supernovae detection in each redshift bin are sufficient to differentiate between the different cosmological models.

Contents

List of Figures

List of Tables

Chapter 1

Introduction

One of the outstanding questions in current cosmological theory is the nature and origin of dark matter in the universe. The aim of this thesis is to explore the possibility that dark matter is made up, in a large part, by a cosmological distribution of compact objects. In particular this thesis will investigate whether the microlensing effects of such a population could explain the long term variation of the apparent luminosity of quasars. Further, it will explore how observations of high redshift supernovae could be used to constrain estimates of the amount of matter in this form.

1.1 Basic Cosmology

This section outlines the cosmological background for this thesis.

1.1.1 The expanding Universe

One of the major breakthoughs in the field of cosmology during the 20^{th} century was the discovery by Edwin Hubble that the Universe is expanding (Hubble, 1929). This expansion means that, ignoring the local peculiar velocity, galaxies are receding from us in every direction with a velocity which depends directly on their distance from us. This result is known as *Hubble's Law* and can be expressed quantitatively for a galaxy with a velocity $\vec{v}$ at a distance $\vec{r}$ as:

$$\vec{v} = H(t)\,\vec{r} \tag{1.1}$$

where $H(t)$ is the *Hubble constant*. The observable value of $H(t)$ in the present epoch is generally denoted by H_0. Throughout this thesis the subscript 0 will indicate the value of the variable in the present epoch.

At first sight Hubble's Law appears to imply that we occupy a special place in the Universe at the centre of the expansion. This would contradict the *Cosmological Principle* which states that the Universe is both isotropic and homogeneous and hence that there can be no favoured observers. However, consider two galaxies which are sufficiently distant from each other that the effects of gravitational binding and peculiar motion can be neglected. As the Universe expands over time, the proper physical distance between the two galaxies increases with observers in *both* galaxies seeing the same recession law, Equation 1.1. In fact, Equation 1.1 holds for all *comoving* observers, *i.e.*, observers who move along with the expansion. Hence there are no favoured observers and Hubble's law is in agreement with the Cosmological Principle.

A general metric to describe a dynamic, homogeneous and isotropic universe was put forward by H. P. Robertson and A. G. Walker in 1936 (see Weinberg (1972) for example):

$$ds^2 = c^2dt^2 - R^2(t)\left[\frac{dr^2}{1-kr^2} + r^2d\theta^2 + r^2\sin^2\theta d\phi^2\right] \tag{1.2}$$

This is known as the *Robertson-Walker metric*. It enables the definition of the interval ds^2 between events at any epoch or location in the expanding universe. The coordinates $(r,\ \theta,\ \phi)$ are comoving spherical polar coordinates. k is the *curvature constant* and takes the value 1, 0 or -1 depending on whether the Universe is closed, flat or open. $R(t)$ is the *scale factor* which describes how the spatial dimensions scale with time, t. The scale factor is related to the Hubble constant through the relation:

$$H(t) = \frac{\dot{R}(t)}{R(t)}$$

Redshift

The expansion of the Universe causes a shift in the frequency of spectral lines seen by an observer. This is known as *redshift*. The Robertson-Walker metric can be used to relate redshift to the scale factor of the expanding Universe.

Consider a light wave of frequency ν_e which leaves a distant galaxy at time t_e to arrive at an observer at time t_o (see Weinberg (1972)). Defining the co-ordinate system such that the observer sits at the origin, the wave travels towards the observer in the $-r$ direction with constant θ and ϕ co-ordinates. This allows the Robertson-Walker metric given by Equation 1.2 to be written as:

$$ds^2 = 0 = dt^2 - R^2(t)\frac{dr^2}{1-kr^2}$$

Integrating along the radial coordinate gives:

$$\int_{t_e}^{t_0} \frac{dt}{R(t)} = F(r_e) \tag{1.3}$$

where

$$F(r_e) \equiv \int_0^{r_e} \frac{dr}{\sqrt{1-kr^2}} = \begin{cases} \sin^{-1} r_e & k = +1 \\ r_e & k = 0 \\ \sinh^{-1} r_e & k = -1 \end{cases}$$

Assuming that the expansion of the Universe can be ignored on the timescale of the wavelength of light, the next light ray leaves the galaxy with the same r, θ and ϕ coordinates at time $t_e + \delta t_e$. The time $t_o + \delta t_o$ at which the second light ray arrives can be written in a similar manner to Equation 1.3:

$$\int_{t_e+\delta t_e}^{t_o+\delta t_o} \frac{dt}{R(t)} = F(r_e) \tag{1.4}$$

As the scale factor $R(t)$ is taken to be constant between the emission of the two light rays, Equation 1.3 can be subtracted from Equation 1.4 to give:

$$\frac{\delta t_o}{R(t_o)} = \frac{\delta t_e}{R(t_e)}$$

Thus the frequency of the emitted light ray, ν_e, is related to the frequency of the observed light ray, ν_o, by:

$$\frac{\nu_o}{\nu_e} = \frac{\delta t_e}{\delta t_o} = \frac{R(t_e)}{R(t_o)}$$

Redshift is defined as:

$$z = \frac{\nu_e - \nu_o}{\nu_o}$$

Thus the redshift is related to the expansion of the Universe through the scale factor as:

$$z = \frac{R(t_o)}{R(t_e)} - 1$$

The redshift can therefore be thought of as providing a measurement of how the wavelength of light stretches as the Universe expands. Thus, redshifts of distant galaxies can be obtained by observing the spectra of the light emitted by the elements they contain.

1.1.2 The Friedmann Equations

The expansion of the Universe can be expressed through the *Einstein field equation*:

$$G^{\mu\nu} = \frac{8\pi G}{c^2} T^{\mu\nu}$$

which relates space-time curvature to energy density. Here $G^{\mu\nu}$ is the Einstein tensor, $T^{\mu\nu}$ is the energy-momentum tensor and G is the gravitational constant. When Einstein first developed the theory of general relativity, it was thought that the universe was static. In order to allow a static solution to the field equations, Einstein added an addition term involving a new physical constant Λ, known as the *cosmological constant*:

$$G^{\mu\nu} - \Lambda g^{\mu\nu} = \frac{8\pi G}{c^2} T^{\mu\nu} \tag{1.5}$$

This new term was an *ad hoc* addition to the field equations and was quickly dropped by Einstein once the expansion of the universe was established. However, it has continued to reappear over the years and is now interpreted in terms of the energy density of the vacuum. As a consequence of this interpretation, the $\Lambda g^{\mu\nu}$ term nowadays typically appears on the right hand side of Equation 1.5. A review of the cosmological constant is given in Carroll *et al.* (1992).

Substituting the Robertson-Walker metric (Equation 1.2) into Equation 1.5 and assuming a perfect fluid leads to a pair of coupled equations known as the *Friedmann equations*:

$$\frac{\ddot{R}}{R} = -\frac{4\pi G}{3}\left(\rho + 3\frac{p}{c^2}\right) + \frac{\Lambda c^2}{2} \tag{1.6}$$

$$\left(\frac{\dot{R}}{R}\right)^2 = H^2 = \frac{8\pi G}{3}\rho + \frac{\Lambda c^2}{3} - \frac{kc^2}{R^2} \tag{1.7}$$

where p is the pressure and ρ represents the mass and radiation density. At the present epoch the radiation density is negligible and ρ will be taken to represent the mass density of the universe.

The three terms which drive the expansion of the Universe can be thought of, respectively, as a mass term, a cosmological constant term and a curvature term. Re-writing equation 1.7 to make these terms explicit with respect to their values in the current epoch gives:

$$1 = \Omega_M + \Omega_\Lambda + \Omega_k$$

where

$$\Omega_M \equiv \frac{8\pi G}{3H_0^2}\rho,\ \Omega_\Lambda \equiv \frac{\Lambda c^2}{3H_0^2},\ \Omega_k \equiv -\frac{kc^2}{R_0^2 H_0^2}$$

Thus the dynamics of the expansion of the Universe are described by just a few parameters. One of the main aims of astronomy is to try to obtain accurate values for the Hubble constant H_0, the density of matter in the Universe ρ and the cosmological constant Λ.

Hubble's Constant

Although Hubble's constant appears in many astrophysical calculations, it has proved to be difficult to obtain an accurate value for it. This is primarily due to the requirement for accurate distance measurements for cosmologically distant objects. Hubble's first measurement of $H_0 = 500\,km\,s^{-1}\,Mpc^{-1}$ resulted from his underestimation of galaxy distances. Indeed, it is only in the past few years that the various methods of measuring the Hubble constant have begun to produce a consistent value of $H_0 = 72 \pm 8\,km\,s^{-1}\,Mpc^{-1}$ (Freedman (2000), Freedman *et al.* (2000)).

The most common method of estimating distances to relatively nearby objects makes use of *standard candles*. These are objects whose luminosity is either constant or related to some property which is independent of distance, *e.g.*, colour or period of oscillation. The objects used as standard candles are calibrated against objects whose distance can be calculated from other observations. Clearly the accuracy of such a method depends on the accuracy of the calibration which, in turn, depends on understanding the underlying physical processes in the standard candle.

Among the most commonly used standard candles are Cepheid variables (Tanvir, 1999). These are variable stars whose periods generally vary between 2 to 100

days. The period of a Cepheid variable is directly related to its luminosity, providing a distant-independent method of obtaining its absolute luminosity. Cepheid variables are considered to provide a good distance indicator out to a range of around 20 Mpc. Beyond that, brighter objects, such as Type *Ia* supernovae or entire galaxies are required.

Type *Ia* supernovae are believed to result from the explosion of a carbon-oxygen white dwarf. Their high luminosity - comparable to that of moderately bright galaxies - means that they can be observed at far greater distances than can Cepheid variables (Branch, 1998). Their use as standard candles derives from the fact that they have a narrow spread of maximum luminosities and there appears to be a close relationship between the maximum luminosity and the rate at which the luminosity drops from this maximum. Currently the evidence for this relationship is purely empirical, as the mechanism which triggers the supernovae has yet to be established (Hillebrandt & Niemeyer, 2000). A further discussion of Type *Ia* supernovae as standard candles can be found in Chapter 5.

Techniques have also been developed for using galaxies as standard candles. The *Tully-Fisher* relation (Tully & Fisher, 1977) for spiral galaxies gives a correlation between the total face-on luminosity and the maximum rotational velocity of the galaxy. The relationship derives from the fact that more massive - and therefore more luminous - galaxies have to rotate more rapidly in order to support themselves. As rotation rate is independent of a galaxy's distance, it can be used to obtain a measurement of the absolute luminosity (Sakai *et al.*, 2000). A similar relationship exists for elliptical galaxies between the stellar velocity dispersion and luminosity (Faber & Jackson, 1976).

The methods for measuring H_0 outlined above are all *indirect* methods in that they rely on accurate calibration of the effect being measured. In contrast, gravitational lensing provides a method of measuring H_0 *directly*. Different images of the single source have the same underlying variations in luminosity. However, the difference in the paths of light in each image can lead to the apparent variations in luminosity being offset relative to other images. This time delay between different images can be measured to give a geometric estimation of H_0 (see §1.2.1 for further details of this method).

The density of matter in the Universe

The first estimates of the amount of matter in the universe (Hubble, 1926) were based on counts of galaxies and estimates of their mass derived from the gravitational energy required to keep the stars and gas within the galaxy. It was, however, obvious that this method failed to take into account matter outside the luminous parts of galaxies. Within a decade of Hubble's initial estimates, Zwicky (1933) and Smith (1936) measured of the velocities of galaxies within the Coma and Virgo clusters. These measurements allowed them to estimate the amount of mass required to gravitationally bind the galaxies moving at the observed velocity dispersions. Their results showed that if the Coma and Virgo clusters are gravitationally bound then their masses are about two orders of magnitude larger than can be accounted for by summing the luminous mass in their constituent galaxies. To account for the observations galaxies must contain *dark matter* in addition to the observed luminous matter.

Smith (1936) suggested that a more accurate estimate of the mass of a galaxy could be obtained by measuring the motion of material in the galactic halo. If a galaxy is in virial equilibrium then the mass within a distance r of the centre of the galaxy, $M(r)$, is related to its rotational velocity, v, as:

$$M(r) \propto \frac{v^2 r}{G}$$

The rotational velocity can be measured from the 21cm emission lines in HI regions. If most of the mass in the galaxy is associated with its luminous region, then $M(r)$ would be constant and $v^2 \propto 1/r$ outside this region. In practice this is not the case: many galaxies show almost flat rotation curves (Trimble, 1987) where $v \sim$ constant.

Evidence for dark matter in elliptical galaxies comes from X-ray emitting hot gas. Fabricant & Gorenstein (1983) and Stewart *et al.* (1984) mapped out detailed profiles of the temperature and density of the hot X-ray emitting gas regions in M87. These measurements can be used to determine the overall mass distribution in the galaxy necessary to bind the hot gas. Again, the total mass for the galaxy found by these measurements is far greater than the mass which can be directly observed. This discrepancy has been confirmed by similar estimates made for other elliptical galaxies.

Mass estimates for clusters of galaxies can also be made using gravitational lensing

techniques. As discussed in §1.2.1, distribution in the shapes of images of lensed galaxies can be used to produce a two-dimensional mass map for the cluster. As with the earlier work of Zwicky (1933) and Smith (1936), such mass maps show that clusters contain significantly more mass than can be accounted for by summing the mass estimates for individual galaxies.

On even larger scales, recent work on high redshift Type *Ia* supernovae and the results from the Boomerang and Maxima experiments have constrained the value for Ω_M to values far larger than can be accounted for by matter which can be directly observed. Both these experiments are discussed in more detail in the next section.

Estimates for values of Ω_M can be also be obtained from galaxy redshift surveys. Such surveys are distorted by the peculiar velocities of the galaxies along the line of sight. On large scales, where linear theory can be applied, the amplitude of these distortions can be used to measure the *linear redshift distortion parameter*, β (see Hamilton (1996)). β is related to Ω_M through the equation:

$$\beta \equiv \frac{\Omega_M^{0.6}}{b}$$

where b is the light-to-mass bias and provides an estimate of how closely the mass distribution follows the light distribution. Recent results based on the IRAS Point Source Catalog Redshift Survey (PSCz) give values of β of $0.41^{+0.13}_{-0.12}$ (Hamilton *et al.*, 2000) and 0.4 ± 0.1 (Ballinger *et al.*, 2000).

Having considered the observational evidence for the existence of dark matter in the universe, the obvious question becomes: What does dark matter consist of? The simplest answer is that it is baryonic material which is in some form other than visible stars. A number of candidates for dark baryonic matter, such as snowball-like objects made of hydrogen gas and hot and cold gas, were ruled out by Hegyi & Olive (1986) as they were either unstable or ruled out by observational evidence. The remaining possible candidates for baryonic dark matter can be divided into three main categories:

- *Very faint stars.* Estimates of the amount of baryonic matter in stars are based on counts of visible objects. Clearly there is some lower limit on the luminosity of observable objects below which they are not bright enough to be seen. Whether or not such 'invisible' stars contribute significantly to the amount of dark matter within a galaxy halo depends on the distribution

of mass in stars. Richer & Fahlmann (1992) found that, while the number of stars increases for smaller masses, there appears to be an insufficient amount of mass in this form to account, on its own, for the amount of dark matter implied by rotation curves.

- *Sub-stellar objects with insufficient mass for fusion to occur.* In order for fusion to occur, a star must have a mass of greater than $0.08 \pm 0.01 M_{\odot}$ (Peacock, 1999). If its mass is smaller than this limit, then an object can only generate energy gravitationally. Such objects are known as *brown dwarfs*. Limits on the amount of matter contained in brown dwarfs have been obtained from microlensing surveys. The results of these surveys are discussed in §1.3.

- *Stellar remnants.* Objects such as white dwarfs, neutron stars and black holes are formed at the end of the life-cycle of massive stellar objects. When stars leave the main sequence they eject heavy elements. Thus, the existence of a large population of stellar remnants would effect the chemical composition of the inter-stellar medium and of new stars.

A major constraint on the amount of dark matter which could be in any of the forms outlined above comes from Big Bang Nucleosynthesis (BBN). Nucleosynthesis arguments set a limit on the baryon density of $\Omega_B \approx 0.03 - 0.05$ for $H_0 = 70\, km\, s^{-1}\, Mpc^{-1}$ (Olive *et al.*, 2000). However, the observational evidence suggests that Ω_M is at least 0.2 (Peacock, 1999). Thus some form of *non-baryonic* matter is required to bridge the difference between the amount of baryonic matter allowed by BBN arguments and the observational evidence for Ω_M.

A number of non-baryonic particles have been proposed. These range from massive neutrinos to more exotic particles such as axions. Non-baryonic particles can be grouped according to when they *decouple*. Decoupling occurs when a particle's mean free path exceeds the horizon size at that time. This results in the particle's abundance being frozen at its thermal equilibrium value at the time when decoupling occurred. Non-baryonic particles can be divided into three general classes:

- *Hot Dark Matter (HDM).* In this case particles decouple when they are still relativistic and their number density is similar to that of photons. They are

called *hot* to denote their large velocities. The velocities of non-baryonic particles in HDM models has implications for the formation of structure in the Universe. High velocity particles tend to stream towards under-dense regions resulting in a more uniform density. This results in structure forming from the top down.

- *Warm Dark Matter (WDM).* In the WDM model particles are still relativistic when they decouple but they decouple much earlier. This allows the relative number of photons to be increased by particle interactions. That larger proportion of photons results in non-baryonic particles with mass roughly an order of magnitude higher than for HDM and a number density roughly an order of magnitude lower. More density fluctuations survive than within the HDM model and thus structure formation begins with smaller structures.

- *Cold Dark Matter (CDM).* Within CDM models the non-baryonic particles decouple while non-relativistic and streaming of particles into low density regions no longer occurs. This means that structure formation can occur from the bottom up with the initial formation of small structures which can then merge to form larger ones.

A number of potential new particles have been put forward as possible candidates for non-baryonic dark matter. These can be combined with the models outlined above (or some combination of these models) to mimic a structure formation hierarchy which matches current observations. Discussions about the different particles proposed as candidates for non-baryonic dark matter are likely to continue until their existence (or absence) can be established experimentally.

A cosmological population of compact objects such as primordial black holes (PBHs) could provide an alternative solution to the question of the nature of non-baryonic dark matter. PBHs can be formed during the quark-hadron phase transition when dense regions collapse (Crawford & Schramm, 1982). While PBHs are made of *baryonic* material, they are formed before nucleosynthesis occurs. This means that they are exempt from the limits placed on the amount of baryonic material in the Universe.

The Cosmological Constant

The *cosmological constant* was originally introduced by Einstein in order to obtain a steady state solution to the field equation. However, once the expansion of the Universe had been established it fell out of favour, with Einstein himself famously describing it as "the biggest blunder of my life."

Over the last few years, the cosmological constant has again re-appeared as a means of reconciling theory with observation. The motivations for re-introducing the cosmological constant are outlined in Lahav *et al.* (1991):

- The value for the age of the Universe for $\Omega_\Lambda = 0$ models with $H_0 \sim 70\,km\,s^{-1}\,Mpc^{-1}$ is less than the age of globular clusters (Reid, 1997). For a fixed value of Ω_M, increasing Ω_Λ increases the age of the Universe.

- The theory of inflation requires that $k = 0$ in Equation 1.7. Observational evidence (Perlmutter *et al.* (1999), Riess *et al.* (1998) and Susperregi (2001)) seems to indicate that $\Omega_M \approx 0.3$. Thus a positive value for Ω_Λ is necessary to fit with inflation's $k = 0$ requirement.

- The number counts of galaxies at high redshift are incompatible with $\Omega_M = 1$. As discussed in detail in Carroll *et al.* (1992), the variation of spatial volume with redshift varies considerably with Ω_Λ.

- 'Standard' CDM models with $\Omega_M = 1$ produce substantially less large scale structure than is indicated by observations (Efstathiou *et al.*, 1990).

Thus, there are both observational and theoretical motives for including a positive value of Ω_Λ in cosmological models. In addition, there exist a number of methods for estimating the value of Ω_Λ: these include high redshift supernovae and measurements of the angular power spectrum of the Cosmic Microwave Background (CMB).

- *High redshift supernovae*
  The idea of using high redshift Type Ia supernovae to constrain the values of Ω_M and Ω_Λ was first put forward by Goobar & Perlmutter (1995). The technique is based on the relationship between the absolute magnitude, M,

and the apparent magnitude, m. These two quantities are related through the luminosity distance, d_l. The relationship can be expressed as:

$$m = M + 5\log d_l + K + 25$$

where K is a correction due to the difference in wavelengths between the emitted and detected photons from the receding source. The luminosity distance gives the relation between the rest frame luminosity of an object, $\mathcal{L}$, and its apparent flux, $\mathcal{F}$, (Carroll *et al.*, 1992):

$$d_l = \left(\frac{\mathcal{L}}{4\pi\mathcal{F}}\right)^{1/2}$$

d_l is related to the angular diameter distance, d_A, through the relation $d_L = (1+z)^2 d_A$ (see Appendix A for a derivation of the angular diameter distance, d_A). The luminosity distance can be written in terms of Ω_M and Ω_Λ:

$$d_l = -\frac{(1+z)}{\sqrt{|\Omega_k|}}\text{sinn}\left[c\sqrt{|\Omega_k|}\int_0^z \frac{[(1+\Omega_M z) - z(2+z)\Omega_\Lambda]^{-1/2}}{(1+z)}dz\right]$$

where

$$\text{sinn} = \begin{cases} \sinh & \text{if } k = -1 \\ 0 & \text{if } k = 0 \\ \sin & \text{if } k = 1 \end{cases}$$

Perlmutter *et al.* (1997) and Perlmutter *et al.* (1999) analysed the light curves from 42 Type *Ia* supernovae at redshifts of $0.18 \leq z \leq 0.86$. This data was combined with results from the low-redshift Calán/Tololo survey (Hamuy *et al.*, 1996) to obtain a value for Ω_M of 0.28 for $\Omega_M + \Omega_\Lambda = 1$ models. Similar results were obtained by Riess *et al.* (1998) for a set of 16 Type *Ia* supernovae at redshifts of $0.16 \leq z \leq 0.62$.

- *Angular power spectrum of the CMB*
  Primordial fluctuations in the early universe show up as anisotropies in the CMB. Density perturbations at the time of last scattering cause photons in high density regions to expend more energy escaping from deeper potential wells than photons in low density areas. This is observed as fluctuations in the temperature of the CMB. These fluctuations are thought to have grown through gravitational instability to form the large scale structure

seen today. Experiments such as Boomerang and Maxima measured the CMB anisotropies at a resolution of 10′ (Mauskopf *et al.* (2000) and Hanany *et al.* (2000)).

The results from these experiments were used to generate a power spectrum for the CMB. Sets of theoretical spectra were generated for a range of values of the various cosmological parameters. These sets were then compared with the experimental spectrum by evaluating a likelihood function for each of the model power spectra. This evaluation gives a measure of the probability of a particular set of model parameters being correct given the experimental data (Melchiorri *et al.* (2000), Balbi *et al.* (2000)).

The results from Boomerang and Maxima combined with earlier data from COBE/DMR (Bennett *et al.*, 1996) give $\Omega_M = 0.49 \pm 0.13$ and $\Omega_\Lambda = 0.63^{+0.08}_{-0.09}$ (Jaffe *et al.*, 2000). When this CMB data is combined with the Type 1a supernova results discussed above they give a combined value of $\Omega_M = 0.37 \pm 0.07$ and $\Omega_\Lambda = 0.71 \pm 0.05$ (Jaffe *et al.*, 2000).

1.2 Gravitational Lensing

There are a number of different observational techniques used to investigate the distribution of matter within the Universe. However many of them, such as X-ray emission from hot gas, only deal with matter in certain specific forms. Gravitational lensing provides a method of directly investigating the gravitational potential of matter. As such it is independent of the properties of matter. This feature has led to it becoming a widely used tool for understanding the fundamental parameters of the Universe.

Consider an observer looking at a distant quasar through a telescope. Light from the quasar may be bent by the gravitational potential of a galaxy situated along the line of sight between the observer and the quasar. This can result in the observer seeing multiple images of the quasar (see Figure 1.1). This effect is known as *gravitational lensing* with the intervening galaxy acting as a *gravitational lens.*

The theory of gravitational lensing remained an intellectual curiosity until the discovery in 1979 of the double lensed quasar Q0957+561 by Walsh *et al.* (1979). This lensing system consists of two images, A and B with a redshift of 1.41,

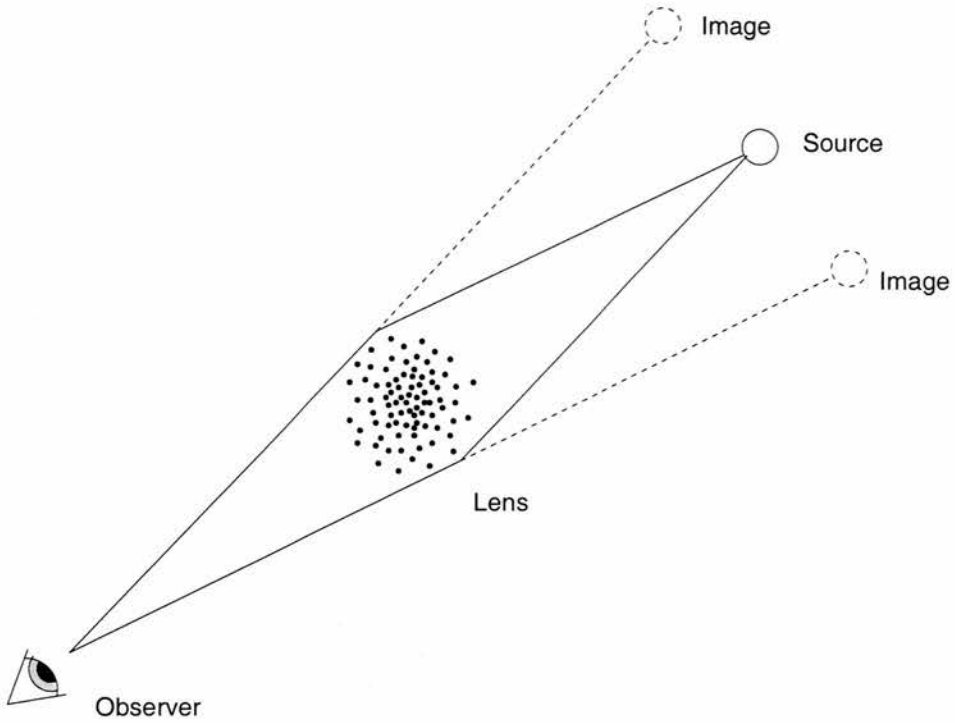

Figure 1.1: Light from a distant quasar is bent by the intervening galaxy.

separated by 6″. This discovery showed that gravitational lenses existed and could be observed. Since then lensing has become one of the most important tools for understanding the Universe.

1.2.1 Applications of Gravitational Lensing

As mentioned above, the gravitational lensing effect depends on the gravitational potential of matter and is independent of the form of the matter. These properties have made lensing an effective tool for increasing our understanding of the Universe. This section outlines some of the applications of lensing.

For general reviews of gravitational lensing and its applications, see Blandford & Narayan (1992), Refsdal & Surdej (1994), Wu (1996), Wambsganss (1998) and Claeskens & Surdej (2000). Schneider *et al.* (1993) set out the theoretical background for gravitational lensing.

Modelling individual lensing systems

Observations of lensed quasars can be used to determine the mass of the lensing galaxy. However, it is important to establish how objects can be identified as

images of a single source rather than simply quasars which happen to be located close to each other. Wambsganss (1998) lists five criteria which can be used to establish if objects are lensed:

- There are two or more point-like images of similar optical colour.
- The redshifts of the images are identical or very similar.
- The images' spectra are also identical or very similar.
- A lensing object can be identified between the images. The potential lens should have a much smaller redshift than the images.
- The images should have similar patterns of variability, although there may be a lag between the images.

Most identified lensing systems meet only a subset of these criteria. There are a number of reasons why not all the criteria cannot be met. For example, dust absorption may affect the spectra of one of the images or the lensing galaxy may be too faint to observe. A list of $\sim$ 60 lensing candidates together with their observational parameters and theoretical models has been made available by the CASTLES survey (Kochanek *et al.*, 1999).

Once the images have been identified as part of a lensing system, the mass of the lensing galaxy can be estimated. In the case where a source is located directly behind a spherically symmetric deflector, a ring shaped image, known as the *Einstein ring*, will be formed (see §2.1.1). The radius of the Einstein ring, θ_E, gives a direct measurement of the amount of mass located within the Einstein radius. Even in cases where the lensing system is not sufficiently aligned to have an Einstein ring as an image, θ_E remains a fundamental parameter of the lensing system and its value can be estimated from the position of the images.

The small size of quasars makes it highly unlikely that there will be sufficient alignment within a lensing system to produce an Einstein ring image. However, more extended radio sources have produced Einstein rings. The first radio ring, MG 1131+0456 (Hewitt *et al.*, 1988), has a diameter of around 1.75 arcsec. The source has been identified as a radio lobe at $z = 1.13$ with the lens a galaxy at $z = 0.85$. A number of radio rings have now been found (Langston *et al.* (1989), Jauncey *et al.* (1991), King *et al.* (1998) and Kochanek *et al.* (2000)), some

with optical or infrared counterparts. Many of the sources identified have both compact and extended components. Some of the compact sources are variable - providing a means to measure time delay and the Hubble constant H_0 (see below).

Number Counts

As well as providing information on the mass of the lensing galaxy, the distribution of lensing systems and their observational parameters can be used to provide information on cosmological parameters.

For example, the frequency of lensing events can be used to constrain Ω_M and Ω_Λ. The angular diameter distance to the source and lens depends on both Ω_M and Ω_Λ. For an object at a particular redshift, lowering the value of Ω_M increases the distance to the object, while lower values of Ω_Λ decrease the distance. Thus the volume in which lensing can occur varies with Ω_M and Ω_Λ.

The first theoretical study of the distribution of gravitational lenses was carried out by Turner *et al.* (1984). Fukugita *et al.* (1992) extended this work to include cosmologies with a non-zero cosmological constant. The first comparisons between theory and observation were made by Maoz *et al.* (1993), Surdej *et al.* (1993) and Kochanek (1993) who all found that roughly 1% of all quasar images have been lensed. However, the small number of lensing systems found made it difficult to extract values for Ω_M and Ω_Λ. For example, Maoz *et al.* (1993) concluded that the frequency of lensing events is inconsistent with large values of Ω_Λ; Kochanek (1993) suggests an upper bound for Ω_Λ of between $0.45 - 0.8$; and Surdej *et al.* (1993) felt that it was hazardous to use the data available at that time to estimate Ω_Λ.

More recent surveys, such as CLASS (Browne & Myers, 2000), JVAS (King *et al.*, 1999) and CASTLE (Falco *et al.*, 1999) have increased the number of confirmed gravitational lenses. Results from these surveys give lower and upper bounds on $\Omega_\Lambda - \Omega_M$ of -1.78 and 0.27 respectively (Helbig *et al.*, 1999). For a flat universe, this leads to an upper limit on Ω_Λ of 0.64, close to the values obtained from high redshift supernovae and CMB anisotropies.

Measuring the Hubble constant H_0

The idea of using gravitational lensing systems to measure H_0 was first put forward by Refsdal (1964). Refsdal realised that the time delay between the two lensed images of a variable source is proportional to the absolute scale of the lensing system. Thus, the time delay provides an independent method of measuring H_0 which does not rely on standard candles.

In principle, H_0 can be determined simply by monitoring the variation in apparent luminosity between images over some period of time. If the monitoring period is longer than the time delay it should be possible to obtain an accurate measurement of the time delay. However, it is not always straightforward to obtain good quality, comparable light curves for different images. The light curves are discretely sampled and different images may be sampled at different intervals. In addition *microlensing* by individual stars within the lensing galaxies (see §1.3) can cause additional variations in the apparent luminosity. One of the most intensively studied gravitational lensing systems is the double lens Q0957+561A,B, the 'original' lensing system discovered in 1979. This system has been extensively monitored for over 20 years. However, it was only after the observation that an unusually distinctive event in image A was repeated in image B that a value for the time delay of 417 days was established (Kundic *et al.*, 1997).

Even after the time delay for a system has been established, the value obtained for H_0 depends on the lensing model used. While the error due to the lack of firm values for Ω_M and Ω_Λ is not large for source and lens redshifts of less than ~ 2.0 and ~ 0.5 respectively (Claeskens & Surdej, 2000), the requirement of accurate knowledge of the lens mass distribution can difficult to fulfil. Frequently a number of different lens models will reproduce the observed parameters of the lensing system but result in different values of H_0.

While there are a number of difficulties in using gravitational lensing systems to measure H_0, the method has a number of advantages over the other methods outlined in §1.1.2:

- The lensing systems are at high enough redshifts that the effects of peculiar velocity can be ignored.
- Gravitational lensing provides an independent measure of H_0. Other methods which rely on distance ladders to get to high redshift are prone to errors

in calibration.

- It is based on fundamental physics. Other methods rely on the correct models for standard candles.

The most promising method of obtaining a value of H_0 from lensing systems comes from monitoring lensed radio sources. Radio sources have a more extended structure than quasar sources, permitting the observation of complete and partial Einstein rings. The structure observed in the images of radio sources provides additional information on the mass distribution of the lensing system, helping to constrain the lensing model. Also, the images of the radio sources so far studied have smaller separations than those obtained from quasar sources and thus smaller time delays. As long as the source varies intrinsically on a smaller timescale than the time delay, such systems should require less monitoring to obtain a value for the time delay. Finally, the size of the radio sources makes it unlikely that microlensing will affect the light curves. Thus, the light curves obtained from different radio images should be in reasonable agreement.

Current estimates of H_0 from lensing include $69^{+13}_{-19}\,km\,s^{-1}\,Mpc^{-1}$ from B0218+357 (Biggs *et al.*, 1999), $60^{+15}_{-12}\,km\,s^{-1}\,Mpc^{-1}$ from B1600+434 (Koopmans *et al.*, 2000) and $63^{+7}_{-6}\,km\,s^{-1}\,Mpc^{-1}$ from B1608+656 (Koopmans & Fassnacht, 1999) with $\Omega_M = 0.3$ and $\Omega_\Lambda = 0.7$. These values are in close agreement with those obtained using standard candles (see §1.1.2).

Lensing in clusters

The existence of giant arcs in galaxy clusters was first reported by Soucail *et al.* (1987) and Lynds & Petrosian (1986). The idea that these arcs could be the images of background galaxies lensed by the foreground cluster was put forward by Paczyński (1987). Subsequent measurements of the redshifts of both the arc and the galaxy cluster (Soucail *et al.*, 1988) confirmed that the redshift of the arc was significantly higher than the cluster.

To make an effective lens, a cluster of galaxies must be sufficiently centrally concentrated to produce critical curves. Prior to the discovery of giant arcs it had been thought that the cores of clusters were not sufficiently dense to produce critical curves. Such arcs lie close to the critical curve which marks the Einstein ring and can be used to estimate the value of θ_E. As with single galaxy lensing

systems, if the redshifts of the cluster and the arc are known, a good approximation should be obtainable for the mass of the core of the cluster. Initially, estimates of the central mass of clusters derived from X-ray observations proved to be 2–3 times smaller than the gravitational lensing results suggest (Miralda-Escudé & Babul, 1995). However, these discrepancies have been resolved with the development of more complex models which account for the effects of cooling flows on X-ray data (Allen, 1998).

While giant arcs can be used to measure the core mass of a cluster, the distribution of weakly lensed galaxies can be used to construct a detailed map of the mass distribution of the cluster. These weakly lensed galaxies, commonly referred to as *arclets*, were first identified by Fort *et al.* (1988) who noticed a number of faint, elongated objects in a study of A370. While a change in shape might not be obvious for an individual arclet, the effect of the weak lensing on each object is not independent – it produces a coherent deformation over a number of objects. This makes it possible to measure the effect over a group of arclets. A technique to use the correlation in the ellipticity and orientation of cluster galaxies to map the dark matter distribution of the cluster was put forward by Tyson *et al.* (1990) and Kaiser & Squires (1993). Since then, weak lensing has been used to estimate the mass distributions of a number of clusters (see, for example Bonnet *et al.* (1994), Broadhurst (1995), Smail *et al.* (1997a) and Clowe *et al.* (2000)). A review of weak lensing and its applications can be found in Mellier (1999).

In addition to providing a direct measurement of the mass of a cluster, the structure of the arcs can also be used to study the structure of a high redshift source galaxy. Galaxies lying close to critical curves along our line of sight will be strongly magnified, making it possible to observe galaxies which would otherwise be too faint to see. Thus, the study of high redshift lensed galaxies can provide important information on the formation and evolution of galaxies (Smail *et al.* (1997b), Pelló *et al.* (1999)).

Weak Lensing by Large Scale Structure

Understanding the large scale distribution of matter in the universe is a major goal for cosmology. However, most observational techniques only provide measurements for luminous matter, although it is known that the majority of the matter in the universe is in some form of dark matter. Gravitational lensing

provides a method of directly measuring the gravitational effect of both luminous and dark matter. This idea – that the large scale structure of the universe could cause distortions in the images of galaxies – was first put forward by Kristian & Sachs (1966) and Gunn (1967).

Kaiser (1992) showed that the power spectrum of the weak lensing distortion can be directly related to the mass fluctuation power spectrum. This means that weak lensing can provide a direct measurement of the mass fluctuations predicted by different cosmological models without making any assumptions about their origins. However, the effect of lensing by large scale structure is very weak and a large number of galaxies have to be imaged with great care before a coherent effect can be observed.

The first theoretical predictions of the statistical distribution of distortions expected from the large scale structure were carried out by Jaroszyński *et al.* (1990), Bartelmann & Schneider (1991), Blandford *et al.* (1991) and Miralda-Escudé (1991) for an Einstein-de Sitter universe. These results were generalised for different cosmological models by Villumsen (1996). More recently, the increase in sophistication of N-body simulations has resulted in more complex models of dark matter distribution which can be used to simulate the effects of weak lensing (for example Wambsganss *et al.* (1998) and Jain *et al.* (2000)).

The weakness of distortions caused by lensing by the large scale structure makes the effect susceptible to noise and observational distortions. Nevertheless, recent observational surveys have detected the effects of weak lensing (Bacon *et al.* (2000) and Van Waerbeke *et al.* (2000)). These results seem to be in agreement with the current popular cosmological model with $\Omega_M = 0.3$ and $\Omega_\Lambda = 0.7$. Results from future, larger surveys should improve the constraints on the cosmological models.

1.3 Microlensing

The images of lensed quasars were discussed in the previous section as though they resulted from lensing by a smooth distribution of matter. However, we know that this is not the case and that galaxies consist, in part at least, of a collection of compact objects such as stars, planets and brown dwarfs. In addition, the typical separation of the quasar image from the centre of the lensing galaxy is in the order of $1''$, smaller than the radius of a typical lensing galaxy. Thus the

light from the quasar image must pass through the edge of the galaxy. As the separation of the images formed by individual stars is proportional to the mass of the star, for a typical star the image separation would be $\sim 10^{-6}{}''$ – too small to resolve. However, the presence of a number of such objects, each moving relative to the quasar image, leads to a variation of the apparent brightness of the quasar images with time. This effect, first described by Chang & Refsdal (1979), is known as *microlensing*. The microlensing objects were christened MACHOs[1] by Griest (1991) as an alternative to the WIMP[2] class of dark matter.

Variations in the apparent brightness of quasar images caused by microlensing are independent of the intrinsic variation of the quasar. In addition, as light rays from different images pass through different regions of the lensing galaxy, the effects of microlensing will be different in each image. As discussed in the previous section, microlensing can cause difficulties in measuring the time delay in the intrinsic variation of the source quasar between different images.

Gott (1981) suggested using microlensing of quasar images to study the population of the lensing galaxy's halo. The recent agreement on a time delay of 417 days for the lensed quasar 0957+561 A,B (Kundic *et al.*, 1997) has enabled the intrinsic variability of the quasar source to be subtracted from the image variability to produce microlensing lightcurves. These results have been used to investigate the mass and number density of MACHOs. For example, Refsdal *et al.* (2000) looked at a number of different microlensing population models. They found that, for cases with between 100% and 10% of the halo mass modelled as MACHOs, lens masses could only be constrained to the range of $M_{\odot}^{-6}$ to $5M_{\odot}$. Wambsganss *et al.* (2000) used shorter time scale data for Q0957+561 A,B to *exclude* MACHOs in the mass range $M_{\odot}^{-6}$ to $M_{\odot}^{-2}$.

The idea that it might be possible to measure microlensing events caused by lenses *within* our own galaxy was put forward by Paczyński (1986). He suggested that it would be possible to investigate the population of MACHOs in the Milky Way halo by monitoring the variation in the apparent brightness of stars in the Large Magellanic Cloud (LMC). If such a population exists, a MACHO's critical curve should intermittently pass close to the line of sight to a background star, causing a variation in that star's apparent brightness on a timescale which is dependent on the mass of the MACHO. Such events have a number of features

[1] *M*assive *A*strophysical *C*ompact *H*alo *O*bjects
[2] *W*eakly *I*nteracting *M*assive *P*article

which allow them to be distinguished from variable stars:

- The density of MACHO objects in the galactic halo is such that there should only be one microlensing event observed in any given star's light curve. In contrast, the light curves of variable stars vary periodically.
- Gravitational lensing is independent of wavelength. Thus the colour of the star should not change during the microlensing event. Variable stars, in contrast, tend to change colour as their temperature changes during their period of variation.
- Microlensing events have characteristic shapes with sharp peaks and broad wings (see Figure 1.2).

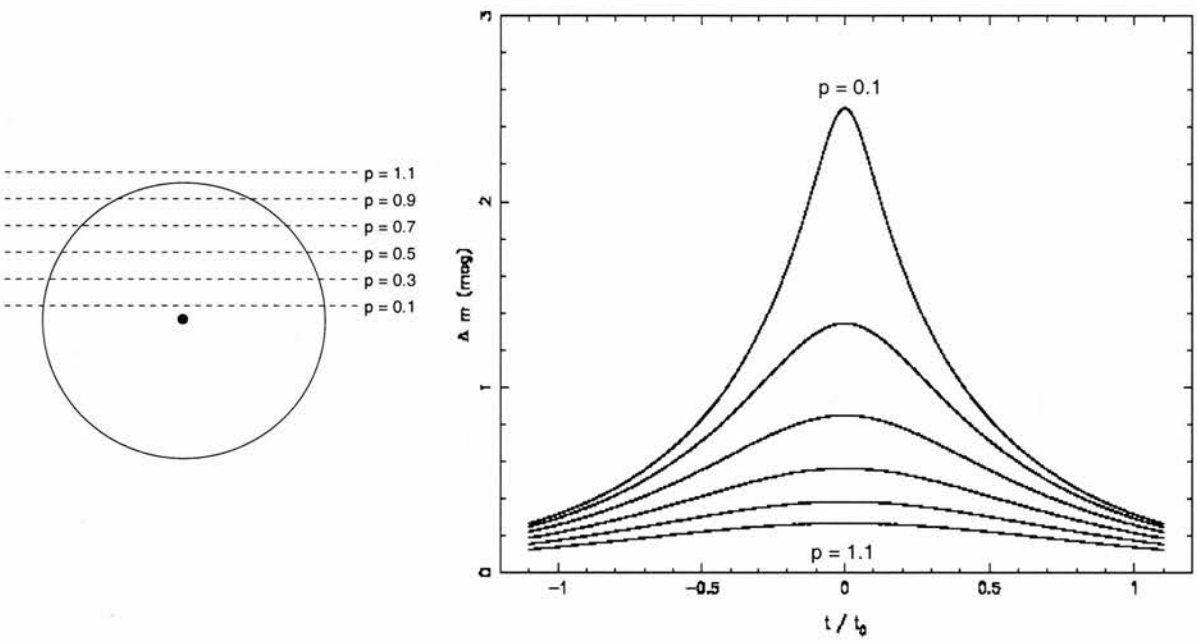

Figure 1.2: Variation in magnification for a microlensing event.

In addition to showing the existence of compact objects in the galactic halo, measurements of the characteristics of microlensing events can be compared with predictions from different models of the galaxy. The number of microlensing events observed can also be used to measure the *optical depth* of microlensing through different parts of the Milky Way. The optical depth gives the mean number of lenses where the line of sight between observer and background source

passes within an Einstein radius of a lens. Thus it provides a measurement of the density of lenses along a particular line of sight. The theory and practice of microlensing studies within the Milky Way and neighbouring galaxies is reviewed in Paczyński (1996)

Paczyński's proposal led to the MACHO[3], EROS[4] and OGLE[5] observational surveys being instigated in an attempt to identify microlensing events in the light curves of background stars in the LMC and towards the galactic bulge. The first microlensing events were reported by Alcock *et al.* (1993) (MACHO) and Aubourg *et al.* (1993) (EROS) towards the LMC and by Udalski *et al.* (1993) (OGLE) towards the galactic bulge. These were followed by the first detection of microlensing by a binary system (Udalski *et al.*, 1994) and detections towards the Small Magellanic Cloud (SMC) (Alcock *et al.*, 1997) and in the Galactic disk (Derue *et al.*, 1999).

In addition, a number of other collaborations have been set up: AGAPE[6] are trying to detect microlensing events towards the Andromeda galaxy; PLANET[7] are looking for "wiggles" in the light curves of the microlensing events caused by planets orbiting the lens; DUO[8] are monitoring microlensing events towards the Galactic bulge.

The MACHO consortium have now looked at 11.9 million stars in the LMC and found between 13 and 17 microlensing events (Alcock *et al.*, 2000). From their observations they estimate the optical depth towards the LMC to be $1.2^{+0.4}_{-0.3} \times 10^{-7}$ with an additional systematic error of around 20% to 30%. From this data they find the best fit model predicts around 20% of the dark matter content of the Galactic halo in the form of MACHOs in the range $0.15 - 0.9 M_{\odot}$. The EROS collaboration found 3 microlensing events towards the LMC and 1 towards the SMC. Their results constrain the amount of mass in the range $10^{-7} M_{\odot} - 4 M_{\odot}$ and, in particular, exclude the possibility that the Galactic halo consists of more than 40% MACHOs with a mass of up to $1 M_{\odot}$ (Lasserre *et al.*, 2000). Although the small number of microlensing events detected make analysis of the data prone to

[3] `http://wwwmacho.mcmaster.ca/`

[4] Expérience de Recherche d'Objets Sombres, `http://www.lal.in2p3.fr/recherche/eros`

[5] Optical Gravitational Lensing Experiment, `http://bulge.princeton.edu/~ogle/`

[6] Andromeda Galaxy Amplified Pixel Experiment, `http://cdfinfo.in2p3.fr/Experiences/AGAPE/`

[7] Probing Lensing Anomalies NETwork, `http://www.astro.rug.nl/~planet/`

[8] Disk Unseen Objects

statistical errors, the results from both MACHO and EROS collaborations agree surprisingly well. In particular, both sets of results rule out the possibility that the Milky Way halo consists entirely of MACHOs. Thus, some other form of dark matter is still required to explain observed rotation curves.

Such microlensing search programmes have provided direct evidence that microlensing can be observed in the lightcurves of background objects. The data from these searches has been used to constrain the total mass and the mass range of the lensing objects within our galaxy. This thesis investigates whether similar techniques can be used to determine whether a cosmological population of primordial black holes could be detected via microlensing of background objects and whether this could be used to determine the fraction of Ω_M which exists in this form.

1.4 Microlensing by a cosmological population of compact objects

As discussed in §1.1.2, it is not yet possible to observationally account for all the mass measured in the Universe. One possible explanation is the existence of a population of compact objects such as primordial black holes (PBHs). Such a population, distributed on a cosmological scale, could account for a significant proportion of the so-called dark matter.

The possibility of using gravitational lensing to detect a cosmological population of compact objects was first proposed by Press & Gunn (1973). They considered the possibility of detecting such objects by looking for image splitting in high redshift quasars. A lensing mass of $10^4 M_\odot$ would result in the image being split by $\sim 10^{-4}$ arcsec and would be detectable by radio VLBI. They considered a number of different values of Ω_M finding that the lensing effect was small for $\Omega_M \ll 1$ due to the corresponding low probability of lenses along the line of sight to the quasar. The lensing effect becomes larger as Ω_M increases, with practically every line of sight to $z \sim 1$ being lensed in an $\Omega_M = 1$ universe. In particular, they showed that for fixed values of Ω_M the lensing effect of compact objects in a particular mass range is directly proportional to the density of objects in that mass range. They concluded that it should be possible to constrain the density of compact objects with a mass greater than $\sim 10^4 M_\odot$ in this way.

Canizares (1982) looked at the effect of a cosmological population of compact objects in the mass range $0.01 < M < 10^5 M_\odot$ on the properties of high redshift quasars. For this range of masses the quasar can be treated as extended sources and lensing effects should show up through asymmetries in line profiles and variations in the line-to-continuum ratios as well as producing large-amplitude variations in flux. Canizares concludes that the widespread absence of such effects from observations excludes a density of $\Omega_M = 1$ in such objects.

The aim of this thesis is to investigate the effect of a population of compact objects on both the long term variability of the apparent luminosity of quasars and on the on-going efforts to measure cosmological parameters using high redshift supernovae.

1.4.1 The long term variability of quasars

As discussed in §1.3, it is now generally accepted that some quasar variability is caused by microlensing. There have been a number of investigations into this effect (see Kayser *et al.* (1986), Schneider & Weiss (1987), Refsdal & Stabell (1991), Refsdal *et al.* (2000) and Wambsganss *et al.* (2000) for examples). Such studies have, however, concentrated on the short-term variation caused by microlensing effects in a lensing galaxy. In addition to the short-term variation in the apparent luminosity of quasars there is also a longer term variation, with a period of ~ 10 years. The short-term variability is typically accompanied by other phenomena such as radio emission which indicates that the variability of the apparent luminosity is linked to the intrinsic properties of quasars. The long-term variability, however, is not linked with such phenomena and its origin is less well understood (Rees, 1984).

The idea that the long-term variation of the apparent brightness of quasars was due to lensing by a population of PBHs was put forward by Hawkins (1993). This proposal was based analysis of the data from a long term monitoring program of ~ 300 quasars (Véron & Hawkins, 1995). Hawkins (1996) identified a number of features which were difficult to interpret in terms of an intrinsic mechanism. These features, discussed in detail in Hawkins (1996), include:

- *The timescale of the long-term variation appears to be independent of redshift.* If the variation were due to some intrinsic property of the quasar then

it would be expected that time dilation effects would cause the timescale of the variation to increase with redshift by a factor of $(1 + z)$. However, if the effect were due to microlensing, the timescale would increase with the redshift of the lens, not the quasar. It has been argued that as the most effective lenses are at a redshift of $z \approx 0.5$ (Turner *et al.*, 1984), one would not expect to see a significant time dilation in the quasar survey. However, lensing can be effective over a wide range of redshifts (Turner *et al.*, 1984) so some change in timescale with quasar redshift would be expected.

An investigation into the effect of microlensing on the relationship between redshift and variability was carried out by Alexander (1995). Although he concluded that his results ruled out microlensing by a uniform distribution of microlenses, this was based on fitting to a reported decrease in the timescale with redshift (Hawkins, 1993). More recent results (Hawkins, 1996) reduce the significance of this decrease to the point where it may be possible to fit Alexander's model to the observed data.

Baganoff & Malkan (1995) proposed a model in which the lack of dependence of the timescale of variability on redshift could be explained in terms of intrinsic properties of the quasar. This model results in the timescale of the variations increasing with decreasing optical wavelength, thus cancelling out the effect of time dilation at high redshift. As pointed out in Hawkins & Taylor (1997) such an model would also result in a change in the structure of quasar lightcurves with wavelength. However, as discussed below, the majority lightcurves for the quasar samples are achromatic.

- *There is evidence of a correlation between the amplitude of the variation and the luminosity but not between the amplitude and redshift.* Attempts to model quasar variability either through propagation of instabilities across a quasar accretion disk or through supernovae powered quasars do not reproduce the observed correlations with luminosity and redshift (Hawkins, 2000). For the microlensing model, the lightcurves are considered to be a non-linear combination of the effects of the individual lenses. Schneider & Weiss (1987) showed that with microlensing by a large optical density of lenses, even though the overall magnification is large, the variation in magnification is generally small, ~ 0.5 magnitudes. This is similar to the observed data (see Hawkins (2000)).

- *Nearby quasars do not appear to exhibit long-term variation.* For microlensing to have a significant effect there must be a reasonable density of lenses. For low redshift quasars, the probability of lensing would decrease and the effect of microlensing on the luminosity of the quasar would become progressively smaller. The survey data shows that for quasars with $z < 0.3$ there is little evidence of variation on timescales longer than a year. As the redshift increases to $z > 0.5$, the long-term variation becomes increasingly clear. This is about the same redshift at which any microlensing effects would become apparent.

- *There is a statistical symmetry between the rising and falling parts of the light curves.* The light curves of individual microlensing events are extremely symmetrical, see Figure 1.2. While such strong symmetry would not be expected in the individual features of lightcurves for objects with a large optical depth, there should be some statistical symmetry between the rising and falling parts of the lightcurves. Analysis of the light curves show that there is a very close symmetry between increasing and decreasing magnitudes. Mechanisms for intrinsic variability tend to produce asymmetric features in the lightcurves and symmetry between rising and falling parts of the lightcurves would not be expected.

- *The quasar lightcurves are achromatic.* As discussed in §1.3, one of the main features of microlensing events is that the lightcurves are achromatic. Conversely, mechanisms for intrinsic variation would tend to produce different lightcurves at different wavelengths. The majority of quasars in the sample have achromatic lightcurves. The few which aren't achromatic have features which are consistent with a colour gradient across the quasar disk.

While it is clearly difficult to make detailed observations of objects whose period of variability is ~ 10 years, the quasar survey of Véron & Hawkins (1995) provides an excellent observational basis for investigating the long-term variability of quasars. Moreover, the data shows a number of features which are not easily explained by quasar models but could be consistent with the quasars undergoing microlensing by a cosmological population of compact objects.

An initial study of the effects of microlensing by a cosmological population of compact objects was carried out by Schneider (1993) who looked at the effect of

a random population of compact objects on an extended source. The simulation results showed that the existence of a cosmological distribution of compact objects would indeed cause a variation in the apparent luminosity of background quasars. Taking the results of Hawkins & Véron (1993) to represent an upper bound on the long-term variability of quasars, Schneider finds that the upper bound on the mass of compact objects in the mass range $10^{-3}M_{\odot} < M < 10^{-2}M_{\odot}$ is about $0.1\Omega_M$. However, these simulations assumed that the magnification of individual lenses can be multiplied to give a total magnification. Pei (1993) showed that for some situations this is a reasonable approximation and it has been widely applied. However there are a number of simple lensing situations where it fails. In addition, the results are based on only on the maximum flux variation over a 10 year time period published in Hawkins & Véron (1993) rather than on the lightcurves themselves.

In order to extend the work presented by Schneider (1993), a computer model has been developed to simulate a 3-dimensional cosmological distribution of compact objects. The simulation has been designed to make use of massively parallel computers allowing for more realistic simulations. In particular, this has allowed the assumption that magnifications can be multiplied to be avoided. Chapter 2 outlines the theoretical background to the model, while the implementation itself is described in Chapter 3. A detailed comparison of the lightcurves produced by the simulation with those from the observational survey is presented in Chapter 4.

1.4.2 Measurements of high redshift supernovae

The existence of a cosmological population of compact objects would have consequences for observations of high redshift objects. The microlensing effects of such objects would result in an additional variation in apparent luminosity on top of any observational and intrinsic effects. The idea that supernovae can be used to investigate the presence of compact objects was put forward by Linder *et al.* (1988) and Rauch (1991). The recent publication of results from high redshift supernovae projects (Perlmutter *et al.* (1999) and Riess *et al.* (1998)) has resulted in a number of investigations into the effect of lensing on the results (Seljak & Holz (1999), Metcalf & Silk (1999) and Barber (2000) for example).

Chapter 2

Lensing by a 3D Mass Distributions

2.1 An Introduction to Gravitational Lensing

This section reviews the basic theory of gravitational lensing used in the implementation described in Chapter 3. A complete overview of the theory of gravitational lensing can be found in Schneider *et al.* (1993).

The first mathematical formulation of gravitational lensing was published by Soldner (1804). He used Newton's corpuscular theory of light, in which light rays are considered to be made up of a stream of tiny particles, to derive the angle of deflection, α, by which the path of a particle travelling at a constant velocity, v, would deviate when passing a spherical mass, M, at a distance of r:

$$\tan \frac{\alpha}{2} = \frac{GM}{v^2 r}$$

For small values of α this becomes:

$$\alpha \simeq \frac{2GM}{v^2 r}$$

However, calculating the effect of a gravitational field on the path of light rays requires the use of General Relativity. Using General Relativity to derive α, the following value is obtained:

$$\alpha = \frac{4GM}{c^2 r}$$

This is twice the value obtained from the classical derivation. Subsequent observational measurements of the deviation of light rays round the Sun during eclipses

have verified the relativistic value to within 1%. The story of the measurements of the bend angle of light during the 1919 eclipse and surrounding events are given in Coles (2001).

2.1.1 The Single Lens Equation

A simple gravitational lens system, such as the one illustrated in Figure 2.1, consists of a source, a lens and an observer. A coordinate system is chosen with the origin at the observer and the z-axis lying along the line of sight between the source and the observer.

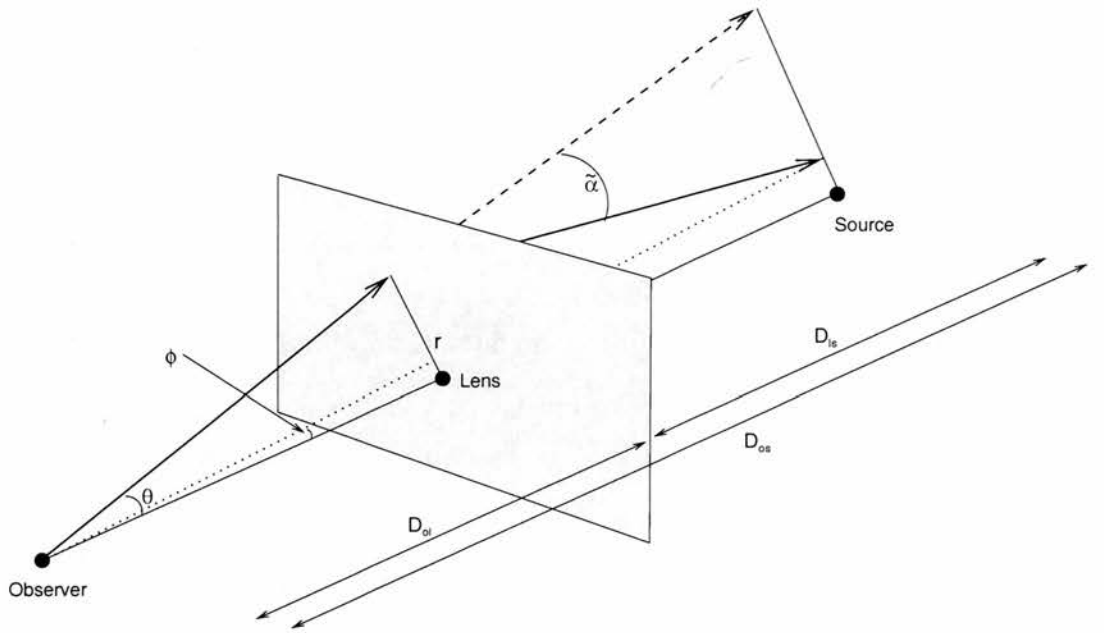

Figure 2.1: A simple gravitational lensing system

Consider a light ray which leaves the source at an angle $\vec{\theta}$. It is deflected by an angle $\vec{\tilde{\alpha}}$ by a lens situated at a distance D_{ol} from the observer. The light ray then travels a distance D_{ls} before arriving at the source plane. The final position of the light ray on the source plane is at an angle $\vec{\phi}$ at a distance of D_{os} from the observer.

Considering the geometry of the system shown in Figure 2.1, it can be seen that:

$$\vec{\theta} D_{os} = \vec{\tilde{\alpha}} D_{ls} + \vec{\phi} D_{os}$$

As $\vec{\tilde{\alpha}}$ is a function of $\vec{r} = D_{ol}\vec{\theta}$, this equation can be rearranged to give $\vec{\phi}$ as a

function of $\vec{\theta}$:

$$\vec{\phi} = \vec{\theta} - \vec{\tilde{\alpha}}\frac{D_{ls}}{D_{os}} \tag{2.1}$$

for a fixed source position $\vec{\phi}$. Equation 2.1 is known as the *lens equation.* It should be noted that this equation may have multiple solutions. Each solution corresponds to an image position for a lensed source.

Due to the large scale of gravitational lensing systems, the distances in Equation 2.1 are *angular diameter distances*, for which in general $D_{os} \neq D_{ol} + D_{ls}$. §2.5 outlines the relationship between the angular diameter distance of an object and its redshift.

The deflection angle $\vec{\tilde{\alpha}}$ in Equation 2.1 depends on the mass distribution of the lens and the relative positions of the ray and lens. In the most general case of an extended object of density $\rho(r_x, r_y, r_z)$ the thickness of the lens can be ignored as long as it is small relative to observer-lens-source separations. This approximation holds good for a large number of gravitational lensing cases where the majority of the deflection occurs when the light ray is closest to the lens and the path of the light ray can be closely approximated by two asymptotes. This is known as the *thin screen* approximation.

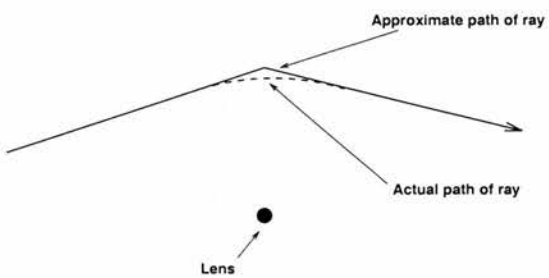

Figure 2.2: The path of the light ray is calculated using the thin screen approximation.

Using the thin screen approximation, the extended mass distribution can be projected onto a *lens plane* orthogonal to the line of sight. The surface mass density of this lens plane is given by:

$$\Sigma(r_x, r_y) = \int \rho(r_x, r_y, r_z) dr_z$$

For a general two-dimensional mass distribution, the angle $\vec{\tilde{\alpha}}$ by which a light ray

would be deflected is:

$$\vec{\tilde{\alpha}}(\vec{r}) = \frac{4G}{c^2} \int \Sigma(\vec{r'}) \frac{\vec{r} - \vec{r'}}{|\vec{r} - \vec{r'}|^2} d^2r' \tag{2.2}$$

In the case of a circularly symmetric lens, the deflection angle points towards the centre of the lensing mass. If $\vec{r}$ is the distance between the light ray and the centre of the mass distribution and $M(\vec{r})$ is the mass contained in radius $\vec{r}$ then:

$$\vec{\tilde{\alpha}}(\vec{r}) = \frac{4GM(\vec{r})}{c^2} \frac{\vec{r}}{r^2} \tag{2.3}$$

From the definition of the angular diameter distance (see Equation A.1) $\vec{r} = D_{ol}\vec{\theta}$. Thus the final position of a ray on the source plane can be calculated directly using Equations 2.1 and 2.3 if the following quantities are known:

- the angle at which the ray leaves the observer,
- the angular position and redshift of the lens,
- the redshift of the source plane.

While Equations 2.1 and 2.3 are straightforward to solve directly, inverting the lens equation, for example to find all the images of a given source, is not trivial. It involves finding all the roots for a 2 dimensional system of equations without necessarily knowing in advance the number of solutions. Thus, where possible, simulations of gravitational lens systems trace the paths of rays from the observer to the source.

Einstein Radius

A special solution of the lens equation can be obtained for a circularly symmetric lens lying along the line of sight between the source and observer. Choosing the coordinate system to lie along the line of sight, Equation 2.1 can be expanded for $\vec{\tilde{\alpha}}$ to give:

$$\begin{aligned} \vec{\phi} &= \vec{\theta} - \frac{4GM(<r)}{c^2} \frac{\vec{r}}{r^2} \frac{D_{ls}}{D_{os}} \\ &= \vec{\theta} - \frac{4GM(<\theta)}{c^2} \frac{\vec{\theta}}{\theta^2} \frac{D_{ls}}{D_{os} D_{ol}} \end{aligned}$$

In this particular case, the deflection of the light rays by the lens is rotationally symmetric around the line of sight. Thus the image of the source when $\phi = 0$ is a circle. The radius of this image, θ_E, can be obtained by setting $\phi = 0$:

$$\theta_E = \sqrt{\frac{4GM(\theta_E)}{c^2}\frac{D_{ls}}{D_{os}D_{ol}}} \tag{2.4}$$

θ_E is known as the *Einstein radius*. The Einstein radius can be used to define a dimensionless form of Equation 2.1. Multiplying Equation 2.1 by $1/\theta_E$ and defining:

$$\begin{aligned} \vec{x} &= \frac{\vec{\theta}}{\theta_E} \\ \vec{y} &= \frac{\vec{\phi}}{\theta_E} \\ \vec{\alpha} &= \frac{\vec{\alpha}}{\theta_E}\frac{D_{ls}}{D_{os}} \end{aligned}$$

gives the *dimensionless lens equation*:

$$\vec{y} = \vec{x} - \vec{\alpha}(\vec{x}) \tag{2.5}$$

The Deflection Potential

An alternative formulation for the deflection angle can be obtained using the identity $\nabla \ln|\vec{x}| = \vec{x}/|\vec{x}|^2$. As shown in Blandford & Narayan (1986) and Schneider (1985), this allows $\vec{\alpha}$ to be expressed as the gradient of a scalar potential Ψ. Thus Equation 2.2 for the deflection angle can be written as:

$$\vec{\alpha}(\vec{x}) = \nabla\Psi(\vec{x})$$

where:

$$\Psi(\vec{x}) = \int \Sigma(\vec{x'}) \ln|\vec{x} - \vec{x'}| d^2x'$$

Thus the lens equation can be written as:

$$\vec{y} = \nabla\left(\frac{1}{2}\vec{x}^2 - \Psi(\vec{x})\right)$$

or:

$$\nabla\Phi(\vec{x}, \vec{y}) = 0 \tag{2.6}$$

where $\Phi(\vec{x}, \vec{y})$ is the scalar function:

$$\Phi(\vec{x}, \vec{y}) = \frac{1}{2}(\vec{x} - \vec{y})^2 - \Psi(\vec{x})$$

$\Phi(\vec{x}, \vec{y})$ is known as the *deflection potential.* With this formulation of the lens equation images of the source are formed at coordinates where $\Phi(\vec{x}, \vec{y})$ is a minimum, maximum or saddle point.

2.2 Simulation Overview

The computer model used to simulate the effects of microlensing by a cosmological distribution of compact objects on high redshift sources requires a more complex situation that that described thus far. In particular, the model is required to simulate a three dimensional distribution of lensing objects. It is useful, at this stage, to outline the basic method by which is achieved. The volume in which the simulation takes place is divided in to a number of equal comoving sub-volumes (see Figure 2.3). A lens plane is placed at the centre of each sub-volume and a number of lenses are placed randomly onto the lens planes in such a way that each subvolume contains an equal density of lenses equivalent to the proportion of Ω_M in lenses specified for the simulation.

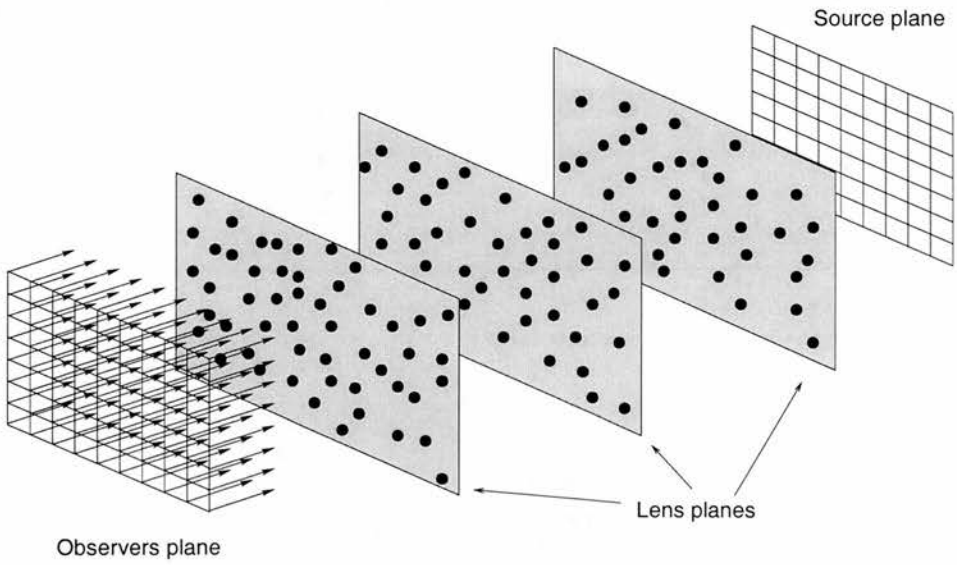

Figure 2.3: A schematic overview of the computer simulation.

Once the lensing distribution is in place a series of rays are 'fired' from the observer through the lens planes. The rays pass through each of the lens planes

in turn until they reach the source plane. At the source plane their position is recorded. Once all the rays have reached the source plane, the change in solid angle between rays due to their passage through the lens planes can be used to calculate a magnification pattern.

This process is repeated as the simulation evolves over time. The lenses each have a random velocity drawn from a gaussian velocity, with the lens planes period boundaries mimicking the effect of a continuous distribution of lenses.

The remainder of this chapter discusses the theoretical background to the simulation. Chapter 3 discusses the implementation of the simulation in detail.

2.3 Multiple Lens Planes

In many gravitational lensing systems one would expect to find more than one lens affecting the path of a light ray. Each lens will contribute to the final position of the light ray depending on its mass and the distance at which the ray passes the lens. Rather than evaluating the lens equation separately for each lens, the lenses are divided into two groups:

- Lenses whose separation along the line of sight is sufficiently small that they can be considered to make up a single thin lens.
- Lenses whose separation along the line of sight is sufficiently large that they deflect the light rays independently of each other.

In practice this allows the lenses to be grouped into a series of thin lenses, or *lens planes*, which can be considered independently (Blandford & Narayan (1986) and Kovner (1987)).

The angle at which a ray approaches a lens plane depends on how its path has been altered by its passage through previous lens planes. Consider the situation shown in Figure 2.4 where a ray has passed through three lens planes before approaching the source:

By considering the geometry of the system, itself similar to §2.1.1, it can be seen that:

$$\vec{\theta} D_{os} = \vec{\phi} D_{os} + \vec{\alpha}_1 D_{1s} + \vec{\alpha}_2 D_{2s} + \vec{\alpha}_3 D_{3s}$$

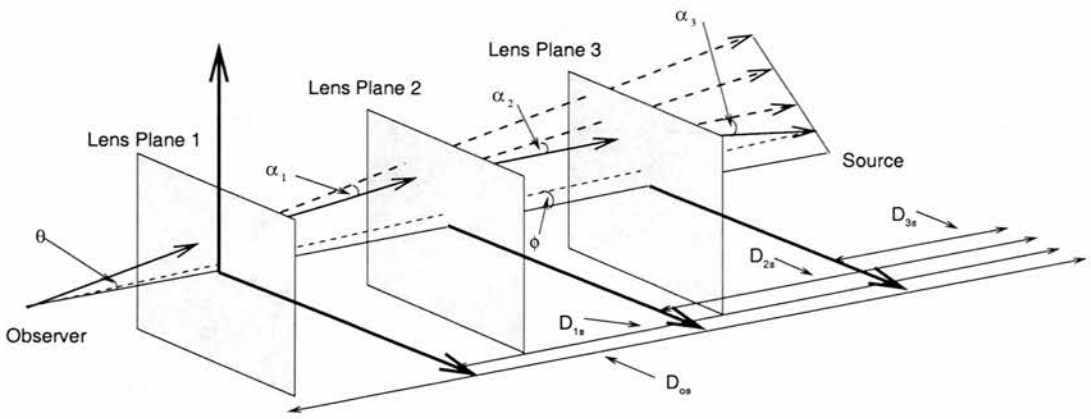

Figure 2.4: A multiple lensing system.

Rearranging:

$$\vec{\phi} = \vec{\theta} - \left(\frac{\vec{\alpha}_1 D_{1s} + \vec{\alpha}_2 D_{2s} + \vec{\alpha}_3 D_{3s}}{D_{os}} \right)$$

This can be written in a more general form as:

$$\vec{\phi}_N = \vec{\theta} - \frac{\sum_{i=1}^{N} \vec{\alpha}_i D_{is}}{D_{os}} \tag{2.7}$$

where D_{is} is the angular diameter distance from plane i to the source plane.

The vector $\vec{\xi}$ denoting the angle at which the ray intersects a lens plane can be found from

$$\vec{\xi} = \vec{\theta} - \frac{\sum_{i=1}^{j-1} \vec{\alpha}_i D_{ij}}{D_{os}} \tag{2.8}$$

Equation 2.8 agrees with Equation 2.7 when $j = s = N + 1$.

As in the case of the single lens equation, the position of the ray on the source plane and any intermediate lens planes can be directly calculated. The inverse lens equation becomes significantly harder to solve numerically as additional lens planes are added.

2.4 Magnification

A consequence of the gravitational deflection of light rays is the change in magnification of the image of a source seen by an observer relative to an unlensed image. The magnification effect can be illustrated by considering a bundle of four

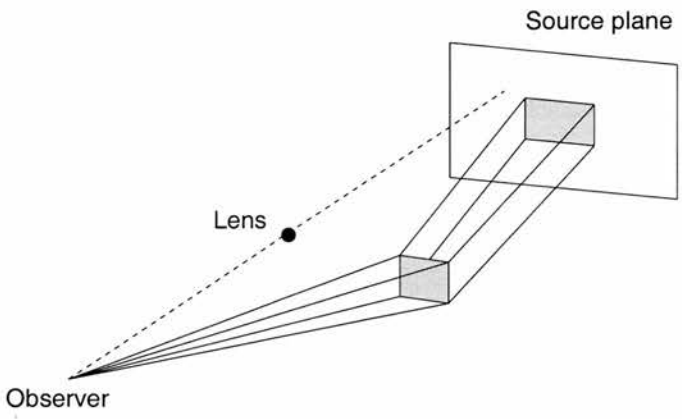

Figure 2.5: Gravitational lensing changes the area of a ray bundle.

rays, as illustrated in Figure 2.5. The rays closest to the lens are deflected more than those further away, leading to an increase in the area of the ray bundle.

The flux of an image, S_υ, at frequency υ is related to the solid angle $\Delta\omega$ of the image by:

$$S_\upsilon = I_\upsilon \Delta\omega$$

where I_υ is the surface brightness of the image at frequency υ. As surface brightness is unaffected by gravitational lensing, the surface brightness of the image is identical to that of the source. The magnification of a source, μ, is given by the ratio of the lensed to unlensed flux:

$$\mu = \frac{S_\upsilon}{(S_\upsilon)_0} = \frac{\Delta\omega}{(\Delta\omega_0)}$$

where 0 denotes the unlensed quantity.

To allow comparison the observational data, the magnification is converted into *magnitudes*:

$$m = -2.5 \log_{10} \mu \tag{2.9}$$

It should be noted that the convention for m is such that negative values represent magnification and positive values de-magnification.

2.5 Angular Diameter Distance

The distances used in the lens equation are angular diameter distances. In order to calculate the path of a light ray through a series of lenses, an expression

for the angular diameter distance between two arbitrary redshifts, z_1 and z_2, is required. Since this methodology is not covered in standard cosmology textbooks, the expressions are derived in Appendix A for models which include a cosmological constant. To summarise, for a flat universe the expression for angular diameter distance is:

$$d_A = -\frac{c}{(1+z_2)} \int_{z_1}^{z_2} \left[(1+z)^2(1+\Omega_M z) - z(2+z)\Omega_\Lambda\right]^{-1/2} dz \qquad (2.10)$$

For open and closed universes the expression becomes:

$$d_A = -\frac{1}{\sqrt{|\Omega_k|}(1+z_2)} \text{sinn}\left[c\sqrt{|\Omega_k|} \in t_{z_1}^{z_2} \frac{\left[(1+\Omega_M z) - z(2+z)\Omega_\Lambda\right]^{-1/2}}{(1+z)} dz\right] \qquad (2.11)$$

where

$$\text{sinn} = \begin{array}{ll} \text{sinh} & \text{for an open universe} \\ \text{sin} & \text{for a closed universe} \end{array}$$

2.6 Lenses

The microlensing simulation described in Chapter 3 is characterised by the density parameter, $\Omega = \Omega_\Lambda + \Omega_M$. A number of cosmological models were considered with varying values for Ω_Λ and Ω_M, but all with $\Omega = 1$. The lensing mass within the simulation consists of N_{lens} lenses each of mass M_i which makes up a fraction $f \leq 1$ of the total mass, Ω_M. The angular size and redshift of the lensing planes are set to ensure that the total lensing mass within the simulation volume corresponds to a lensing mass of $f\Omega_M$.

Considering the density of lenses in the simulation, ρ, as a fraction of the critical density, ρ_c, gives:

$$\rho = f\Omega_M \rho_c = f\Omega_M \frac{3H_0^2}{8\pi G}$$

The simulation volume V_{sim} can be found by calculating the fraction of the volume out to the source redshift, $V(< z_s)$, contained within the solid angle subtended by a plane of size θ_{plane}, where $\theta_{plane} \ll 1$:

$$V_{sim} = V(z_s)\frac{\theta_{plane}^2}{4\pi}$$

If the lensing mass content of the universe is made up of lenses of variable mass, M_i, then:

$$f\Omega_M \frac{3H_0^2}{8\pi G} V(z_s) \frac{\theta_{plane}^2}{4\pi} = \sum_{i=1}^{N_{lens}} M_i \tag{2.12}$$

Thus the size of the lens and source planes in the simulation can be obtained directly from Equation 2.12, while the redshifts of the planes can be obtained by considering the volume required to contain the mass of the lens plane for a given Ω_Λ and Ω_M.

2.6.1 Volume

The comoving volume out to a redshift z_i can be obtained by integrating the comoving volume element of the Robertson-Walker metric:

$$dV = R_0^3 \frac{r^2}{\sqrt{1-kr^2}} dr d\Omega \tag{2.13}$$

where $d\Omega$ is the solid angle element.

Again consider the three values for k individually.

$k = 0$: **Flat universe** In this case equation 2.13 reduces to:

$$dV = R_0^3 r^2 dr d\Omega$$

which can be integrated to give:

$$V(z_i) = R_0^3 \frac{4\pi}{3} r(z_i)^3$$

This can be expressed in terms of the angular diameter distance, d_A, using equations A.2 and A.3:

$$V(z_i) = \frac{4\pi}{3}(1+z_i)^3 d_A^3 \tag{2.14}$$

$k = -1$: **Open universe** Making the substitution $r = \sinh u, dr = \cosh u du$ in equation 2.13 gives:

$$dV = R_0^3 \frac{\sinh^2 u}{\cosh u} \cosh u du d\Omega$$

Thus:

$$V(z_i) = R_0^2 \int\int \sinh^2 u du d\Omega$$

This can be integrated to give:

$$\begin{aligned} V(z_i) &= 4\pi R_0^3 \left[\frac{\sinh 2u}{4} - \frac{u}{2}\right] \\ &= 4\pi R_0^3 \left[\frac{2\sinh u \cosh u}{4} - \frac{u}{2}\right] \\ &= 2\pi R_0^3 \left[\sinh u(1+\sinh^2 u)^{1/2} - u)\right] \\ &= 2\pi R_0^3 \left[r(1+r)^{1/2} - \sinh^{-1} r\right] \end{aligned}$$

This formula can be expressed in terms of the angular diameter distance, d_A, using equations A.2 and A.3:

$$V(z_i) = 2\pi R_0^3 \left[\frac{d_A(1+z_i)}{R_0}\left(1 + \frac{d_A^2(1+z_i)^2}{R_0^2}\right)^{1/2} - \sinh^{-1}\left(\frac{d_A(1+z_i)}{R_0}\right)\right]$$

$V(z_i)$ then can be expressed in terms of Ω_k using equation A.6:

$$\begin{aligned} V(z_i) = \frac{2\pi}{H_0^3\Omega_k}\Big[&d_A(1+z_i)H_0\sqrt{1+d_A^2(1+z_i)^2\Omega_k} - \\ &|\Omega_k|^{-1}\sinh^{-1}(d_A(1+z_i)H_0|\Omega_k|^{1/2})\Big] \end{aligned} \quad (2.15)$$

$k = 1$: **Closed universe** Making the substitution $r = \sin u, dr = \cos u du$ in equation 2.13 gives:

$$dV = R_0^3 \frac{\sin^2 u}{\cos u} \cos u du d\Omega$$

Thus:

$$V(z_i) = R_0^2 \int\int \sin^2 u du d\Omega$$

This can be integrated to give:

$$\begin{aligned} V(z_i) &= 4\pi R_0^3 \left[\frac{\sin 2u}{4} - \frac{u}{2}\right] \\ &= 4\pi R_0^3 \left[\frac{2\sin u \cos u}{4} - \frac{u}{2}\right] \\ &= 2\pi R_0^3 \left[\sin u(1+\sin^2 u)^{1/2} - u)\right] \\ &= 2\pi R_0^3 \left[r(1+r)^{1/2} - \sin^{-1} r\right] \end{aligned}$$

This formula can be expressed in terms of the angular diameter distance, d_A, using equations A.2 and A.3:

$$V(z_i) = 2\pi R_0^3 \left[\frac{d_A(1+z_i)}{R_0} \left(1 + \frac{d_A^2(1+z_i)^2}{R_0^2} \right)^{1/2} - \sin^{-1} \left(\frac{d_A(1+z_i)}{R_0} \right) \right]$$

$V(z_i)$ then can be expressed in terms of Ω_k using equation A.6.

$$V(z_i) = \frac{2\pi}{H_0^3 \Omega_k} \left[d_A(1+z_i) H_0 \sqrt{1 + d_A^2(1+z_i)^2 \Omega_k} - |\Omega_k|^{-1} \sin^{-1}(d_A(1+z_i) H_0 |\Omega_k|^{1/2}) \right] \quad (2.16)$$

Equations 2.15 and 2.16 can be combined using the definition given for sinn in equation A.8:

$$V(z_i) = \frac{2\pi}{H_0^3 \Omega_k} \left[d_A(1+z_i) H_0 \sqrt{1 + d_A^2(1+z_i)^2 \Omega_k} - |\Omega_k|^{-1} \mathrm{sinn}^{-1}(d_A(1+z_i) H_0 |\Omega_k|^{1/2}) \right] \quad (2.17)$$

2.6.2 Size of Lens Plane

Once an expression has been obtained for the volume out to the source redshift, $V(z_s)$, the angular size of the lens planes can be obtained by re-arranging equation 2.12 to give:

$$\theta_{plane}^2 = \frac{4\pi}{V(z_s)} \frac{8\pi G}{\Omega_M 3 H_0^2} \left[M_{smooth} + \sum_{i=1}^{N_{lens}} M_i \right]$$

2.6.3 Plane Redshifts

The redshifts for the planes can be calculated by considering the number of lenses on each plane. While the number of lenses per plane can vary, the density of matter in lenses is fixed by the amount of Ω_M specified in lenses, $f\Omega_M$. The plane redshifts are obtained by considering the volume difference, $\Delta V(z_i, z_j)$, between two redshifts z_i and z_j, where $z_j > z_i$. $\Delta V(z_i, z_j)$ is the volume required to hold the number of lenses for the plane, given the density $f\Omega_M$.

The volume difference can be calculated using the relationship between density, volume and mass:

$$\Delta V(z_i, z_j) = V(z_j) - V(z_i) = \sum_{i=1}^{N_{lenses/plane}} M_i \frac{4\pi}{\theta_{plane}^2} \frac{8\pi G}{3 H_0^2 f \Omega_M}$$

Redshifts are calculated by starting from the observer at $z_i = 0$ and stepping through the redshifts until the correct number of planes are obtained and $z_j = z_s$. For a $k = 0$ universe, equation 2.14 can be inverted to give z_j. In the case of a $k = 1$ or a $k = -1$ universe, equation 2.17 is solved numerically to give z_j.

2.6.4 Lens Parameters

In order to ensure that the parameters for the simulation are consistent with each other, the number of lenses on each plane along with their individual masses are specified along with the cosmological parameters. The simulation uses this information to calculate a size for the planes which ensures that the total mass specified in lenses is consistent with the mass density specified by $f\Omega_M$. Once a size, θ_{plane}, has been calculated, the total lens mass on each individual plane is used to divide the simulation volume in to a number of sub-volumes, each with the same density of lenses. Finally a redshift is calculated such that each plane is positioned at the *centre* of each volume (see Figure 2.6). The lenses themselves

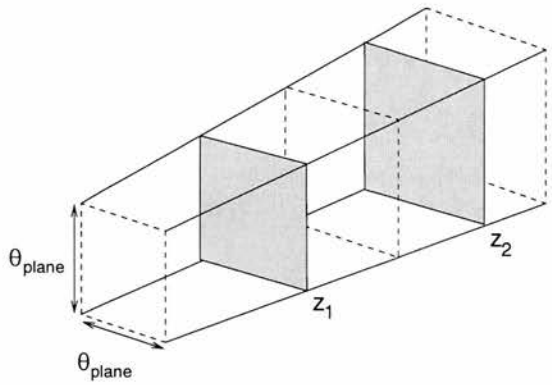

Figure 2.6: The total mass in lenses is used to calculate the size of the simulation planes. The lens planes are then positioned at redshifts which ensure a constant density of lenses throughout the simulation.

are randomly positioned on the planes. In the absence of any observational data, a random distribution was deemed the most appropriate for a cosmological population of compact objects.

Each lens was also assigned a random velocity taken from a Gaussian distribution with a mean velocity of $300\,km\,s^{-1}$. Again there is no observational evidence to back up this value. This value is similar to the typical velocities of stars in

a galaxy and of galaxies themselves. It seems unlikely that any cosmological distribution of compact objects would have a radically different velocity profile. It should be noted that previous lensing simulations, such as Schneider (1993) and Lewis *et al.* (1993) for example, considered a source moving behind a field of lenses with fixed positions. Thus a magnification pattern was modelled for a single lens distribution and the lightcurves generated by moving the source (and possibly the observer) across the magnification patterns. This avoided the need to model the evolution of the lensing field over time and was done in order to reduce the computational overhead. In order to avoid this simplification, the simulation described in detail in the next section has been designed to run on high performance computers. This has provided the necessary performance to allow the positions of lenses to evolve over time, producing a more realistic simulation.

The lenses in the simulation either had an identical mass or a mass taken from the power law:

$$N(M)dM \propto M^{-1}dM \tag{2.18}$$

where $N(M)$ is the number of lenses in the mass range dM. Such a power law produces a lens mass distribution with more lenses towards the lower end of the distribution. To reduce computation time the lower end of the mass range was set to be an order of magnitude below the upper range.

As mentioned above, the simulation was allowed to evolve over a number of timesteps. Each timestep was set to be some multiple of an Einstein radius. Thus, from Equation 2.4, for a particular set of cosmological parameters, the Einstein radii and therefore the simulation timestep is directly proportional to $\sqrt{M}$ where M is the mass of the lens. Thus, reducing the lens masses by a factor of 100 simply reduces the timescale of the simulation by a factor of 10. Therefore, only a single simulation is required for each set of lens masses.

Chapter 3

Numerical Simulations of Microlensing

To test the hypothesis that long term variability in the apparent luminosity of quasars is due to microlensing, observational light curves were compared with light curves generated by a computer simulation. This chapter describes previous approaches to microlensing simulations and discusses their applicability to this problem. §3.2 describes in detail the algorithm used to generate the results for this thesis.

3.1 Microlensing Simulations

A number of different methods have been implemented to calculate the effect of microlensing. Most are variations on one of two strategies:

1. methods that identify microlensing images by solving the lens equation.

2. methods that follow the path of light rays through a distribution of lensing objects.

This section outlines some of the approaches taken within each category and discusses them in relation to the approach taken for the simulations described in this thesis.

3.1.1 Solving the Lens Equation

While the form of the lens equation is simple, its direct solution is far from trivial to perform. Microlensing typically involves complex mass distributions such as stars within a galaxy. This makes it impossible to obtain the images of a source analytically by inverting the lens equation. In consequence, microlensing simulations which involve finding images by directly solving the lens equation use numerical rather than analytical solutions. An implementation of this approach was outlined by Paczyński (1986).

In this paper Paczyński investigated the effect of the individual stars within a lensing galaxy on the final image. The model simulates a random distribution of stars within a circular galaxy. Microlensed images, referred to as *microimages* by Paczyński, are identified for a subset of these stars by searching for possible image positions and iteratively solving the lens equation. A number of different search types were used to determine the positions of the microimages. However, all involve making an initial guess for the microimage position and then iterating until a solution for the lens equation is found. Once a microimage is found, its position is compared to a list of previously identified microimages. If it proves to be a previously unidentified microimage then the new microimage position is added to the list.

While this approach has the attraction of using the direct solution of the lens equation to identify images, it is computationally expensive to carry out. In addition, as the number of microimages cannot be predicted in advance, it is impossible to tell if all the microimages have been identified. Thus a very detailed search is required to ensure that sufficient microimages are detected. In the model outlined in Paczyński (1986), the search criteria is set so that the combined microimages identified should account for at least 95% of the total intensity. However, in general, the higher the density of stars, the more microimages there are and the more detailed the search required to meet this criteria.

An interesting refinement on Paczyński's approach was put forward by Lewis *et al.* (1993). Rather than trying to find the images of a point source, they looked at the image plane for images of a straight line. They show that the image of a straight line consists of one curve of infinite length and a series of closed loops, all of which are connected to stars. The infinite curve can be identified by looking outside the star field where the position of the image curve approaches the position of

the original line. The image curve can then be followed through the star field using an adaptive step size with the position of the next point estimated from the tangent to the image line. The closed loops are then identified by searching all the stars within a predefined radius which do not intersect with the infinite curve. When a closed loop is identified it is followed in a similar manner to the infinite curve until it arrives back at the star it started from.

The simulation repeats this process for a number of lines until a magnification pattern is obtained for the source plane. While this approach can be applied successfully to microlensing within a galaxy, where all the lenses are at the same redshift, the simulation described in this thesis requires a three dimensional cosmological distribution of lenses. This requires the use of multiple planes of lenses. In this case the image of the straight line would be calculated for the first plane. The resulting infinite curve and loops would then be lensed by the second lens plane. As there is no solution equivalent to that for a straight line for the infinite curve and loops, this method is infeasible for multiple plane simulations.

In summary, the inverse lens equation can only be solved analytically for the simplest cases. For point mass lenses it is impossible to know in advance the number of images present. This makes searching for lens images computationally intensive due to the fine grain search required to ensure that a sufficient number of the images are identified. This problem can be avoided by searching for images of a straight line where the image properties are known in advance, making the image search section of the algorithm less computationally intensive. However, this approach only works for a single lens plane and is not suitable for the multiple lens plane case described in this thesis.

3.1.2 Ray Shooting

Ray shooting algorithms approach microlensing simulations in a very different manner to the methods described in §3.1.1. They make no attempt to identify the individual images of a source but instead calculate the path taken by a light ray through a specified mass distribution. In general, the light ray's path is traced from the observer to the source redshift. This is numerically equivalent to tracing the ray's path from the source to the observer but has the advantage of ensuring that all the light rays reach the observer. The area the rays 'land on' at the source redshift is then divided up into a number of pixels. A magnification pattern is

generated from the number of light rays in each source plane bin. Light curves can then be generated for both point and extended source by recording changes in magnification patterns over a period of time.

A simple ray shooting method was first outlined by Kayser *et al.* (1986). They traced the paths of a grid of rays through a field of 100 randomly distributed equal mass lenses and generated light curves for extended constant surface brightness sources. However, to accomplish such a simulation for more than $\sim$ 100's of lensing masses would require a large amount of computational time. In order to reduce the computational requirements of the algorithm, the ray shooting technique is commonly used in combination with methods to reduce the number of deflection angle calculations required for each ray. These methods typically calculate accurately the contribution of lenses close to the light ray and estimate the contribution of lenses greater than some predetermined distance from the light ray. As the major details in the light curves are caused by interactions of the light rays with nearby lenses, this method of approximating the deflection angle for a light ray can give statistically satisfactory results.

An implementation of this type of approach was given by Schneider & Weiss (1987) and extended in Schneider & Weiss (1988). The ray shooting area was divided into a series of squares. The deflection angle was calculated for individual stars within an area of $\sim$ 15 times the area of the squares. This result was then combined with an estimate of the contribution of the remaining stars outside that perimeter. Schneider & Weiss obtained further performance benefits by testing whether or not rays within the squares reached the collecting area in the source plane.

Another variation on this method is the hierarchical tree. Originally developed for calculating gravitational forces in N-body simulations by Barnes & Hut (1986), this algorithm provides a computationally efficient way to store different groupings of lenses. The algorithm was first applied to lensing simulations in by Wambsganss *et al.* (1990b). The lenses are stored in an inverted tree structure (see § 3.4.1 for details) which can quickly be traversed in either direction. Different groupings of lenses are used to calculate the deflection angle depending on the impact parameter between the light ray and the lensing mass.

All of the applications outlined in this section so far have examined microlensing by stars within a galaxy. In such cases, the lensing stars are all at the same

redshift and can be represented within the simulation by a mass distribution on a single lens plane. However, when considering lensing by a cosmological mass distribution, the lensing mass is at a range of redshifts. In this case, multiple planes must be used to approximate the mass distribution's three-dimensional nature. One possible approach was proposed by Wambsganss *et al.* (1998). They investigated the gravitational lensing properties of cosmological simulations. The mass distributions from simulations were divided into a series of mass cubes and then collapsed onto a single plane. The mass plane was then divided into a grid with each pixel treated as a point mass lens. This approximation would break down if the impact parameter tended towards zero because the deflection angle then diverges. In order to ensure that this approximation remained valid throughout the simulation, the deflection angle was calculated at the centre of a group of four of these point mass lenses and was then interpolated to give the value at the ray position. This method ensured that the relative positions of the masses and the points at which the deflection angle is calculated remained constant for each plane, leading to computational savings.

Ray shooting provides a simple method of modelling complex lens distributions for both single and multiple lens planes. Its assumption that most of the deviation in the light ray's path is caused by lenses close to the light ray allows for the algorithm to be optimised by approximating the contribution for distant lenses. The ability to implement this the ray shooting method effectively for multiple lens planes makes it ideal for the simulation described in this thesis.

3.2 Implementing the Ray Shooting Algorithm

To generate a statistically significant set of light curves which can be compared with observational data, the microlensing simulation must meet three requirements:

1. The resolution of the ray grid must be sufficiently fine to resolve the lensing effect of a single lens, regardless of the plane it is on.

2. The simulation must cover a large enough volume that a statistically significant number of independent light curves can be obtained for a range of source sizes. As the density of lenses is specified through the cosmologi-

cal parameters for the simulation, this requires the simulation to contain a large number of lenses.

3. The microlensing system must evolve over a period of time long enough to ensure that the long timescale features are fully sampled but with sufficiently short timesteps that individual high magnification events are fully resolved.

Independently, each of these criteria is computationally difficult to meet. The following three sections describe the approach taken to combine the three requirements in such a way that all three can be met without compromising the accuracy of the simulation.

3.3 Ray grid

The grid of rays to be traced through the lensing mass distribution must be fine enough to ensure that the effect of a single lens can be resolved. The microlensing simulation includes a number of lens planes and, for some of the simulation runs, a range of lens masses. Quantitatively, this criterion was set to ensure that the grid spacing is at least as large as the Einstein radius of the smallest mass lens on the highest redshift lens plane.

In addition to fine grid resolution, a large grid is also required to ensure that a sufficiently large number of independent light curves can be obtained. One advantage of the ray shooting technique is that the calculations of the paths of the individual rays are independent of each other. Whilst the path a ray follows will, in general, be closely related to the paths of the neighbouring rays on the grid, the calculations of the ray's position at each point throughout the simulation do not depend on the position of other rays. This property can by exploited by implementing the algorithm on a parallel computer.

3.3.1 What is parallel computing?

Most common desktop computers consist of one processor with some memory attached to it (see Figure 3.1). This is known as a sequential computer as it executes one instruction at a time. Even programs such as UNIX and Windows

NT which give the illusion of multitasking are serial in nature and thus executed one instruction at a time.

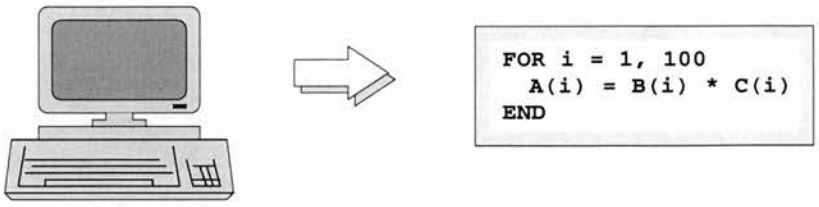

Figure 3.1: Schematic diagram of serial machine.

In contrast a parallel machine consists of multiple instances of the processor and memory combination. There are a number of different architectures for parallel machines. The work described here was carried out on distributed memory parallel computers (see Figure 3.2).

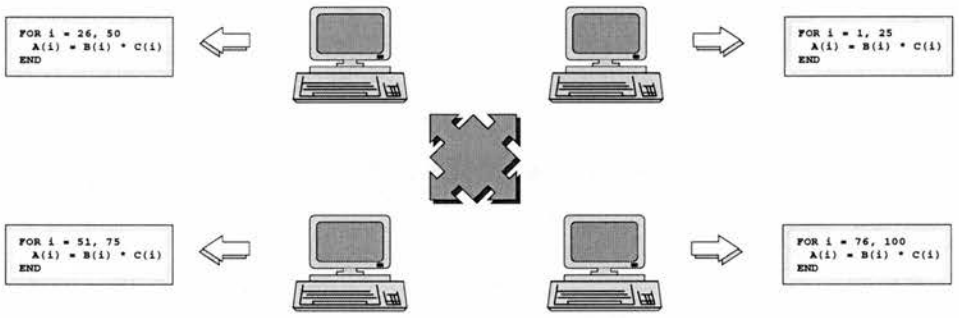

Figure 3.2: Schematic diagram of a distributed memory parallel machine.

These consist of a number of processors, each of which has its own private local memory. All the processors are connected using some interconnect mechanism which allows processors to communicate with each other. This class of parallel architecture can be applied to a variety of machines ranging from networks of workstations to specialised Massively Parallel Platforms.

3.3.2 Problem Decomposition

The microlensing simulation consists of a grid of rays travelling through a series of lens planes. The path of each ray is independent of the other rays in the simulation. Thus the most effective method of running the simulation on a parallel machine is to divide the rays equally between the processors as shown in Figure 3.3.

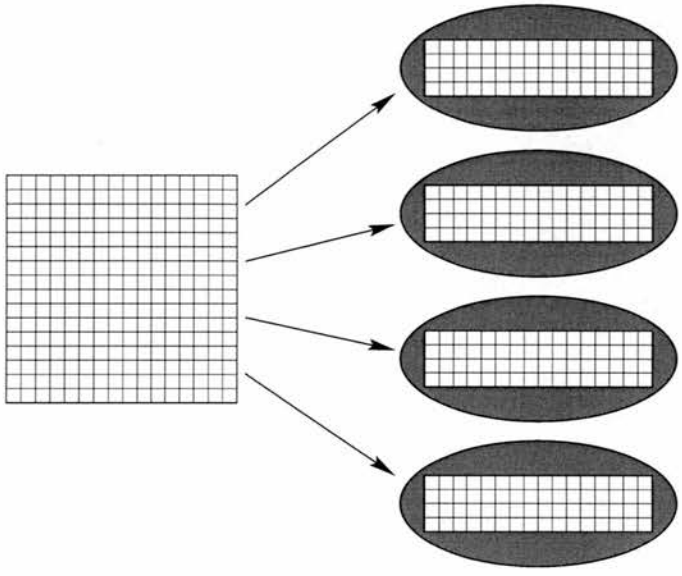

Figure 3.3: Grid divided between the processors.

Each processor is given a block of rays to work on and the results are gathered together at the end. The paths of the rays in each block are calculated independently. The program is designed so that each process has access to the entire set of lenses on each lens plane. Thus each process can calculate the ray path to the accuracy specified in the simulation.

The *Message Passing Interface (MPI)* standard (Message Passing Interface Forum, 1995) was used for communication between processors with the simulation itself written in C. The use of MPI enabled the simulation to be run on a variety of parallel platforms, including networks of workstations, requiring only recompilation to work on each machine.

3.4 Large numbers of lenses

To ensure that the simulation produces a statistically significant number of light curves, the simulation must be run with a large number of lenses. The size of the area on which the rays land at the source plane is determined by the total mass of lenses. This mass must be in agreement with the specified total mass density. In practice, the majority of CPU time for the simulation is spent calculating the deflection angle for the light rays. Thus the computation time depends on the number of lenses in the simulation and is only indirectly related to their mass. The number of lenses required for these simulations varies between ~ 3000 to $100,000$

depending on the simulation parameters and the mass distribution between the lenses (see Chapter 4 for a detailed description of the simulation parameters).

An initial implementation was developed using the idea of a cutoff radius, r_s, for the lens calculation. The lens planes were divided into a series of boxes with sides the same length as the cutoff radius (see Figure 3.4). This means that all the lenses on the plane within a distance r_s of the light ray will either be in the box that the ray lands in or its neighbouring boxes. The deflection angle is then calculated for lenses where the impact parameter is less than r_s.

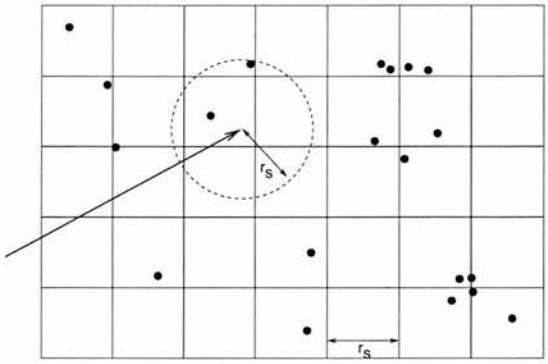

Figure 3.4: The lens planes are divided into boxes the same size as the search radius, r_s.

This idea of dividing the lens plane into boxes is similar to the approach taken by Schneider & Weiss (1987). However they used much smaller size boxes and therefore had a larger number of boxes to search.

In addition to the mass in lenses on the plane, an additional smooth negative mass distribution, $-\Sigma_*$, was introduced. This was set so that the integral of Σ_* over the lens plane equals the total mass in lenses, giving a total mass of zero for the lens plane. The effect of $-\Sigma_*$ is to ensure that while lenses close to the light ray continue deflect the path of ray, lenses a large distance away have no effect. In other words, the mass fluctuations caused by the combination of point mass lenses and $-\Sigma_*$ is a small scale effect which cancels out over much of the lens plane. As mentioned in §3.1.2 the majority of the interactions which make up the light curves involve lenses which are close to the light ray. Such an approach reduces the number of lenses involved in the simulation without altering the statistical properties of the light curves.

The idea of a smooth negative surface density was introduced by Lewis *et al.*

(1993) for modelling microlensing within a lensing galaxy. However, unlike microlensing in galaxies, this simulation of a cosmological distribution of microlensing bodies did not have a finite extent. Infinite planes were simulated by copying the lenses in the planes onto a repeating pattern of 'virtual' lens planes.

When the light rays reach the source plane their positions are recorded. However, many rays from the edge of the original ray grid will have moved outside the lens planes and been traced through the virtual planes. Most of these rays will therefore be outside the area of the source plane when they reach the source redshift. In addition rays which, were the grid was larger, would have moved into the source plane are missing from the simulation. This leads to the edge area of the source plane having, on average, a lower magnification than the interior of the source plane.

One method of avoiding this situation is to allowed the simulation to conserve rays by wrapping the positions of any rays which fall outside the source plane back onto it. This is possible as the virtual planes have the same lens distribution as the lens plane. Figure 3.5 illustrates the wrapping technique. The solid arrow represents the original ray position and the dotted arrow the wrapped ray position.

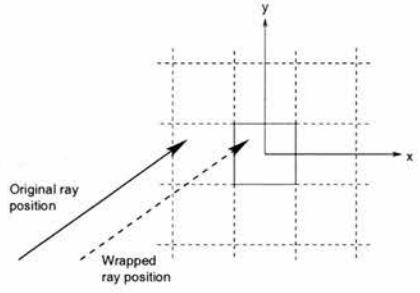

Figure 3.5: Rays whose coordinates at the source redshift fall outside the area of the source plane are wrapped back into the source plane.

However, this technique of wrapping rays back into the source plane cannot be used in conjunction with the smooth negative mass density. For the wrapping to be correct the mass lensing the ray must be the same on the virtual plane as for the source plane. While this is true for the lenses, it is not true for the smooth negative density. The contribution of the negative density depends on the ray's distance from the origin. This is clearly different for rays on the virtual plane than for rays on the lens plane. The microlensing simulation therefore gave inaccurate results when the two techniques were combined. While the smooth negative

density reduced the time required for the microlensing simulation, the inability to combine this with ray wrapping on the source plane led to the generation of significantly smaller magnification patterns and thus fewer light curves.

As this does not meet the criteria set out at the start of this section, the smooth negative density model was rejected and the hierarchical tree algorithm implemented instead.

3.4.1 Hierarchical Tree

The hierarchical tree algorithm is widely used in cosmological simulations (Barnes & Hut, 1986). It provides a method whereby masses close to the point of interest are considered individually while masses further away are clustered together and treated as a single object. This ensures that nearby masses, which provide most of the detail, are calculated exactly while the effect of more distant masses are approximated. Therefore, rather than using negative mass to 'remove' distant lenses from the simulation, an estimate of the effect of distant lensing mass is included in the deflection angle calculation.

In two dimensions the algorithm works by recursively dividing the plane into four equally sized sections until each section contains either one or zero lenses. For example, consider the plane of lenses shown in the left of Figure 3.6 which contains 20 randomly placed lenses.

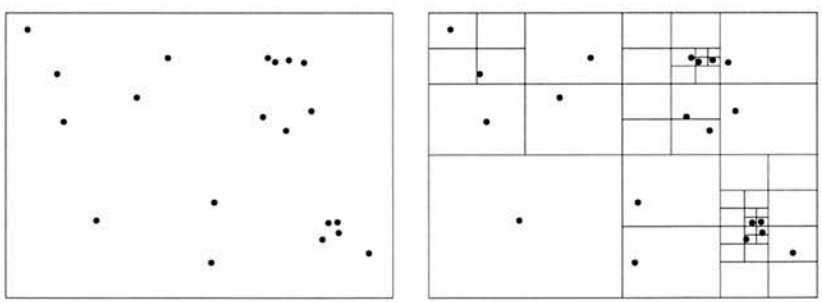

Figure 3.6: The hierarchical tree algorithm recursively divides the lens plane into four sections until each section either contains one or zero lenses.

The hierarchical tree algorithm divides the plane into four sections. If a given section contains more than one lens then it in turn is divided into four further sections. This process continues until each section contains either one or zero lenses. The right diagram in Figure 3.6 shows the final division of the example

plane.

The structure of the divided lens plane is stored in an inverted tree, from which the algorithm takes its name. Each recursive division of the plane is represented as a division of the tree into four new branches. Thus the tree structure contains a hierarchy of individual and clustered lenses. The tree structure for the lens plane in Figure 3.6 is shown in Figure 3.7.

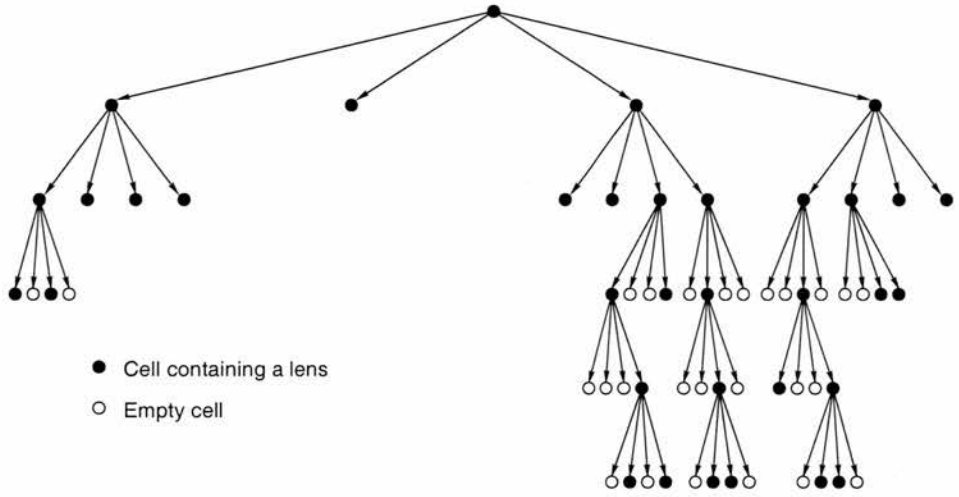

Figure 3.7: The lenses from Figure 3.6 are stored in a tree structure.

There are two main advantages to this type of structure:

1. Each branch point stores information on the total mass of the lenses below it in the tree hierarchy as well as the position of the centre of mass. Thus, for approximate calculations of the bend angle of a cluster of masses beyond some specified distance from the ray, the branch point can be treated as a lens in the calculations.

2. While the tree structure appears complicated at first glance, if efficiently implemented the time required to initially construct and then to search the tree is relatively small. In particular, the *pointer* feature of the C programming language enables the structure to be efficiently constructed and searched with minimal memory requirements.

The microlensing simulation produces a single tree for each plane of the simulation. As each lens in the simulation has an associated velocity the positions of the lenses change as the simulation evolves over time. This requires the tree

structure to be updated for each time-step. Rather than attempting to move lenses between different branches of the tree as their positions change, the tree structures are generated anew for each time-step. In order to reduce the memory required to store the trees, the positions of the lenses are pre-calculated for each time-step. The resulting reduction in memory requirements is significant and allows the parallel version of the simulation to store copies of the whole trees in each processes' memory. This avoids the need to distribute the tree structure between processes and reduces communications overheads.

Once the hierarchical tree has been constructed, the light rays are 'fired' from the observer through each of the lens planes until they reach the source redshift. The position of the light ray on each lens plane is obtained from Equation 2.8. The bend angle, α, can then be calculated by summing Equation 2.3 over the mass in the plane. The mass used in this calculation is either the mass of individual lenses or the plane sections generated by the hierarchical tree algorithm. The decision about which mass to use is based on the angle subtended by the section of the lens plane at the light ray. This angle is known as the *opening angle*, θ. Figure 3.8 shows the opening angle for two sections of the lens plane in Figure 3.6.

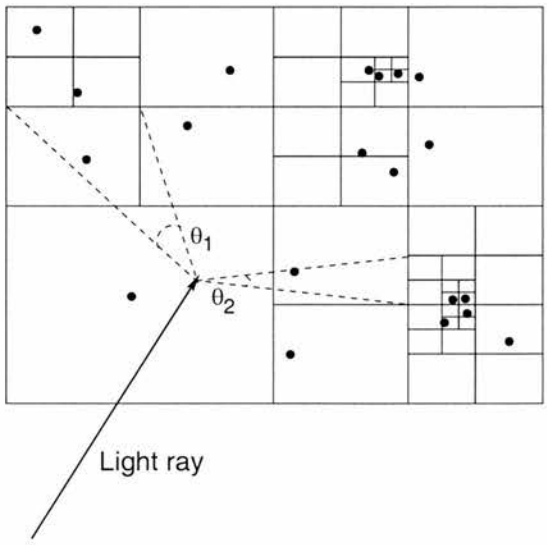

Figure 3.8: For each ray in the simulation, the tree is searched until the opening angle meets a predetermined accuracy criteria.

The tree is searched from the top down and at each level the value of the opening angle, θ, is compared with a predetermined value, θ_c. If $\theta < \theta_c$ then the mass and centre of mass position of the plane section is used in the calculation. However,

if $\theta > \theta_c$ the search algorithm moves down to the next level of the tree and the opening angles are calculated for this new tree level. This procedure continues until all the plane mass has been included in the calculation of α. The tree search algorithm is constructed to ensure that no mass is counted more than once. Clearly the value of θ_c is critical to the accuracy of the algorithm. The determination of θ_c for this microlensing simulation is discussed in §3.8.

The tree search algorithm repeats the calculation of α on these virtual planes out to a predetermined search radius, r_s, from the light ray as shown in Figure 3.9. The hierarchical tree structure need only be generated for the original lens plane as the positioning of the lenses on the virtual planes is identical to the original plane. The value for the search radius was determined experimentally and is discussed in more detail in §3.8.

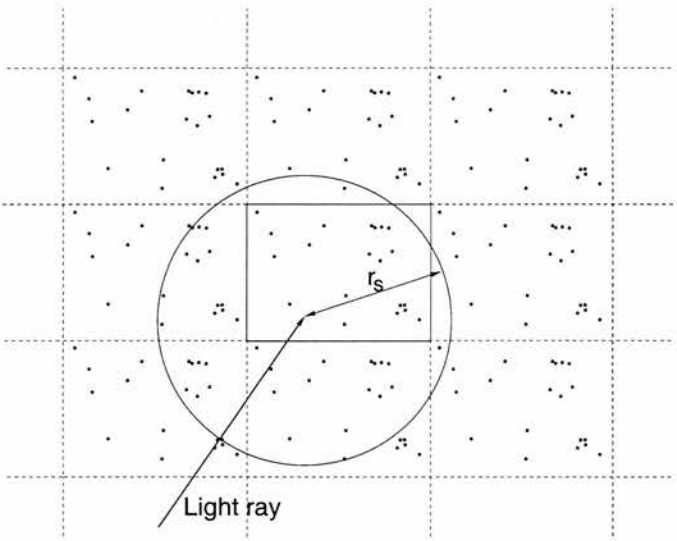

Figure 3.9: The bend angle is calculated over a series of virtual planes out to a specified distance, r_s.

One issue which must be considered when implementing a search radius for a lensing simulation is that the bend angle calculated for the light ray drops to zero at the edge of the search radius. The final result of the simulation is a series of magnification patterns which will be used to generate light curves. As the magnification is dependent on the gradient of the bend angle, the fact that it drops to zero at the edge of the search radius leads to negative magnification spikes at the edge of each ray's search radius. In order to avoid this effect, the bend angle for mass-lens separations of $95\% r_s < r < r_s$ is multiplied by a cosine

function which curves the bend angle towards a zero value at the search radius.

3.5 Long time period

The light curves will be analysed using spectral analysis techniques to determine the power over a range of frequencies (see §4.4). As described in §2.6.4, for a lens of mass, M:

$$M \propto t^2$$

where t is the simulation timestep. For simulations for lenses with identical mass, the power spectra can be moved around on the frequency axis to get the best fit to the observational data. This is then equivalent to scaling the mass of the lenses in the simulation.

The highest frequency for which the power can be determined is known as the *Nyquist critical frequency*. This is the frequency for which there are two data points per cycle. If N data points are sampled over a time interval T, then the Nyquist critical frequency, ω_c, is:

$$\omega_c \equiv \frac{\pi N}{T}$$

The complete set of frequencies within the data set are:

$$\omega_k = \frac{2\pi k}{T}, k = 1, \ldots \frac{N}{2}$$

Rather than attempting to cover the whole of the required sample range with one simulation run which would be prohibitively expensive in computational time, the frequency ranges were divided into between 3–5 overlapping regions. These were used to determine the time interval covered by the simulation and the number of sample points required.

3.6 Magnification patterns

The final result of the microlensing simulation is a coordinate position for each light ray at the source redshift. In order to compare the simulation results with observed data, the series of ray coordinates must be converted into light curves

showing the variation in the apparent brightness of a source over a period of time. This is done by generating magnification patterns for each simulation time-step.

In order to obtain the magnification pattern a pixel grid is positioned at the source redshift. The size of the pixels in the grid is the same as the separation between the light rays when they leave the observer. Thus if the intervening lenses were removed from the simulation, the area between any bundle of four adjacent rays would be the same at both the observer and the source. The value of the magnification in the presence of lenses can be obtained by calculating the relative area of the same ray bundle with and without lenses, as illustrated in Figure 3.10. In practice this is done by looking at each source plane pixel and estimating the fraction of the area of each ray bundle which covers the pixel. If the magnification for the un-lensed pixel is taken to be 1 then the fractions from each ray bundle can simply be summed to obtain the magnification for the pixel. This method automatically accounts for multiple images.

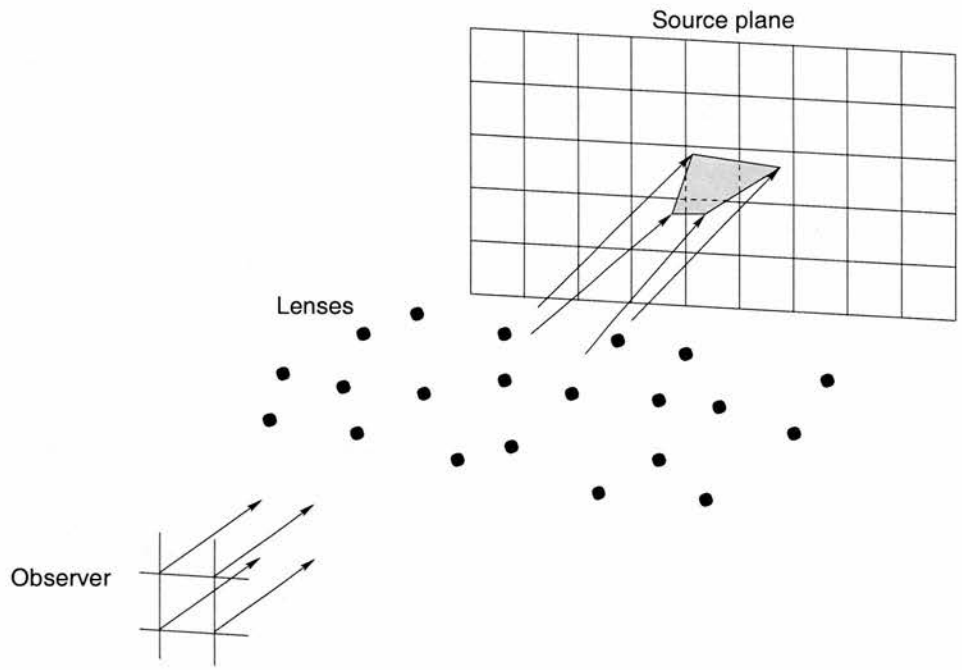

Figure 3.10: The magnification pattern is generated by summing the percentage area of a pixel covered by a ray bundle.

For a magnification pattern to be properly, resolved neighbouring light rays must follow similar paths through the lenses, *i.e.*, their paths are correlated. From this it is assumed that if any additional rays were placed between the neighbouring

rays, their final positions in the source plane could be interpolated. Light rays which fall outside the area of the pixel grid are wrapped round to fall in the opposite side of the grid, ensuring that the magnification pattern is periodic and that no rays are lost from the simulation. Each ray bundle is subdivided into N_v virtual' rays. Taking the magnification of the un-lensed ray bundle to be 1 each 'virtual' ray is allocated a magnification of $1/N_v$. The number of virtual rays from a ray bundle falling within a source plane pixel gives an estimate of the fractional area of the ray bundle which falls over each pixel. The full magnification pattern can be built up by summing the number of virtual rays which fall into each pixel for all the ray bundles.

This section of the simulation was also carried out using parallel computers to reduce the time required to generate the magnification patterns. Unlike calculation of the final positions of the light rays at the source plane, the grid points for the magnification calculations are *not* independent. As described above, the calculation considers ray bundles consisting of four neighbouring light rays. Thus each light ray in the bundle is required for four separate magnification calculations. This needs to be taken into account when the ray grid is divided up between the processes and the edge data replicated on different processes as required. This was implemented using the MPI-2 parallel file I/O routines and also using the C language's file pointer routines to offset file I/O on different processes. The two implementations were necessary: although the MPI-2 parallel file routines provide significant performance benefits over hand code I/O routines, they were not available on all the platforms on which the simulation was run.

Each parallel process then calculates a partial magnification pattern using the ray bundles in its memory. Once this has been completed, the processes perform a parallel reduction operation to obtain the final magnification patterns.

Once the magnification patterns have been calculated for each time-step, the magnitude is then calculated for each pixel using equation 2.9. The light curves themselves are then generated for a range of source sizes. This is discussed in §4.3.

3.7 Simulation Program

The final version of the simulation program consists of three separate programs:

- A setup program with calculates the plane redshifts, the size of the ray grid, the timestep and the position and velocities of the lenses.

- The main raytracing program which calculates the positions of the rays on the source plane for a specified number of timesteps.

- A final program with generates magnification patterns from the final ray positions.

The total set of programs consist of roughly 5000 lines of code programmed in the C language. There were a number of reasons for choosing the C programming language over the more traditional scientific programming language, Fortran. These include:

- The hierarchical tree algorithm results in a non-uniform memory access pattern for the program. The C languages pointer feature allows the programmer direct access to the memory addresses where data is stored. In particular, pointers within the tree structure are used to hold the next memory address to be searched. The memory addresses held in pointers can be altered to reflect the changing structure of the tree as the lenses move over time. Thus a complex memory access pattern can be represented in a relatively simple manner.

- The program was required to be portable across a range of platforms. While Fortran 90 would have provided the pointer functionality outlined above, at the time the program was developed, Fortran 90 compilers weren't widely available. In addition there are complications in using Fortran 90 with MPI. While an interface definition exists for Fortran 90 in MPI, the compiler implementation of a number of Fortran 90 features, such array subscripts, can lead to incorrect results when used with MPI calls. In contrast, C is a small and tightly defined language which is easily portable and has a robust MPI interface.

- A quality C implementation of a hierarchical tree algorithm is freely available[1]. This code forms the basis of the hierarchical tree section of the program.

[1] http://www.ifa.hawaii.edu/~barnes/software.html

These three issues combined to make C the preferred language for this simulation.

The program has been run on a number of different platforms including a Cray T3D, Meiko CS-2, Sun HPC 3500/6500 and networks of Sun and Compaq workstations. C compiler directives were used to compile in platform specific details such as file path names and to switch between parallel and sequential versions of the program. The final simulations were carried out on a Hitachi SR2201.

The SR2201 used consisted of 16-processors and is based on the HP PA-RISC architecture. A number of extensions have been made to the PA-RISC architecture. In particular the pseudo-vectorisation extensions allow the processors to mimic vector processors giving a per processor performance in the 250-300 Mflop range for certain operations. While this number is low compared to most desktop machines today, the SR2201 is an old machine and was a couple of years ago replaced by the SR8000. In addition the uneven memory access pattern in the main program reduces the effectiveness of the psuedo-vectorisation extensions. This has led to a per-processor performance of around 100 Mflops per processor, substantially below optimal. Initial tests on a state of the art SUN HPC 6500 system, indicates a performance increase of around an order of magnitude compared to the Hitachi SR2201 system. In addition to faster processors, the Sun HPC system has a much more efficient file access system than the SR2201. As there is a significant amount of file access carried out in the program, these two features are probably equally responsible for such a substantial increase in performance. While the SR2201 gave less than optimal performance for the program, the system was little used and so there was the opportunity to run the simulations for a considerable amount of cpu time.

3.8 Simulation Parameters

The simulation program has a number of parameters which can be adjusted to give the required balance between accuracy and computation time for any cosmological model. These parameters are:

- The number of lenses in the simulation. This parameter sets the size of the lens and source planes. Too large a number of lenses and the source plane pixels will be too large to resolve detailed features.

- The search radius for each ray. This value set the maximum impact parameter which is searched for each ray. The search radius must be sufficiently large that all the lenses which make a significant contribution to the bend angle are included.

- The opening angle for each ray. This parameter controls the depth to which the hierarchical tree is searched. If its value is too large then the effect of individual lenses on the deviation angle will be smoothed out.

- The number of lens planes included in the simulation. If the lenses are distributed across too small a number of planes then the simulation is effectively modelling a single massive feature, such as a galaxy, rather than a 3-dimensional distribution of lenses.

With this type of large numerical simulation there is, in practice, some compromise required between the level of accuracy of the simulation and the computational resources available. The vast majority of the computing time will be used to calculate lightcurves for comparison with observational lightcurves of quasars (see Chapter 4). The analysis of these simulated lightcurves involves a study of their power spectra. Thus, rather than focussing on the accuracy of individual timesteps, the parameters of the simulation were set to ensure that the power spectra did not vary significantly from the best available calculation. A 'best' power spectra was calculated by setting all the parameters to the maximum accuracy possible.

In practice, the limit on the maximum accuracy was determined by the largest time-slot available on the Hitachi SR2201 used for the simulations[2]. A single timestep was calculated by this method and pseudo-lightcurves generated by moving a source across the source plane. The power spectrum for these lightcurves was then generated using the method outlined in §4.4.

It is clear from the power spectra plotted in graph d) of Figure 3.11 that the number of lens planes used in the simulation has a significant effect on the power spectra. In particular, a simulation with all the lenses on one plane (dotted line) has significantly lower power at virtually all frequencies than the multiple plane simulations. While there is clearly a difference between the power spectra

[2]The maximum run time available was 16 hours on the full 16-processor machine which is equivalent to almost 11 days worth of CPU time.

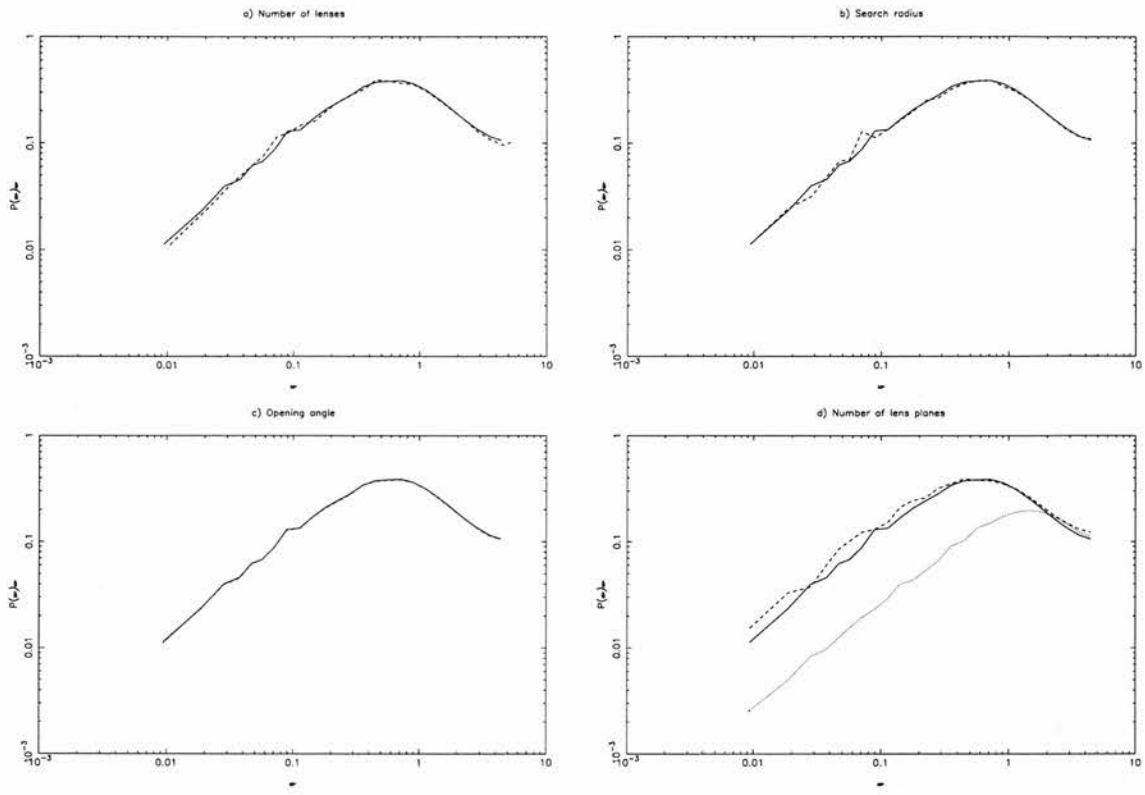

Figure 3.11: The simulation parameters. The parameters were initially set to give a high degree of accuracy (solid line). The final value for the parameter is set to the point just before the results diverge (dashed line). The parameters used to obtain the solid and dashed lines are shown in Table 3.1. In graph d), results for a single lens plane are also shown (dotted line).

for 10 planes (dashed line) and 5 planes (solid line), the accuracy of the other parameters had to be reduced to compensate for the extra computational time required to calculate the paths of the rays through the additional planes. It was felt that the extra accuracy gained by using 10 planes was not sufficient to justify an almost 4-fold increase in the time required to compute a single timestep. The number of lens planes was therefore fixed to 5. In order to test the accuracy of this number of lens planes further, a subset of timesteps for simulation i (see §4.2) were re-calculated with 10 planes. The results of both simulations are shown in Figure 3.12. It is clear from these results that there is little difference between the two power spectra.

The value of the other parameters were then altered and new power spectra produced. This process continued until the power spectra diverged. A final value for each parameter was chosen at a point were there was little or no different

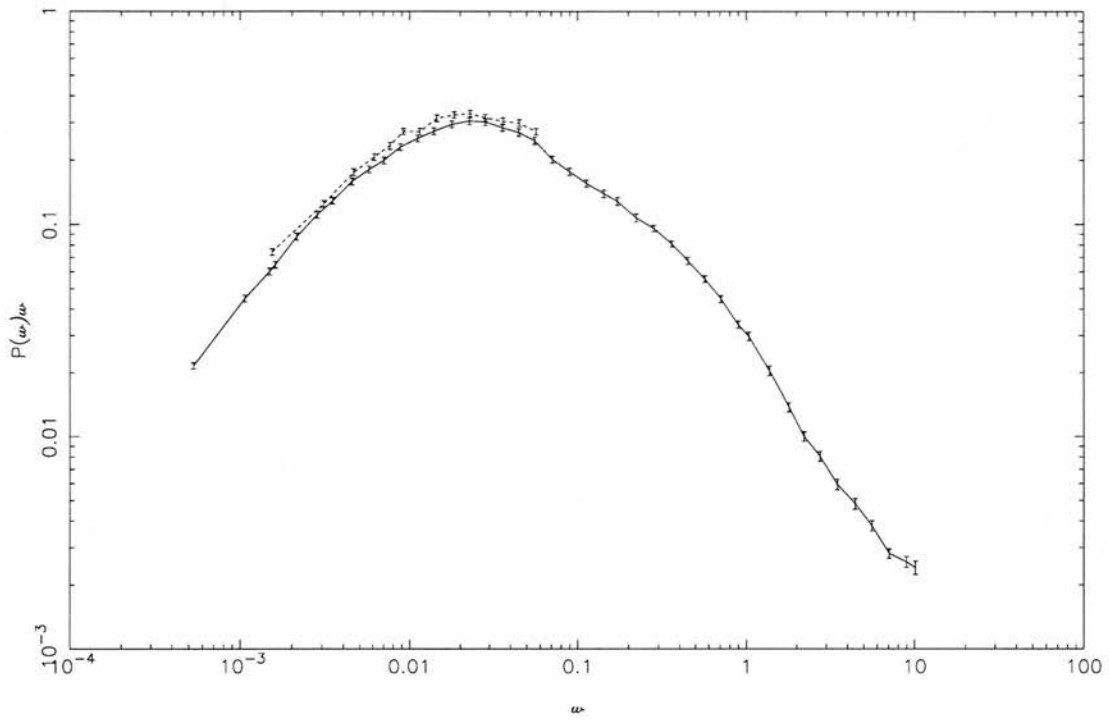

Figure 3.12: A section of simulation i (solid line) was re-calculated with with 10 planes (dotted line).

	Long timescale lightcurves	Single timestep
Max number of lenses	100000	4000
Search radius[3]	$50\theta_E$	$500\theta_E$
Opening angle	0.20 radians	0.002 radians
Number of lens planes	5	5

Table 3.1: The parameter values used for the simulation of microlensing lightcurves.

between the power spectra. The power spectra for the chosen parameter values are shown as the dashed line in Figure 3.11, with the values themselves listed in Table 3.1. For this final set of parameters, each timestep of the simulation required on average $\sim$ 30 minutes on the full 16 processor Hitachi SR2201. The full set of timesteps calculated for the simulations described in Chapter 4 required roughly 7 years of CPU time.

As the time required to calculate the lightcurves is significant, a comparison was made between the power spectrum obtained for simulation i (see §4.2) and a

power spectrum calculated from a set of pseudo-lightcurves generated by moving a source across a single source plane of simulation i. As can be seen in Figure 3.13, there are significant differences in the slope and the peaks of the two power spectra. The graph shows the average power for 800 independent lightcurves[4]. The error bars are calculated from the scatter of the individual power spectra used to calculate the average power. The error bars for the power spectra calculated from the pseudo-lightcurves have significantly larger error bars than the power spectra for simulation i. The differences between the power spectra and the relatively large error bars for the 'moving source' power spectra justify the decision to generate lightcurves from long timescale simulations of a moving population of lenses.

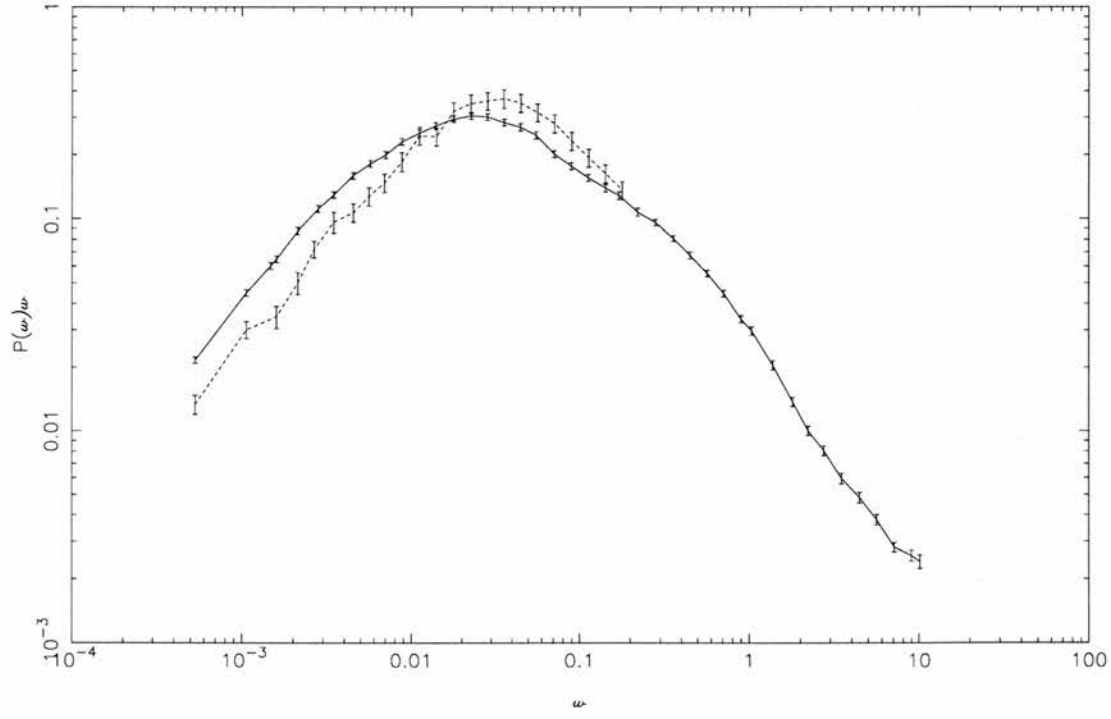

Figure 3.13: The power spectra of simulation i (solid line) and a power spectrum from lightcurves generated by moving a source across a single source plane (dashed line). It should be noted that the values for ω for the 'moving source' power spectra depend on the conversion from source position to timestep.

[4]Sources more than 4 Einstein radii apart are taken to be independent.

In Chapter 5, single timestep simulations are performed for different models over a range of redshifts. The distribution in the magnifications is then used to calculate a series of probability distribution functions (pdfs) for the different models. In this case a high degree of accuracy is required in the magnification patterns generated by the simulation. The parameters for this simulation were set to the most accurate value for which it is possible to calculate a single timestep in the maximum time-slot available on the SR2201. In addition, the number of lenses was reduced to ensure that the high amplification events were sufficiently resolved in the magnification patterns. The set of parameters used for these simulations are also shown in Table 3.1.

Chapter 4

Microlensing Simulation Results

This chapter provides an overview of the observational data. A detailed study of the results of the microlensing simulation is presented. These results are then compared with the observational data.

4.1 Observational Data

The observational data used in this analysis was produced by an ongoing large scale survey and monitoring program which began in 1975. The survey is based on plates taken with the UK $1.2m$ Schmidt telescope at the Siding Spring Observatory in Australia. The field used for the survey is ESO/SERC 287 centred on 21^h28^{min}, $-45°$ (1950), at galactic latitude $-47°$. Although the total area of the Schmidt field is $\sim 40\text{deg}^2$, only the central 18.8deg^2 was used in order to minimise the effect of changes in sensitivity at large distances from the field centre.

The Schmidt plates produced a catalogue of some $200,000$ objects. Quasars were selected from the Schmidt plates on the basis of variability. This selection method has the advantage of being independent of the colour of the quasar candidate. This means that it can be applied over a broad range of redshifts (see Figure 4.1 for the redshift distribution of quasars in the survey and Figure 4.2 for the variation in apparent magnitude with redshift.). The selection criteria require that quasars vary over a time scale of $\sim$ 1 year and that they should not vary significantly within this period. This ensures that short period variables such as RR Lyrae stars are excluded. However, it will also eliminate quasars which vary significantly over short periods. In addition to variability, quasars which were detected in radio

and objective prism surveys of the field were also included. Further details on the survey can be found in Hawkins (1996).

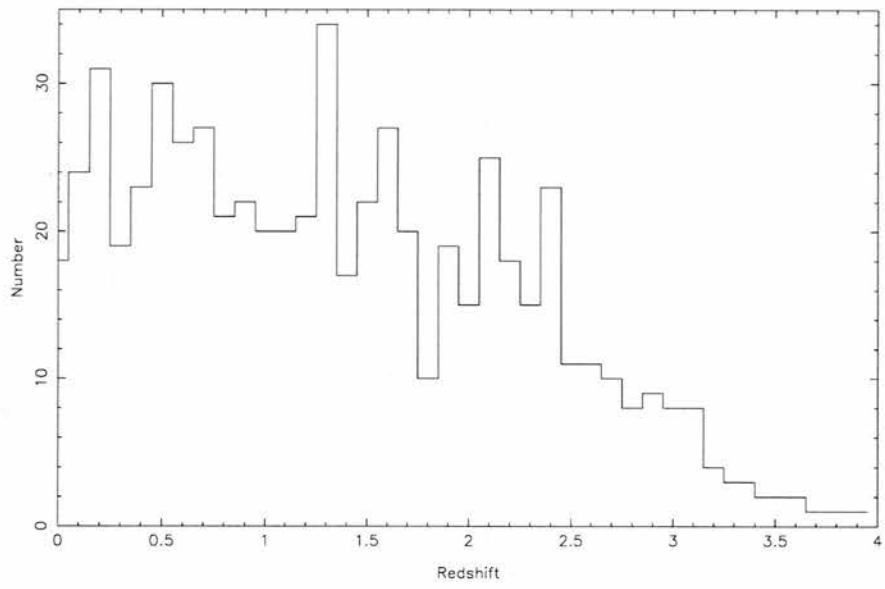

Figure 4.1: Distribution of quasar redshifts for observational data.

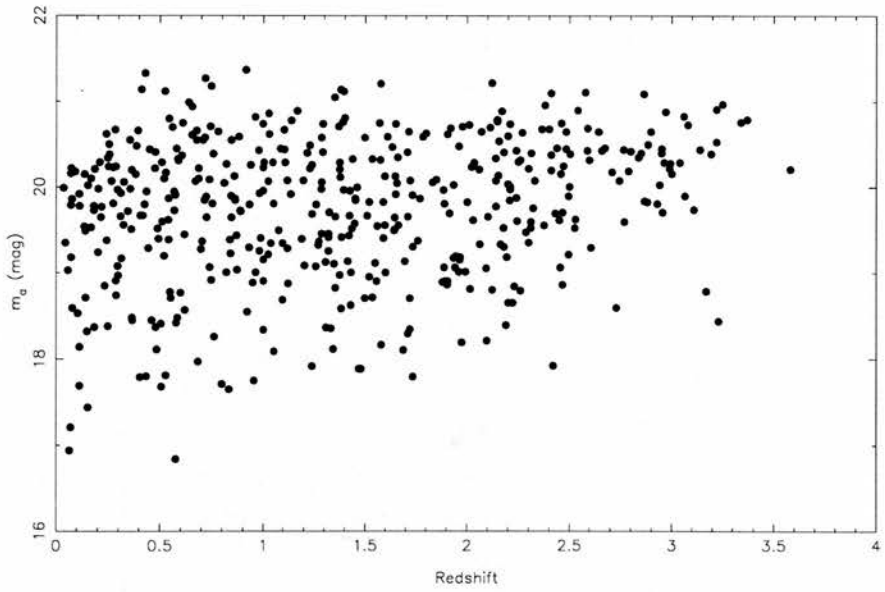

Figure 4.2: The variation of the apparent magnitude m_a with redshift is shown for the quasar sample.

Initial observations of the quasars selected for inclusion in the survey[1] identified a long term variability in the apparent luminosity of the quasar with a period of roughly 10 years (Hawkins, 1993). As discussed in §1.4.1, variability on this timescale does not appear to be linked with phenomena such as radio emission, which typically accompanies short term quasar variability. In particular, the timescale of the variability appears to be independent of the redshift of the quasar, suggesting an external cause for the variation.

Lightcurves are generated for the quasars identified by the survey. As different years have varying numbers of plates, the magnitude for each year is taken as the average over the plates for that year. Figure 4.4 shows some example lightcurves from quasars in the survey. The lightcurves show the variation in apparent luminosity around the mean quasar magnitude for the same 20 year period. The top two lightcurves are for quasars with a redshift of $z \sim 3.0$, the next two $z \sim 2.0$, then $z \sim 1.0$, $z \sim 0.5$ with the bottom row containing lightcurves for quasars with $z \sim 0.1$. For quasars with redshifts of $z \geq 0.5$, the lightcurves clearly show a long term variation with a period of roughly 10 years. Further, the period of variation does not appear to change systematically with the redshift of the quasars. The lowest redshift quasars, with $z \sim 0.1$ show little variation on this timescale. These observations are consistent with the optical depth for microlensing increasing with redshift. Comparisons are made in §4.3.1 and §4.3.2 between these observational lightcurves and lightcurves from microlensing simulations.

In order to make a quantitative comparison between lightcurves from the observational survey and those produced by the microlensing simulation, a measurement of the statistical properties of both data sets is required. In the analysis described in §4.4, power spectra are used to compare the observational and simulation data sets. Power spectra for the observational survey data are shown in Figure 4.3, where the power for a particular angular frequency ω is given by $P(\omega)$. The observational data was divided into redshift bins of $0.5 \leq z < 1.5$ and $1.5 \leq z < 2.5$ and luminosity bins of with apparent magnitude $m_a < 20$ and $m_a \geq 20$. The power spectra shown are the mean spectra for the set of lightcurves in the sample. The error bars show the error on the mean of the power spectra.

The power spectra for the most luminous quasars is significantly lower that for the full sample. In the simulation power spectra (see §4.4), a similar drop in power

[1]The initial sample contained ~ 300 quasars. This number has now risen to over 600.

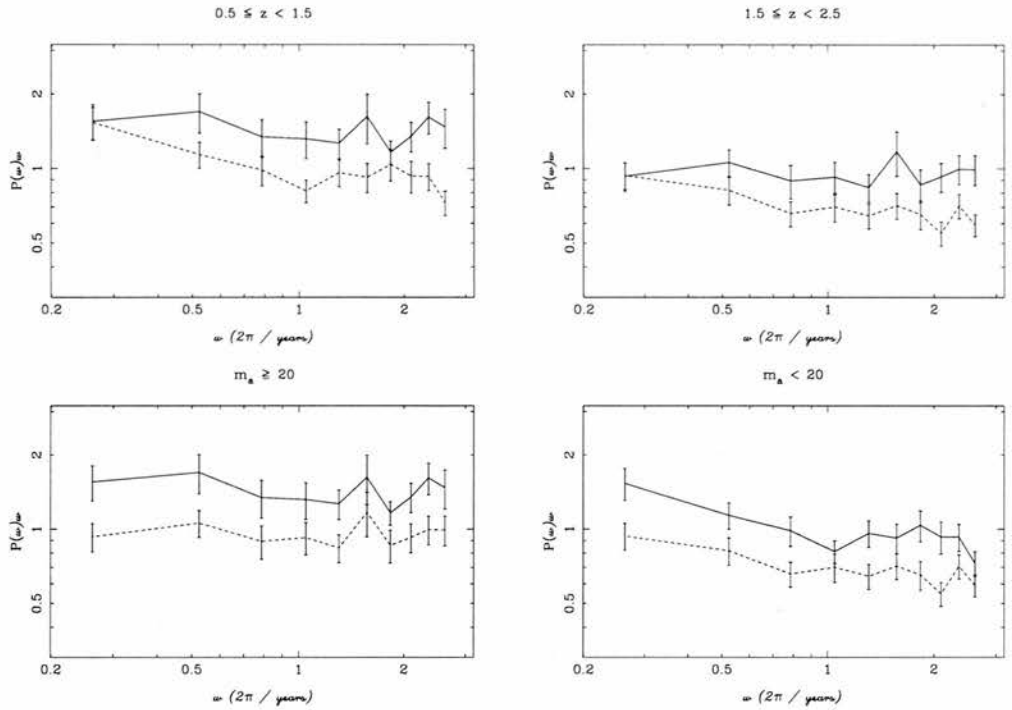

Figure 4.3: Power spectrum for observational data. The top two graphs show the variation in power for two different apparent magnitude samples in a low redshift bin (left graph) and a high redshift bin (right graph). In both graphs the solid line represents quasars with an apparent magnitude $m_a \geq 20$ and the dashed line quasars with $m_a < 20$. The bottom two graphs show the power for two different redshift bins in a sample with $m_a \geq 20$ (left graph) and $m_a < 20$ (right graph). In both graphs the solid lines represent the low ($0.5 \leq z < 1.5$) redshift bin and the dashed line the high ($1.5 \leq z < 2.5$) redshift bin.

is observed for increasing source size. This would fit with the interpretation that more luminous objects are generally larger if the variability is caused by microlensing. A comparison between the power spectrum for the observational data and those for the different microlensing simulations can be found in §4.4.

4.2 Numerical Simulation Models

The microlensing simulation was repeated for a number of variations on two cosmological models. These models were the Einstein-de Sitter model and a flat, non-zero cosmological constant model. In the case of the model with a positive cosmological constant, the current favourite values of a total mass density $\Omega_M = 0.3$ and a cosmological constant of $\Omega_\Lambda = 0.7$ were chosen. This model was

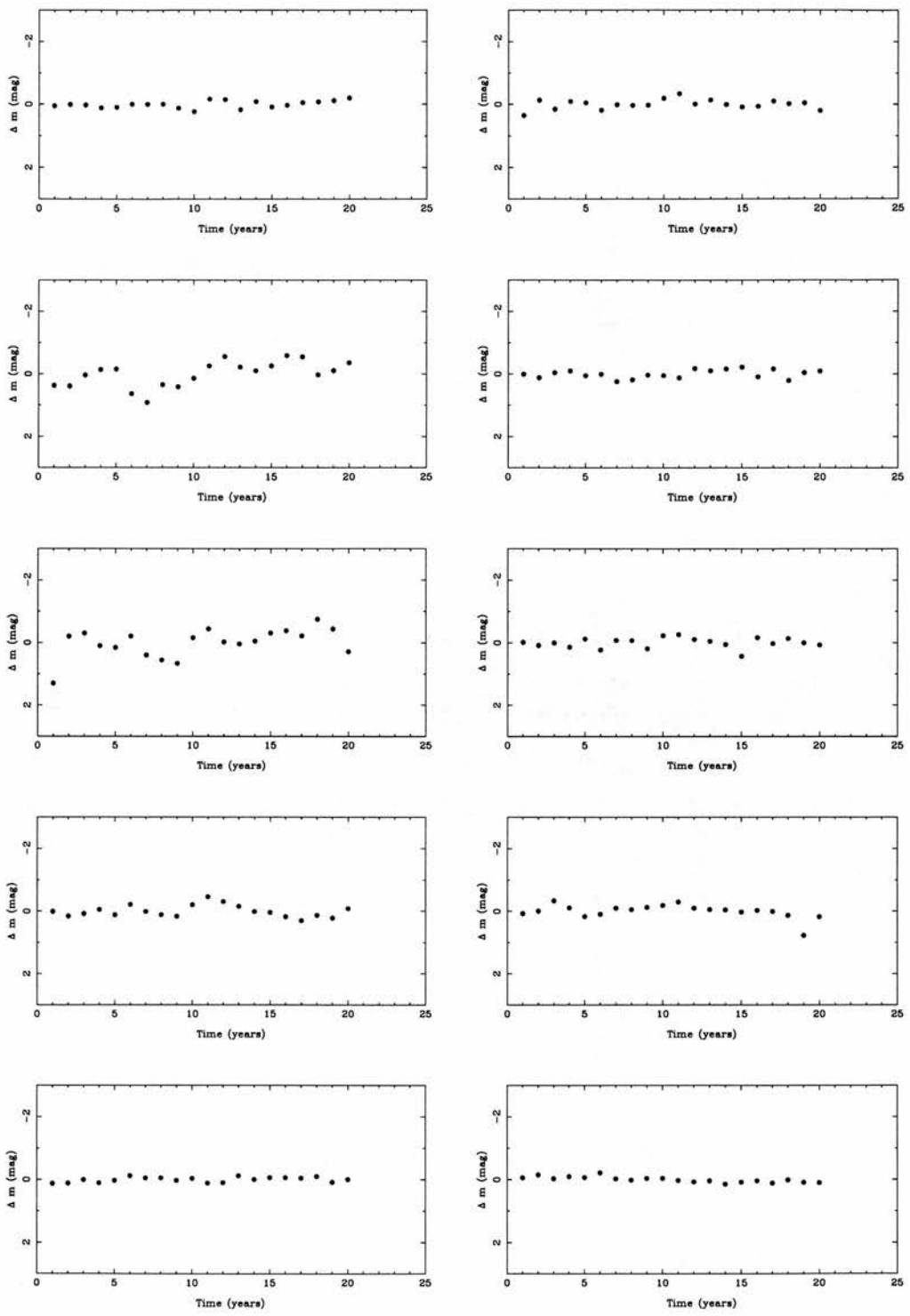

Figure 4.4: Observational lightcurves for quasars with redshifts of $z \sim 3.0$ (top row), 2.0, 1.0, 0.5 and 0.1 (bottom row).

Number	No. Lenses	No. Planes	Lens Mass	Z_{source}	Ω_M	Ω_{Lens}	Ω_Λ
i	100000	5	$1M_\odot$	2.0	1.0	1.0	0.0
ii	100000	10	$1M_\odot$	2.0	1.0	1.0	0.0
iii	87875	5	$1M_\odot$	2.0	0.3	0.3	0.7
iv	23000	5	$1M_\odot$	1.0	0.3	0.3	0.7
v	29291	5	$1M_\odot$	2.0	0.3	0.1	0.7
vi	2929	5	$1M_\odot$	2.0	0.3	0.01	0.7
vii	20000	5	$0.1M_\odot \leq M \leq M_\odot$	2.0	0.3	0.1	0.7

Table 4.1: Simulation parameters

used as the basis for a number of simulations with varying proportions of Ω_M in lenses. The parameters are summarised in Table 4.1.

As discussed in §3.5, each simulation of a particular cosmology and value of Ω_{Lens} is repeated with a number of different timesteps. Varying the timestep of the simulation allowed for a greater range of frequencies to be covered than would otherwise have been computationally feasible. In general, three different time periods were covered for each cosmological model giving a coverage of around 3–4 orders of magnitude in the frequency scale depending on the source profile (see §4.4).

The exceptions to this are the Einstein-de Sitter model which was run initially for 5 different timesteps. This was done in order to establish a set of timesteps which, as well as covering as wide a frequency range as possible, also provided sufficient overlap in frequencies to allow the individual power spectra to be joined together accurately. In addition, the first timestep setting for the Einstein-de Sitter model was repeated with twice the number of lens planes. This was carried out in order to confirm the number of planes selected in §3.8.

A detailed summary of the time periods for the different simulations is shown in Table 4.2. The time periods shown are for a lens mass of $10^{-4}M_\odot$.

For each timestep in the simulation, the paths of a 1024^2 grid of rays are followed through the simulation and their final positions at the source redshift recorded. These positions are then used to generate magnification patterns using the approach outlined in §3.6. Examples of magnification patterns from simulation *iii* are shown in Figures 4.5 – 4.7. The lightcurves produced from these magnification

	No of Timesteps	Simulation Period (years)
Simulation *i*		
(*a*)	251	0.00 → 4.92
(*b*)	341	0.52 → 0.82
(*c*)	501	0.00 → 118.31
(*d*)	241	0.00 → 685.61
(*e*)	251	0.00 → 42.56
Simulation *ii*		
(*a*)	201	0.000 → 41.12
Simulation *iii*		
(*a*)	261	0.000 → 81.58
(*b*)	261	0.000 → 6.79
(*c*)	251	0.000 → 39.20
Simulation *iv*		
(*a*)	231	0.000 → 5.94
(*b*)	261	0.000 → 80.66
(*c*)	261	0.000 → 40.30
Simulation *v*		
(*a*)	261	0.000 → 30.48
(*b*)	261	0.000 → 5.14
(*c*)	261	0.000 → 61.73
Simulation *vi*		
(*a*)	301	0.000 → 46.65
(*b*)	361	0.000 → 9.33
(*c*)	361	0.000 → 112.03
Simulation *vii*		
(*a*)	1461	0.000 → 122.50
(*b*)	361	0.000 → 15.09
(*c*)	361	0.000 → 2.51

Table 4.2: The simulation of a particular set of cosmological parameters is repeated for different sampling rates.

patterns form the data set used in the analysis of the simulation data.

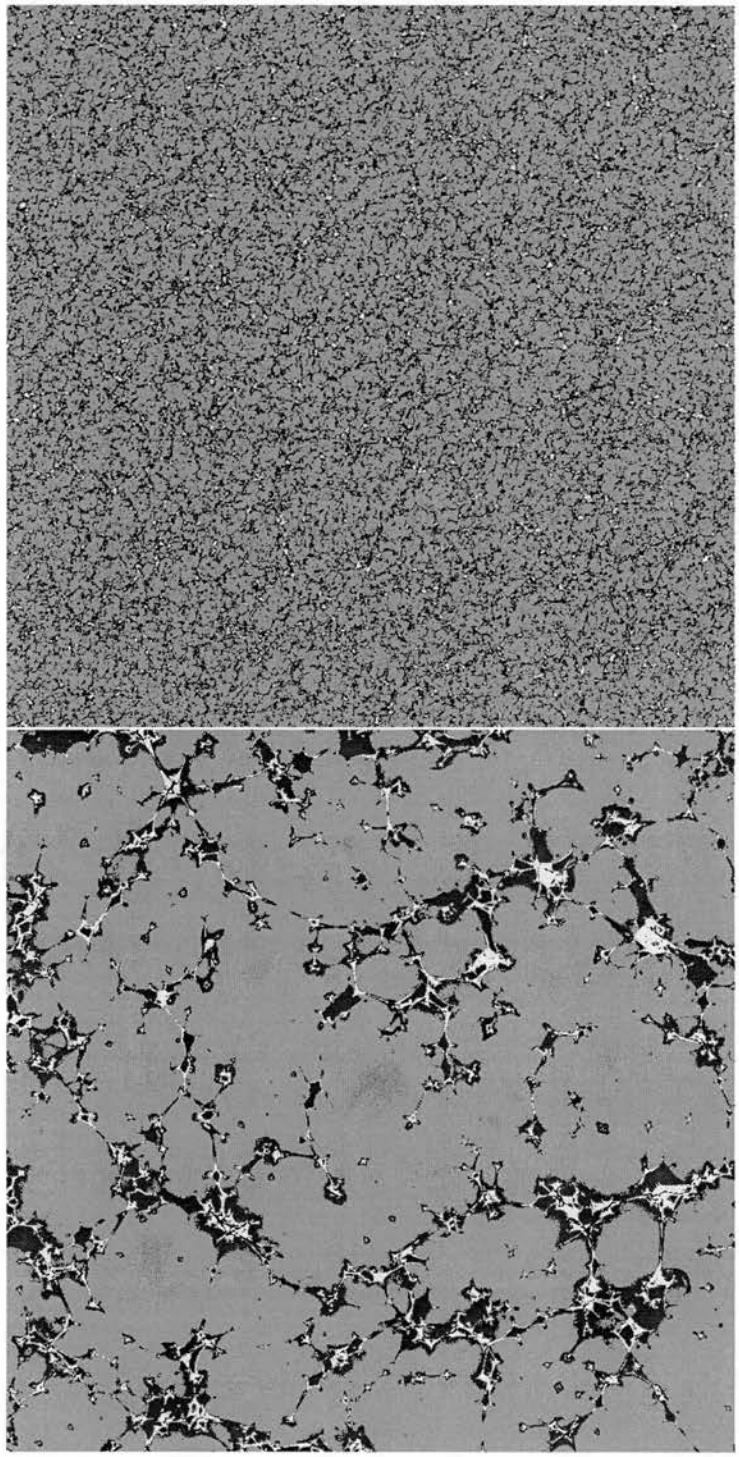

Figure 4.5: Magnification patterns for areas of $\sim 600^2\theta_E$ (top) and $\sim 60^2\theta_E$ (bottom) of simulation i. The colour represents magnitude with black corresponding to $m < -2$, yellow $-2 \leq m < -1$, red $-1 \leq m < 0$, green $0 \leq m < 1$, cyan $1 \leq m < 2$ and blue $m \geq 2$.

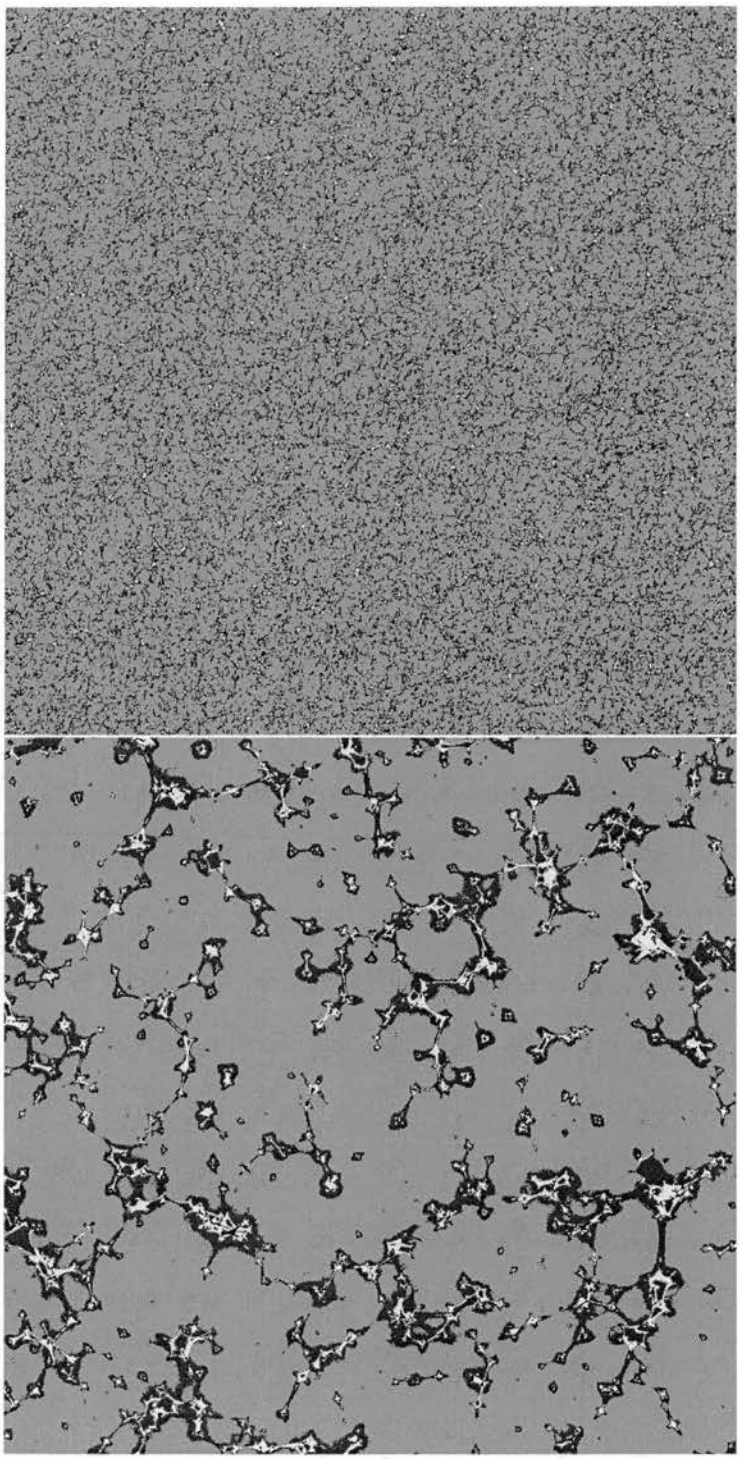

Figure 4.6: Magnification patterns for areas of $\sim 600^2\theta_E$ (top) and $\sim 60^2\theta_E$ (bottom) of simulation *iii*. The colour represents magnitude with black corresponding to $m < -2$, yellow $-2 \leq m < -1$, red $-1 \leq m < 0$, green $0 \leq m < 1$, cyan $1 \leq m < 2$ and blue $m \geq 2$.

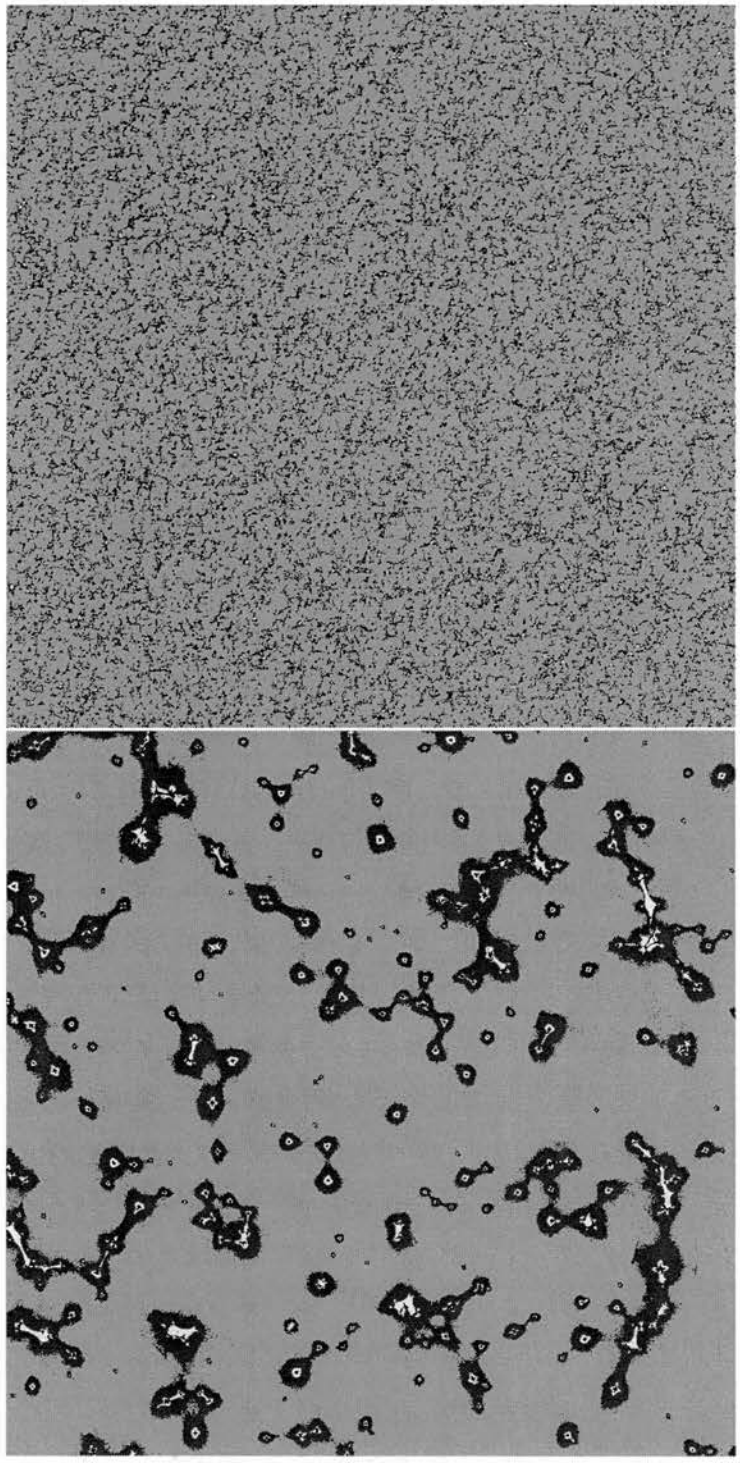

Figure 4.7: Magnification patterns for areas of $\sim 600^2\theta_E$ (top) and $\sim 60^2\theta_E$ (bottom) of simulation v. The colour represents magnitude with black corresponding to $m < -2$, yellow $-2 \leq m < -1$, red $-1 \leq m < 0$, green $0 \leq m < 1$, cyan $1 \leq m < 2$ and blue $m \geq 2$.

4.3 Lightcurves

Once a set of magnification patterns is generated for each model under investigation, they are used to produce lightcurves showing the variation of a source due to microlensing over a period of time. A single set of magnification patterns can be used to generate light curves for a variety of source profiles. This section presents light curves generated for pixel sized sources and extended sources with gaussian and constant surface brightness profiles.

4.3.1 Pixel Sources

The resolution of the magnification pattern is limited by the size of the source plane pixels. Thus the smallest source available is the single pixel source. The size of the pixel is significantly smaller than the extended sources under consideration and for all practical purposes can be treated as a point source.

Lightcurves for the point sources are generated by picking a set of random coordinates from the pixel plane. These coordinates are checked to ensure that none are closer than 4 Einstein radii apart. This ensures that the lightcurves obtained are independent. Once the coordinates for the pixel sources have been obtained, the magnification for the coordinates are recorded for each of the timesteps to produce the light curve. Repeating the simulations with different timesteps produces multiple versions of sections of the lightcurves each sampled at a different rate.

A selection of lightcurves is shown for different cosmological models in Figures 4.8–4.12. In each figure the left hand column shows the different timesteps generated in each simulation. For the sections where the shorter timestep data overprints the longer timestep data, it can be seen that the same broad features are present in both lightcurves. The shorter timestep data can be seen to add addition fine detail to the lightcurve. The right hand column shows the same light curves sampled on a yearly basis. This is the same sampling rate used for the observational data.

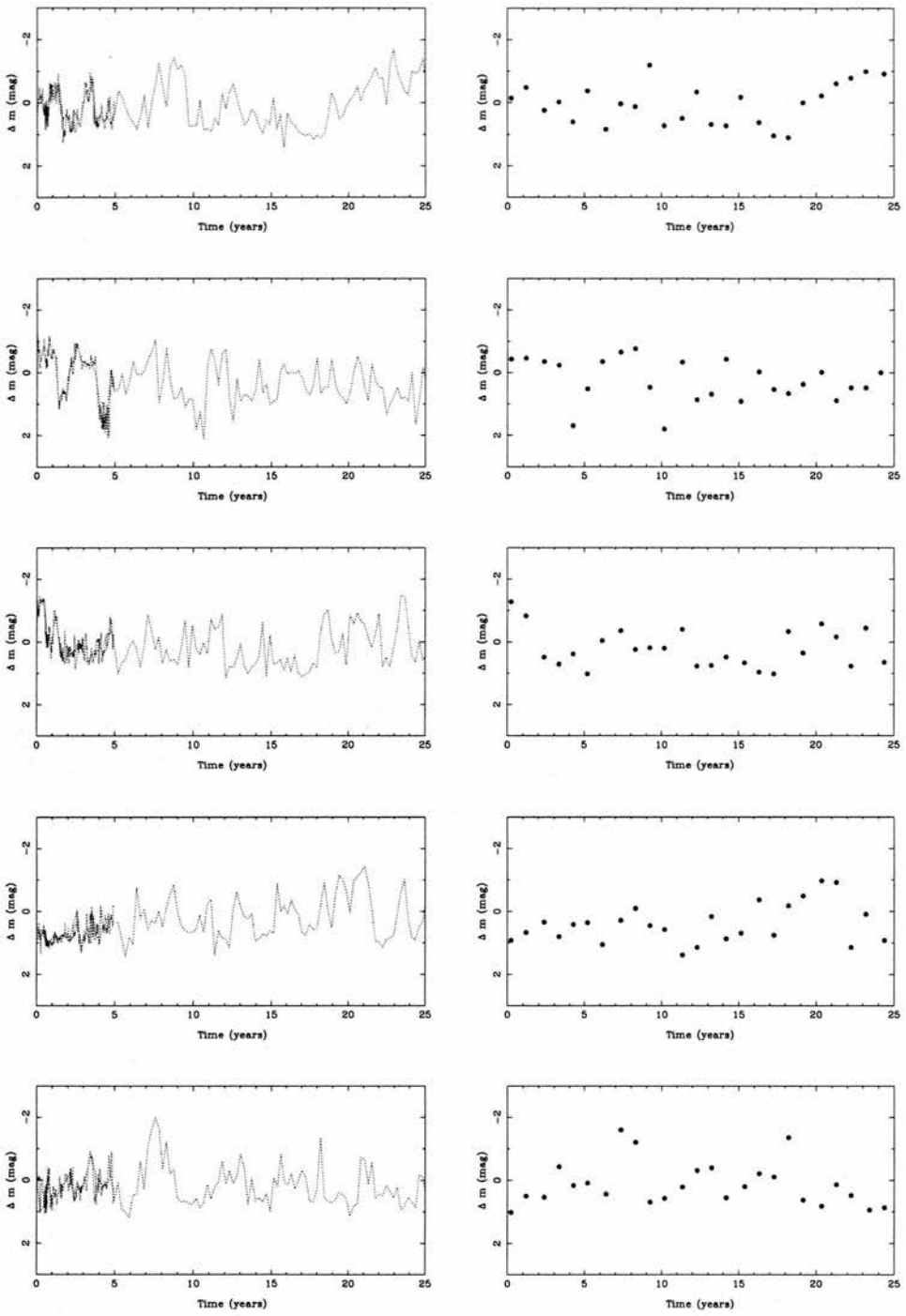

Figure 4.8: Simulation i. The left column contains example light curves from an Einstein-de Sitter model with $z_{src} = 2.0$. The lightcurve is overprinted with two shorter timestep lightcurves. The right column shows these light curves sampled on a yearly basis.

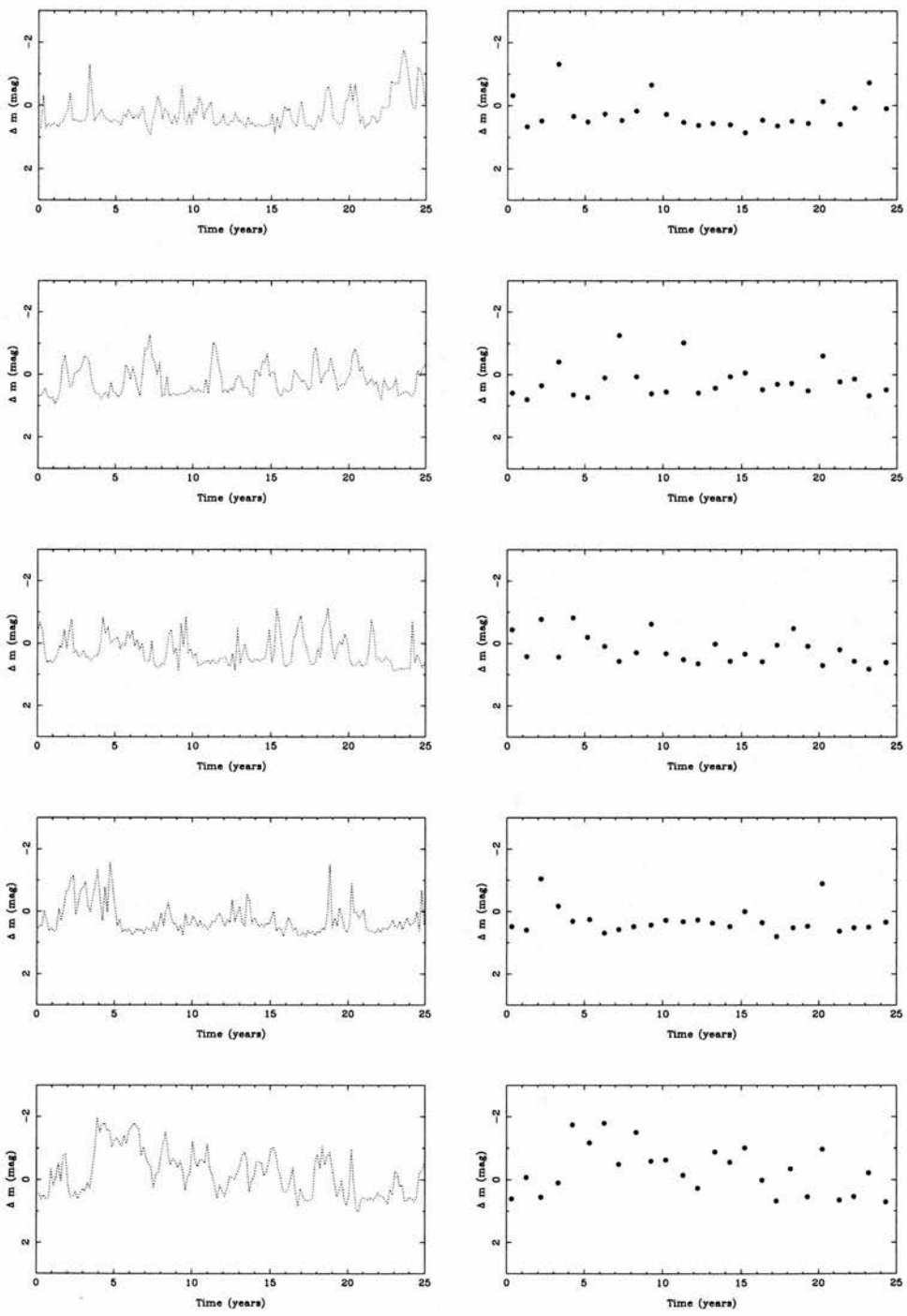

Figure 4.9: Same as Figure 4.8 for simulation *iii* ($\Omega_M = 0.3$, $\Omega_\Lambda = 0.7$, $z_{src} = 2.0$).

A number of general comparisons can be made from the lightcurves shown in Figures 4.8–4.12. Details of the cosmological parameters used for each of the simulations can be found in Table 4.1.

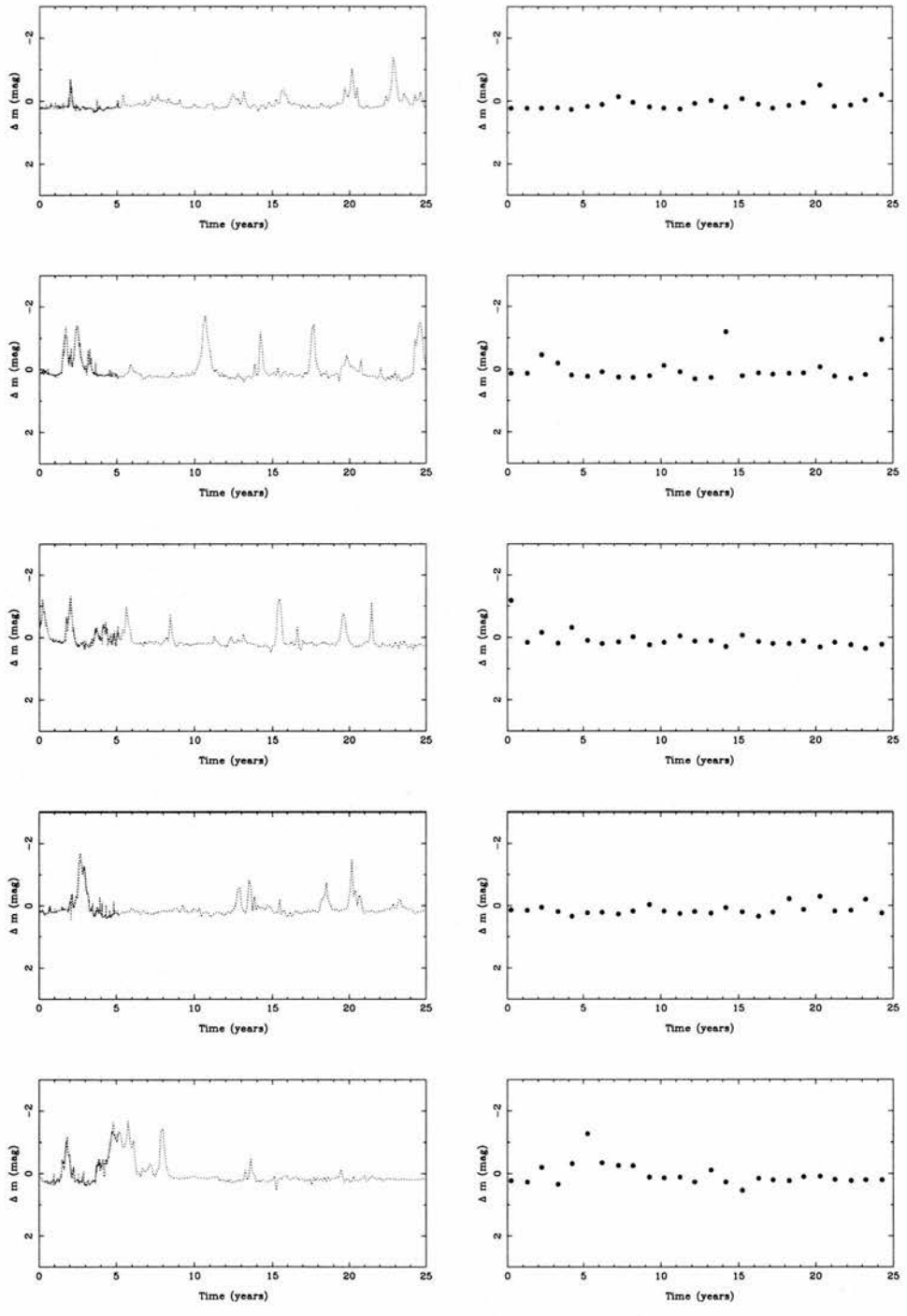

Figure 4.10: Same as Figure 4.8 for simulation *iv* ($\Omega_M = 0.3$, $\Omega_\Lambda = 0.7$, $z_{src} = 1.0$).

The lightcurves for the Einstein-de Sitter cosmology of simulation *i* (Figure 4.8) show a much greater variance than those for the non-zero cosmological constant model of simulation *iii* shown in Figure 4.9. In both models all the mass in

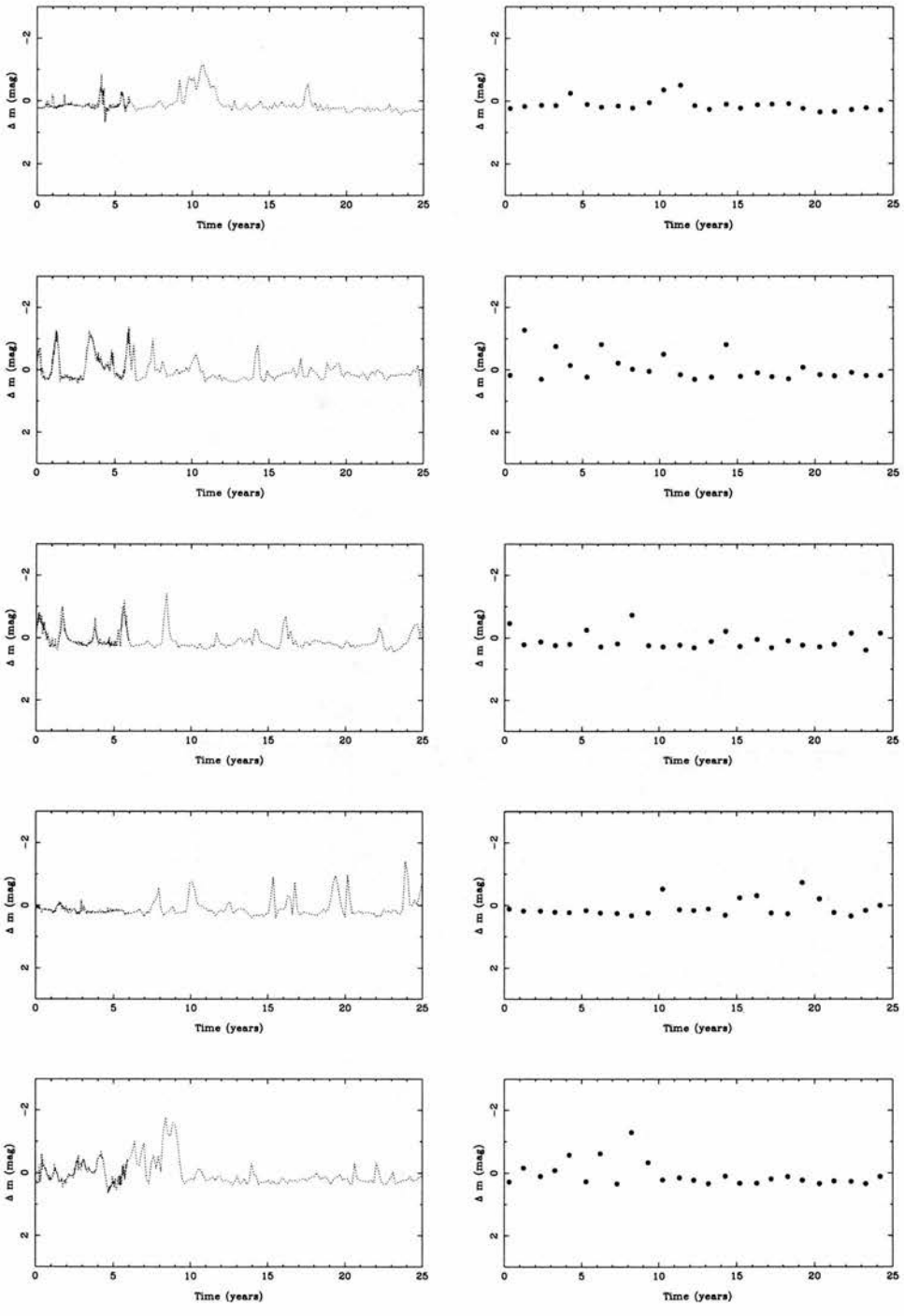

Figure 4.11: Same as Figure 4.8 for simulation v ($\Omega_M = 0.3$ (0.1 in lenses), $\Omega_\Lambda = 0.7$, $z_{src} = 2.0$).

the simulation is in the form of lenses. The larger mass density of simulation i therefore corresponds to a greater optical depth. In fact, it can be seen from the lightcurves that all the light rays are lensed to some extent. Thus a light ray

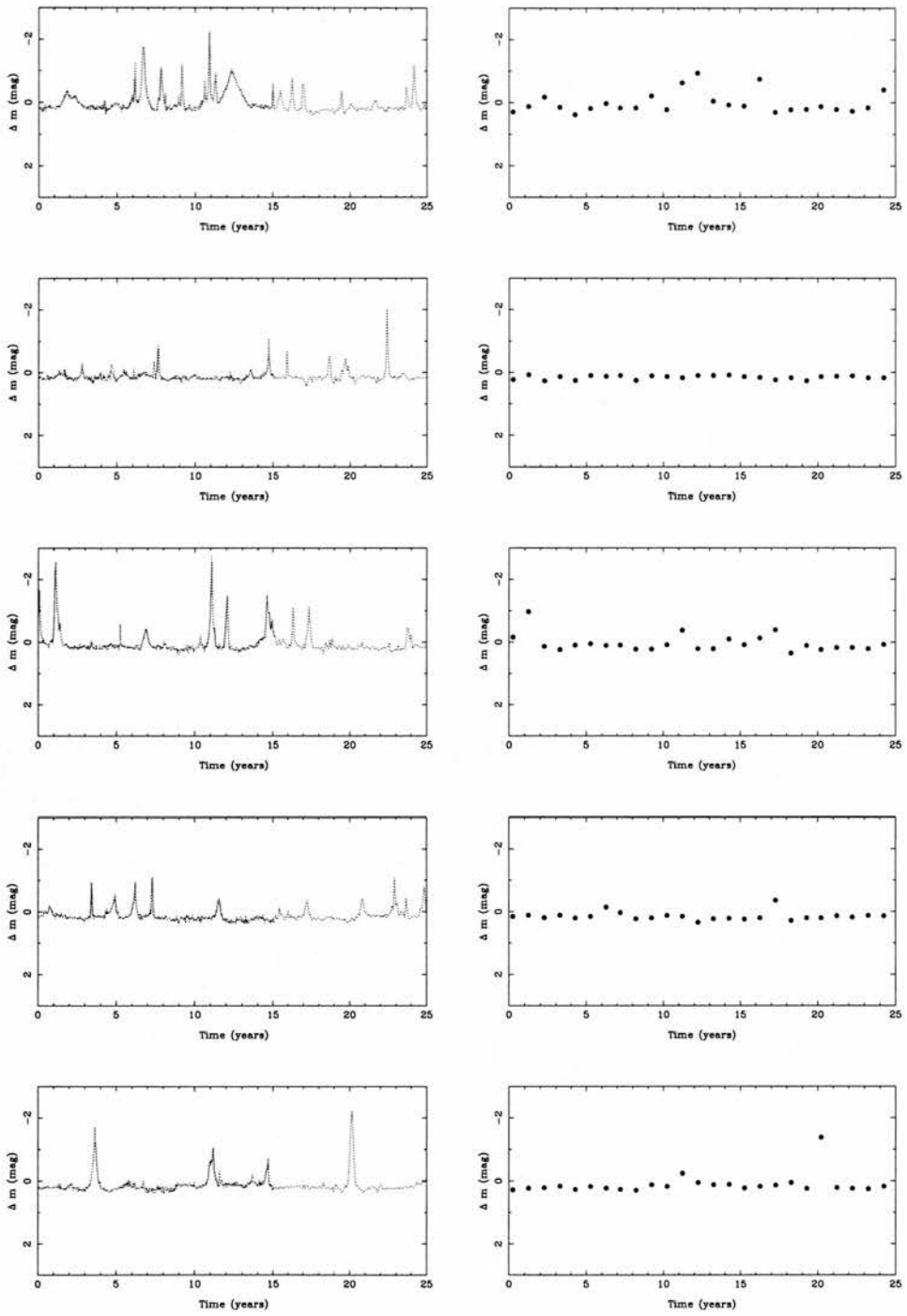

Figure 4.12: Same as Figure 4.8 for simulation *vii* ($\Omega_M = 0.3$ (0.1 in lenses with mass distributed according to Equation 2.18, $\Omega_\Lambda = 0.7$, $z_{src} = 2.0$).

passing through simulation *i* will be deflected, on average, by a larger number of lenses than a light ray in simulation *iii*. In both cases, the lightcurves consist of a non-linear combination of multiple lensing deflections, although some individual

lensing events can be seen in simulation *iii*.

For a fixed cosmological model with $\Omega_M = 0.3$ and $\Omega_\Lambda = 0.7$, the lightcurves of simulation *iii* (Figure 4.9) and simulation *v* (Figure 4.11) show the effect of lowering the proportion of Ω_M in lenses. As the amount of mass in lenses drops from all of Ω_M in simulation *iii* to 1/3 in simulation *v*, the optical depth is also reduced. Again, this results in a smaller variance for the lightcurves of simulation *v* relative to simulation *iii*. Also individual lensing events are clearly visible in simulation *v*.

A similar effect can be observed for the lightcurves of simulation *iii* (Figure 4.9) and simulation *iv* (Figure 4.10). In this case proportion of Ω_M in lenses is held constant while the redshift of the source plane is reduced from $z_{src} = 2.0$ to $z_{src} = 1.0$. As discussed in §1.4.1, while the most effective lenses are found at a redshift of $z \approx 0.5$, lenses at other redshifts will also contribute to the final magnification. Thus, a variation with source redshift would be expected if microlensing were the cause of the variation. It would be interesting to compare in detail whether there is any variation in the observational power spectra for samples selected at different redshifts.

The lightcurves of simulation *v* (Figure 4.11) and simulation *vii* (Figure 4.12) illustrate the effects of changing the distribution of lens masses in the simulation. The two simulations use the same cosmological model, again $\Omega_M = 0.3$ and $\Omega_\Lambda = 0.7$ and source redshift. In both cases, 1/3 of Ω_M is in the form of lenses. The lenses in simulation *v* all have the same mass, while those in simulation *vii* are distributed according to the power law in Equation 2.18. This mass distribution results in more low mass lenses than high mass lenses. The effect of this can be seen in the two sets of lightcurves. The lightcurves of simulation *vii* show the occasional distinct high amplification events due to a small number of high mass lenses with an underlying variation due to the much larger population of small mass lenses.

As well as the complete lightcurves for the first 30 years of the simulation period, the right column of Figures 4.8–4.12 shows the same lightcurves sampled on a yearly basis. These can be compared with the observational lightcurves of Figure 4.4. While some of the simulation lightcurves show the same level of long term variation as the observation lightcurves, it is clear that the high amplification events present in simulation lightcurves are not seen in the observational

lightcurves. These high amplification events are present due to the small size of the sources, *i.e.*, a single pixel source. As quasars are extended sources, the absence of high amplification events from the observational lightcurves is unsurprising. The following section examines the effect of extended sources on the simulation lightcurves.

4.3.2 Extended Sources

In addition to the pixel sized sources, two types of extended sources were considered: a source with a constant surface brightness profile (Refsdal & Stabell, 1991) and a source with a gaussian surface brightness profile (Wambsganss *et al.* (1990a) and Wambsganss *et al.* (1990b)).

With the constant surface brightness profile, the source has a surface brightness of 1.0 everywhere. The sources modelled have a radius of 3, 6, 12, 24 and 48 pixels.

For the gaussian surface brightness profile a source has a surface brightness $F(r)$ a distance r from the centre.

$$F(r) = F_0 e^{-r^2/2\sigma^2}$$

where σ is the halfwidth of the source and F_0 is chosen so that the maximum surface brightness is 1.0. Five different source sizes with values of σ of 1, 2, 4, 8 and 16 pixels were used. Each source has a radius of 3σ. Thus the constant and gaussian profile sources cover the same total area of the source plane. The source profiles for the different values of σ are shown in Figure 4.13.

For each of the surface brightness profiles, the source positions are chosen so that each source is separated from the neighbouring source by at least four Einstein radii. This ensures that each lightcurve generated is independent. The source positions are fixed for each lightcurve. The lightcurves are generated by convolving the source profile with the pixels it covers in the magnification patterns. The resulting magnification are then integrated over the surface of the source. This process is repeated for each magnification pattern in the simulation.

Figures 4.14 and 4.15 show lightcurves for the gaussian and constant surface brightness profiles. In each case, the left hand column of the figure shows the change in the lightcurves for sources with the same central coordinates as the

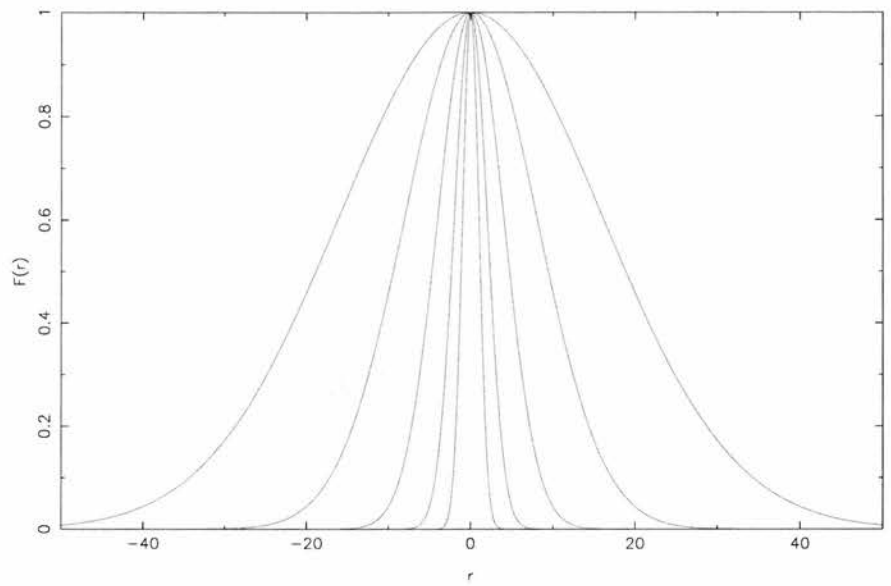

Figure 4.13: Gaussian source brightness profiles for different values of σ. The inner profile is for $\sigma = 1$ and the outer is for $\sigma = 16$.

source size increases. It can be clearly seen in both sets of lightcurves that, as expected, the peaks in magnification are smoothed out as the source size increases. Also the individual lensing features remain prominent in the gaussian source profile for larger sources than with the constant source profile. This is because with the gaussian source brightness profile, the majority of the magnification for the source comes from roughly the central third of the source. Thus the high amplification events aren't smoothed out by surrounding lower magnification pixels when compared to the constant surface brightness profile.

Again, it is interesting to compare the sampled lightcurves shown in the right had columns of Figures 4.14 and 4.15 with lightcurves from the observational survey (see Figure 4.4). The absence of the high amplification events from both sets of extended source lightcurves, when compared to the point source lightcurves, clearly increases the similarity between the observational and simulation lightcurves. In particular, the simulation lightcurves in Figures 4.14 and 4.15 both show evidence of an underlying long term variation of a similar period to the observational lightcurves.

While the lightcurves illustrate a number of features of the different simulations and source sizes, it is difficult to compare them quantitatively with the observational data. The following section outlines a more rigorous power spectral

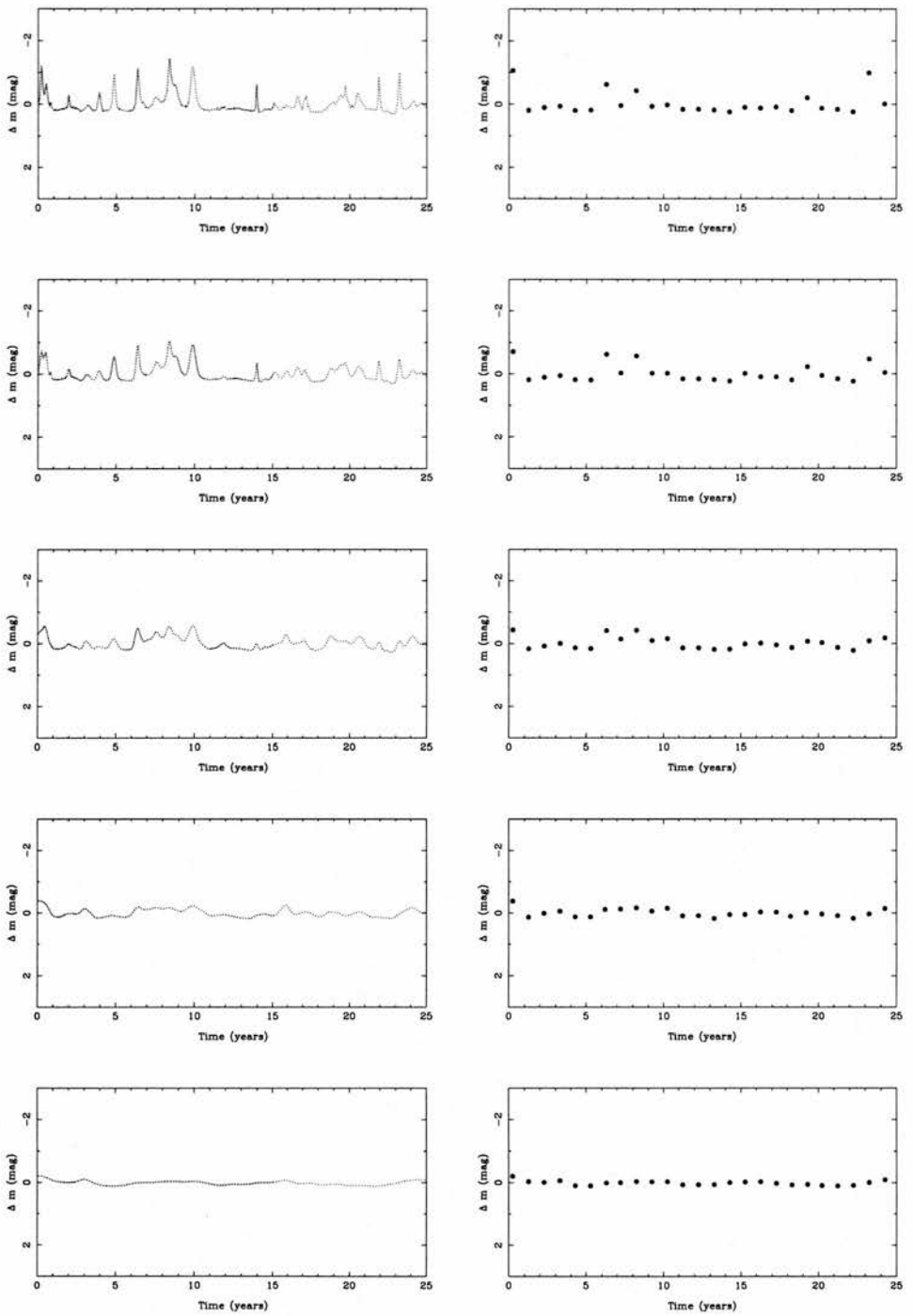

Figure 4.14: Simulation *vii* with gaussian source profiles. The left column shows the lightcurves of sources with the same central coordinates as the source size increases. The top lightcurve is for $\sigma = 1$ pixel and the bottom is for $\sigma = 16$ pixels. The right column shows the lightcurves sampled on a yearly basis.

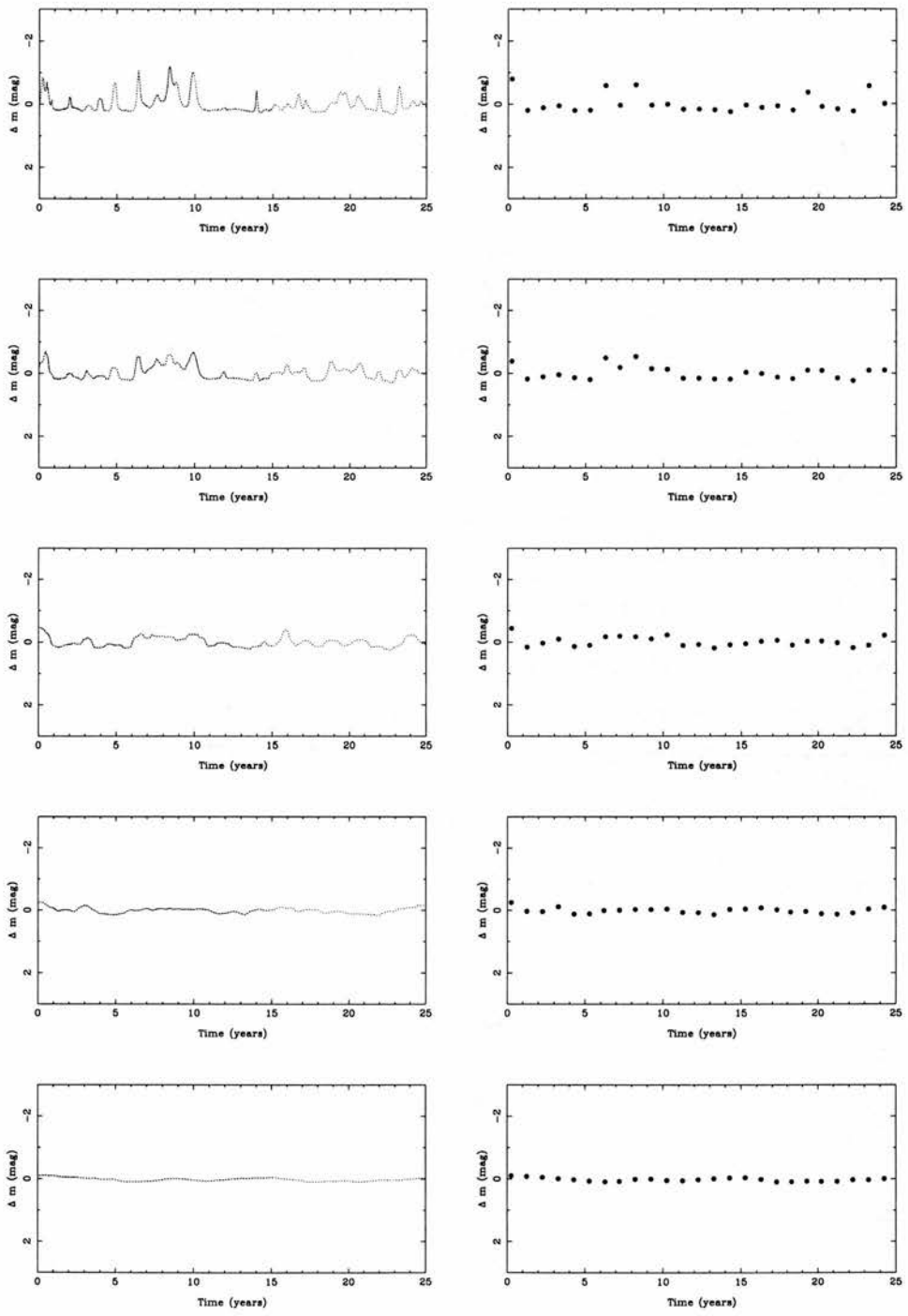

Figure 4.15: Simulation *vii* with constant source profiles. The left column shows the lightcurves of sources with the same central coordinates as the source size increases. The top lightcurve has a source radius of 3 pixels and the bottom lightcurve has a source radius of 48 pixels. The right column shows the lightcurves sampled on a yearly basis.

analysis which was used to compare the statistical properties of the observational and simulation data sets.

4.4 Power Spectra

Power spectra provide a reliable statistical method for comparing different sets of data. While individual lightcurves may differ dramatically for the same cosmological model, the overall power spectra should remain consistent. If a signal is considered to be made up of a combination of different frequency sine waves, the power spectra measures the amount of power in the signal from a given frequency. Power spectra have the advantage that power values at different frequencies are uncorrelated. This is particularly important if, as in this case, models are going to be fitted to the power spectra, as it ensures that there is no systematic shift in the data caused by correlated data points.

The lightcurves $A_0(t)$ produced by the numerical simulations consist of N discretely sampled data points taken over a period of time T. The discrete lightcurve, $A_0(t)$, is an approximation of the underlying continuous lightcurve $A(t)$. Thus,

$$A_0(t) = A(t)W(t)$$

$W(t)$ is the sampling window function for measurements taken at times $t = t_i$:

$$W(t) = \sum_{i=1}^{N} \delta^D(t - t_i)$$

where $\delta^D(x)$ is the Dirac delta function.

The underlying power spectrum for a set of discretely sampled data can be expressed as:

$$P(\omega) \simeq \frac{T \langle |A_0(\omega)|^2 \rangle}{\sum_{\omega_i} |W(\omega - \omega_i)|^2}$$

where ω is the angular frequency $\omega = 2\pi k/T$, $k = 1, N$ for a simulation with a duration of time T. This expression is derived in Appendix B.

A power spectrum is calculated for each simulation lightcurve. As each simulation was repeated for a number of different timescales, this results in a set of power spectra, with each set covering a different range of frequencies. The mean power

spectrum, $\hat{P}$, for each range of frequencies is found by taking the average of the individual power spectra. The error on $\hat{P}$ is taken as the variance of the power spectra which make up $\hat{P}$ (see Appendix B.1).

As each simulation was repeated over different timescales, a different $\hat{P}$ is obtained for each timescale. Figure 4.16 shows the different $\hat{P}$s obtained for the pixel source of simulation *vii*. It is clear from this graph that the method of calculating different $\hat{P}$s individually for different timescales can be used to obtain an accurate measure of the power over a large range of frequencies. The same plots for the other simulations and source sizes show a similar agreement between $\hat{P}$s for different timescales.

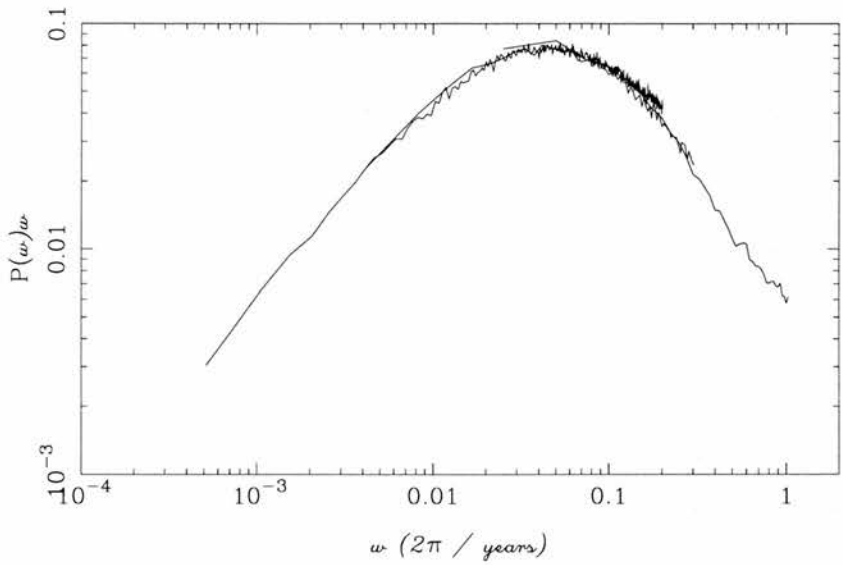

Figure 4.16: The power spectra obtained for each of the three different timesteps modelled for the point source in simulation *vii* are plotted. For each simulation and source profile, a final power spectrum is calculated by combining the individual power spectra from each of the different timescales modelled.

The $\hat{P}$s for different timescales are combined to give the final underlying power spectrum for each simulation. A χ^2 fit is then calculated for the final power spectra using the function:

$$P(\omega)\omega = \frac{A\omega^a}{\left[1 + (\frac{\omega}{\omega_0})^{a+b}\right]^c} \tag{4.1}$$

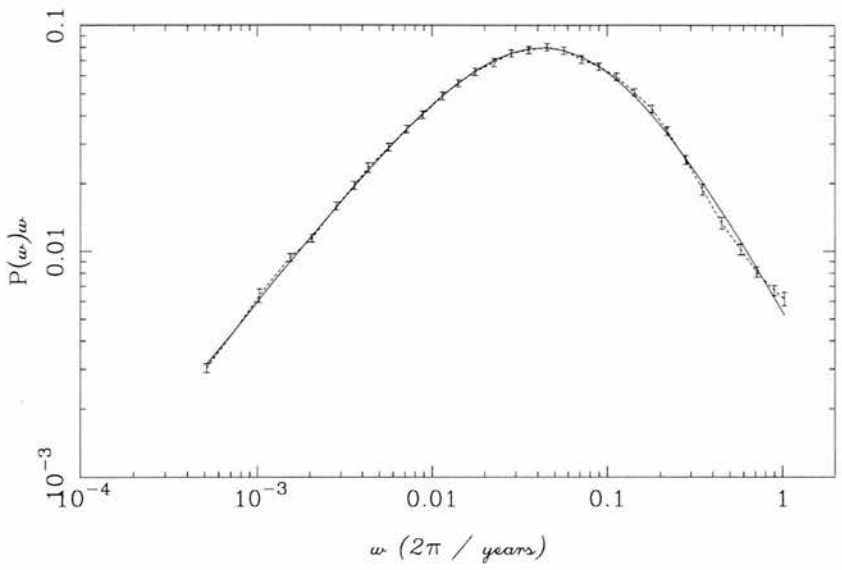

Figure 4.17: The final power spectrum for the point source profile of simulation *vii* is plotted (dashed line) along with the best fit from Equation 4.1 (solid line). This fitting process is repeated for each of the source profiles and simulations.

The fit for the power spectrum in Figure 4.16 for the combined power spectra of simulation *vii* is shown in Figure 4.17.

The final power spectra for each of the different source sizes and simulations were fitted using Equation 4.1. The resulting best fits are shown as graphs in Figures 4.18 and 4.19. The best fit parameters are listed in Appendix C, Tables C.1, C.2, C.3 and C.4.

The power spectra shown in Figures 4.18 and 4.19 show a number of interesting features. The most obvious feature in each of the simulations is the drop in power across all frequencies as the source size increases. In each graph, the source size increases moving down from the pixel sized source in the top line. This reduction of power with increasing source size can be predicted from the lightcurves for the different source sizes shown in Figures 4.14 and 4.15. As the source size increases, the variation in magnitude of the sources decreases, reducing the variance of the lightcurve. As the area under the power spectra is the variance of the data, this drop in variance is seen in the power spectra as a reduction in the level of power for larger source sizes. A similar effect can be seen in the observational power spectra (Figure 4.3) if the high luminosity quasars with $m_a < 20$ are interpreted as corresponding a larger source size.

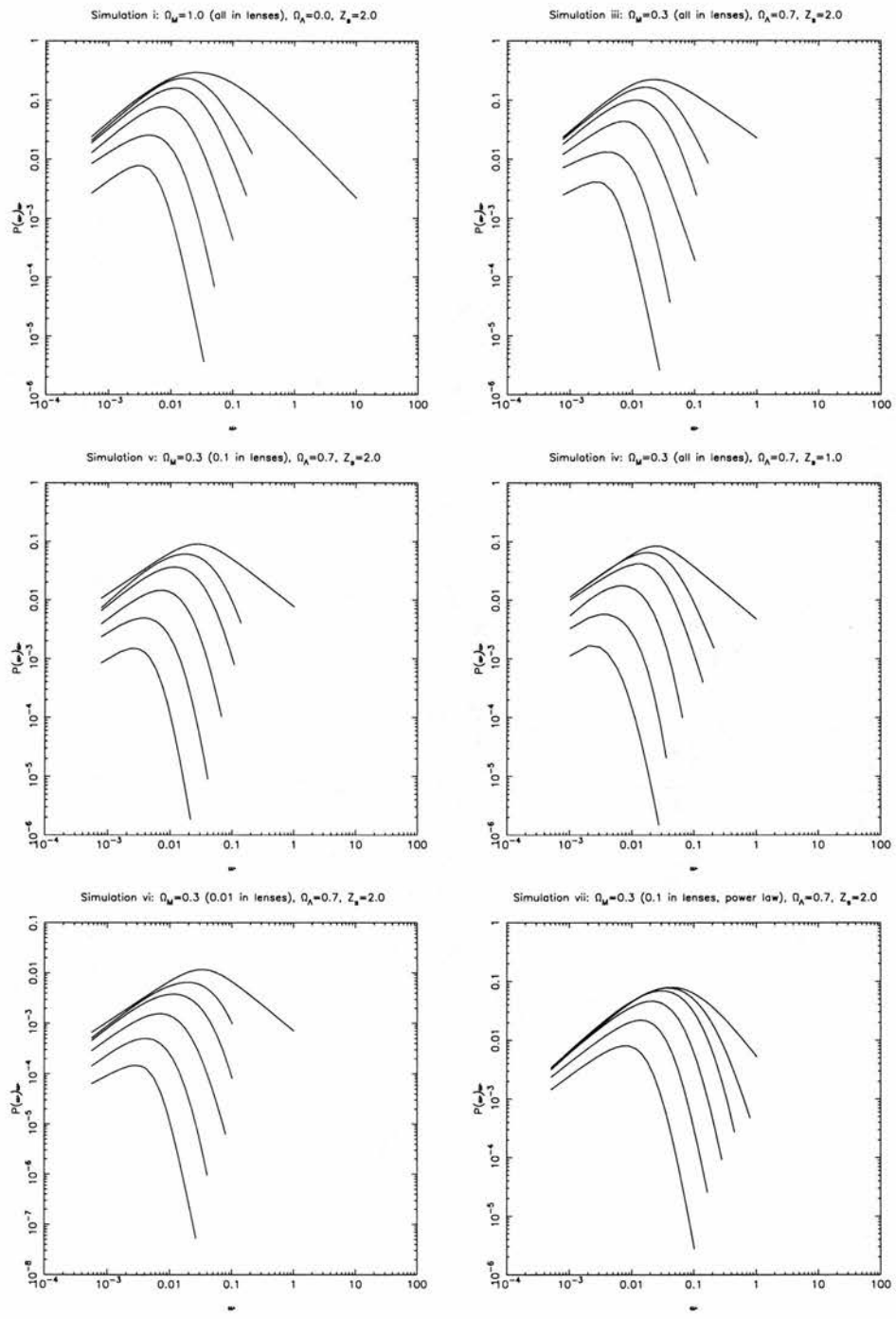

Figure 4.18: Graphs of the best fit to Equation 4.1 for the different simulations and gaussian source profile sizes. For each of the simulations the top most line on the graph is the pixel sized source with the source sizes increasing with each line down the graph through the five different gaussian source profiles under consideration.

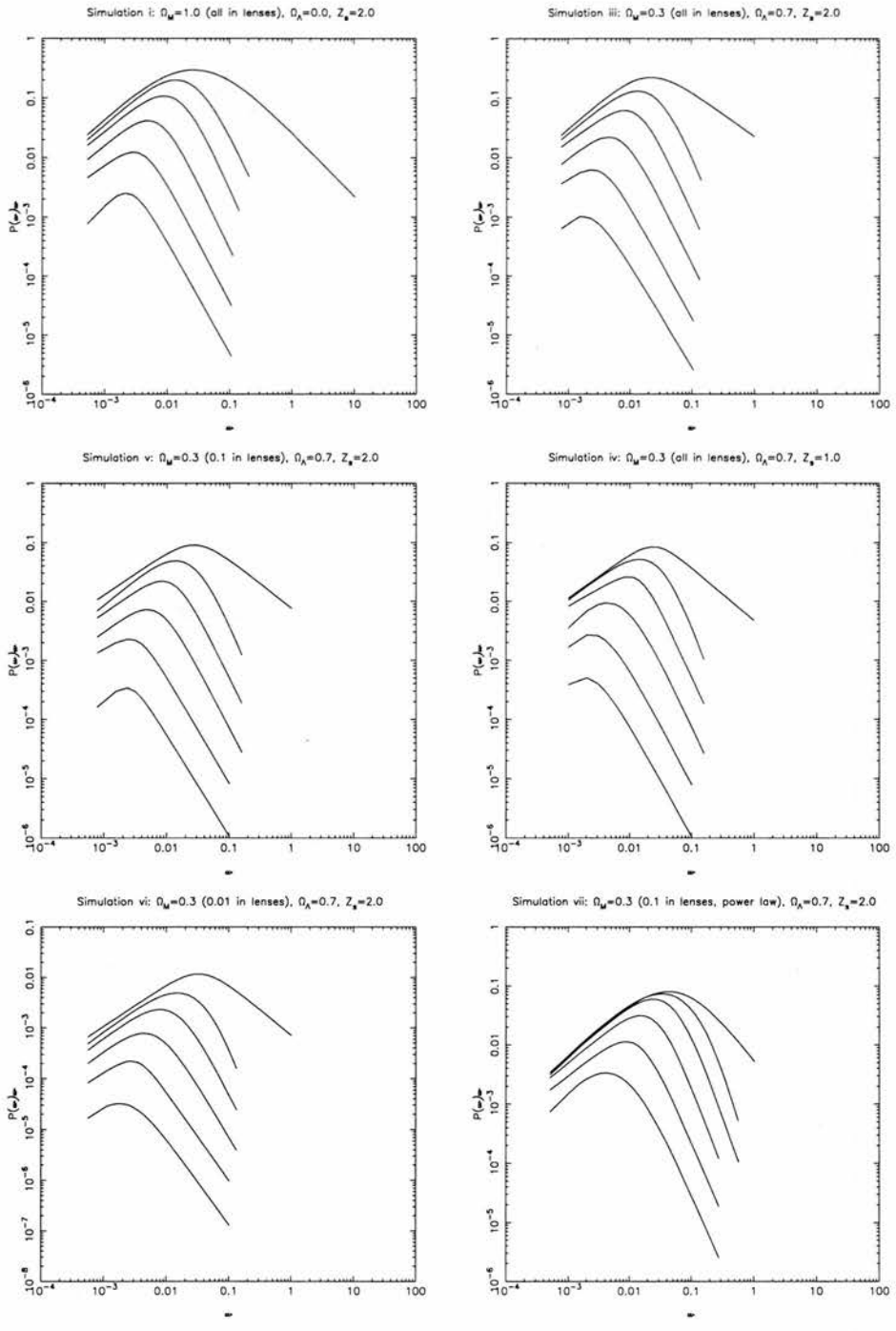

Figure 4.19: Graphs of the best fit to Equation 4.1 for the different simulations and constant source profile sizes. For each of the simulations the top most line on the graph is the pixel sized source with the source sizes increasing with each line down the graph through the five different constant source profiles under consideration.

Also, as the source size increases, the high frequency side of the power spectra drops off more rapidly than at the low frequency end. This is due to the increasing source sizes smoothing out the fine detail in the lightcurves which largely contributes to the high frequency component of power spectra. It is interesting to note that this drop off is more pronounced in the sources with a gaussian surface brightness profile than those with a constant surface brightness profile. This is probably due to the sharp drop in magnification at the edge of the constant surface brightness profile source introducing high frequency artifacts components which artificially increase the power at the high frequency end of the range.

It is difficult to make detailed comparisons between different models as the source sizes vary between each cosmology. Each source is specified in terms of the number of pixels it covers on the source plane. As the angular diameter distance to the source plane at a specified redshift depends on both Ω_M and Ω_Λ (Equation 2.11), the proper size of the source varies between cosmologies. The variation of the power with different proper source sizes is discussed in detail in §4.5.

Within a fixed cosmology, the proportion of Ω_M in the form of lenses also affects the power spectra. For the $\Omega_M = 0.3$ and $\Omega_\Lambda = 0.7$ cosmology, as the amount of mass in lenses drop from the whole of Ω_M to $\Omega_M/3$ and finally to $\Omega_M/30$ the power levels drop also.

The distribution of the mass between the lenses within the simulation also affects the form of the power spectra. Comparing the power spectra for simulations *v* and *vii*, the peak of the power spectra are at roughly the same level for the pixel sized sources. However, the reduction in power as the source sizes increase is much less for the power law mass distribution of lenses in simulation *vii* than for the single mass lenses in simulation *v*. Also, the peaks occur at a higher frequency in simulation *vii* than the corresponding peaks in simulation *v*.

4.5 Comparison of Observational and Simulation Power Spectra

In order to compare the power spectra from different microlensing simulations with the observational power spectrum, it is important to take into account the effects of the relatively short timescale of the observations and the discrete sampling of the lightcurves. Therefore the discrete observational power spectra of

Figure 4.3 can not be directly compared with the continuous power spectra of Figures 4.18 and 4.19. Instead the simulation power spectra are convolved with a window function which mimics the yearly sampling of the observational data.

The observational power spectra of Figure 4.3 vary depending on the objects included in the sample. For the purpose of this analysis data is binned in luminosity and redshift. The redshift bins include objects in the ranges $0.5 \leq z < 1.5$ and $1.5 \leq z < 2.5$ while the luminosity bins split the data into between objects which have an apparent magnitude of $m_a < 20$ and those with $m_a \geq 20$.

As discussed in §2.6.4, the timescale of the microlensing lightcurves, and therefore the power spectra, only depend on the mass of the lenses in the simulation. For a simulation of timescale T, the mass M of the lenses varies as $T \propto \sqrt{M}$. Thus the power spectra can be scaled to different lens mass ranges by moving it along the frequency axis.

The graphs shown in Figures 4.20 to 4.25 show the results of scaling the power spectra for the gaussian source brightness profiles to different mass ranges and convolving with the window function. Figures 4.26 to 4.31 illustrate the same for the constant source brightness profiles.

The solid lines in the graphs represent the convolved power spectra from the microlensing simulation, while the dashed line is the power spectra obtained from the observational data sample with $1.5 < z < 2.5$ and $m_a < 20$. Each graph shows the convolved power spectra for lens masses ranging from $10^{-5} M_\odot$ to $1 M_\odot$. It should be noted that, as scaling the mass also scales the size of the simulation source plane, sources containing the same number of pixels correspond to different proper source sizes for different lens masses. The proper sizes of the pixels for each lens mass is shown in Table 4.3. The relation between proper source size and lens mass will be discussed later in this section.

The first observation to make about the graphs shown in Figures 4.20 to 4.31 is the difference in shape between the simulated power spectra and the observational one. In all the cases considered the peak of the power spectra is narrower than the frequency range covered by the observational data. Thus, while each of the observational power spectra is roughly flat, the simulated spectra show an appreciable turn down.

It is useful to consider the relative levels of power between the observational and simulation spectra. With the exception of simulation *vi*, for each simulation

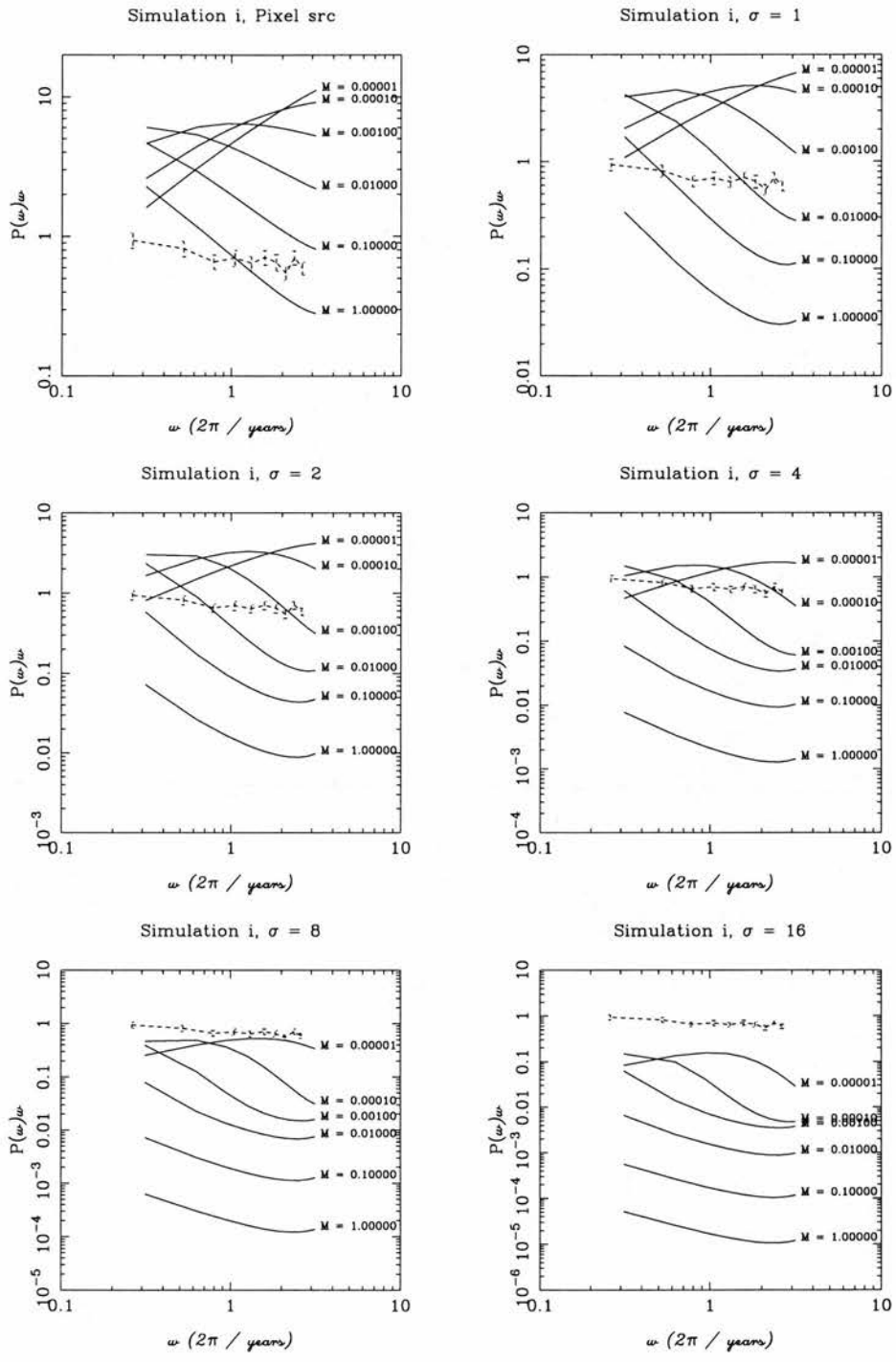

Figure 4.20: Simulation i: The solid lines show the power spectra of the pixel sized source and a range gaussian surface brightness profile sources convolved with the window function for different lens masses. The dashed line is the power spectra for the observational data sample with $1.5 < z < 2.5$ and $m_a < 20$.

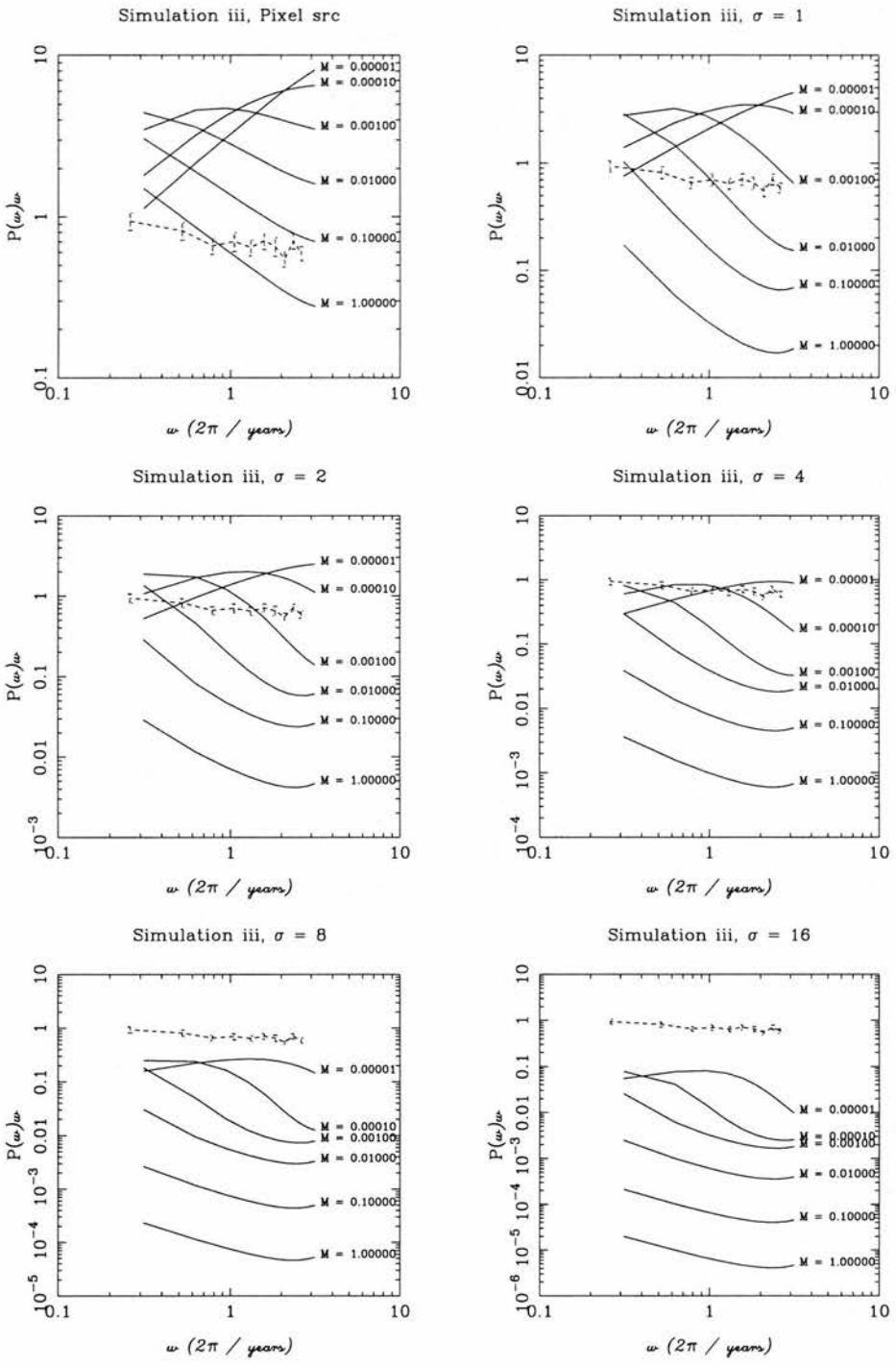

Figure 4.21: Same as Figure 4.20 for simulation *iii*.

some combinations of source size and lens mass reproduces a similar power level to each of the observational datasets. Simulation *vi* contains $0.01\Omega_M$ in the form of lenses and the low levels of power reflect the low probability of lensing of

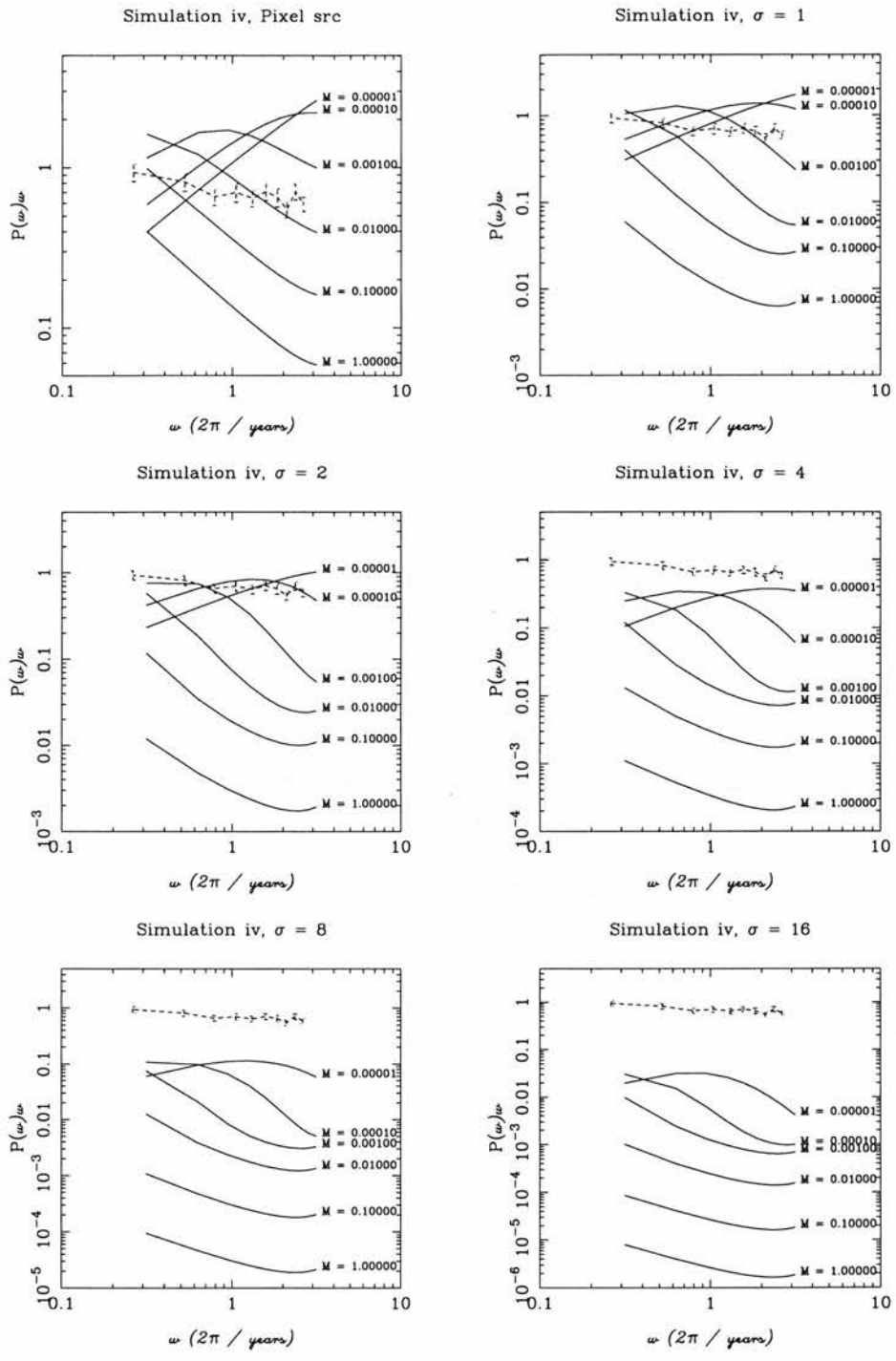

Figure 4.22: Same as Figure 4.20 for simulation *iv*.

individual quasars in such a model. The long term variation in the apparent luminosity of quasars is seen in the vast majority of quasars with a redshift of $z \gtrsim 0.3$. If this effect is due to microlensing, the low optical depth in simulation

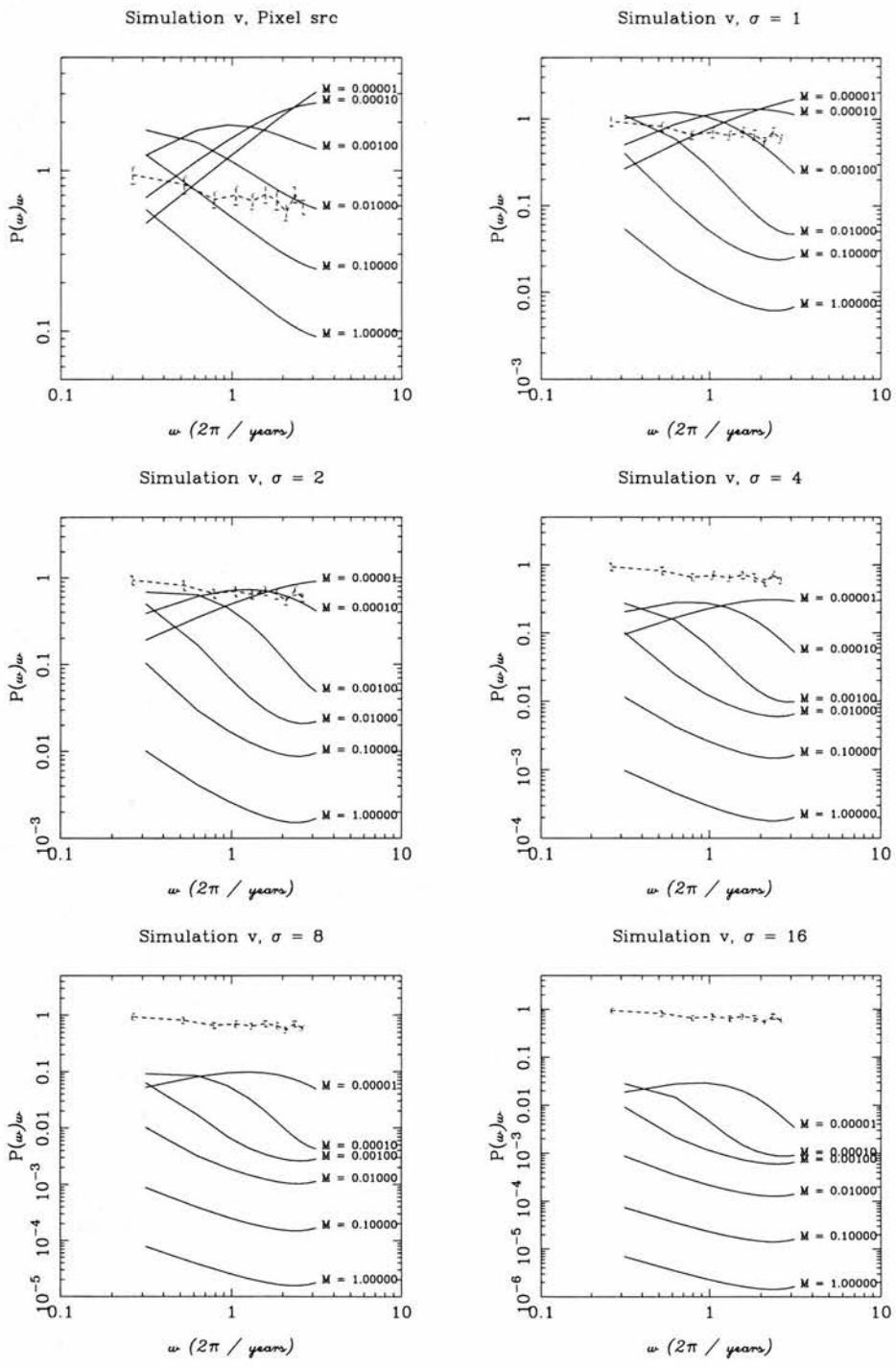

Figure 4.23: Same as Figure 4.20 for simulation v.

vi would not be able to account for such a widespread effect.

It is difficult to interpret the results further without considering the proper sizes of the sources. In order to investigate the relationship between the proper source

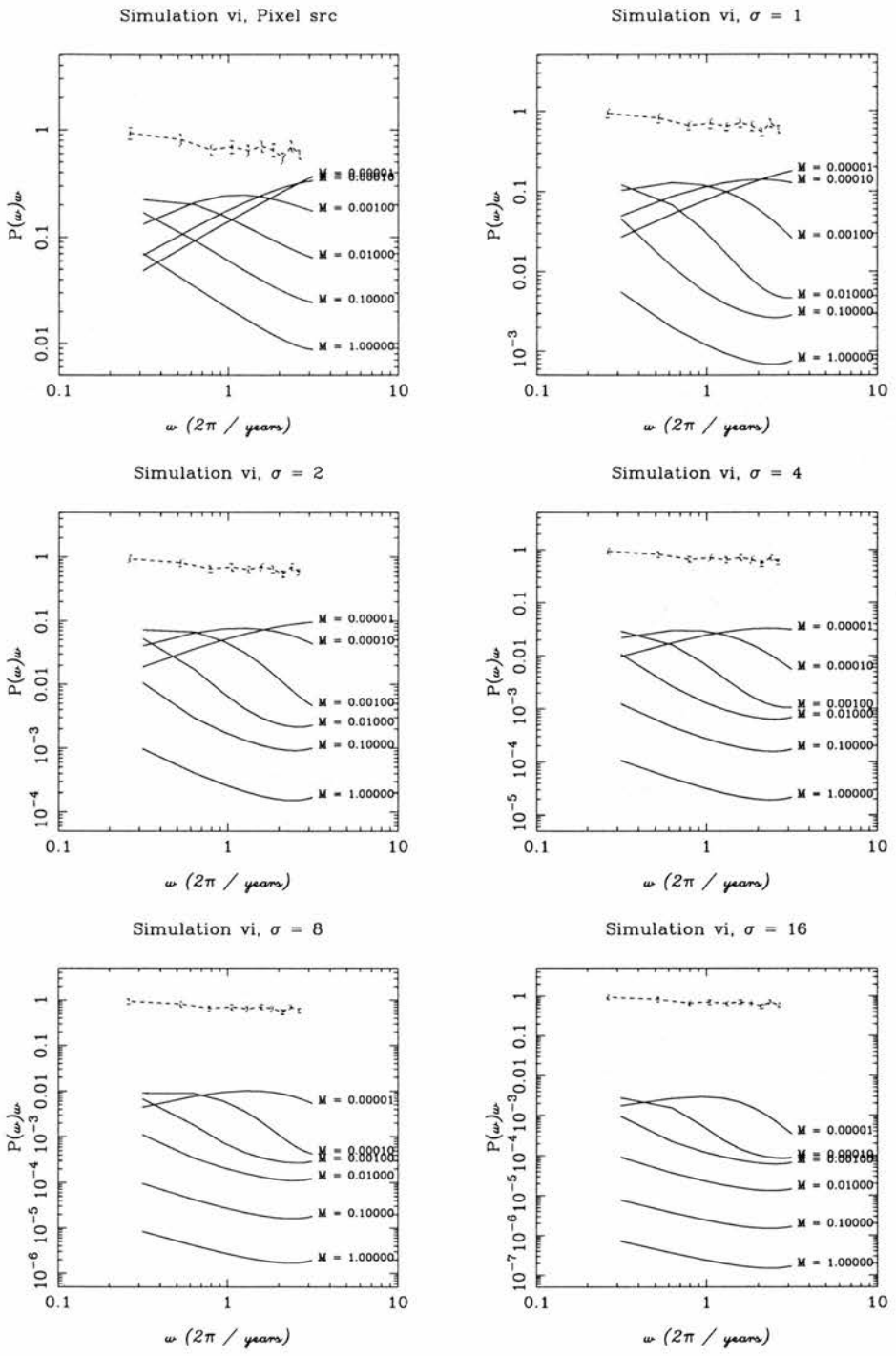

Figure 4.24: Same as Figure 4.20 for simulation *vi*.

sizes and the lens masses, a χ^2 fit was calculated between each of the convolved simulation power spectra and the four observational power spectra. The number of source sizes covered was increased by interpolating the power spectra shown

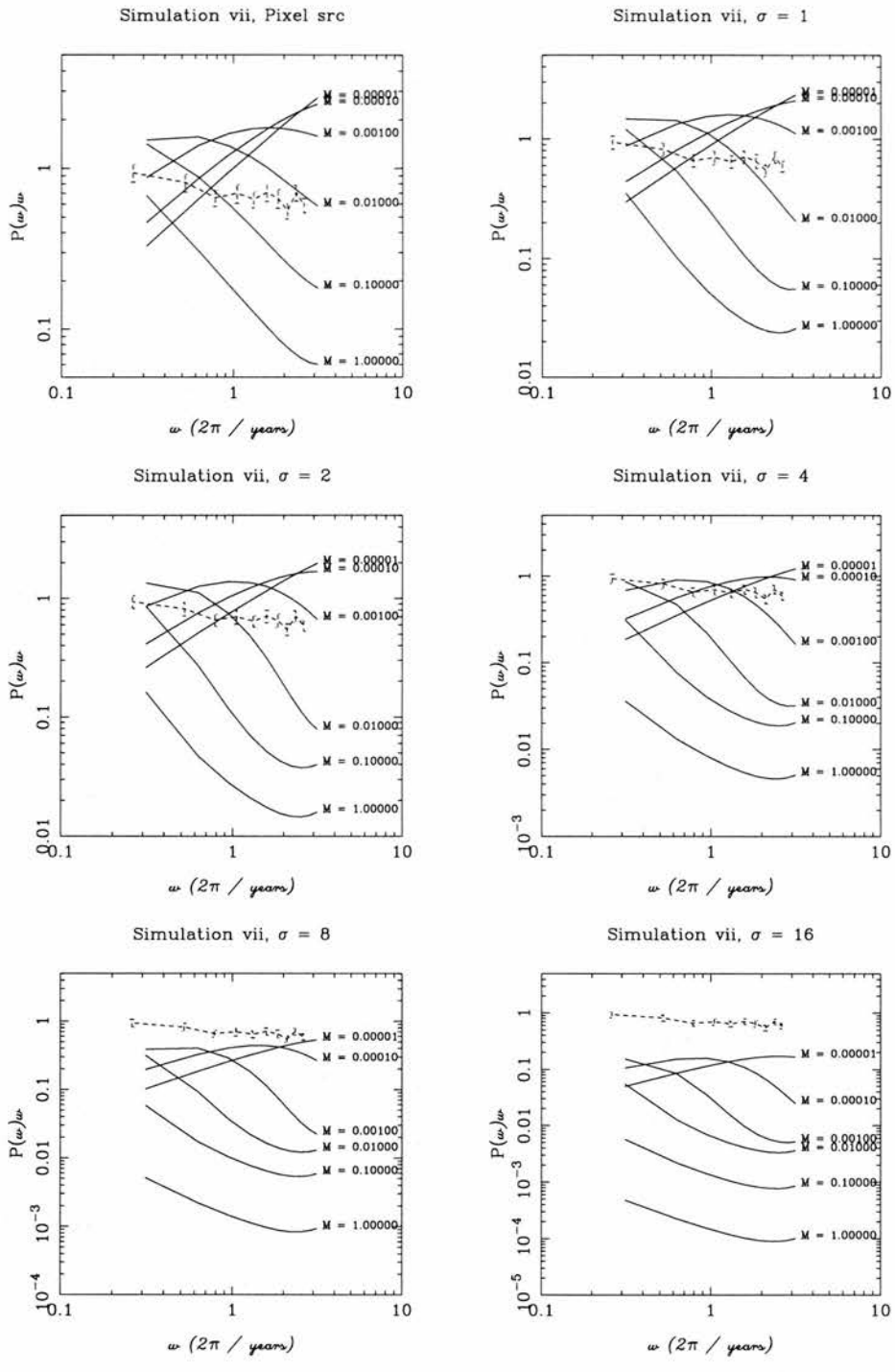

Figure 4.25: Same as Figure 4.20 for simulation *vii*.

in Figures 4.18 and 4.19 to fill in source sizes for which lightcurves were not calculated.

Figures 4.32 – 4.35 and and 4.36 – 4.39 show the results of this fit for the gaussian

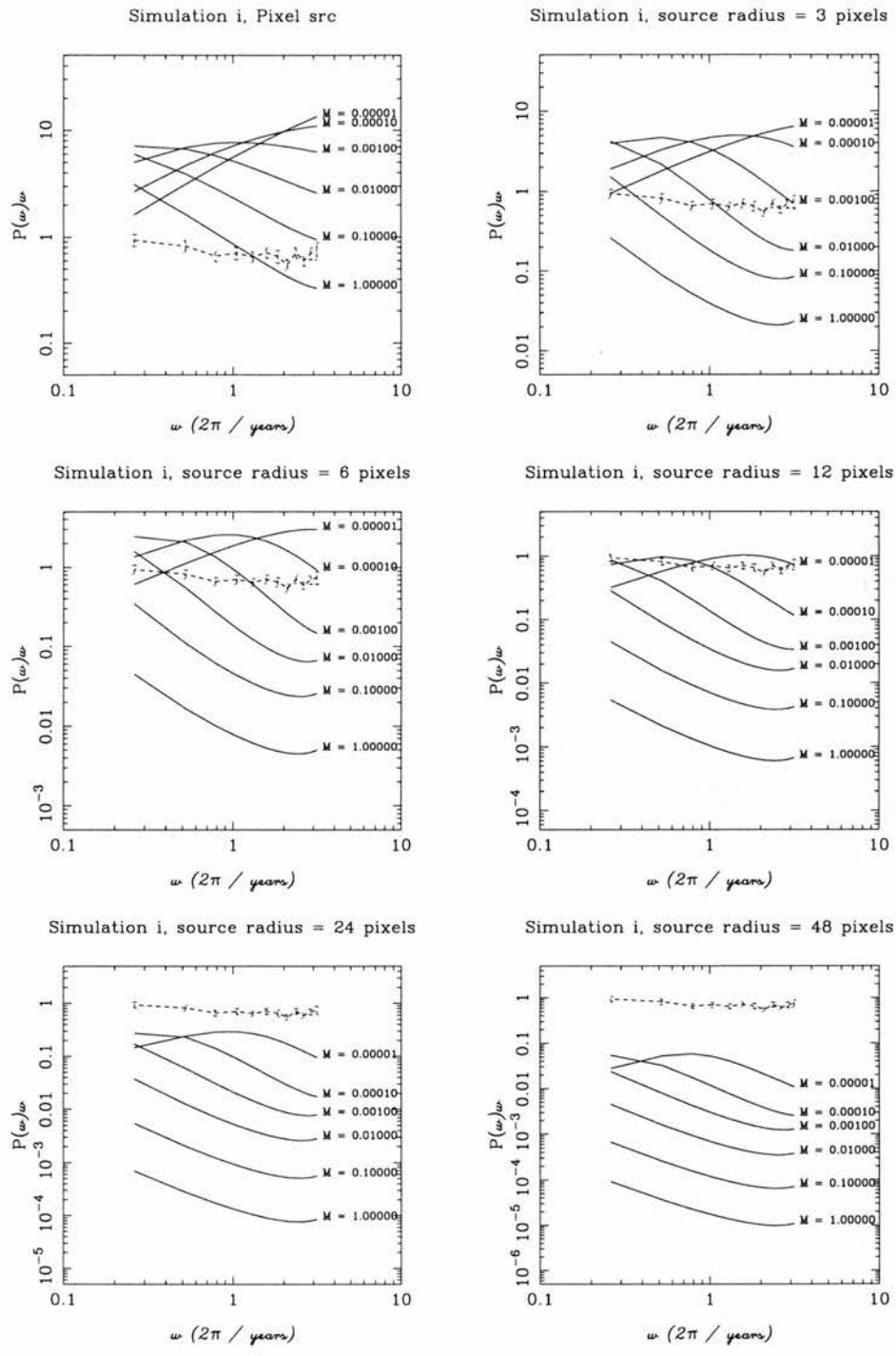

Figure 4.26: Simulation i: The solid lines show the power spectra of the pixel sized source and a range constant surface brightness profile sources convolved with the window function for different lens masses. The dashed line is the power spectra for the observational data sample with $1.5 < z < 2.5$ and $m_a < 20$.

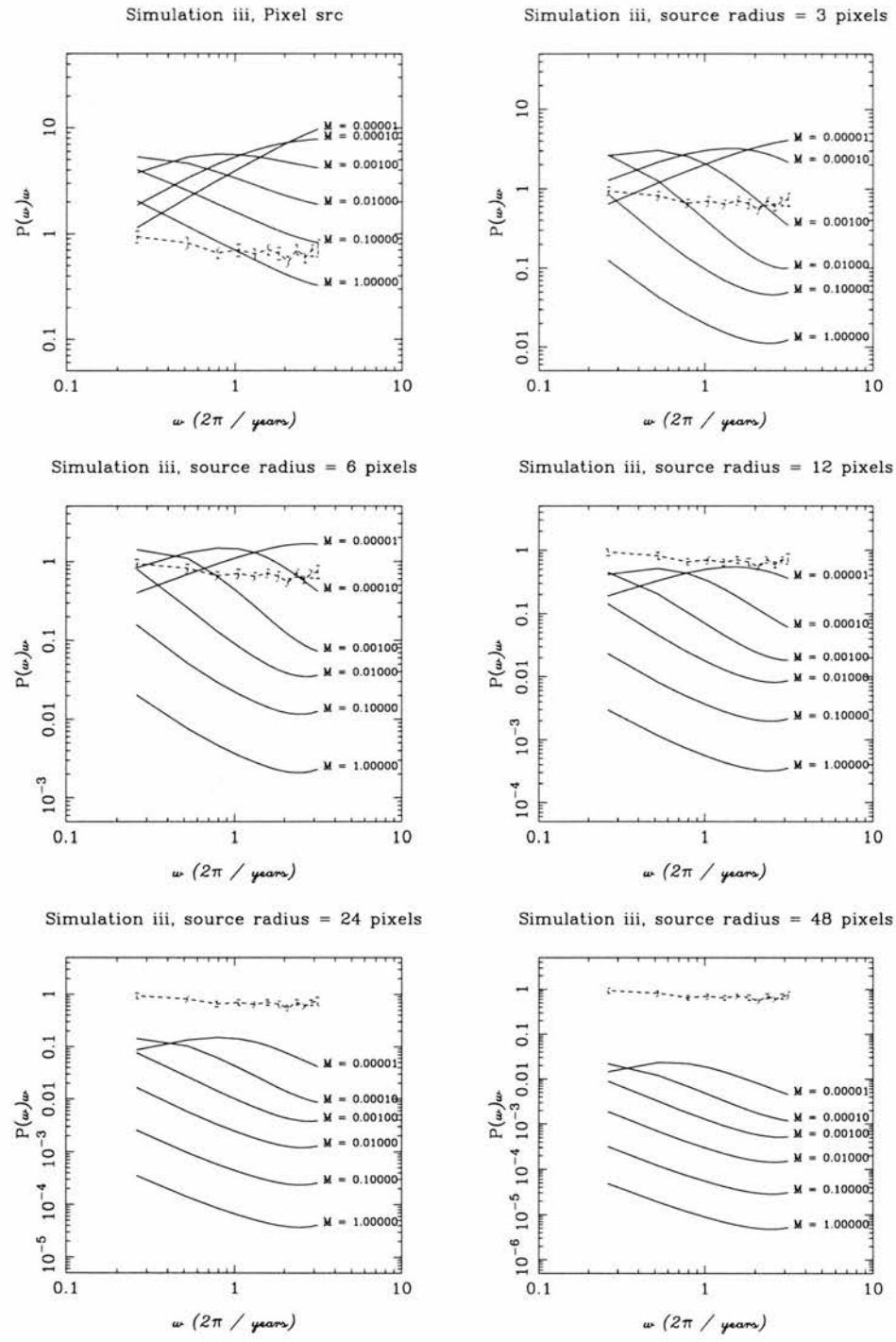

Figure 4.27: Same as Figure 4.26 for simulation *iii*.

and constant surface brightness profile sources to different subsets of the observational data. The x-axis of these graphs shows the proper size of the source (in metres) with each line representing a constant lens mass. The left most line is for

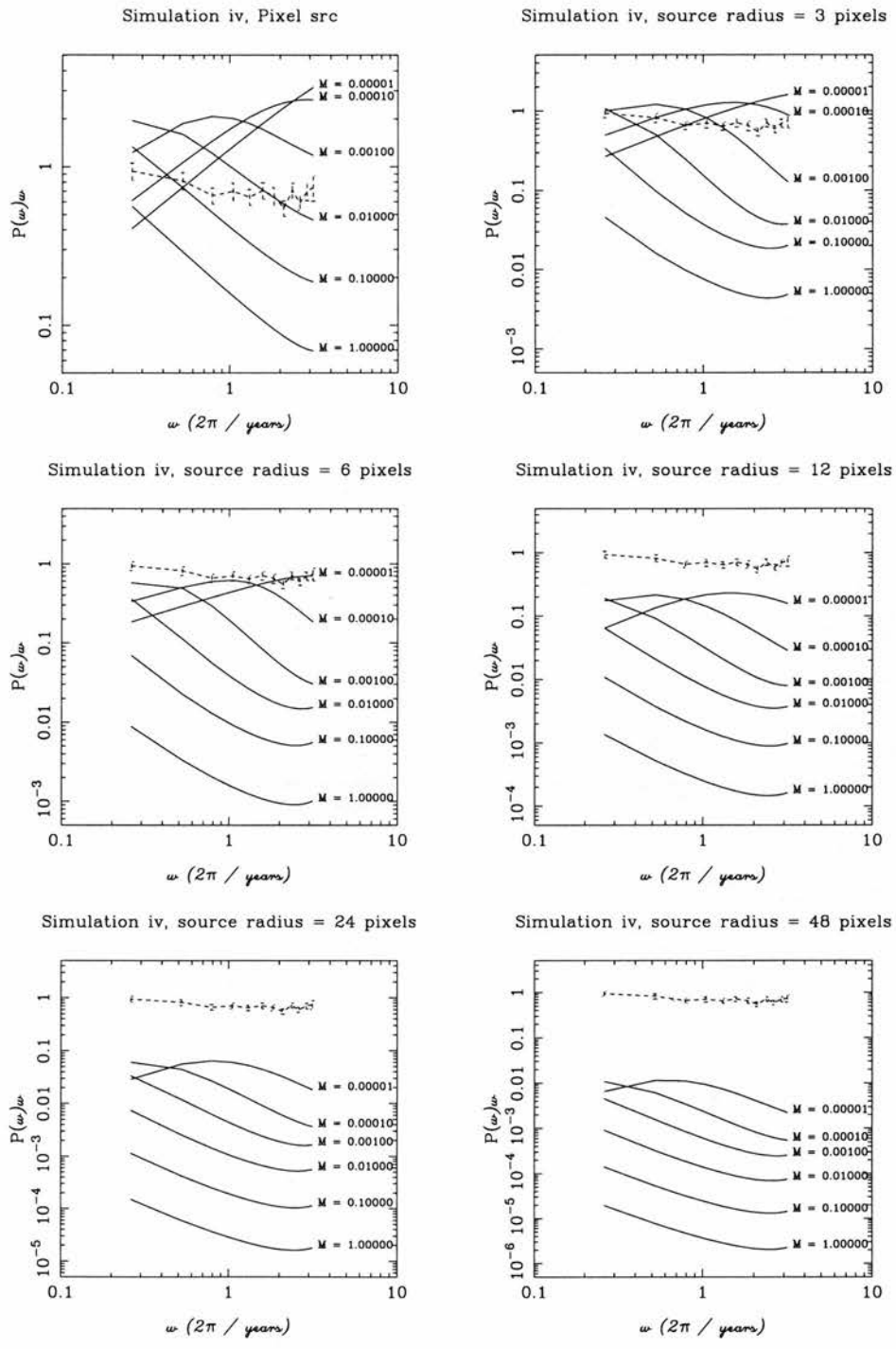

Figure 4.28: Same as Figure 4.26 for simulation *iv*.

the smallest $10^{-5}M_{\odot}$ lens with the mass increasing to $1M_{\odot}$ in the furthest right line. Tables of the best fit parameters for each of the cases considered are shown in Appendix D.

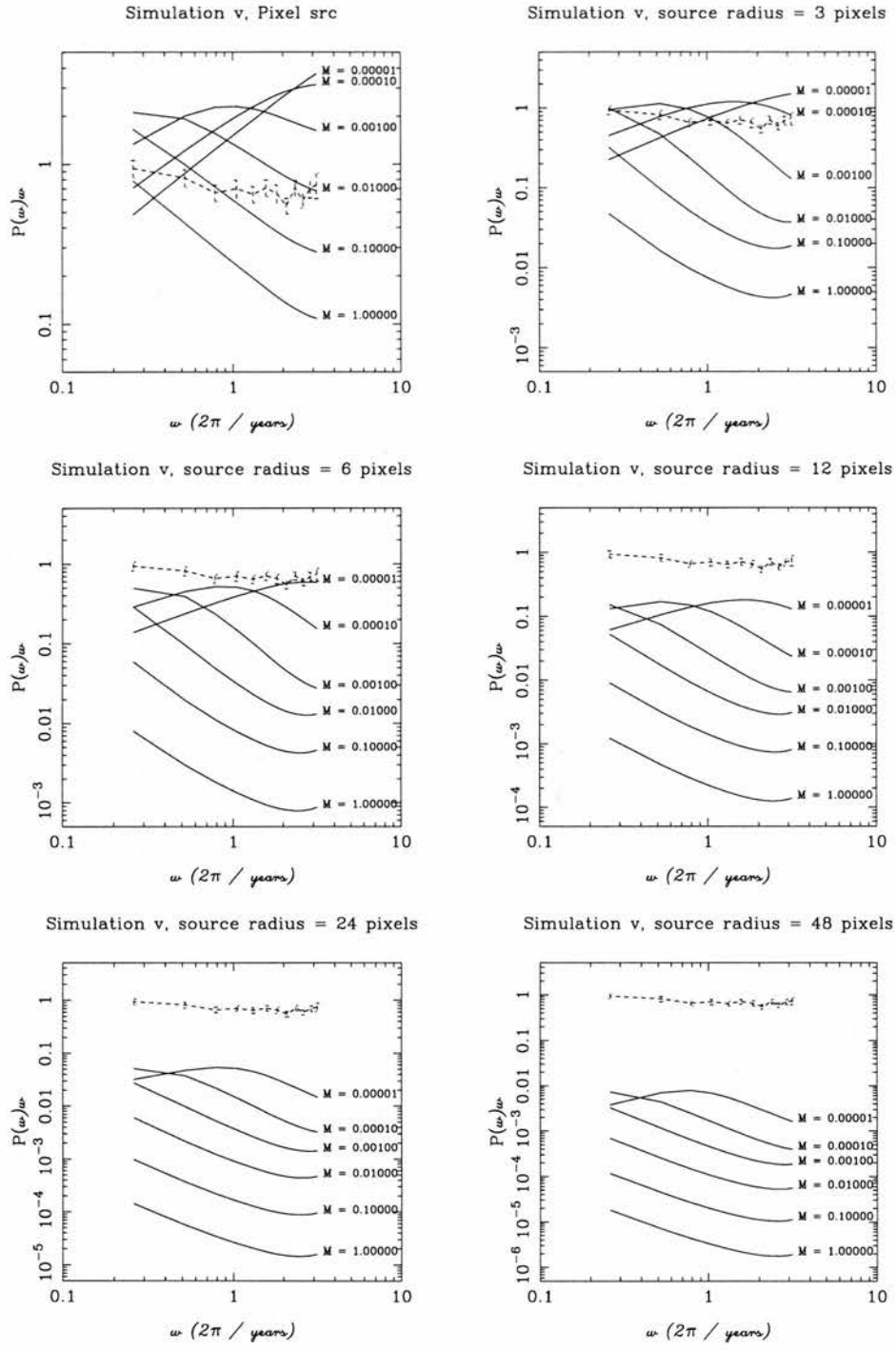

Figure 4.29: Same as Figure 4.26 for simulation v.

With the exception of simulation vi, all the models under consideration have a reasonably low reduced χ^2 value for some combination of source size and lens mass, although none of the best fit parameter values gives a formally acceptable

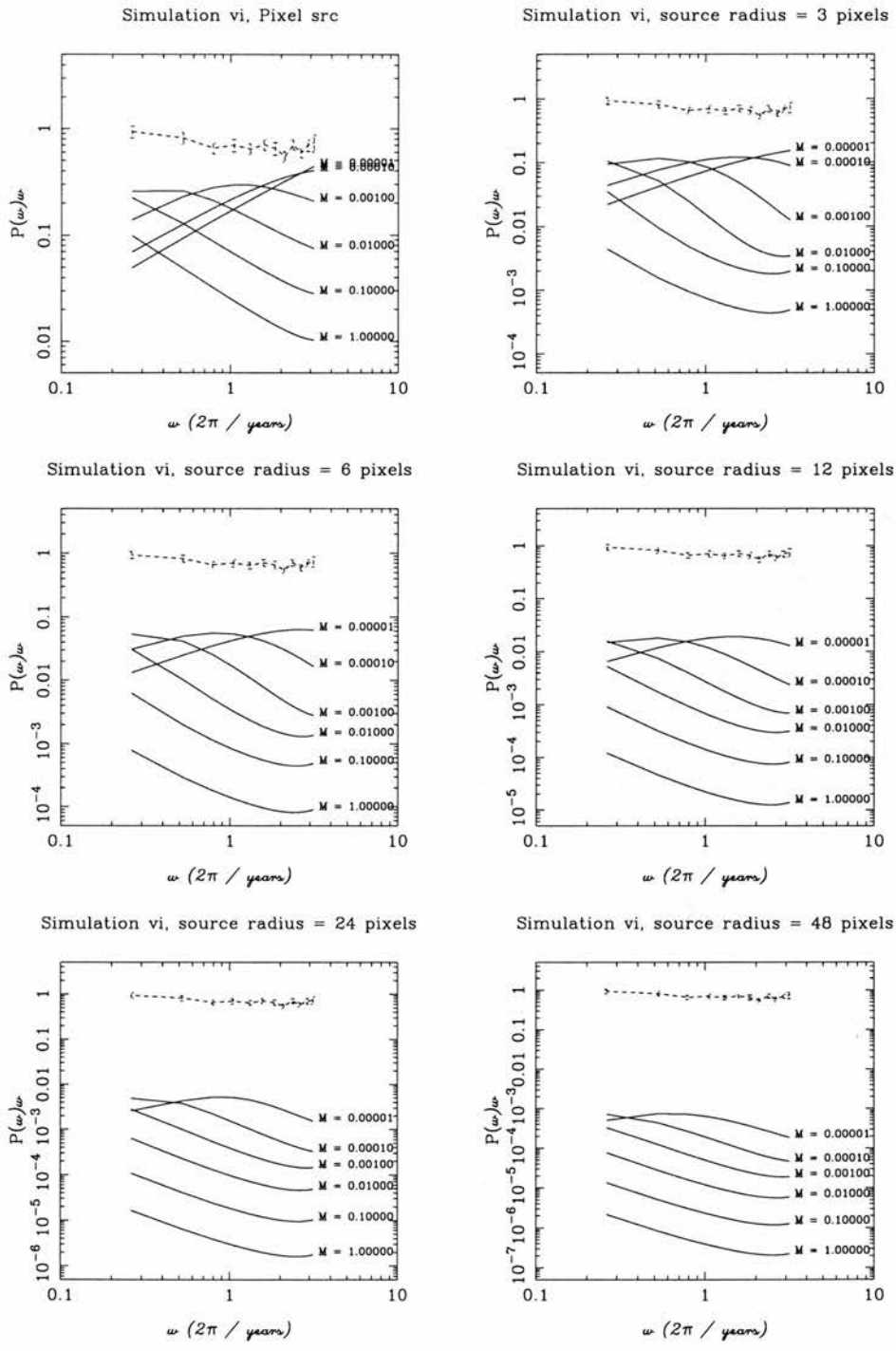

Figure 4.30: Same as Figure 4.26 for simulation *vi*.

fit. The lowest χ^2 values relate to the gaussian source brightness profile simulations and the sampled observational data with $0.5 \leq z < 1.5$ and $m_a \geq 20$ (see Table D.1). The χ^2 fits for simulation *vi* confirm that this model can be

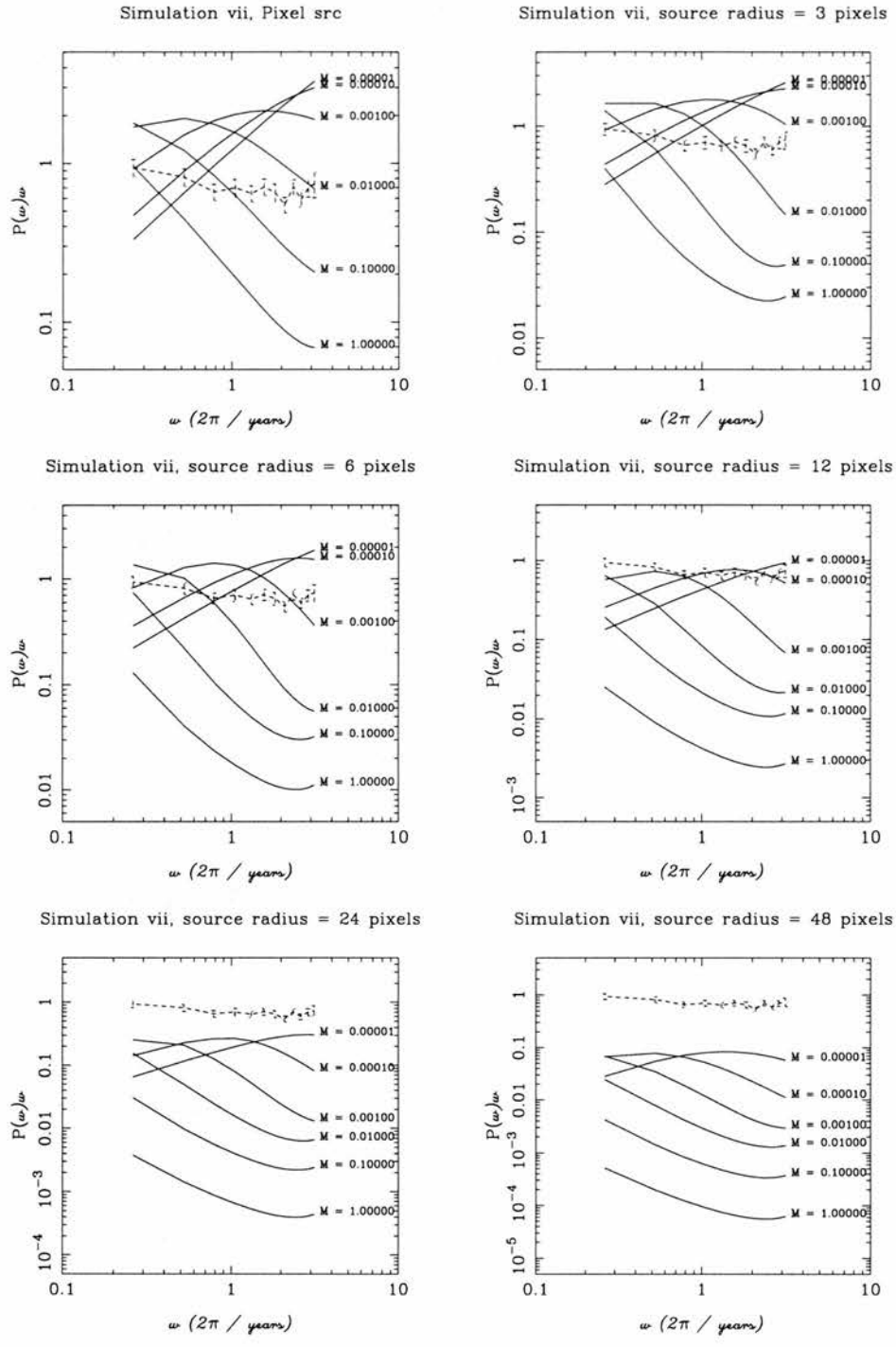

Figure 4.31: Same as Figure 4.26 for simulation *vii*.

excluded from consideration as its low proportion of lensing mass results in an optical depth which is too low to match observations.

The reduced χ^2 fits for the remaining 5 simulations all suggest a best fit for the

Simulation	Lens mass ($M_\odot$)	Pixel size (m)
i	1.0	2.1×10^{14}
	0.1	6.6×10^{13}
	0.01	2.1×10^{13}
	10^{-3}	6.6×10^{12}
	10^{-4}	2.1×10^{12}
	10^{-5}	6.6×10^{11}
iii, v, vi	1.0	3.0×10^{14}
	0.1	9.4×10^{13}
	0.01	3.0×10^{13}
	10^{-3}	9.4×10^{12}
	10^{-4}	3.0×10^{12}
	10^{-5}	9.4×10^{11}
iv	1.0	2.9×10^{14}
	0.1	9.0×10^{13}
	0.01	2.9×10^{13}
	10^{-3}	9.0×10^{12}
	10^{-4}	2.9×10^{12}
	10^{-5}	9.0×10^{11}
vii	1.0	7.9×10^{13}
	0.1	2.5×10^{13}
	0.01	7.9×10^{12}
	10^{-3}	2.5×10^{12}
	10^{-4}	7.9×10^{11}
	10^{-5}	2.5×10^{11}

Table 4.3: The proper size of a pixel in the source plane for each simulation.

lens mass of $10^{-5} \leq M_{lens} \leq 10^{-4}$ and for the source size of between roughly $1.0 - 3.6 \times 10^{13}\, m$ across the different observational data samples. The different source surface brightness profiles make little difference to the results. Sampling the observational data in redshift and luminosity bins makes little difference to the χ^2 values. This result is unsurprising as it is clear from Figure 4.3 that the underlying shape of the observational power spectra is reasonably constant between the different samples with the main difference between the observational data sets being the level of power. The small variations in the χ^2 values of each of the sampled observational datasets for the same simulations may well be due

to fitting the observational data to discrete rather than continuous values of lens mass and source size. Thus, the following discussion will focus on differences between the χ^2 results for the simulation data. Tables summarising the best fit parameters for the gaussian and constant source brightness profiles are shown in Table D.1 - D.4 and D.5 - D.8.

In both the Einstein-de Sitter model of simulation *i* and the $\Omega_M = 0.3$ and $\Omega_\Lambda = 0.7$ model of simulation *iii*, the best fits are provided by lenses with a mass of $10^{-5} M_\odot$. The lower limit on the lens mass considered is set by the lower frequency end of the simulation. Extending the power spectra beyond this point would require extrapolating the fit significantly beyond the end of the data. While there is no sign in any of the power spectra of a break at the low frequency end, it was decided not to do this. Thus it is not possible to test whether lenses with masses $< 10^{-5}$ would provide a better fit to the observational data for simulations *i* and *iii*.

For a fixed cosmology of $\Omega_M = 0.3$ and $\Omega_\Lambda = 0.7$, a drop in the proportion of mass in the form of lenses appears to have the same effect on the two source brightness profiles. In both cases, a higher mass lens of $10^{-4} M_\odot$ is favoured by simulation *v*. The effect of reducing the lens mass is to move the power spectra shown in Figures 4.18 and 4.19 to the right. Thus different lens masses sample different sections of the power spectra's curve. It seems likely that the best fit for both the gaussian and constant sources for simulation *v* occurs for a power level at which the lens masses between $10^{-5} M_\odot$ and $10^{-4} M_\odot$.

For this same cosmology, the lower redshift sources of simulation *iv* also favours lenses with a slightly higher mass of $10^{-4} M_\odot$. The exception is for observational data in the $1.5 \leq z < 2.5$ and $m_a < 20$ range where the 10^{-5} lens mass provides a slightly better fit. However, for each of the observational power spectra, the difference in χ^2 values between 10^{-5} and $10^{-4} M_\odot$ lenses is small and, again, it seems likely that the best fitting mass lies between these two values.

For models with the same cosmology and the same proportion of Ω_M in lenses, the χ^2 fits are either better for simulation *vii* than simulation *v*, or about the same. Lens masses of $10^{-4} M_\odot$ give a better fit than $10^{-5} M_\odot$. However, as the mass quoted for simulation *vii* is the upper end of the mass range used in the simulation, the low χ^2 values for 10^{-5} and $10^{-3} M_\odot$ lenses may indicate that a wider range of lens masses should also be considered. However this would significantly increase

the computational time required for the microlensing simulations.

The main conclusion of this chapter is that microlensing may account for the long term variability of quasars. The sole case where the simulation power spectra cannot be fitted to the observational data to some degree is a very low mass $\Omega_M = 0.3$ and $\Omega_\Lambda = 0.7$ model with only $0.01\Omega_M$ in the form of lenses. The remaining models all produce broad fits to the different ranges of observational data.

In general, there is a remarkable degree of agreement between the different cosmologies, source profiles and observational data samples. From the results presented in this chapter it is possible to conclude that although we have been unable to find a model which fits the complete observational sample adequately, if microlensing is the cause of the long term variation in the apparent brightness of quasars, the lens mass is in the range 10^{-5} - $10^{-4} M_\odot$ and the source size in the range 1.0×10^{13} - 3.6×10^{13} metres.

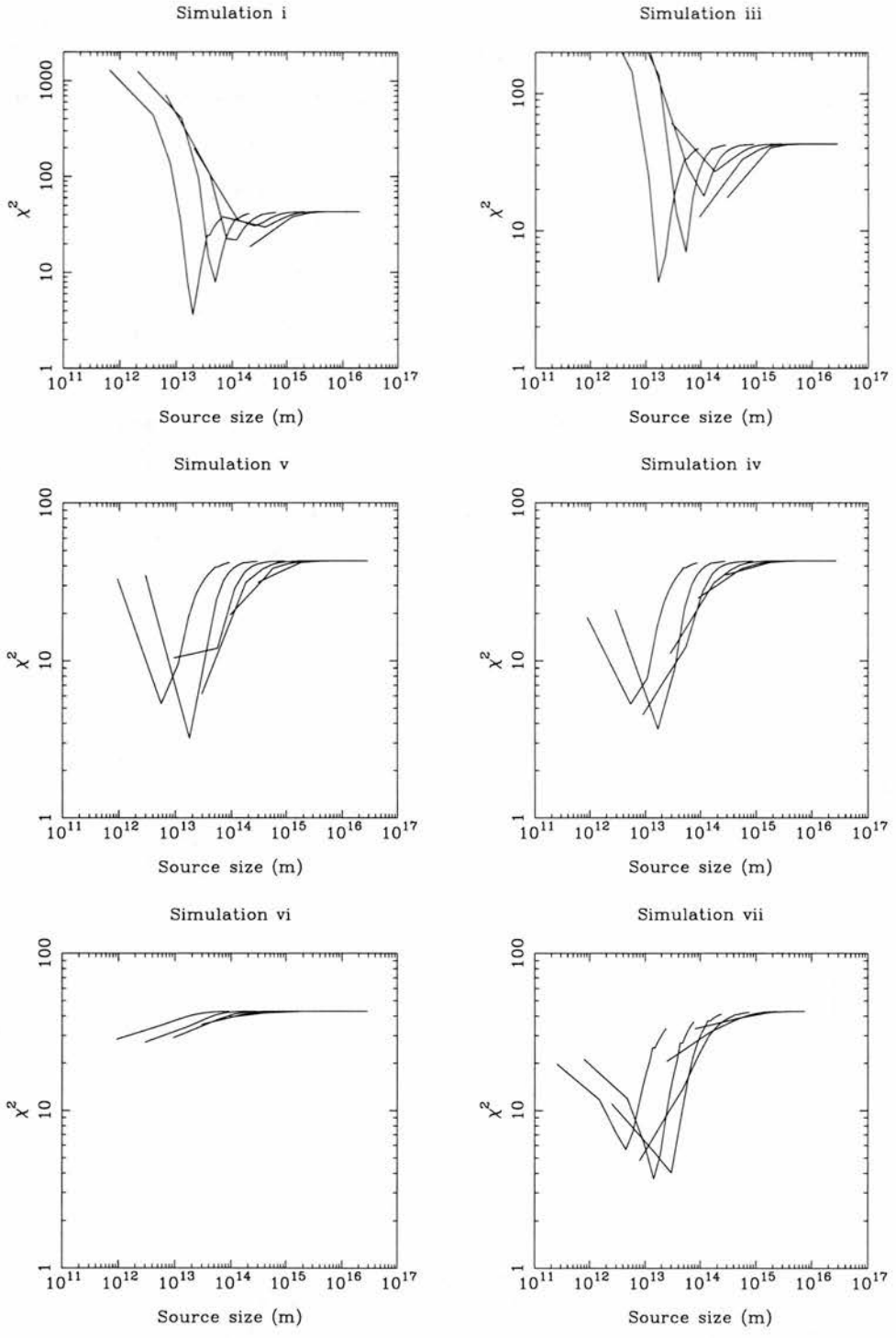

Figure 4.32: Reduced χ^2 fits of the gaussian surface brightness profile sources to observational data in the range $0.5 \leq z < 1.5$ and $m_a \geq 20$. Each line shows the fit for a constant lens mass. The left hand line represents lenses with masses of $10^{-5} M_\odot$ with the mass increasing by an order of magnitude with each line to the right up to $1 M_\odot$.

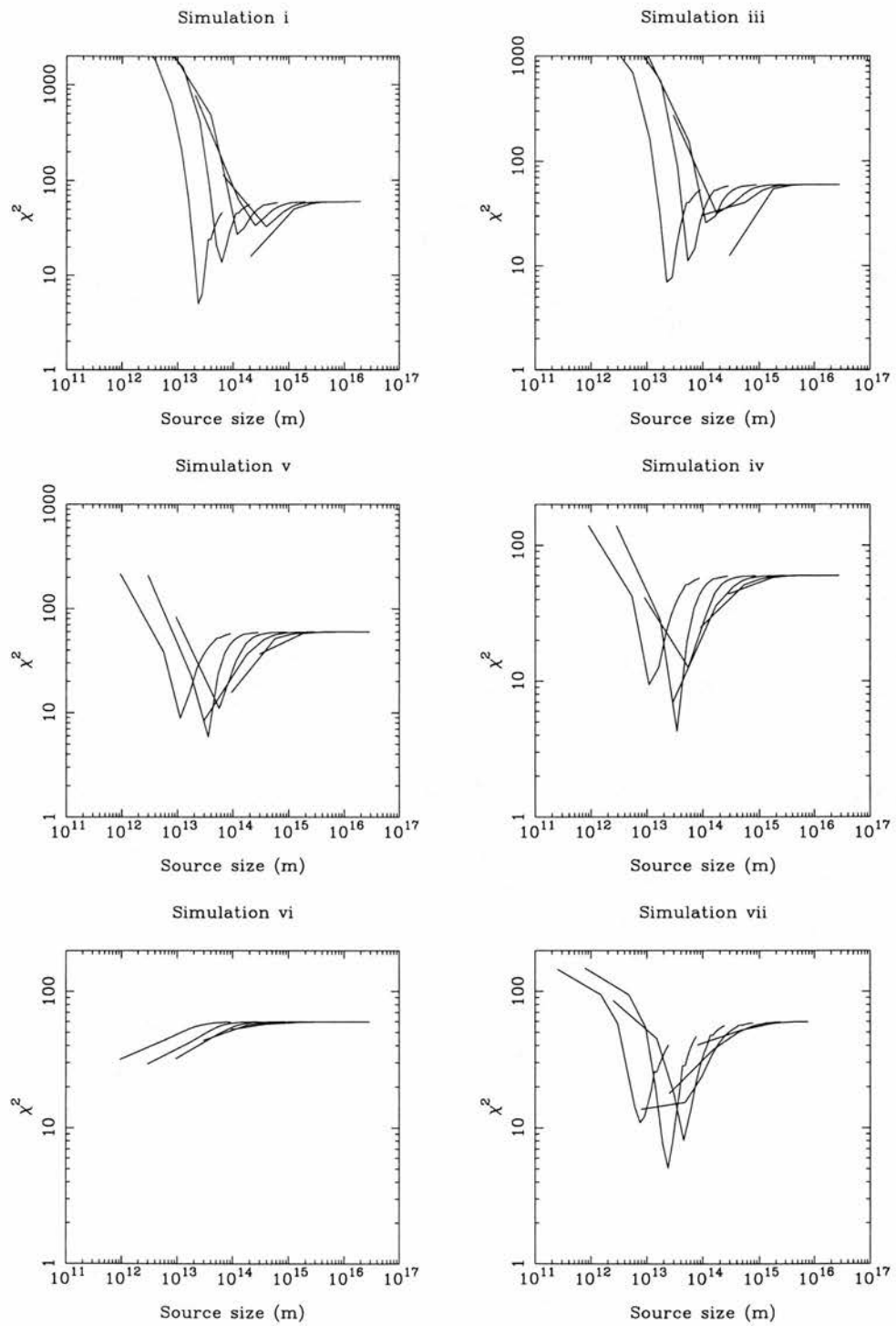

Figure 4.33: Same as Figure 4.32 for observational data in the range $0.5 \leq z < 1.5$ and $m_a < 20$.

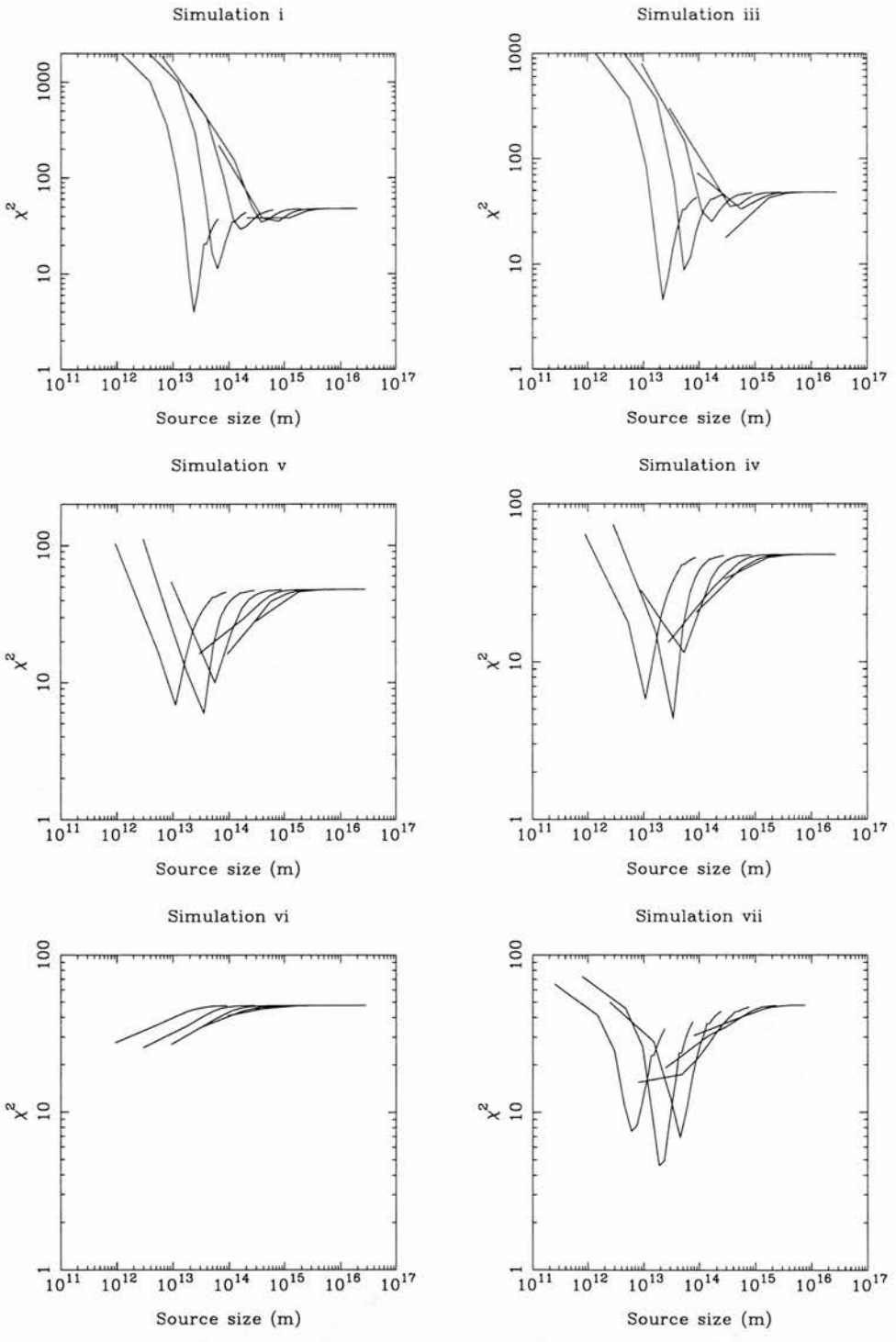

Figure 4.34: Same as Figure 4.32 for observational data in the range $1.5 \leq z < 2.5$ and $m_a \geq 20$.

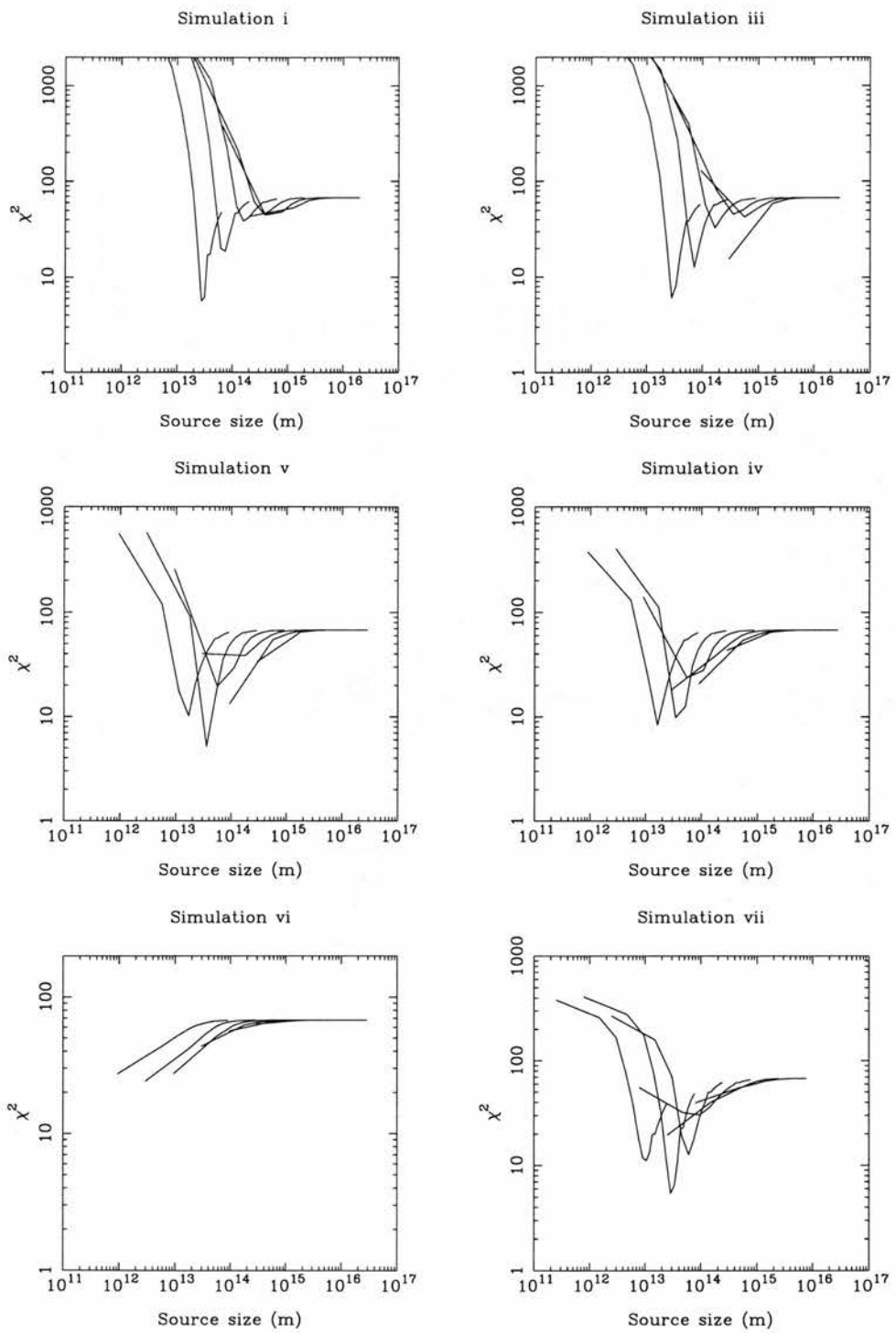

Figure 4.35: Same as Figure 4.32 for observational data in the range $1.5 \leq z < 2.5$ and $m_a < 20$.

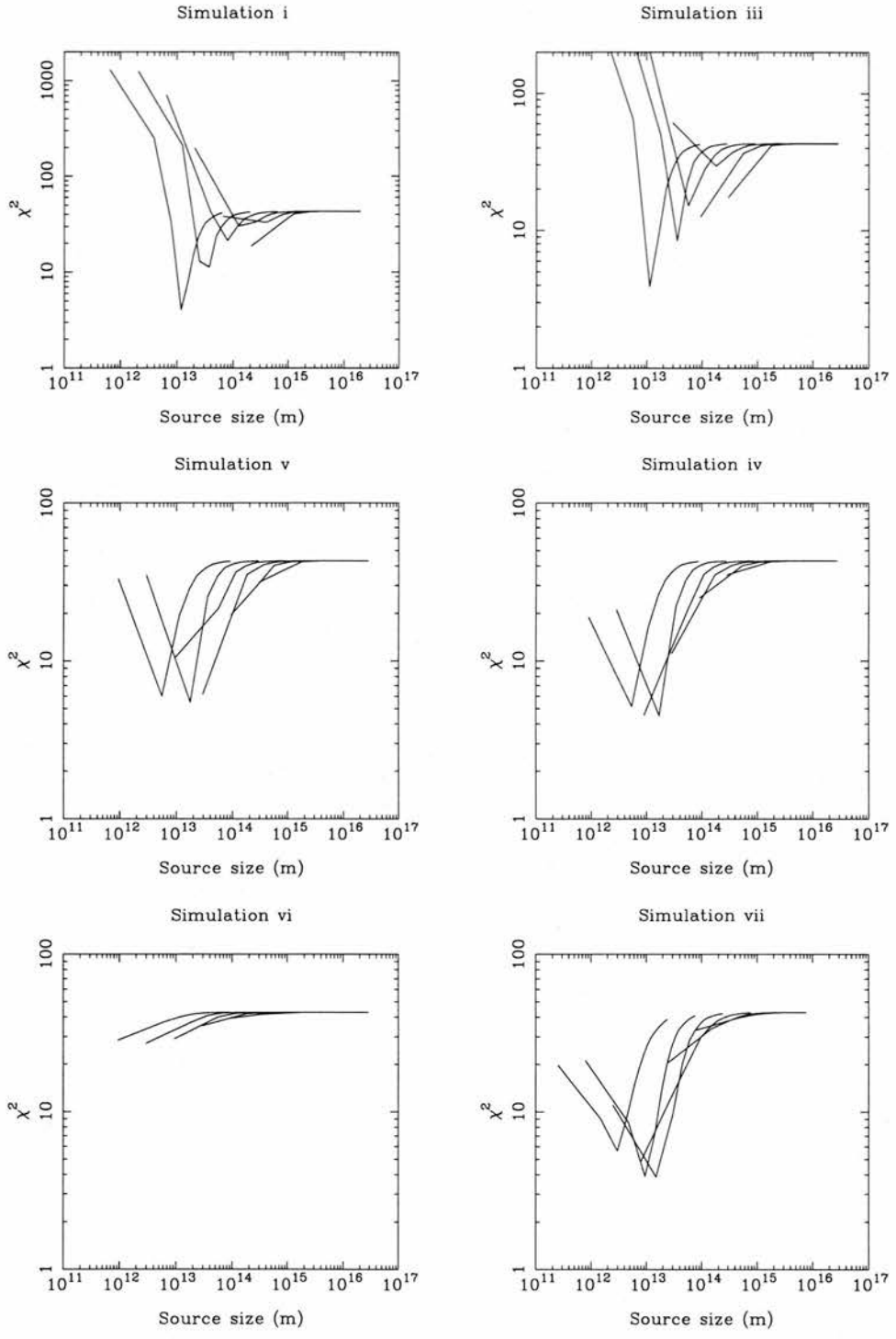

Figure 4.36: Reduced χ^2 fits of the constant surface brightness profile sources to the observational data in the range $0.5 \leq z < 1.5$ and $m_a \geq 20$. Each line shows the fit for a constant lens mass. The left hand line represents lenses with masses of $10^{-5} M_\odot$ with the mass increasing by an order of magnitude with each line to the right up to $1 M_\odot$.

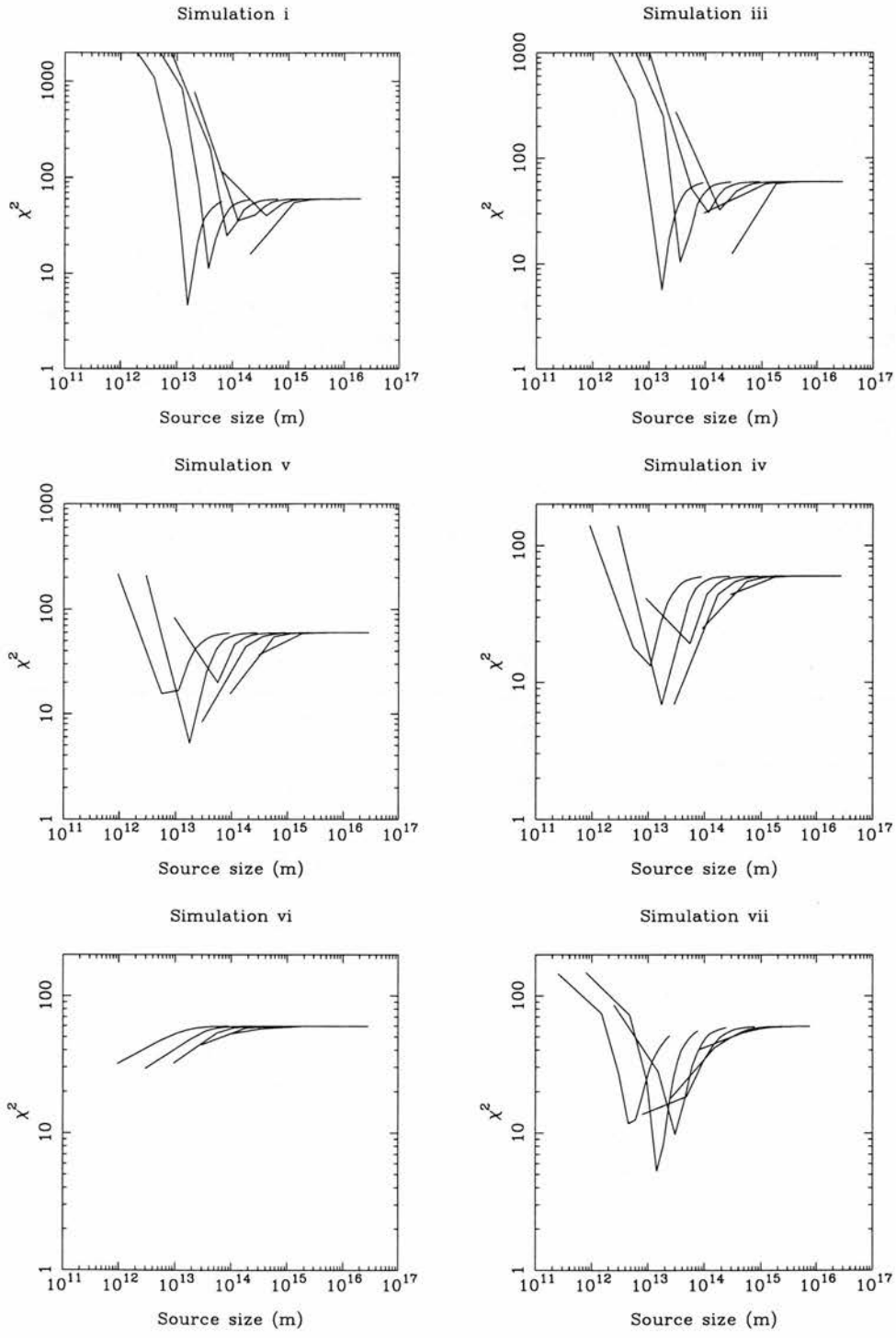

Figure 4.37: Same as Figure 4.36 for observational data in the range $0.5 \leq z < 1.5$ and $m_a < 20$.

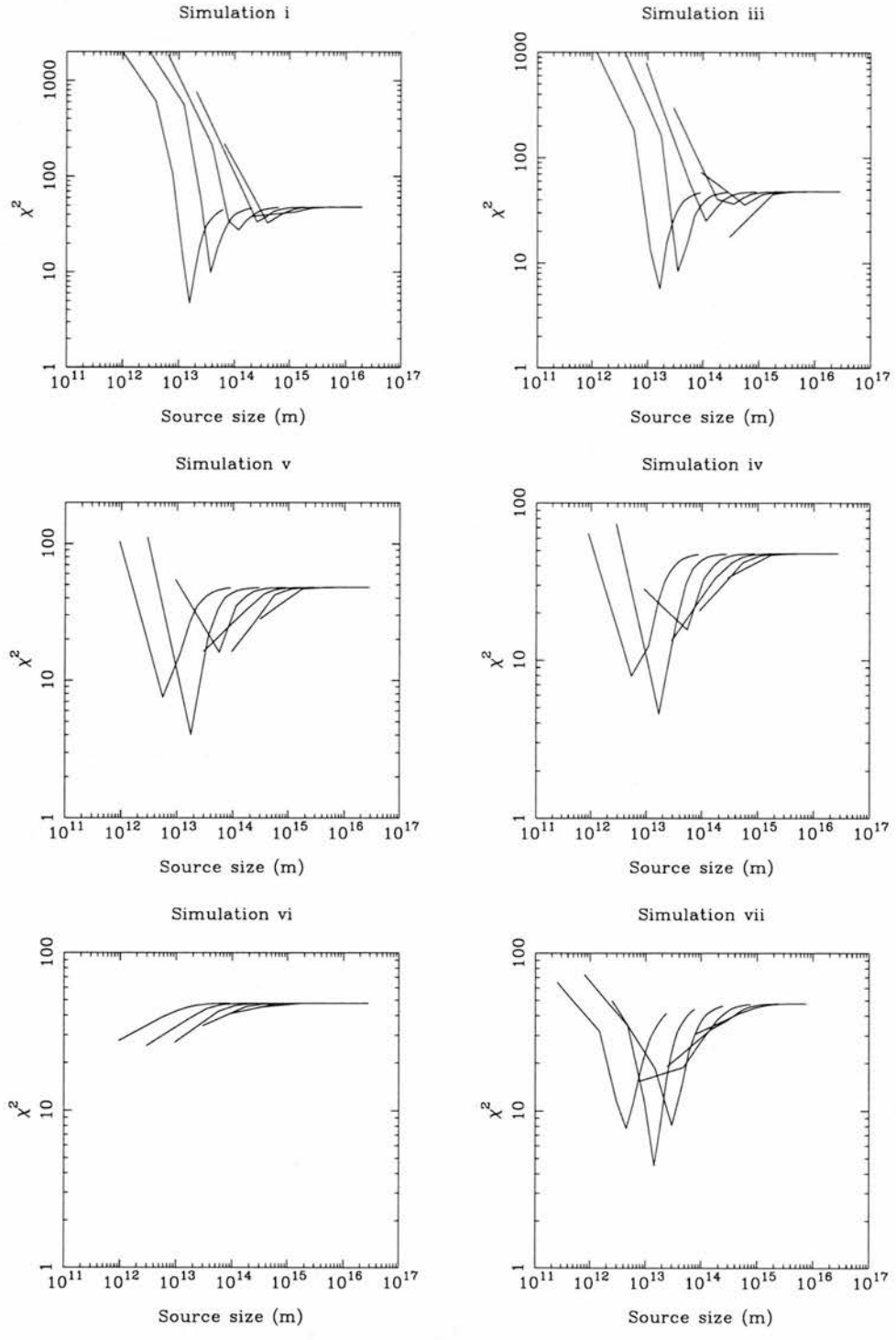

Figure 4.38: Same as Figure 4.36 for observational data in the range $1.5 \leq z < 2.5$ and $m_a \geq 20$.

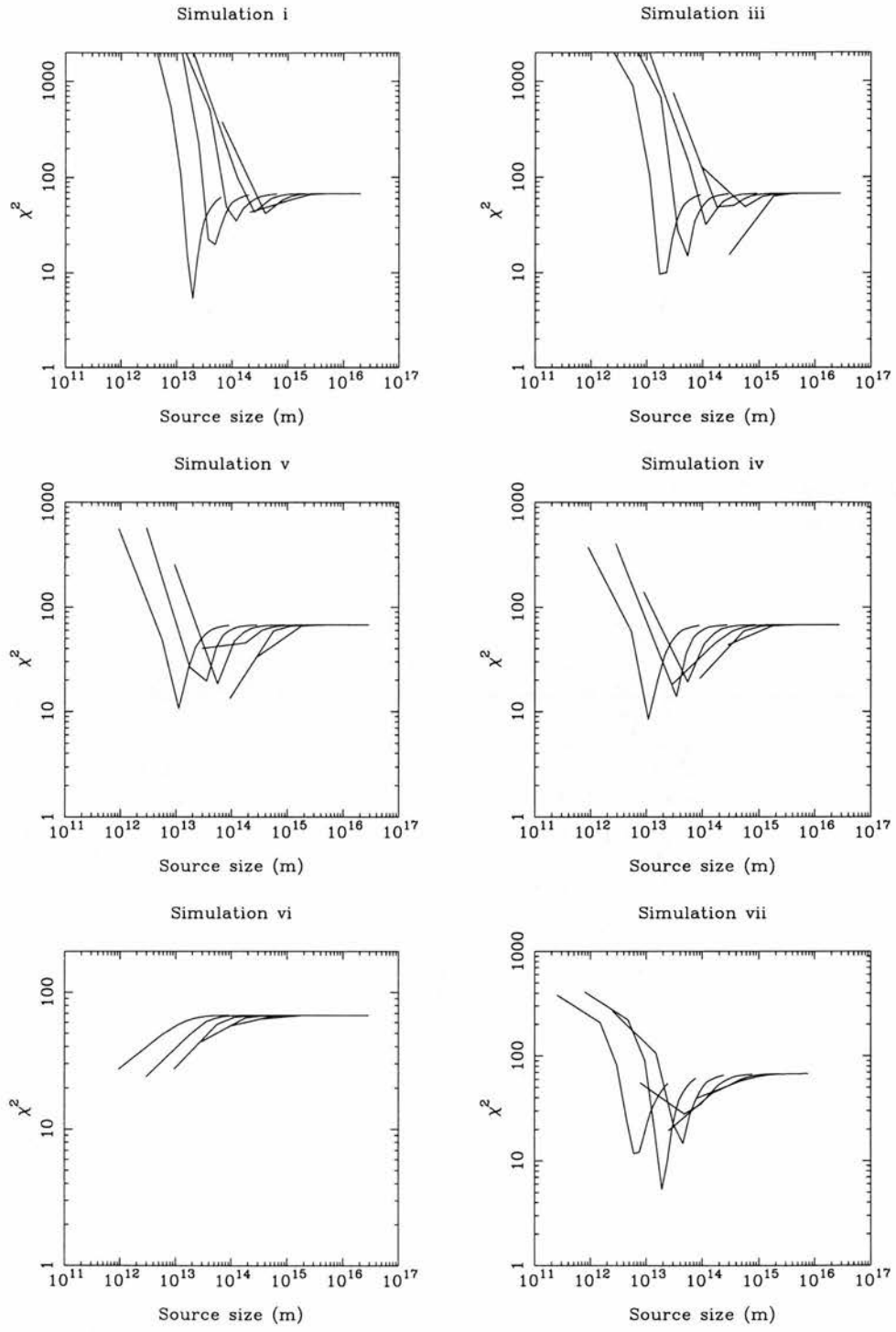

Figure 4.39: Same as Figure 4.36 for observational data in the range $1.5 \leq z < 2.5$ and $m_a < 20$.

Chapter 5

Testing Dark Matter with High-redshift Supernovae

One of the classic tests of the geometry of the Universe involves the construction of a flux-redshift diagram, known as a Hubble diagram. At high redshifts the model lines for different values of Ω_M and Ω_Λ begin to diverge and, in theory, it becomes possible to use observations of high redshift objects to constrain the geometry of the universe. However, until recently it has proved difficult, in practice, to obtain reliable independent distance measurements at a sufficiently high redshift to distinguish between cosmological models. But, in recent years there has been a resurgence of interest in this method of measuring the geometry of the Universe. This is due to success of the high redshift Type *Ia* supernovae searches.

As discussed in §1.1.2, Type *Ia* supernovae are thought to act as standard candles and therefore their Hubble diagram may be used to constrain cosmological models. Dedicated discovery and follow-up programmes (Perlmutter *et al.* (1997), Perlmutter *et al.* (1999), Schmidt *et al.* (1998)) have established their Hubble diagram to $z \simeq 1$, leading to the constraints on H_0, Ω_M and Ω_L discussed in §1.1.2. Most notable of their findings is the requirement for a positive cosmological constant (Riess *et al.*, 1998). However, it was soon realised that the Hubble diagram for the supernovae would be affected by gravitational lensing if significant quantities of dark matter existed in the form of a cosmological distribution of compact objects such as PBHs (Holz & Wald (1998), Metcalf & Silk (1999), Weller & Albrecht (2000), Huterer & Turner (2000)). Such a population had already been proposed to account for the long-term variability of quasars (Hawkins, 1993). Measurements of supernova lightcurves have also been proposed as a means of

searching for microlensing events within the Large Magellanic Cloud (Graff & Kim, 2001).

These studies have shown that lensing can have a significant effect on estimates of cosmological parameters. In addition, the authors have also suggested that the distribution of supernova fluxes could be used to determine the amount of dark matter which exists in the form of compact objects. Metcalf & Silk (1999) showed that, provided the cosmology was known, microscopic dark matter, such as weakly interacting particles, could be distinguished from macroscopic dark matter, such as PBHs, with relatively small numbers of supernovae. The reason for this sensitivity is that, in a universe of reasonable density dominated by such macroscopic dark matter, most bunches of light rays do not undergo large magnifications and the most probable flux received is close to that expected in empty-beam models (Dyer & Roeder, 1974). This shifts the most probable Hubble diagram systematically, changing the estimates of the cosmological parameters (Holz & Wald, 1998). Thus both the underlying cosmology and the amount of the matter density in the form of lenses effect the Hubble diagram and both quantities need to be taken into account when fitting observational data. While this is ambitious, it seems likely to be attempted once larger supernova searches such as those proposed by SNAP[1] and VISTA[2] are underway.

In this chapter, the study is more limited and focuses on how extra scatter due to lensing in supernova fluxes can be used to constrain the quantity of dark matter in the form of compact objects. The variance in the supernovae measurements will have contributions from intrinsic variations in the supernova properties, instrumental error, and lensing by a cosmological population of compact objects. The first two of these should be virtually independent of the cosmological model, so we are directly testing the contribution from macroscopic compact objects by including the lensing effect.

The level at which this test can detect dark matter candidates depends on the accuracy with which the variance can be estimated from sets of supernovae data. For gaussian distributions, this is straightforward. However, although it may be a reasonable approximation to model the intrinsic and instrumental effects as gaussian, the lensing effect is highly skewed towards rare high-magnification events. Thus a gaussian distribution would not provide an accurate measure of

[1] `http://snap.lnl.gov`
[2] `http://www.vista.ac.uk`

the variance due to lensing. The numerical ray-tracing simulations outlined in Chapter 3 were used to model the effects of lensing and the results were analysed using a Bayesian method (§5.1.1).

Lensing induces an extra scatter which rises with redshift, contributing as much as 0.5 magnitudes at a redshift $z = 1.5$ for an Einstein-de Sitter model with all the matter in the form of compact objects. Thus it should be possible to distinguish this from a no-lensing model, provided data is available for sufficient supernovae. This study shows, in general, that with ~ 2600 supernovae uniformly selected from $0.1 \lesssim z \lesssim 1.7$, as proposed by SNAP, the scatter alone can select between several cosmological models at 99.9% confidence level. This method of distinguishing between different models has the advantage that it is insensitive to any evolution in the mean luminosity of supernovaa. However it would be dependent on any evolution in the scatter of intrinsic properties.

5.1 Method

As discussed in Chapter 4, the effects of microlensing on sources at high redshifts result on average from a non-linear combination of a number of individual lensing events. Thus the microlensing effect on the brightness of a supernova at a redshift of $z \sim 1$ is not necessarily accurately modelled by a single-scattering event. Therefore, the computer simulation outlined in Chapter 3 is used to model the lensing of distant supernova. For this simulation the model uses high accuracy model parameters set out in Table 3.1 for single timestep simulations. This ensures that the sampling of the magnification pattern is sufficiently accurate to detect high amplification events and that small changes in the deflection angle due to lenses with a large impact parameter are included. While such details have little effect on the power spectra outlined in Chapter 4, they are necessary for these simulation in order to obtain an accurate probability of distinguishing between different cosmologies and lens populations.

As in Chapter 4, the Universe is assumed to be populated with compact dark matter candidates of a single mass randomly distributed over a series of planes. The results of the simulations are independent of the lens mass provided the source is small compared to the Einstein radius.

Four separate models are considered, one with no lensing, one an Einstein-de

Model	Matter density Ω_M	Cosmological constant Ω_Λ	Density in lenses Ω_{Lens}
1			0
2	0.3	0.7	0.1
3	0.3	0.7	0.3
4	1.0	0.0	1.0

Table 5.1: Models considered. Model 1 includes scatter only from measurement error and intrinsic variations.

Sitter model with all matter in lenses, and two flat models with $\Omega_M = 0.3$ and cosmological constant $\Omega_\Lambda = 0.7$. These last two models differ in the proportion of the matter in lenses. The models are detailed in Table 5.1 and are listed in order of increasing Ω_{Lens}. While this is a small number of models, it covers the cases of most current interest and should provide a useful indication of the ability of searches like SNAP to distinguish different models.

Two analyses are performed – a preliminary study of the 42 high-redshift supernovae in the Supernova Cosmology Project and a second study investigating whether SNAP should be capable of distinguishing between the different models. In the former case, the errors are taken from the observational data given in Perlmutter *et al.* (1999). For the SNAP study, it is assumed that there is an intrinsic variation in supernovae properties of 0.157 mag (Perlmutter *et al.*, 1999), and a measurement error of 0.08 mag (Metcalf & Silk, 1999). These errors (measured in magnitudes) are assumed to be gaussian, and independent of redshift and cosmology, although these assumptions could be relaxed if desired. Model 1 contains only these components of variance.

Figure 5.1 shows the scatter in the magnitudes induced by lensing for models 2–4, as a function of redshift. The r.m.s deviation has been shown as symmetric around the mean. In practice the distribution is highly skewed towards high amplifications. Given that the intrinsic plus instrumental scatter is ~ 0.2 mag, it can be seen that the additional variance from lensing becomes very significant at redshifts $\gtrsim 1$.

5.1.1 Statistics

It is anticipated that SNAP will result in data for $N \sim 170$ supernovae per redshift interval of $\Delta z = 0.1$. The statistical analysis uses the r.m.s. of the

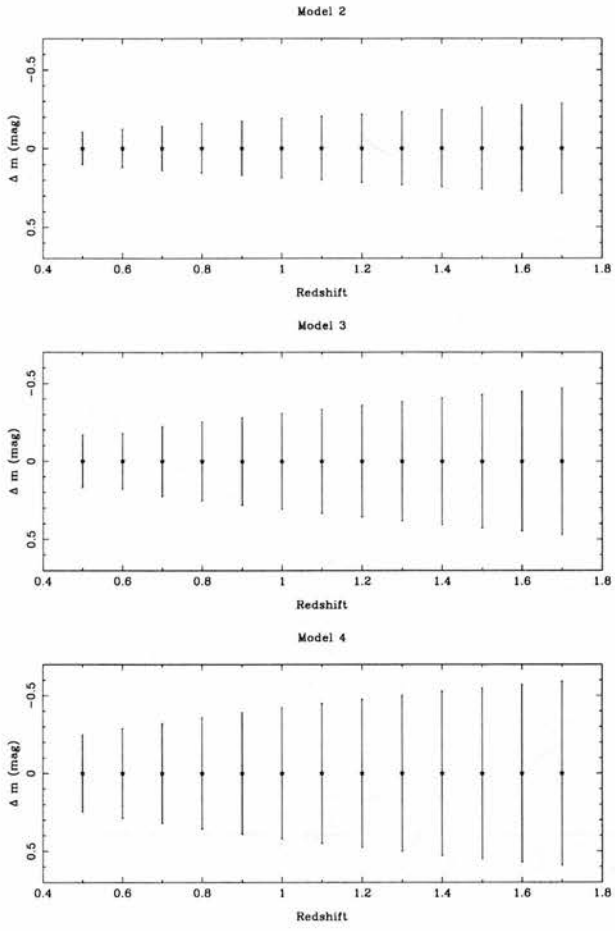

Figure 5.1: Mean and r.m.s. deviation of supernova brightness vs. redshift, due to lensing alone.

supernovae brightness in each bin. Thus the ability of SNAP and other surveys to discriminate between the different models listed in Table 5.1 depends on the accuracy with which the r.m.s. of the supernovae brightness can be measured from N supernovae. For gaussian distributions, this can be calculated analytically. However, as can be seen in Figure 5.2, the distribution of magnifications induced by lensing is far from gaussian. Thus a numerical approach is applied in order to generate a set of probability distribution functions (pdfs) for the data which can then be used to calculate the probabilities of distinguishing between different models for different sizes of supernova data sets.

For each model listed in Table 5.1, magnification patterns are generated for redshifts in the range $0.5 \leq z \leq 1.7$. For each model, N magnitudes are repeatedly drawn at random from the magnification patterns for the various redshifts, noting that the probability of a supernova lying in a distorted pixel in

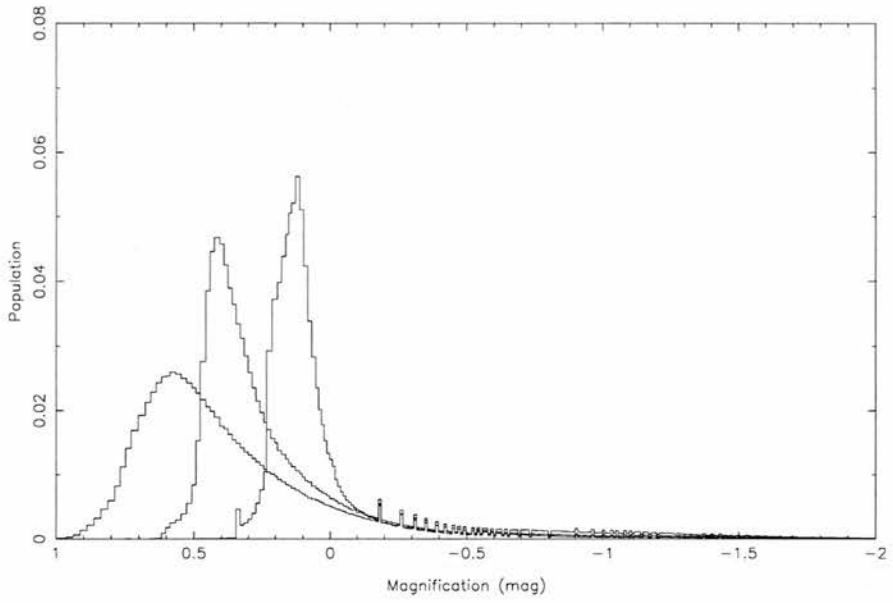

Figure 5.2: The distribution of magnifications arising from lensing in the three lensing models at redshift $z = 1.7$.

the source plane is proportional to the solid angle of the pixel. These magnifications are applied to magnitudes drawn from gaussian distributions of width $\sigma = \sqrt{\sigma^2_{intrinsic} + \sigma^2_{observational}}$. For the proposed SNAP survey, the values are taken as $\sigma_{intrinsic} = 0.157$ mag (Perlmutter *et al.*, 1999) and $\sigma_{observational} = 0.08$ mag. For the current data, σ is taken to be the measured r.m.s. given in Perlmutter *et al.* (1999), which includes both intrinsic and observational errors. This calculation is repeated many times and the results used to compute the distribution of the sample variance as a function of redshift. Some representative distributions are shown in Figure 5.3 for a redshift of $z = 1.7$.

The probability distribution of the variance *estimator* D_i can be computed.

$$D_i = \sum_j (m_{j,i} - \bar{m}_i)^2/(N-1)$$

where the sum extends over $j = 1 \ldots N$ supernovae in a redshift bin i. $\bar{m}_i$ is the mean magnitude in bin i. D_i is computed by Monte-Carlo simulation of N supernovae drawn from the ray-tracing simulations. This gives, for a given model M_k, the probability of obtaining a set of variances $\{D_i\}$,

$$p(\{D_i\}|M_k, N).$$

As the bins are independent, the probability of the set of variances is the product

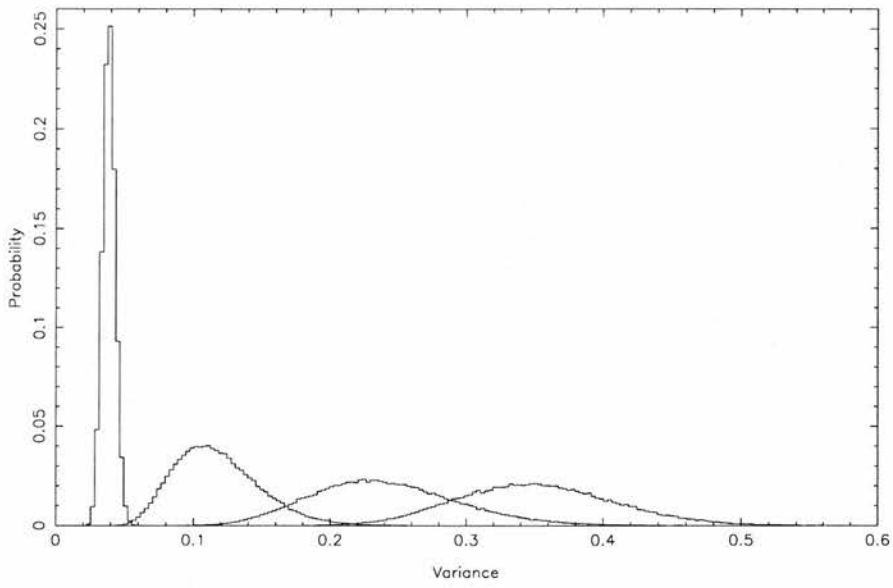

Figure 5.3: The distribution of the r.m.s. scatter of $N = 150$ supernovae at redshift $z = 1.7$, for the four models (1–4, from the left).

of individual probabilities for each redshift,

$$p(\{D_i\}|M_k, N) = \prod_i p(D_i|M_k, N)$$

From now on, N is suppressed in these probabilities.

The complication arises because there is, as yet, no data from the surveys. In order to distinguish between the different models, the probability of deducing the correct model M_{cor} is required. Marginalising over the (unknown at this stage) true model, this is

$$\begin{aligned} p(M_{cor}) &= \sum_k p(M_{cor}, M_k) \\ &= \sum_k p(M_{cor}|M_k)p(M_k) \\ &= \frac{1}{N_k}\sum_k p(M_{cor}|M_k) \end{aligned}$$

where the last step follows if equal prior probabilities are assumed for the models. N_k is the number of models considered.

To compute the conditional probability in the last equation, the distribution of sets of variances $\{D_i\}$ is used, given that the true model is M_t:

$$p(M_{cor}|M_t) = \int d\{D_i\}p(M_{cor}|\{D_i\}))p(\{D_i\}|M_t) \qquad (5.1)$$

Now, using Bayes' theorem,

$$p(M_k|\{D_i\}) = \frac{p(\{D_i\}|M_k)p(M_k)}{p(\{D_i\})}$$

Thus the probability of getting the *correct* model, given a set of data is

$$p(M_{cor}|\{D_i\}) = \frac{p(\{D_i\}|M_t)p(M_t)}{\sum_k p(\{D_i\}|M_k)p(M_k)}$$

where the *evidence* $p(\{D_i\})$ cancels out top and bottom. If uniform priors are assumed for the models, the probability simplifies, and substitution into Equation 5.1 gives

$$p(M_{cor}|M_t) = \int \frac{p(\{D_i\}|M_t)^2}{\sum_k p(\{D_i\}|M_k)p(M_k)} d\{D_i\}$$

Approximating the integral over sets of data by a set of N_r random drawings (labelled by α), gives:

$$p(M_{cor}) = \frac{1}{N_k} \sum_{M_t} \frac{1}{N_r} \sum_{\alpha} \left[\frac{p(\{D_i\}_\alpha|M_t)}{\sum_k p(\{D_i\}_\alpha|M_k)p(M_k)} \right]$$

5.2 Results

The relative likelihood of the four models considered is computed for the existing 42 high-redshift supernova published from the Supernova Cosmology Project (Perlmutter *et al.*, 1999). The data used is the stretch luminosity-corrected effective B-band magnitude. The expected magnitude for model 2 (or 3) is subtracted from the magnitude of the data and the variance computed using the standard estimator for 4 bins between $z = 0.45$ and $z = 0.85$. The reason for subtracting the expected magnitude of the model is that the redshift bins for which we have microlensing amplification distributions are quite broad and the mean apparent magnitude varies substantially over the bin (see Figure 5.4). For the Einstein-de Sitter model, the additional variance from subtracting the wrong evolution is negligible. Figure 5.5 shows the results of removing the expected magnitude from the data.

The variances in the four bins are 0.064, 0.170, 0.076 and 0.043, containing 11, 8, 3 and 3 supernovae respectively. Various effects conspire to make the $0.55 < z < 0.65$ bin the crucial one: first, at lower redshift, the lensing makes little difference

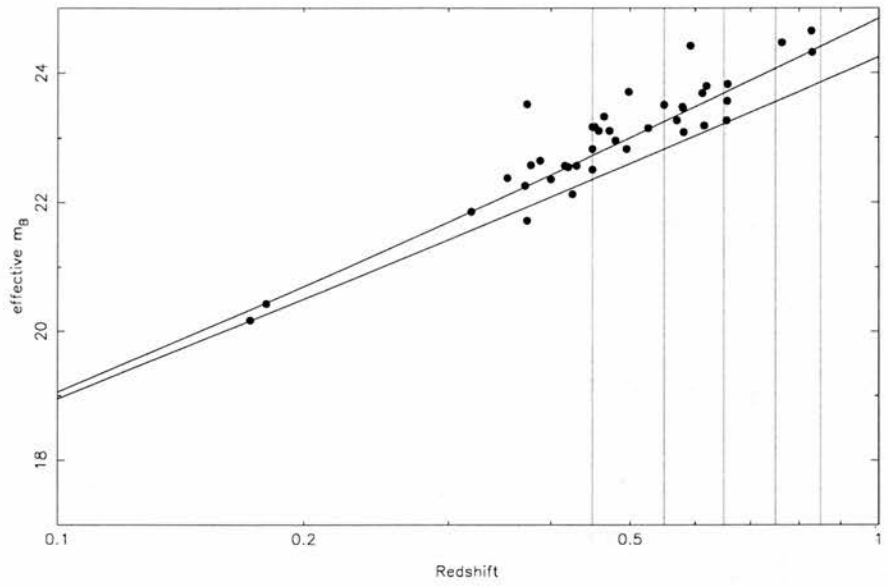

Figure 5.4: Distance redshift relation for the Supernova Cosmology Project data (Perlmutter *et al.*, 1999). The vertical lines show the redshift ranges in which the data was binned for analysis.

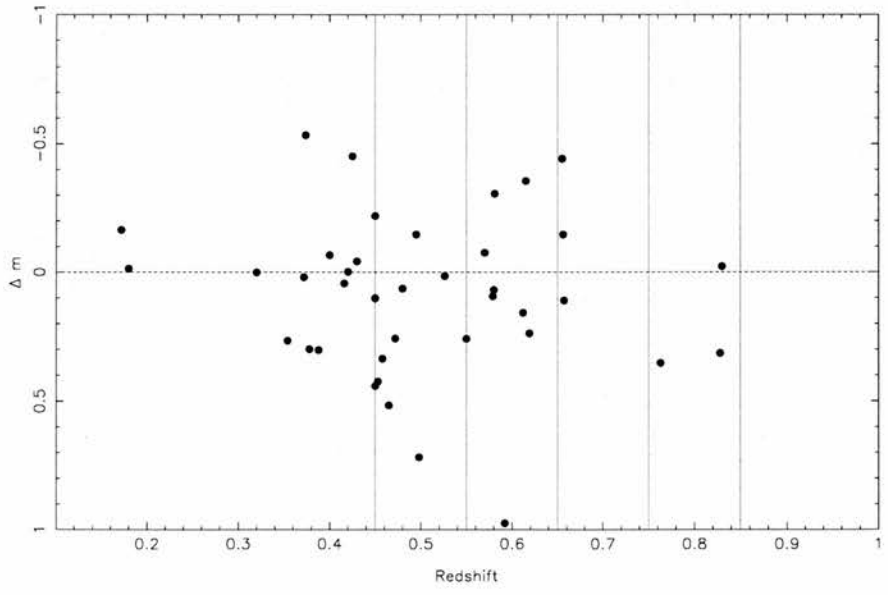

Figure 5.5: The scatter of the Supernova Cosmology Project data around the $\Omega_M = 0.3, \Omega_\Lambda = 0.7$ cosmological model.

to the variance; second, at higher redshift, there are very few supernovae in the bins; finally, the observed variance is high in the second bin. Thus the second redshift bin favours models with more microlensing, since the expected no-lensing

Model	Ω_M	Ω_Λ	Ω_{Lens}	Relative likelihood	SN1997K removed
1			0	0.58	1.0
2	0.3	0.7	0.1	0.92	0.88
3	0.3	0.7	0.3	0.96	0.66
4	1.0	0.0	1.0	1.0	0.32

Table 5.2: Relative likelihood for the four models, from the high-redshift supernovae observed as part of the supernova cosmology project.

variance is only 0.04. Combining the results gives the relative likelihoods shown in Table 5.2, where the likelihood of the favoured model is set to unity. The variances in the data have a slight preference for a population of compact objects, but the significance is low. In fact, removing a single supernova (SN1997K) from the dataset reduces the variance to 0.053, reversing the conclusions and making the no-lensing model the preferred choice (see Table 5.2). There is little a priori justification for removing this point. In fact it is anomalously faint, so it is not a good candidate for a lensing event. Thus, unsurprisingly, there is little to be learned from this test on current data.

Future experiments should be able to do this task with greater success. In Table 5.3, the conditional probabilities of selecting models are shown for varying numbers of supernovae per redshift interval of $\Delta z = 0.1$, for supernovae in the range $0.1 \lesssim 1.7$. SNAP expects ~ 167 per bin. Probabilities less than 0.0005 are set to zero in the table.

In Figure 5.6 we show how the probability of obtaining the correct model changes as we increase the number of sources per $\Delta z = 0.1$ bin. A uniform prior is assumed: *i.e.*, all models are equally likely *a priori*.

It can be seen that SNAP should be able to distinguish between these models with 99.9% confidence, provided systematic errors can be controlled.

The work presented in this chapter demonstrates how the scatter in supernova fluxes can be used to support or rule out models with dark matter in the form of a cosmological population of compact objects. Lensing by compact objects increases the variance in the fluxes, and for models with a high density dark matter in this form, the variance can be increased by a factor greater than 3 at redshifts accessible by supernova searches. Simply put, if the observed variance in supernova magnitudes is too small, it can eliminate a population of compact objects as the dominant dark matter candidate. The existing data from the

Correct model	Model	Number per $\Delta z = 0.1$						
		25	50	75	100	125	150	175
1	1	0.998	1.000	1.000	1.000	1.000	1.000	1.000
	2	0.002	0.000	0.000	0.000	0.000	0.000	0.000
	3	0.000	0.000	0.000	0.000	0.000	0.000	0.000
	4	0.000	0.000	0.000	0.000	0.000	0.000	0.000
2	1	0.004	0.000	0.000	0.000	0.000	0.000	0.000
	2	0.927	0.986	0.996	0.998	0.999	1.000	1.000
	3	0.069	0.014	0.004	0.002	0.001	0.000	0.000
	4	0.000	0.000	0.000	0.000	0.000	0.000	0.000
3	1	0.000	0.000	0.000	0.000	0.000	0.000	0.000
	2	0.065	0.014	0.004	0.002	0.001	0.000	0.000
	3	0.838	0.949	0.977	0.990	0.996	0.999	1.000
	4	0.097	0.037	0.019	0.008	0.002	0.001	0.000
4	1	0.000	0.000	0.000	0.000	0.000	0.000	0.000
	2	0.000	0.000	0.000	0.000	0.000	0.000	0.000
	3	0.088	0.032	0.016	0.006	0.003	0.001	0.000
	4	0.902	0.968	0.984	0.994	0.997	0.999	1.000

Table 5.3: Probability of deducing correct and incorrect models given the true model.

Supernova Cosmology Project data do not rule out dark matter in this form and conclusions about whether compact objects are preferred or not are sensitive to inclusion or exclusion of individual supernovae. Future planned surveys, such as the proposed SNAP survey should be able to distinguish models readily, and in principle provide an accurate measurement for the quantity of MACHO dark matter.

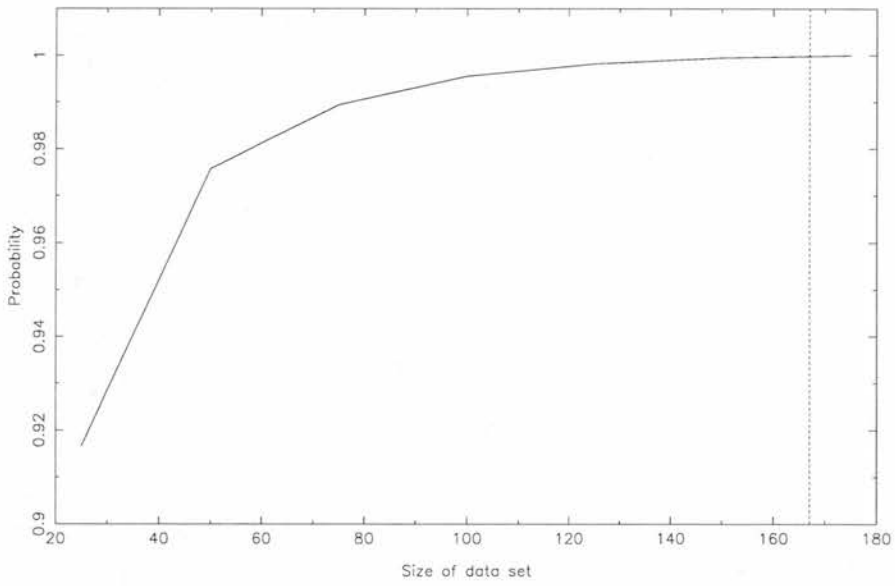

Figure 5.6: The probability of obtaining the correct model, plotted against the number of supernovae per redshift interval $\Delta z = 0.1$. In all cases it is assumed that supernovae are observed up to $z = 1.7$. SNAP expects about 167 (dotted line).

Chapter 6

Conclusions

Developments in the field of cosmology over the last hundred years have radically changed our view of the Universe. However, there is still one fundamental question we cannot answer – of what does the majority of the mass of the Universe consist? Observational data on all scales provide substantial evidence that luminous matter which can be directly observed constitutes a relatively small proportion of the matter in the universe. A number of theories have been put forward to explain this, offering so-called 'dark matter' in forms such as new fundamental particles, PBHs, brown dwarves, *etc.*. However, the sheer range of candidates and the mass ranges postulated provide perhaps the best illustration of how little is actually known.

This thesis investigates two methods by which it may be possible to observationally identify dark matter in the form of a cosmological distribution of compact objects such as PBHs. In particular, it explores the effect of the existence of this type of dark matter on quasar lightcurves and high redshift supernova observations. In both cases this investigation is carried out by simulating the effects of a cosmological distribution of compact objects and comparing the results with existing observations.

6.1 Long term variability of quasars

Observations from a large scale survey and monitoring programme of $\sim$ 600 quasars provide evidence for a long term variation in the apparent luminosity of quasars (Hawkins, 1993). This variation appears to be unaccompanied by

phenomena usually associated with intrinsic variability such as radio emission and changes in colour, leading to the suggestion that its origin may be external to the quasar. One possible explanation for the observations is that the light emitted by the quasars is being microlensed by a cosmological population of PBHs.

In order to test this hypothesis, a computer model was designed to simulate the effects of such a population on the quasar lightcurves. The model simulates the effect of microlensing by a three dimensional distribution of point mass lenses over a long time period. A number of different simulations were run to investigate a number of different scenarios. These can be summarised as follows:

- An Einstein-de Sitter model with all the mass in lenses.
- An $\Omega_M = 0.3$ and $\Omega_\Lambda = 0.7$ model with 1.0, 0.1 and 0.01 of Ω_M in lenses.
- $\Omega_M = 0.3$ and $\Omega_\Lambda = 0.7$ models with sources at redshifts of $z = 1.0$ and $z = 2.0$.
- $\Omega_M = 0.3$ and $\Omega_\Lambda = 0.7$ models with different distributions of lensing mass.

For each cosmological model, simulated lightcurves were generated for a number of different source sizes. These were used to produce power spectra which could be directly compared to the observational data. The observational data consists of the average power spectra of quasar lightcurves monitored over a 25 year timescale (Hawkins, 1993). The data was divided into redshift bins in the ranges $0.5 \leq z < 1.5$ and $1.5 \leq z < 2.5$ and luminosity bins $m_a < 20$ and $m_a \geq 20$. A series of reduced χ^2 fits were calculated between the simulated data and the different observational data sets. Although none of the models considered fits the complete sample adequately, the results of these comparisons can be summarised as follows:

- An $\Omega_M = 0.3$ and $\Omega_\Lambda = 0.7$ cosmology with $0.01\Omega_M$ in lenses is ruled out.
- The remaining models provide a best fit to the observational data sets with lenses with masses $10^{-5} M_\odot \lesssim M \lesssim 10^{-4} M_\odot$.
- The best fit for source sizes is found to be in the range $1.0 \times 10^{13}\, m$ and $3.6 \times 10^{13}\, m$.

While none of the models considered gives a formally acceptable fit to the complete observational data set, the simulations show that there are a range of cosmologies and mass ranges where PBHs could account for the long term variation in the apparent luminosity of quasars. In addition, the lens mass and source size ranges are surprisingly consistent between the different cosmologies and lens mass fractions of Ω_M studied.

While the computer model used to generate the simulated lightcurves required a substantial amount of development time there are, as always, a number of improvements which could be made to the algorithm. These include extending the distribution of lenses both in terms of lens masses and positions, increasing the use of knowledge of the paths of previous rays in calculations and a more efficient distribution of the hierarchical tree used to store the lens positions between processes.

6.2 High redshift supernova

The use of standard candles to measure distances is one of the classic methods for measuring the cosmological parameters. The extension of observations for Type *Ia* supernova to high redshifts has been one of the corner stones of the current popular $\Omega_M = 0.3$ and $\Omega_\Lambda = 0.7$ cosmological models. If dark matter is, at least partially, made up of a cosmological population of compact objects, then there is the possibility that magnitude measurements for the high redshift supernova are affected by gravitational lensing.

Chapter 5 looked at the likely strength of such an affect and whether it might be possible to use the results to differentiate between different cosmologies and proportions of dark matter in the form of compact objects. Specifically, the probability of differentiating between the following models was calculated.

- A model where there is no lensing and all the scatter in the data is due to intrinsic and observational effects.
- Two models with $\Omega_M = 0.3$ and $\Omega_\Lambda = 0.7$. These models differed in the proportion of Ω_M in lenses.
- An Einstein-de Sitter model with all of Ω_M in lenses.

A computer simulation was used to produce highly accurate simulations of the effects of the models listed above on supernova observations at a redshifts in the range $0.5 \leq z \leq 1.7$. The results of these simulations were used to generate a series of pdfs.

Calculations using these pdfs were made based on the current data published by the Supernova Cosmology Project (Perlmutter *et al.*, 1999) These calculations showed a preference for models with some lensing mass. However this prediction could be reversed by excluding a single point from the calculation. It is clear from these results that there is, as yet, insufficient data to distinguish between the proposed models.

The current data set of observations of high redshift supernova should be greatly enlarged if proposed surveys such as SNAP and VISTA go ahead. The amount of observational data required from these surveys to differentiate between different models was investigated. The pdfs generated from the simulations were used to calculate the probability of deducing the correct model for a variety of different sizes of data sets with sizes ranging from 25 per $\Delta z = 0.1$ bin to 175. The results of these calculation show that the 167 data points per $\Delta z = 0.1$ proposed for SNAP should be sufficient to differentiate between different models at a confidence level of 99.9% provided systematic errors can be controlled.

With future surveys proposing to find ~ 170 per $\Delta z = 0.1$, it is clear that they should provide an excellent observational data set for determining the amount of dark matter in the form of compact objects.

In summary, the work presented in this thesis has shown that describing dark matter as a cosmological distribution of compact objects such as PBHs is in reasonable agreement with the observational results of a long term survey of quasars. While it appears from these results that this method cannot distinguish to any great degree between different cosmological models and lensing populations, it does make strong deductions about the mass of the microlensing objects and the source sizes of quasars. The lensing masses are constrained to the mass range $10^{-5} \lesssim M_{lens} \lesssim 10^{-5}$. In addition, the proposed high redshift supernova searches will also provide a method for probing dark matter in this form. In particular, it should prove possible to use data from these searches to differentiate between different cosmological and lens population models to a high degree of accuracy.

Bibliography

Alcock, C., Akerloff, C. W., Allsman, R. A., Axelrod, T. S., Bennett, D. P., Chan, S., Cook, C. H., Freeman, K. C., Griest, K., Marshall, S. L., Park, H. S., Perlmutter, S., Peterson, B. A., Pratt, M. R., Quinn, P. J., Rodgers, A. W., Stubbs, C. W., Sutherland, W., 1993, Nature, **365**, 621–623.

Alcock, C., Allsman, R. A., Alves, D., Axelrod, T. S., Becker, A., Bennett, D. P., Cook, K. H., Freeman, K. C., Griest, K., Keane, M. J., Lehner, M. J., Marshall, S. L., Minniti, D., Peterson, B. A., Pratt, M. R., Quinn, P. J., Rodgers, A. W., Stubbs, C. W., Sutherland, W., Tomaney, A. B., Vandehei, T., Welch, D., 1997, Ap. J. Lett., **491**, L11–.

Alcock, C., Allsman, R. A., Alves, D. R., Axelrod, T. S., Becker, A. C., Bennett, D. P., Cook, K. H., Dalal, N., Drake, A. J., Freeman, K. C., Geha, M., Griest, K., Lehner, M. J., Marshall, S. L., Minniti, D., Nelson, C. A., Peterson, B. A., Popowski, P., Pratt, M. R., Quinn, P. J., Stubbs, C. W., Sutherland, W., Tomaney, A. B., Vandehei, T., Welch, D., 2000, Ap. J., **542**, 281–307.

Alexander, T., 1995, MNRAS, **274**, 909–918.

Allen, S. W., 1998, MNRAS, **296**, 392–406.

Aubourg, E., Bareyre, P., Brehin, S., Gros, M., Lachieze-Rey, M., Laurent, B., Lesquoy, E., Magneville, C., Milsztajn, A., Moscoso, L., Queinnec, F., Rich, J., Spiro, M., Vigroux, L., Zylberajch, S., Ansari, R., Cavalier, F., Moniez, M., Beaulieu, J. P., Ferlet, R., Grison, P., Madjar, A. V., Guibert, J., Moreau, O., Tajahmady, F., Maurice, E., Prevot, L., Gry, C., 1993, Nature, **365**, 623–625.

Bacon, D. J., Refregier, A. R., Ellis, R. S., 2000, MNRAS, **318**, 625–640.

Baganoff, F. K., Malkan, M. A., 1995, Ap. J. Lett., **444**, L13–L15.

Balbi, A., Ade, P., Bock, J., Borrill, J., Boscaleri, A., De Bernardis, P., Ferreira, P. G., Hanany, S., Hristov, V., Jaffe, A. H., Lee, A. T., Oh, S., Pascale, E., Rabii, B., Richards, P. L., Smoot, G. F., Stompor, R., Winant, C. D., Wu, J. H. P., 2000, Ap. J. Lett., **545**, L1–L4.

Ballinger, W. E., Taylor, A. N., Heavens, A. F., Tadros, H., Redshift distortions and clustering in the pscz survey, in *Proceedings of Moriond 2000 "Energy Densities in the Universe"*, 2000.

Barber, A. J., 2000, MNRAS, **318**, 195–202.

Barnes, J., Hut, P., 1986, Nature, **324**, 446–449.

Bartelmann, M., Schneider, P., 1991, Astron. Astrophys., **248**, 349–353.

Bennett, C. L., Banday, A. J., Gorski, K. M., Hinshaw, G., Jackson, P., Keegstra, P., Kogut, A., Smoot, G. F., Wilkinson, D. T., Wright, E. L., 1996, Ap. J. Lett., **464**, L1–L4.

Biggs, A. D., Browne, I. W. A., Helbig, P., Koopmans, L. V. E., Wilkinson, P. N., Perley, R. A., 1999, MNRAS, **304**, 349–358.

Blandford, R. D., Kochanek, K., Gravitational lenses, in *Dark Matter in the Universe (Jerusalem Winter School on Theoretical Physics*, pages 133–195, 1987.

Blandford, R. D., Narayan, R., 1986, Ap. J., **310**, 568–582.

Blandford, R. D., Narayan, R., 1992, Ann. Rev. Astron. Astrophys., **30**, 311–358.

Blandford, R. D., Saust, A. B., Brainerd, T. G., Villumsen, J. V., 1991, MNRAS, **251**, 600–627.

Bonnet, H., Mellier, Y., Fort, B., 1994, Ap. J. Lett., **427**, L83–L86.

Branch, D., 1998, Ann. Rev. Astron. Astrophys., **36**, 17–55.

Broadhurst, T., Mass Distributions of Clusters from Gravitational Magnification, in *Dark Matter (AIP Conf. Proc.)*, page 336, 1995.

Browne, I. W. A., Myers, S. T., CLASS: a well-defined sample of radio-selected gravitational lens systems for cosmology, in *IAU Symposium*, volume 201, page E47, 2000.

Canizares, C. R., 1982, Ap. J., **263**, 508–517.

Carroll, S. M., Press, W. H., Turner, E. L., 1992, Ann. Rev. Astron. Astrophys., **30**, 499–542.

Chang, K., Refsdal, S., 1979, Nature, **282**, 561–564.

Claeskens, J.-F., Surdej, J., 2000, Astron. Astrophys. Review.

Clowe, D., Luppino, G. A., Kaiser, N., Gioia, I. M., 2000, Ap. J., **539**, 540–560.

Coles, P., 2001, Preprint, astro-ph/0102462.

Crawford, M., Schramm, D. N., 1982, Nature, **298**, 538–540.

Derue, F., Afonso, C., Alard, C., Albert, J. ., Amadon, A., Andersen, J., Ansari, R., Aubourg, É., Bareyre, P., Bauer, F., Beaulieu, J. ., Bouquet, A., Char, S., Charlot, X., Couchot, F., Coutures, C., Ferlet, R., Glicenstein, J. ., Goldman, B., Gould, A., Graff, D., Gros, M., Haıssinski, J., Hamilton, J. ., Hardin, D., de Kat, J., Kim, A., Lasserre, T., Lesquoy, É., Loup, C., Magneville, C., Mansoux, B., Marquette, J. ., Maurice, É., Milsztajn, A., Moniez, M., Palanque-Delabrouille, N., Perdereau, O., Prévot, L., Regnault, N., Rich, J., Spiro, M., Vidal-Madjar, A., Vigroux, L., Zylberajch, S., EROS Collaboration, 1999, Astron. Astrophys., **351**, 87–96.

Dyer, C. C., Roeder, R. C., 1974, Ap. J., **189**, 167–176.

Efstathiou, G., Sutherland, W. J., Maddox, S. J., 1990, Nature, **348**, 705–707.

Faber, S. M., Jackson, R. E., 1976, Ap. J., **204**, 668–683.

Fabricant, D., Gorenstein, P., 1983, Ap. J., **267**, 535–546.

Falco, E. E., Kochanek, C. S., Lehar, J., McLeod, B. A., Munoz, J. A., Impey, C. D., Keeton, C., Peng, C. Y., Rix, H.-W., The CASTLES gravitational lensing tool, in *Gravitational Lensing: Recent Progress and Future Goals (ASP Conference Series)*, 1999.

Fort, B., Prieur, J. L., Mathez, G., Mellier, Y., Soucail, G., 1988, Astron. Astrophys., **200**, L17–L20.

Freedman, W. L., 2000, Physics Reports, **333**, 13–31.

Freedman, W. L., Madore, B. F., Gibson, B. K., Ferrarese, L., Kelson, D. D., Sakai, S., Mould, J. R., Kennicutt Jr., R. C., Ford, H. C., Graham, J. A., Huchra, J. P., Hughes, S. M. G., Illingworth, G. D., Macri, L. M., Stetson, P. B., 2000, Preprint, astro-ph/0012376.

Fukugita, M., Futamase, T., Kasai, M., Turner, E. L., 1992, Ap. J., **393**, 3–21.

Goobar, A., Perlmutter, S., 1995, Ap. J., **450**, 14–18.

Gott, J. R., 1981, Ap. J., **243**, 140–146.

Graff, D. S., Kim, A., 2001, Preprint, astro-ph/0101395.

Griest, K., 1991, Ap. J., **366**, 412–421.

Gunn, J. E., 1967, Ap. J., **150**, 737–754.

Hamilton, A. J. S., Linear redshift distortions: A review, in *Ringberg Workshop on Large-Scale Structure*, 1996.

Hamilton, A. J. S., Tegmark, M., Padmanabhan, N., 2000, MNRAS, **317**, L23–L27.

Hamuy, M., Phillips, M. M., Suntzeff, N. B., Schommer, R. A., Maza, J., Aviles, R., 1996, Astron. J., **112**, 2391–2397.

Hanany, S., Ade, P., Balbi, A., Bock, J., Borrill, J., Boscaleri, A., de Bernardis, P., Ferreira, P. G., Hristov, V. V., Jaffe, A. H., Lange, A. E., Lee, A. T., Mauskopf, P. D., Netterfield, C. B., Oh, S., Pascale, E., Rabii, B., Richards, P. L., Smoot, G. F., Stompor, R., Winant, C. D., Wu, J. H. P., 2000, Ap. J. Lett., **545**, L5–L9.

Hawkins, M. R. S., 1993, Nature, **366**, 242–245.

Hawkins, M. R. S., 1996, MNRAS, **278**, 787–807.

Hawkins, M. R. S., 2000, Astron. Astrophys. Suppl., **143**, 465–481.

Hawkins, M. R. S., Taylor, A. N., 1997, Ap. J. Lett., **482**, L5–L8.

Hawkins, M. R. S., Véron, P., 1993, MNRAS, **260**, 202–208.

Hegyi, D. J., Olive, K. A., 1986, Ap. J., **303**, 56–65.

Helbig, P., Marlow, D., Quast, R., Wilkinson, P. N., Browne, I. W. A., Koopmans, L. V. E., 1999, Astron. Astrophys. Suppl., **136**, 297–305.

Hewitt, J. N., Turner, E. L., Schneider, D. P., Burke, B. F., Langston, G. I., 1988, Nature, **333**, 537–540.

Hillebrandt, W., Niemeyer, J. C., 2000, Ann. Rev. Astron. Astrophys., **38**, 191–230.

Holz, D. E., Wald, R. M., 1998, Phys. Rev. D., **58**.

Hubble, E. P., 1926, Ap. J., **64**, 321–369.

Hubble, E. P., 1929, Publ. Nat. Acad. Sci, **15**, 168.

Huterer, D., Turner, M. S., 2000, Preprint, astro-ph/0012510.

Jaffe, A. H., Ade, P. A. R., Balbi, A., Bock, J., Bond, J. R., Borrill, J., Boscaleri, A., Coble, K., Crill, B. P., de Bernardis, P., Farese, P., Ferreira, P. G., Ganga, K., Giacometti, M., Hanany, S., Hivon, E., Hristov, V. V., Iacoangeli, A., Lange, A. E., Lee, A. T., Martinis, L., Masi, S., Mauskopf, P. D., Melchiorri, A., Montroy, T., Netterfield, C., Oh, S., Pascale, E., Piacentini, F., Pogosyan, D., Prunet, S., Rabii, B., Rao, S., Richards, P. L., Romeo, G., Ruhl, J. E., Scaramuzzi, F., Sforna, D., Smoot, G. F., Stompor, R., Winant, C. D., Wu, J. H. P., 2000, Preprint, astro-ph/0007333.

Jain, B., Seljak, U., White, S., 2000, Ap. J., **530**, 547–577.

Jaroszyński, M., Park, C., Paczyński, B., Gott, J. R., 1990, Ap. J., **365**, 22–26.

Jauncey, D. L., Reynolds, J. E., Tzioumis, A. K., Murphy, D. W., Preston, R. A., Jones, D. L., Meier, D. L., Hoard, D. W., Lobdell, E. T., Skjerve, L., 1991, Nature, **352**, 132–134.

Kaiser, N., 1992, Ap. J., **388**, 272–286.

Kaiser, N., Squires, G., 1993, Ap. J., **404**, 441–450.

Kayser, R., Refsdal, S., Stabell, R., 1986, Astron. Astrophys., **166**, 36–52.

King, L. J., Jackson, N. J., Blandford, R. D., Bremer, M. N., Browne, I. W. A., de Bruyn, A. G., Fassnacht, C., Koopmans, L., Marlow, D., Nair, S., Wilkinson, P. N., 1998, MNRAS, **295**, L41–L44.

King, L. J., Browne, I. W. A., Marlow, D. R., Patnaik, A. R., Wilkinson, P. N., 1999, MNRAS, **307**, 225–235.

Kochanek, C. S., 1993, Ap. J., **419**, 12–29.

Kochanek, C. S., Falco, E. E., Impey, C., Lehar, J., McLeod, B., Rix, H.-W., 1999. Castles survey. Available from `http://cfawww.harvard.edu/castles/`.

Kochanek, C. S., Falco, E. E., Impey, C. D., Lehár, J., McLeod, B. A., Rix, H. ., Keeton, C. R., Muñoz, J. A., Peng, C. Y., 2000, Ap. J., **535**, 692–705.

Koopmans, L. V. E., Fassnacht, C. D., 1999, Ap. J., **527**, 513–524.

Koopmans, L. V. E., de Bruyn, A. G., Xanthopoulos, E., Fassnacht, C. D., 2000, Astron. Astrophys., **356**, 391–402.

Kovner, I., 1987, Ap. J., **316**, 52–69.

Kristian, J., Sachs, R. K., 1966, Ap. J., **143**, 379–399.

Kundic, T., Turner, E. L., Colley, W. N., Gott, J. R. I., Rhoads, J. E., Wang, Y., Bergeron, L. E., Gloria, K. A., Long, D. C., Malhotra, S., Wambsganss, J., 1997, Ap. J., **482**, 75–82.

Lahav, O., Lilje, P. B., Primack, J. R., Rees, M. J., 1991, MNRAS, **251**, 128–136.

Langston, G. I., Schneider, D. P., Conner, S., Carilli, C. L., Lehar, J., Burke, B. F., Turner, E. L., Gunn, J. E., Hewitt, J. N., Schmidt, M., 1989, Astron. J., **97**, 1283–1290.

Lasserre, T., Afonso, C., Albert, J. N., Andersen, J., Ansari, R., Aubourg, É., Bareyre, P., Bauer, F., Beaulieu, J. P., Blanc, G., Bouquet, A., Char, S., Charlot, X., Couchot, F., Coutures, C., Derue, F., Ferlet, R., Glicenstein, J. F., Goldman, B., Gould, A., Graff, D., Gros, M., Haıssinski, J., Hamilton, J. C., Hardin, D., de Kat, J., Kim, A., Lesquoy, É., Loup, C., Magneville, C., Mansoux, B., Marquette, J. B., Maurice, É., Milsztajn, A., Moniez, M., Palanque-Delabrouille, N., Perdereau, O., Prévot, L., Regnault, N., Rich, J., Spiro, M., Vidal-Madjar, A., Vigroux, L., Zylberajch, S., The EROS collaboration, 2000, Astron. Astrophys., **355**, L39–L42.

Lewis, G., Miralda-Escudé, J., Richardson, D., Wambsganss, J., 1993, MNRAS, **261**, 647–656.

Linder, E. V., Wagoner, R. V., Schneider, P., 1988, Ap. J., **324**, 786–793.

Lynds, R., Petrosian, V., 1986, BAAS, **18**, 1014.

Maoz, D., Bahcall, J. N., Schneider, D. P., Bahcall, N. A., Djorgovski, S., Doxsey, R., Gould, A., Kirhakos, S., Meylan, G., Yanny, B., 1993, Ap. J., **409**, 28–41.

Mauskopf, P. D., Ade, P. A. R., de Bernardis, P., Bock, J. J., Borrill, J., Boscaleri, A., Crill, B. P., DeGasperis, G., De Troia, G., Farese, P., Ferreira, P. G., Ganga, K., Giacometti, M., Hanany, S., Hristov, V. V., Iacoangeli, A., Jaffe, A. H., Lange, A. E., Lee, A. T., Masi, S., Melchiorri, A., Melchiorri, F., Miglio, L., Montroy, T., Netterfield, C. B., Pascale, E., Piacentini, F., Richards, P. L., Romeo, G., Ruhl, J. E., Scannapieco, E., Scaramuzzi, F., Stompor, R., Vittorio, N., 2000, Ap. J. Lett., **536**, L59–L62.

Melchiorri, A., Ade, P. A. R., de Bernardis, P., Bock, J. J., Borrill, J., Boscaleri, A., Crill, B. P., De Troia, G., Farese, P., Ferreira, P. G., Ganga, K., de Gasperis, G., Giacometti, M., Hristov, V. V., Jaffe, A. H., Lange, A. E., Masi, S., Mauskopf, P. D., Miglio, L., Netterfield, C. B., Pascale, E., Piacentini, F., Romeo, G., Ruhl, J. E., Vittorio, N., 2000, Ap. J. Lett., **536**, L63–L66.

Mellier, Y., 1999, Ann. Rev. Astron. Astrophys., **37**, 127–189.

Message Passing Interface Forum, 12th June, 1995. MPI: A Message Passing Interface Standard. Available from http://www.mpi-forum.org/.

Metcalf, R. B., Silk, J., 1999, Ap. J. Lett., **519**, L1–L4.

Miralda-Escudé, J., 1991, Ap. J., **380**, 1–8.

Miralda-Escudé, J., Babul, A., 1995, Ap. J., **449**, 18–27.

Olive, K. A., Steigman, G., Walker, T. P., 2000, Physics Reports, **333**, 389–407.

Paczyński, B., 1986, Ap. J., **301**, 503–516.

Paczyński, B., 1986, Ap. J., **304**, 1–5.

Paczyński, B., 1987, Nature, **325**, 572.

Paczyński, B., 1996, Ann. Rev. Astron. Astrophys., **34**, 419–460.

Peacock, J. A., 1999. *Cosmological Physics.* Cambridge University Press.

Pei, Y. C., 1993, Ap. J., **403**, 7–19.

Pelló, R., Kneib, J. P., Le Borgne, J. F., Bézecourt, J., Ebbels, T. M., Tijera, I., Bruzual, G., Miralles, J. M., Smail, I., Soucail, G., Bridges, T. J., 1999, Astron. Astrophys., **346**, 359–368.

Perlmutter, S., Gabi, S., Goldhaber, G., Goobar, A., Groom, D. E., Hook, I. M., Kim, A. G., Kim, M. Y., Lee, J. C., Pain, R., Pennypacker, C. R., Small, I. A., Ellis, R. S., McMahon, R. G., Boyle, B. J., Bunclark, P. S., Carter, D., Irwin, M. J., Glazebrook, K., Newberg, H. J. M., Filippenko, A. V., Matheson, T., Dopita, M., Couch, W. J., The Supernova Cosmology Project, 1997, Ap. J., **483**, 565–581.

Perlmutter, S., Aldering, G., Goldhaber, G., Knop, R. A., Nugent, P., Castro, P. G., Deustua, S., Fabbro, S., Goobar, A., Groom, D. E., Hook, I. M., Kim, A. G., Kim, M. Y., Lee, J. C., Nunes, N. J., Pain, R., Pennypacker, C. R., Quimby, R., Lidman, C., Ellis, R. S., Irwin, M., McMahon, R. G., Ruiz-Lapuente, P., Walton, N., Schaefer, B., Boyle, B. J., Filippenko, A. V., Matheson, T., Fruchter, A. S., Panagia, N., Newberg, H. J. M., Couch, W. J., The Supernova Cosmology Project, 1999, Ap. J., **517**, 565–586.

Press, W., Gunn, J., 1973, Ap. J., **185**, 397–412.

Rauch, K. P., 1991, Ap. J., **374**, 83–90.

Rees, M. J., 1984, Ann. Rev. Astron. Astrophys., **22**, 471–506.

Refsdal, S., 1964, MNRAS, **128**, 307–310.

Refsdal, S., Stabell, R., 1991, Astron. Astrophys., **250**, 62–66.

Refsdal, S., Surdej, J., 1994, Rep. Progr. Phys., **57**, 117–185.

Refsdal, S., Stabell, R., Pelt, J., Schild, R., 2000, Astron. Astrophys., **360**, 10–14.

Reid, I. N., 1997, Astron. J., **114**, 161–179.

Richer, H. B., Fahlmann, G. G., 1992, Nature, **358**, 383–386.

Riess, A. G., Filippenko, A. V., Challis, P., Clocchiatti, A., Diercks, A., Garnavich, P. M., Gilliland, R. L., Hogan, C. J., Jha, S., Kirshner, R. P., Leibundgut, B., Phillips, M. M., Reiss, D., Schmidt, B. P., Schommer, R. A.,

Smith, R. C., Spyromilio, J., Stubbs, C., Suntzeff, N. B., Tonry, J., 1998, Ap. J., **116**, 1009–1038.

Sakai, S., Mould, J. R., Hughes, S. M. G., Huchra, J. P., Macri, L. M., Kennicutt, R. C., Gibson, B. K., Ferrarese, L., Freedman, W. L., Han, M., Ford, H. C., Graham, J. A., Illingworth, G. D., Kelson, D. D., Madore, B. F., Sebo, K., Silbermann, N. A., Stetson, P. B., 2000, Ap. J., **529**, 698–722.

Schmidt, B. P., Suntzeff, N. B., Phillips, M. M., Schommer, R. A., Clocchiatti, A., Kirshner, R. P., Garnavich, P., Challis, P., Leibundgut, B., Spyromilio, J., Riess, A. G., Filippenko, A. V., Hamuy, M., Smith, R. C., Hogan, C., Stubbs, C., Diercks, A., Reiss, D., Gilliland, R., Tonry, J., Maza, J., Dressler, A., Walsh, J., Ciardullo, R., 1998, Ap. J., **507**, 46–63.

Schneider, P., 1985, Astron. Astrophys., **143**, 413–420.

Schneider, P., 1993, Astron. Astrophys., **279**, 1–20.

Schneider, P., Weiss, A., 1987, Astron. Astrophys., **171**, 49–65.

Schneider, P., Weiss, A., 1988, Ap. J., **330**, 1–15.

Schneider, P., Ehlers, J., Falco, E., 1993. *Gravitational Lenses.* Springer Verlag.

Seljak, U., Holz, D. E., 1999, Astron. Astrophys., **351**, L10–L14.

Smail, I., Ellis, R. S., Dressler, A., Couch, W. J., Oemler, A. J., Sharples, R. M., Butcher, H., 1997, Ap. J., **479**, 70–81.

Smail, I., Ivison, R. J., Blain, A. W., 1997, Ap. J. Lett., **490**, L5–L8.

Smith, S., 1936, Ap. J., **83**, 23–30.

Soldner, J., 1804, Berliner Astronomisches Jahrbuch, page 161.

Soucail, G., Fort, B., Mellier, Y., Picat, J. P., 1987, Astron. Astrophys., **172**, L14–L16.

Soucail, G., Mellier, Y., Fort, B., Mathez, G., Cailloux, M., 1988, Astron. Astrophys., **191**, L19–L21.

Stewart, G. C., Fabian, A. C., Nulsen, P. E. J., Canizares, C. R., 1984, Ap. J., **278**, 536–543.

Surdej, J., Claeskens, J., Crampton, D., Filippenko, A. V., Hutsemekers, D., Magain, P., Pirenne, B., Vanderriest, C., Yee, H. K. C., 1993, Astron. J., **105**, 2064–2078.

Susperregi, M., 2001, Ap. J., **546**, 85–99.

Tanvir, N. R., Cepheid Standard Candles, in *ASP Conf. Ser. 167: Harmonizing Cosmic Distance Scales in a Post-HIPPARCOS Era*, pages 84+, 1999.

Trimble, V., 1987, Ann. Rev. Astron. Astrophys., **25**, 425–472.

Tully, R. B., Fisher, J. R., 1977, Astron. Astrophys., **54**, 661–673.

Turner, E. L., Ostriker, J. P., Gott, J. R., 1984, Ap. J., **284**, 1–22.

Tyson, J. A., Valdes, F., Wenk, R. A., 1990, Ap. J. Lett., **349**, L1–L4.

Udalski, A., Szymanski, M., Kaluzny, J., Kubiak, M., Krzeminski, W., Mateo, M., Preston, G. W., Paczynski, B., 1993, Acta Astronomica, **43**, 289–294.

Udalski, A., Szymanski, M., Mao, S., di Stefano, R., Kaluzny, J., Kubiak, M., Mateo, M., Krzeminski, W., 1994, Ap. J. Lett., **436**, L103–L106.

Van Waerbeke, L., Mellier, Y., Erben, T., Cuillandre, J. C., Bernardeau, F., Maoli, R., Bertin, E., Mc Cracken, H. J., Le Fèvre, O., Fort, B., Dantel-Fort, M., Jain, B., Schneider, P., 2000, Astron. Astrophys., **358**, 30–44.

Véron, P., Hawkins, M. R. S., 1995, Astron. Astrophys., **296**, 665–679.

Villumsen, J. V., 1996, MNRAS, **281**, 369–383.

Walsh, D., Carswell, R., Weymann, R., 1979, Nature, **279**, 381–384.

Wambsganss, J., 1998, Living Reviews in Relativity.

Wambsganss, J., Paczyński, B., Scheider, P., 1990, Ap. J., **358**, L33–L36.

Wambsganss, J., Paczyński, B., Katz, N., 1990, Ap. J., **352**, 407–412.

Wambsganss, J., Cen, R., Ostriker, J., 1998, Ap. J., **494**, 29–46.

Wambsganss, J., Schmidt, R. W., Colley, W., Kundić, T., Turner, E. L., 2000, Astron. Astrophys., **362**, L37–L40.

Weinberg, S., 1972. *Gravitation and Cosmology: Principles and Applications of the General Theory of Relativity.* John Wiley & Sons.

Weller, J., Albrecht, A., 2000, Preprint, astro-ph/0008314.

Wu, X., 1996, Fundamentals of Cosmic Physics.

Zwicky, F., 1933, Helv. Phys. Acta, **10**, 110.

Appendix A

Angular Diameter Distance

The angular diameter distance is defined as:

$$d_A = \frac{dl}{d\phi} \tag{A.1}$$

where dl is the proper size of an object and $d\theta$ is its apparent angular size as shown in Figure A.1.

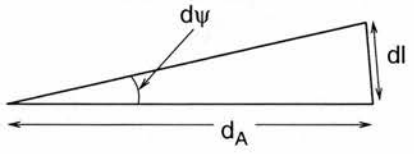

Figure A.1: The angular diameter distance relates the proper size of an object dl to its angular size $d\theta$

Starting from the Robertson-Walker metric (Equation 1.2) and taking $c = 1$:

$$ds^2 = dt^2 - R^2(t)\left[\frac{dr^2}{1-kr^2} + r^2 d\theta^2 + r^2 \sin^2\theta d\phi^2\right]$$

the proper size of the object, dl, can be expressed as:

$$dl^2 = R^2(t)\left[\frac{dr^2}{1-kr^2} + r^2 d\theta^2 + r^2 \sin^2\theta d\phi^2\right]$$

If dl is taken to lie along the θ axis, such that $dr = d\phi = 0$, the angular diameter distance can be expressed as

$$\begin{aligned} d_A &= R(t) r \frac{d\theta}{d\theta} \\ &= R(t) r \end{aligned} \tag{A.2}$$

Equation A.2 can be used to obtain the expression for the angular diameter distance from an observer at $r = 0$ to an object at $r = r_1$. It can also be generalised to obtain an expression for the angular diameter distance between two points at $r = r_1$ and $r = r_2$ by changing the coordinate system so that the origin is at $r = r_1$. This coordinate change does not affect the Robertson-Walker metric (equation 1.2).

Considering a light ray moving radially from r_2 through r_1 towards the observer, gives $ds = d\theta = d\phi = 0$. If the separation of r_1 and r_2 is $\tilde{r}$ then:

$$\frac{d\tilde{r}}{dt} = \frac{\sqrt{1 - k\tilde{r}^2}}{R(t)}$$

An expression for the look-back time for a universe with negligible radiation density can be obtained from (Carroll *et al.*, 1992):

$$\begin{aligned} t_0 - t_1 &= \frac{1}{H_0}\int_0^{z_1} \frac{[(1+z)^2(1+\Omega_M z) - z(2+z)\Omega_\Lambda]^{-1/2}}{(1+z)} dz \\ &= \frac{1}{H_0}\int_0^{z_1} \frac{F(z)}{(1+z)} dz \end{aligned}$$

Thus:

$$\begin{aligned} \frac{d\tilde{r}}{dz} &= \frac{d\tilde{r}}{dt}\frac{dt}{dz} \\ &= \frac{-\sqrt{1 - k\tilde{r}^2}}{R(t)} \frac{F(z)}{H_0(1+z)} \end{aligned}$$

Substituting the relation:

$$R(t) = R_0/(1+z) \tag{A.3}$$

gives:

$$\int \frac{H_0 R_0 d\tilde{r}}{\sqrt{1 - k\tilde{r}^2}} = -\int F(z) dz \tag{A.4}$$

Then, considering the three values for k individually:

$k = 0$: **Flat universe** In this case the left hand side of equation A.4 is simply $H_0 R_0 \tilde{r}$. Using the expression for the angular diameter distance given in

equation A.2, this gives:

$$\begin{aligned} d_A = R(t_2)\tilde{r} &= -\frac{1}{(1+z_2)}\int_{z_1}^{z_2} F(z)dz \\ &= -\frac{1}{(1+z_2)}\int_{z_1}^{z_2} [(1+z)^2(1+\Omega_M z) - \\ &\qquad z(2+z)\Omega_\Lambda]^{-1/2}\, dz \end{aligned} \tag{A.5}$$

$k = -1$: **Open universe** In this case the left hand side of equation A.4 becomes:

$$\int \frac{H_0 R_0}{\sqrt{1+\tilde{r}^2}} d\tilde{r}$$

Making the substitution $\tilde{r} = \sinh u$, $d\tilde{r} = \cosh u du$ and using the relation $\cosh^2 u - \sinh^2 u = 1$ gives:

$$\int \frac{H_0 R_0 \cosh u}{\cosh u} du = H_0 R_0 u = H_0 R_0 \sinh^{-1} \tilde{r}$$

Thus the angular diameter distance becomes:

$$\begin{aligned} H_0 d_A &= H_0 R(t)\tilde{r} \\ &= H_0 \frac{R_0}{(1+z_2)}\tilde{r} \\ &= -H_0 \frac{R_0}{(1+z_2)} \sinh\left[\frac{1}{H_0 R_0}\int dz F(z)\right] \end{aligned}$$

Defining:

$$\Omega_k \equiv -\frac{k}{H_0^2 R_0^2} \tag{A.6}$$

gives:

$$\begin{aligned} d_A &= -\frac{1}{H_0\sqrt{|\Omega_k|}(1+z_2)} \sinh\left[\sqrt{|\Omega_k|}\int dz F(z)\right] \\ &= -\frac{1}{H_0\sqrt{|\Omega_k|}(1+z_2)} \sinh\left[\sqrt{|\Omega_k|}\int_{z_1}^{z_2} \frac{[(1+\Omega_M z) - z(2+z)\Omega_\Lambda]^{-1/2}}{(1+z)} dz\right] \end{aligned}$$

$k = 1$: **Closed universe** For a closed universe, the left hand side of equation A.4 becomes:

$$\int \frac{H_0 R_0}{\sqrt{1-\tilde{r}^2}} d\tilde{r}$$

Making the substitution $\tilde{r} = \sin u$, $d\tilde{r} = \cos u du$ and using the relation $\cos^2 u + \sin^2 u = 1$ gives:

$$\int \frac{H_0 R_0 \cos u}{\cos u} du = H_0 R_0 u = H_0 R_0 \sin^{-1} \tilde{r}$$

The angular diameter distance becomes:

$$\begin{aligned} H_0 d_A &= H_0 R(t) \tilde{r} \\ &= H_0 \frac{R_0}{(1+z_2)} \tilde{r} \\ &= -H_0 \frac{R_0}{(1+z_2)} \sin\left[\frac{1}{H_0 R_0} \int dz F(z)\right] \end{aligned}$$

This can be expressed in terms of Ω_k using equation A.6 as:

$$\begin{aligned} d_A &= -\frac{1}{H_0 \sqrt{|\Omega_k|}(1+z_2)} \sin\left[\sqrt{|\Omega_k|} \int dz F(z)\right] \\ &= -\frac{1}{H_0 \sqrt{|\Omega_k|}(1+z_2)} \sin\left[\sqrt{|\Omega_k|} \int_{z_1}^{z_2} \frac{[(1+\Omega_M z) - z(2+z)\Omega_\Lambda]^{-1/2}}{(1+z)} dz\right] \end{aligned}$$

It is useful to define the function sinn which represents sinh for an open universe and sin for a closed universe:

$$\begin{aligned} \text{sinn} = \ & \sinh \text{if} k = -1 \\ & \sin \text{if} k = 1 \end{aligned} \tag{A.7}$$

Thus the angular diameter distance, in these two cases, becomes:

$$d_A = -\frac{1}{\sqrt{|\Omega_k|}(1+z_2)} \text{sinn}\left[\sqrt{|\Omega_k|} \int_{z_1}^{z_2} \frac{[(1+\Omega_M z) - z(2+z)\Omega_\Lambda]^{-1/2}}{(1+z)} dz\right] \tag{A.8}$$

In addition to the general expression for d_A given in equations A.8, two special cosmological cases can be considered where the values of parameters allow the expression for d_A to be simplified. These two cases are the Friedmann-Robertson-Walker model with $\Omega_\Lambda = 0$ and the Einstein-de Sitter model.

A.1 Friedmann-Robertson-Walker Model with $\Omega_\Lambda = 0$

In the case where $\Omega_\Lambda = 0$, equation A.8 can be simplified to:

$$d_A = -\frac{1}{\sqrt{|\Omega_k|}(1+z_2)H_0} \text{sinn}\left[\sqrt{|\Omega_k|} \int_{z_1}^{z_2} \frac{dz}{(1+z)\sqrt{1+\Omega_M z}}\right] \tag{A.9}$$

Taking the case for $k = 1$, the above integral can be solved analytically by making the substitution $u^2 = \frac{\Omega_M - 1}{\Omega_M(1+z')}$ to give:

$$\begin{aligned}\int_{z_1}^{z_2} \frac{dz}{(1+z)\sqrt{1+\Omega_M z}} &= \int_{u_1}^{u_2} \frac{-2du}{u\sqrt{\Omega_M - 1}\sqrt{\frac{1}{u^2} - 1}} \\ &= \frac{-2}{\sqrt{\Omega_M - 1}} \int_{u_1}^{u_2} \frac{du}{\sqrt{1-u^2}}\end{aligned}$$

Making the substitution $u = \sin x$ gives:

$$\begin{aligned}\frac{-2}{\sqrt{\Omega_M - 1}} \int_{x_1}^{x_2} dx &= \frac{1}{\sqrt{\Omega_M - 1}} \left[\sin^{-1} u_2 - \sin^{-1} u_1\right] \\ &= \frac{-2}{\sqrt{\Omega_M - 1}} \left[\sin^{-1} \sqrt{\frac{(\Omega_M - 1)}{\Omega_M(1+z_2)}} - \sin^{-1} \sqrt{\frac{(\Omega_M - 1)}{\Omega_M(1+z_1)}}\right]\end{aligned}$$

Using the relation $\Omega_M + \Omega_k = 1$ when $\Omega_\Lambda = 0$, equation A.9 for $k = 1$ becomes:

$$\begin{aligned}d_A &= -\frac{1}{\sqrt{1-\Omega_M}(1+z_2)H_0} \sin\left[\sqrt{1-\Omega_M} \int_{z_1}^{z_2} \frac{dz}{(1+z)\sqrt{1+\Omega_M z}}\right] \\ &= -\frac{1}{\sqrt{1-\Omega_M}(1+z_2)H_0} \sin\left[2\sin^{-1} \sqrt{\frac{(\Omega_M - 1)}{\Omega_M(1+z_2)}} - 2\sin^{-1} \sqrt{\frac{(\Omega_M - 1)}{\Omega_M(1+z_1)}}\right]\end{aligned}$$

Using the trigonometric relation $\sin(A - B) = \sin A \cos B - \cos A \sin B$ this becomes:

$$\begin{aligned}d_A = -\frac{1}{\sqrt{1-\Omega_M}(1+z_2)H_0} &\left[\sin\left(2\sin^{-1} \sqrt{\tfrac{(\Omega_M-1)}{\Omega_M(1+z_2)}}\right) \cos\left(2\sin^{-1} \sqrt{\tfrac{(\Omega_M-1)}{\Omega_M(1+z_1)}}\right) - \right. \\ &\left. \cos\left(2\sin^{-1} \sqrt{\tfrac{(\Omega_M-1)}{\Omega_M(1+z_2)}}\right) \sin\left(2\sin^{-1} \sqrt{\tfrac{(\Omega_M-1)}{\Omega_M(1+z_1)}}\right)\right]\end{aligned}$$

This can be expanded using the trigonometric relations $\sin 2\theta = 2\sin\theta\cos\theta$ and $\cos 2\theta = \cos^2\theta - \sin^2\theta = 1 - 2\sin^2\theta$ to give:

$$\begin{aligned}d_A = -\frac{1}{\sqrt{1-\Omega_M}(1+z_2)H_0} &\left[2\sqrt{\tfrac{(\Omega_M-1)}{\Omega_M(1+z_2)}} \left(1 - \tfrac{(\Omega_M-1)}{\Omega_M(1+z_2)}\right)^{1/2} \left(1 - \tfrac{2(\Omega_M-1)}{\Omega_M(1+z_1)}\right) - \right. \\ &\left. \left(1 - \tfrac{2(\Omega_M-1)}{\Omega_M(1+z_2)}\right) 2\sqrt{\tfrac{(\Omega_M-1)}{\Omega_M(1+z_1)}} \left(1 - \tfrac{(\Omega_M-1)}{\Omega_M(1+z_1)}\right)^{1/2}\right]\end{aligned}$$

With some rearrangement this gives

$$d_A = -\frac{2\sqrt{\Omega_M - 1}}{\sqrt{1-\Omega_M}(1+z_2)H_0} \times$$

$$\left[\frac{(1+\Omega_M z_2)^{1/2}(2-\Omega_M+\Omega_M z_1)-(1+\Omega_M z_2)^{1/2}(2-\Omega_M+\Omega_M z_2)}{\Omega_M^2(1+z_1)(1+z_2)}\right]$$

$$= \frac{2}{H_0}\left[\frac{(1+\Omega_M z_2)^{1/2}(2-\Omega_M+\Omega_M z_1)-(1+\Omega_M z_1)^{1/2}(2-\Omega_M+\Omega_M z_2)}{\Omega_M^2(1+z_1)(1+z_2)^2}\right]$$

A similar analysis for $k=-1$ leads to the same result.

A.2 Einstein-de Sitter Model

For an Einstein-de Sitter universe $\Omega_\Lambda = 0$ and $\Omega_M = 1$. In this case equation A.5 reduces to

$$\begin{aligned} d_A &= -\frac{1}{(1+z_2)H_0}\int_{z_1}^{z_2}(1+z)^{-3/2}dz \\ &= -\frac{1}{(1+z_2)H_0}\left[\frac{(1+z_2)^{-1/2}-(1+z_1)^{1/2}}{-1/2}\right] \\ &= \frac{2}{H_0}\left[\frac{(1+z_1)(1+z_2)^{1/2}-(1+z_1)^{1/2}(1+z_2)}{(1+z_1)(1+z_2)^2}\right] \end{aligned} \tag{A.10}$$

in agreement with Blandford & Kochanek (1987).

Appendix B

Power Spectra

The lightcurves can be considered as the product of the underlying continuous lightcurve with a window function. If $A(t)$ is the underlying light curve, then the discrete simulation light curve $A_0(t)$ can be written as

$$A_0(t) = A(t)W(t)$$

The window function $W(t)$ for the N timesteps in the simulation is

$$W(t) = \sum_{i=1}^{N} \delta^D(t - t_i)$$

where $\delta^D(x)$ is the Dirac delta function.

The following conventions will be used for the fourier transform and its inverse:

$$A(\omega) = \int dt A(t) e^{-i\omega t} \tag{B.1}$$

$$A(t) = \frac{1}{2\pi} \int d\omega A(\omega) e^{i\omega t} \tag{B.2}$$

Thus,

$$\begin{aligned} A_0(\omega) &= \int dt A_0(t) e^{-i\omega t} \\ &= \int dt e^{-i\omega t} \int \frac{d\omega'}{2\pi} A(\omega') e^{i\omega' t} \int \frac{d\omega''}{2\pi} W(\omega'') e^{i\omega'' t} \end{aligned}$$

Using the relation $\int e^{ixt} = 2\pi\delta^D(x)$ this can be rewritten as

$$A_0(\omega) = \int \frac{d\omega'}{2\pi} A(\omega') \int d\omega'' W(\omega'') \delta^D(\omega' + \omega'' - \omega)$$

Substituting,

$$\int \delta^D(\omega'' - (\omega - \omega'))W(\omega'') = W(\omega - \omega')$$

leads to the relation

$$A_0(\omega) = \int \frac{d\omega'}{2\pi} A(\omega')W(\omega - \omega')$$

The expectation value of $A_0(\omega)$ is

$$\left\langle |A_0(\omega)|^2 \right\rangle = \int \frac{d\omega'}{2\pi}\frac{d\omega''}{2\pi} \left\langle A(\omega')A^*(\omega'') \right\rangle W(\omega - \omega')W^*(\omega - \omega'')$$

By definition,

$$\left\langle A(\omega')A^*(\omega'') \right\rangle = 2\pi P(\omega')\delta^D(\omega' - \omega'')$$

where $P(\omega')$ is the underlying power spectrum. Thus,

$$\left\langle |A_0(\omega)|^2 \right\rangle = \int \frac{d\omega'}{2\pi} P(\omega')|W(\omega - \omega')|^2$$

Making the assumption that $P(\omega')$ is constant across the width of the window function, this can be rewritten as:

$$\begin{aligned} \left\langle |A_0(\omega)|^2 \right\rangle &= P(\omega) \int \frac{d\omega'}{2\pi} |W(\omega - \omega')|^2 \\ &\simeq \frac{P(\omega)}{2\pi} \sum_{\omega_i} \delta\omega |W(\omega - \omega_i)|^2 \end{aligned}$$

For a simulation of length T, $\delta\omega = 2\pi/T$. Thus,

$$\left\langle |A_0(\omega)|^2 \right\rangle \simeq \frac{P(\omega)}{T} \sum_{\omega_i} |W(\omega - \omega_i)|^2 \tag{B.3}$$

Each simulation produces N_p independent lightcurves for each of the range of source sizes. A final power spectrum for a particular source size is obtained by averaging the individual power spectra to give the mean power spectra $\hat{P}$. Thus:

$$\hat{P} = \frac{1}{N_p} \sum_{i=1}^{N_p} P_i \tag{B.4}$$

B.1 Error Analysis

The errors in the final power spectrum for a particular simulation and source size are estimated from the spread of the power spectra generated from the individual light curves. The variance on the mean power spectrum, σ_p^2 is

$$\begin{aligned}\sigma_p^2 &= \left\langle (\hat{P} - P)^2 \right\rangle \\ &= \left\langle \hat{P}^2 - 2P\hat{P} + P^2 \right\rangle\end{aligned}$$

where P is the true mean value. Using the fact that $\left\langle \hat{P} \right\rangle = P$,

$$\sigma_p^2 = \left\langle \hat{P}^2 \right\rangle - P^2$$

Substituting in Equation B.4,

$$\begin{aligned}\sigma_p^2 &= \left\langle \frac{1}{N_p^2} \left(\sum_{i=1}^{N_p} P_i \right)^2 \right\rangle - P^2 \\ &= \frac{1}{N_p^2} \sum_{i=1}^{N_p} \sum_{j=1}^{N_p} \langle P_i P_j \rangle - P^2\end{aligned}$$

If P_i and P_j are independent then $\langle P_i P_j \rangle = \langle P_i \rangle \langle P_j \rangle$ when $i \neq j$, and:

$$\begin{aligned}\sigma_p^2 &= \frac{1}{N_p^2} \sum_{i=1}^{N_p} \langle P_i^2 \rangle + \frac{1}{N_p^2} \sum_{j=1, j\neq i}^{N_p} P^2 - P^2 \\ &= \frac{1}{N_p^2} \left(N_p \sigma^2 \right) + \frac{P^2 N_p}{N_p^2} + \frac{N_p^2 - N_p}{N_p^2} P^2 - P^2 \\ &= \frac{\sigma^2}{N_p}\end{aligned}$$

where

$$\sigma^2 = \langle P_i^2 \rangle - P^2$$

is the variance of the data in the sample.

Appendix C

Power Spectra Fit Parameters

The following tables list the best fit parameters obtained by fitting the power spectra from the microlensing simulations to Equation 4.1.

a)

Source diameter (pixels)	A	a	b	ω_0	c
1 (unresolved)	39.48	0.98	6.8×10^{-7}	0.029	2.12
6	27.69	0.95	0.40	0.030	2.33
12	18.30	0.91	0.57	0.027	2.66
24	11.97	0.90	0.76	0.017	2.74
48	2.14	0.73	0.99	0.015	3.63
96	1.21	0.81	1.69	0.0066	2.43

b)

Source diameter (pixels)	A	a	b	ω_0	c
1 (unresolved)	14.84	0.90	0.76	0.020	1.00
6	12.44	0.88	0.62	0.032	2.25
12	11.51	0.90	0.46	0.036	3.79
24	2.29	0.73	1.52	0.014	1.73
48	0.37	0.55	1.40	0.013	3.32
96	0.17	0.59	2.26	0.0057	2.01

c)

Source diameter (pixels)	A	a	b	ω_0	c
1 (unresolved)	2.03	0.75	2.01	0.025	0.60
6	2.63	0.79	0.95	0.036	2.00
12	1.41	0.72	1.26	0.029	2.13
24	11.80	1.10	0.010	0.056	11.11
48	5.42	1.04	0.010	0.056	18.67
96	15.25	1.33	0.12	0.0066	5.20

Table C.1: Gaussian source profile parameters for a) Simulation *i*, b) Simulation *iii* and c) Simulation *iv*

a)

Source diameter (pixels)	A	a	b	ω_0	c
1 (unresolved)	1.88	0.72	1.56	0.028	0.68
6	11.31	1.02	1.1×10^{-5}	0.088	6.27
12	4.21	0.90	0.41	0.043	4.48
24	1.91	0.86	0.64	0.026	4.58
48	0.73	0.79	0.70	0.017	5.70
96	0.19	0.75	1.48	0.0068	3.29

b)

Source diameter (pixels)	A	a	b	ω_0	c
1 (unresolved)	0.32	0.83	1.42	0.036	0.81
6	1.01	1.01	7.8×10^{-5}	0.16	9.52
12	1.13	1.04	1.0×10^{-4}	0.091	9.58
24	0.34	0.94	0.51	0.024	4.44
48	0.23	0.98	0.46	0.018	6.43
96	0.010	0.68	2.09	0.0064	2.46

c)

Source diameter (pixels)	A	a	b	ω_0	c
1 (unresolved)	5.05	0.97	0.18	0.059	2.07
6	5.24	0.97	0.049	0.16	4.99
12	6.34	0.99	0.010	0.23	8.63
24	3.23	0.91	0.41	0.092	5.56
48	1.33	0.84	0.84	0.045	4.09
96	0.58	0.79	1.10	0.023	3.64

Table C.2: Gaussian source profile parameters for a) Simulation *v*, b) Simulation *vi* and c) Simulation *vii*

a)

Source diameter (pixels)	A	a	b	ω_0	c
1 (unresolved)	39.48	0.98	6.8×10^{-7}	0.029	2.12
6	20.27	0.92	0.65	0.025	2.07
12	10.61	0.86	1.07	0.015	1.70
24	6.57	0.87	1.48	0.0073	1.32
48	1.63	0.78	2.01	0.0040	1.00
96	5.51	1.18	1.89	0.0025	1.00

b)

Source diameter (pixels)	A	a	b	ω_0	c
1 (unresolved)	14.84	0.90	0.76	0.020	1.00
6	9.66	0.86	0.81	0.026	2.09
12	3.25	0.75	1.63	0.013	1.27
24	2.97	0.83	1.49	0.0068	1.27
48	0.84	0.76	1.89	0.0034	1.00
96	49.95	1.54	0.56	0.0018	1.56

c)

Source diameter (pixels)	A	a	b	ω_0	c
1 (unresolved)	2.03	0.75	2.01	0.025	0.60
6	2.35	0.78	1.01	0.030	2.06
12	0.53	0.60	2.67	0.014	0.87
24	25.50	1.27	0.33	0.0062	2.20
48	49.99	1.46	0.47	0.0028	1.77
96	49.97	1.65	0.37	0.0019	1.74

Table C.3: Constant source profile parameters for a) Simulation *i*, b) Simulation *iii* and c) Simulation *iv*

a)

Source diameter (pixels)	A	a	b	ω_0	c
1 (unresolved)	1.88	0.72	1.56	0.028	0.68
6	3.89	0.88	0.83	0.026	2.05
12	1.11	0.75	1.77	0.013	1.15
24	0.72	0.79	1.59	0.0072	1.18
48	0.13	0.63	2.70	0.0035	0.73
96	0.27	1.04	2.70	0.0026	0.73

b)

Source diameter (pixels)	A	a	b	ω_0	c
1 (unresolved)	0.32	0.83	1.42	0.036	0.81
6	0.51	0.93	0.47	0.041	3.45
12	0.34	0.91	0.97	0.013	1.78
24	0.22	0.93	1.06	0.0065	1.50
48	0.032	0.79	2.70	0.0034	0.73
96	0.10	1.15	0.73	0.0022	1.52

c)

Source diameter (pixels)	A	a	b	ω_0	c
1 (unresolved)	5.05	0.97	0.18	0.059	2.07
6	5.75	0.98	0.039	0.17	5.86
12	2.96	0.89	0.84	0.049	2.29
24	1.73	0.85	1.28	0.026	1.68
48	0.75	0.80	1.49	0.014	1.40
96	9.58	1.23	0.071	0.0069	2.80

Table C.4: Constant source profile parameters for a) Simulation *v*, b) Simulation *vi* and c) Simulation *vii*

Appendix D

Reduced χ^2 fits for observational data

This appendix shows the best fit parameters for the reduced χ^2 fits of the microlensing simulation to the observational quasar survey data. The data from the observational quasar survey is divided into four subsets based on redshift and apparent magnitude. Each subset is individually fitted with the microlensing simulation data. The four subsets of the observational data used are:

- $0.5 \leq z < 1.5$ and $m_a \geq 20$.
- $0.5 \leq z < 1.5$ and $m_a < 20$.
- $1.5 \leq z < 2.5$ and $m_a \geq 20$.
- $1.5 \leq z < 2.5$ and $m_a < 20$.

The following tables show the best fits for each of these datasets with the data for the gaussian and constant surface brightness profile simulation data.

Simulation	$M_{lens}/M_{\odot}$	Source size (m)	Reduced χ^2
i	10^{-5}	2.0×10^{13}	3.6
iii	10^{-5}	1.7×10^{13}	4.2
iv	10^{-4}	1.7×10^{13}	3.7
v	10^{-4}	1.7×10^{13}	3.2
vii	10^{-4}	1.4×10^{13}	3.7

Table D.1: Best fit reduced χ^2 values for gaussian source profile simulations and observational data in the range $0.5 \leq z < 1.5$ and $m_a \geq 20$.

Simulation	$M_{lens}/M_\odot$	Source size (m)	Reduced χ^2
i	10^{-5}	2.4×10^{13}	5.0
iii	10^{-5}	2.3×10^{13}	6.9
iv	10^{-4}	3.4×10^{13}	4.3
v	10^{-4}	3.6×10^{13}	5.9
vii	10^{-4}	2.4×10^{13}	5.1

Table D.2: Same as Table D.1 for observational data in the range $0.5 \leq z < 1.5$ and $m_a < 20$.

Simulation	$M_{lens}/M_\odot$	Source size (m)	Reduced χ^2
i	10^{-5}	2.4×10^{13}	4.0
iii	10^{-5}	2.3×10^{13}	4.5
iv	10^{-4}	3.4×10^{13}	4.3
v	10^{-4}	3.6×10^{13}	5.9
vii	10^{-4}	1.9×10^{13}	4.6

Table D.3: Same as Table D.1 for observational data in the range $1.5 \leq z < 2.5$ and $m_a \geq 20$.

Simulation	$M_{lens}/M_\odot$	Source size (m)	Reduced χ^2
i	10^{-5}	2.8×10^{13}	5.6
iii	10^{-5}	2.8×10^{13}	6.1
iv	10^{-5}	1.6×10^{13}	8.3
v	10^{-4}	3.6×10^{13}	5.2
vii	10^{-4}	2.8×10^{13}	5.4

Table D.4: Same as Table D.1 for observational data in the range $1.5 \leq z < 2.5$ and $m_a < 20$.

Simulation	$M_{lens}/M_\odot$	Source size (m)	Reduced χ^2
i	10^{-5}	1.2×10^{13}	4.0
iii	10^{-5}	1.1×10^{13}	4.0
iv	10^{-4}	1.7×10^{13}	4.5
v	10^{-4}	1.8×10^{13}	5.5
vii	10^{-3}	9.5×10^{12}	3.9

Table D.5: Best fit reduced χ^2 values for constant source profile simulations and observational data in the range $0.5 \leq z < 1.5$ and $m_a \geq 20$.

Simulation	$M_{lens}/M_{\odot}$	Source size (m)	Reduced χ^2
i	10^{-5}	1.6×10^{13}	4.7
iii	10^{-5}	1.7×10^{13}	5.7
iv	10^{-4}	1.7×10^{13}	6.8
v	10^{-4}	1.8×10^{13}	5.3
vii	10^{-4}	1.4×10^{13}	5.3

Table D.6: Same as Table D.5 for observational data in the range $0.5 \leq z < 1.5$ and $m_a < 20$.

Simulation	$M_{lens}/M_{\odot}$	Source size (m)	Reduced χ^2
i	10^{-5}	1.6×10^{13}	4.7
iii	10^{-5}	1.7×10^{13}	5.7
iv	10^{-4}	1.7×10^{13}	4.5
v	10^{-4}	1.8×10^{13}	4.0
vii	10^{-4}	1.4×10^{13}	4.5

Table D.7: Same as Table D.5 for observational data in the range $1.5 \leq z < 2.5$ and $m_a \geq 20$.

Simulation	$M_{lens}/M_{\odot}$	Source size (m)	Reduced χ^2
i	10^{-5}	2.0×10^{13}	5.4
iii	10^{-5}	1.7×10^{13}	9.8
iv	10^{-5}	1.1×10^{13}	8.4
v	10^{-5}	1.1×10^{13}	10.7
vii	10^{-4}	1.9×10^{13}	5.4

Table D.8: Same as Table D.5 for observational data in the range $1.5 \leq z < 2.5$ and $m_a < 20$.

Appendix E

The double quasar Q2138-431: lensing by a dark galaxy?

In addition to work outlined in the main body of this thesis, a small contribution was made to a paper investigating the possibility that the lens for the double quasar Q2138-431 is a dark galaxy. This work involved calculating the lens mass and mass-to-light ratio for the observed parameters as a function of redshift.

Mon. Not. R. Astron. Soc. **291**, 811–818 (1997)

The double quasar Q2138 – 431: lensing by a dark galaxy?

M. R. S. Hawkins,[1] D. Clements,[2] J. W. Fried,[3] A. F. Heavens,[4] P. Véron,[5] E. M. Minty[4] and P. van der Werf[6]

[1]*Royal Observatory, Blackford Hill, Edinburgh EH9 3HJ*
[2]*European Southern Observatory, Karl-Schwarzschild-Strasse 2, 85748 Garching bei München, Germany*
[3]*Max-Planck-Institut für Astronomie, Königstuhl 17, D-69117 Heidelberg, Germany*
[4]*Department of Astronomy, University of Edinburgh, Blackford Hill, Edinburgh EH9 3HJ*
[5]*Observatoire de Haute-Provence (CNRS), F-04870 Saint-Michel l'Observatoire, France*
[6]*Sterrewacht Leiden, Postbus 9513, 2300 RA Leiden, The Netherlands*

Accepted 1997 July 17. Received 1997 June 30; in original form 1996 December 2

ABSTRACT

We report the discovery of a new gravitational lens candidate Q2138 – 431AB, comprising two quasar images at a redshift of 1.641, separated by 4.5 arcsec. The spectra of the two images are very similar, and the redshifts agree to better than 115 km s^{-1}. The two images have magnitudes $B_J = 19.8$ and 21.0, and, in spite of a deep search and image subtraction procedure, no lensing galaxy has been found with $R < 23.8$. Modelling of the system configuration implies that the mass-to-light ratio of any lensing galaxy is likely to be around 1000 $M_\odot/L_\odot$, with an absolute lower limit of 200 $M_\odot/L_\odot$ for an Einstein–de Sitter universe. We conclude that the most likely explanation of the observations is gravitational lensing by a dark galaxy, although it is possible we are seeing a binary quasar.

Key words: galaxies: haloes – quasars: individual: Q2138 – 431 – gravitational lensing.

1 INTRODUCTION

The first secure example of a gravitational lens (Q0957 + 561) was discovered by Walsh, Carswell & Weymann (1979), and comprised two images of a quasar at redshift $z = 1.41$ lensed by a bright cluster galaxy at $z = 0.36$. Since then, many manifestations of gravitational lensing have been observed, including multiply lensed quasars, giant arcs around galaxy clusters, and distortions of the distant galaxy distribution. Historically, systems comprising a pair of quasar images have always had a special significance in the catalogue of lensing phenomena because of the simplicity of the geometry, and the plausibility of using them to measure the Hubble constant (Refsdal 1964). There are at present seven wide-separation (> 2 arcsec), two-component lens candidates known, but progress towards finding a value of the Hubble constant has been slow for several reasons. These include the lack of high-quality light curves over a sufficiently long period of time, the uncertainty of the lensing geometry, the effects of microlensing, and the failure to find the lensing galaxy. In this paper we report the discovery of a new gravitational lens candidate which highlights some of these problems.

This eighth wide-separation system was discovered as part of a systematic survey for lens candidates. It has a separation of 4.5 arcsec, and the two components had B magnitudes of 19.8 and 21.0 in 1995. There is extensive archival photometry of the system over 20 yr, and it appears to be clear of any nearby galaxy concentrations. The two images are strongly variable, but, as for all but two of the other known systems, the lensing galaxy has not so far been detected. The large mass-to-light ratios of the order of several hundred to a thousand implied by these non-detections have prompted several authors to speculate about the possibility of 'dark galaxies'. In this paper we report a variety of observations of the new system, and conclude that in this case too the most probable expanation is that the quasar is being gravitationally lensed by a dark galaxy.

2 OBSERVATIONS

2.1 The lens survey

The survey for gravitational lenses was carried out in the ESO/SERC field 287 centred on 21^h28^m, $-45°$ (1950). Extensive plate material from the UK Schmidt telescope

exists in this field, which has formed the basis for the large-scale quasar survey and monitoring programme of Hawkins & Véron (1995, 1996) and Hawkins (1996). The selection of subsamples of quasars in different redshift bands typically used colour limits together with variability and compactness criteria, but in all cases the quasar images were required to be round. This was to eliminate overlapping images which might masquerade as quasars, or even quasars merged with stars or galaxies where the photometry would give misleading results. One consequence of this was to reject any gravitationally lensed quasars from consideration, where the split image would appear elongated. To rectify this, a search was designed specifically to look for gravitationally lensed systems. The requirements were that the images should have a major-to-minor axis ratio greater than 1.5, and an ultraviolet excess $U-B<-0.4$. Of the 200 000 objects in the field, 500 have $U-B<-0.4$, of which 23 were elongated. Of these, 12 were variable according to our usual criteria (Hawkins & Véron 1995), with an amplitude greater than 0.35 mag. Four of the sample were quasars with overlapping galaxies previously found by Morris et al. (1991), and so we set about obtaining spectra for the remainder, several of which appeared to be excellent candidates for lensed systems. It also seems possible that some lensed quasars will be found among the non-variable objects.

2.2 The double quasar Q2138 – 431

The first candidate to be studied in detail appeared as two star-like images separated by 4.5 arcsec. Spectra of the two components were obtained on the ESO 3.6-m telescope at La Silla by aligning the slit along the line of centres. The spectra were very similar, and the redshifts appeared to be the same, $z=1.64$. There seemed to be a *prima facie* case for a gravitationally lensed system, and so a few nights later we obtained a second, higher signal-to-noise observation in both blue and red wavelength bands covering a combined spectral range from 3700 to 10 000 Å. The spectra are shown in Fig. 1, and it will be seen that they closely resemble each other. Fig. 2 shows the quotient of the two spectra which is almost flat, implying no significant differences.

The redshifts were first calculated by measuring the emission lines in each spectrum, which gave $z=1.638\pm0.004$ and 1.644 ± 0.005 for the two components, the same within the errors. In order to obtain a more accurate measurement, a cross-correlation routine was applied. This gave identical redshifts within the errors, and a velocity difference of 0 ± 114 km s^{-1}.

Optical photometry of the system was obtained with a CCD camera on the ESO 2.2-m telescope at La Silla in 1995 August. The pixel scale was 0.336 arcsec pixel^{-1}, and the seeing averaged 1.2 arcsec, which allowed a clear separation of the images. The R-band frame is shown in Fig. 3, where the faintest visible objects have magnitude $R>24$. The results are shown in Table 1, where the five columns are the colour passband, the apparent magnitudes of the two components, the flux ratio and the lower limit to the magnitude of any lensing galaxy. It will be seen that at the time of observation the magnitude difference between the two components was $\delta m=1.2$, with no significant dependence on

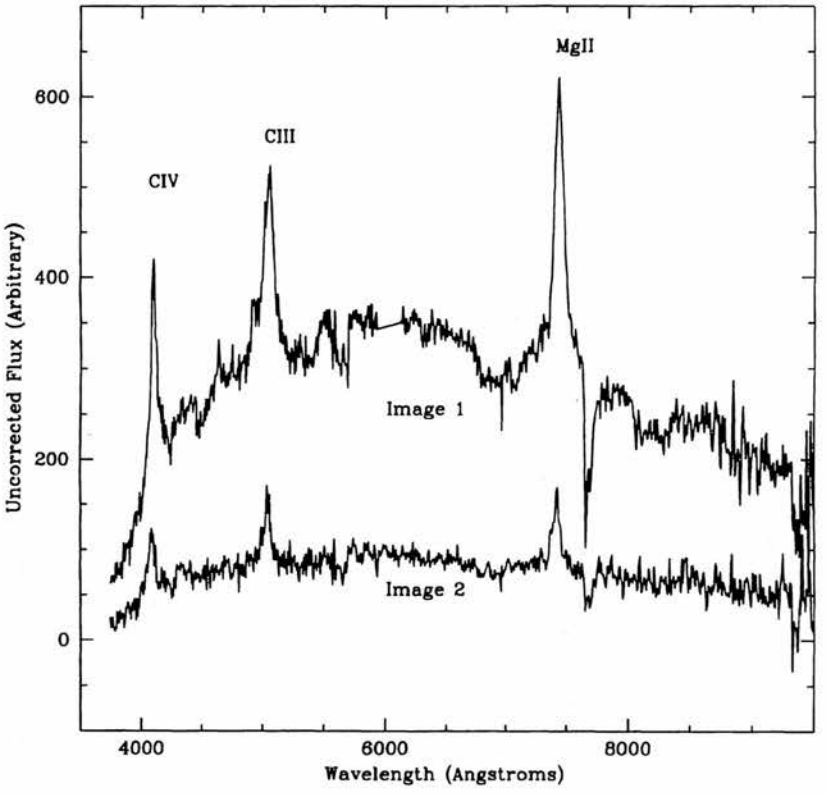

Figure 1. Spectra for the two images of the double quasar Q2138 – 431AB in red and blue passbands.

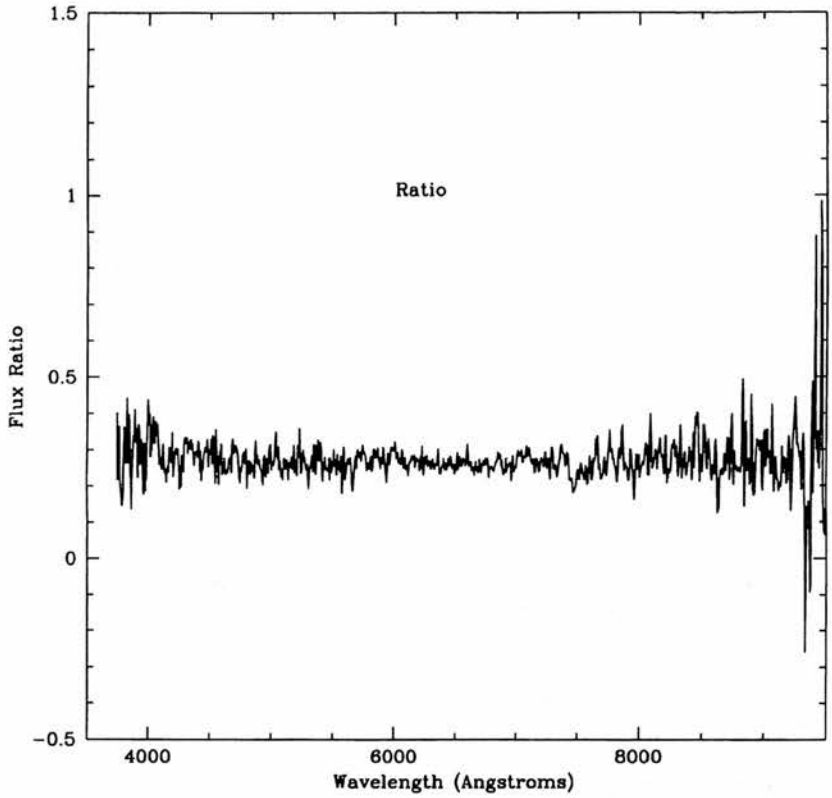

Figure 2. Spectrum of component A divided by that of component B from Fig. 1.

colour. Fig. 4 shows the $V-R$ and $R-I$ colours for the two components of Q2138 – 431, together with photographic measures for 10 other quasars from the sample with very similar redshift. The colours of the double quasar are identical within the errors of the CCD observations, whereas the other 10 quasars in the sample illustrate the wide range of colours which quasars at this redshift can exhibit.

2.3 Search for the lensing galaxy

To understand a gravitational lens system fully, and more specifically to use it to measure the Hubble constant, the lensing galaxy must be located. It is then necessary to measure its redshift, and to estimate the mass distribution relative to the quasar images. In fact, of the seven double quasar systems so far discovered with image separation greater than 2 arcsec, lensing galaxies have been found for only two.

To detect the lensing galaxy for Q2138 – 431, we used the deep CCD frames described above for the photometric measurements. Initial examination of the area around the quasar system showed no objects which might act as gravitational lenses. We obtained a more useful limit by using stars in the vicinity of the quasar images to obtain an accurate measure of the point-spread function (PSF). This was then subtracted from each of the quasar images in the hope of revealing an underlying lensing galaxy. There is an element of uncertainty in the normalization of the PSF in this procedure, but in the event we found that both quasar images subtracted out exactly. To put an upper limit on the magnitude of a possible lensing galaxy, we extracted the faint galaxy visible to the south-east of the quasar in Fig. 3. We then placed it at various points between the two quasar images, varied its brightness and carried out the PSF subtraction procedure. This enabled us to put an upper limit of $R > 23.8$ for a potential lensing galaxy. We also obtained a K-band image of the field with the IRAC2 infrared camera on the ESO 2.2-m telescope. A 5-h integration failed to reveal a lensing galaxy between the two images, although there was evidence for additional K band flux associated with the brighter component. This observation raises the possibility that a very red lensing galaxy may be lying close to the brighter quasar image, a configuration which requires fine-tuning of the model parameters.

One can now ask what limits can be put on the mass-to-light ratio of a lensing galaxy capable of producing the observed image splitting and flux ratio, but constrained to be fainter than the observed magnitude limit. We have modelled the system assuming both a point mass and a more realistic galaxy profile, and have thus derived a lower limit to the mass to light ratio as a function of redshift. If the lens can be modelled as a point mass, the brightness ratio $R > 1$ of the two images and the separation $\Delta\theta$ on the sky can be used to calculate the Einstein radius

$$\theta_{\rm E} = \sqrt{4GMD_{\rm LS}/(D_{\rm OL}D_{\rm OS}c^2)},$$

where M is the lens mass, and the Ds are the angular diameter distances between observer, lens and source.

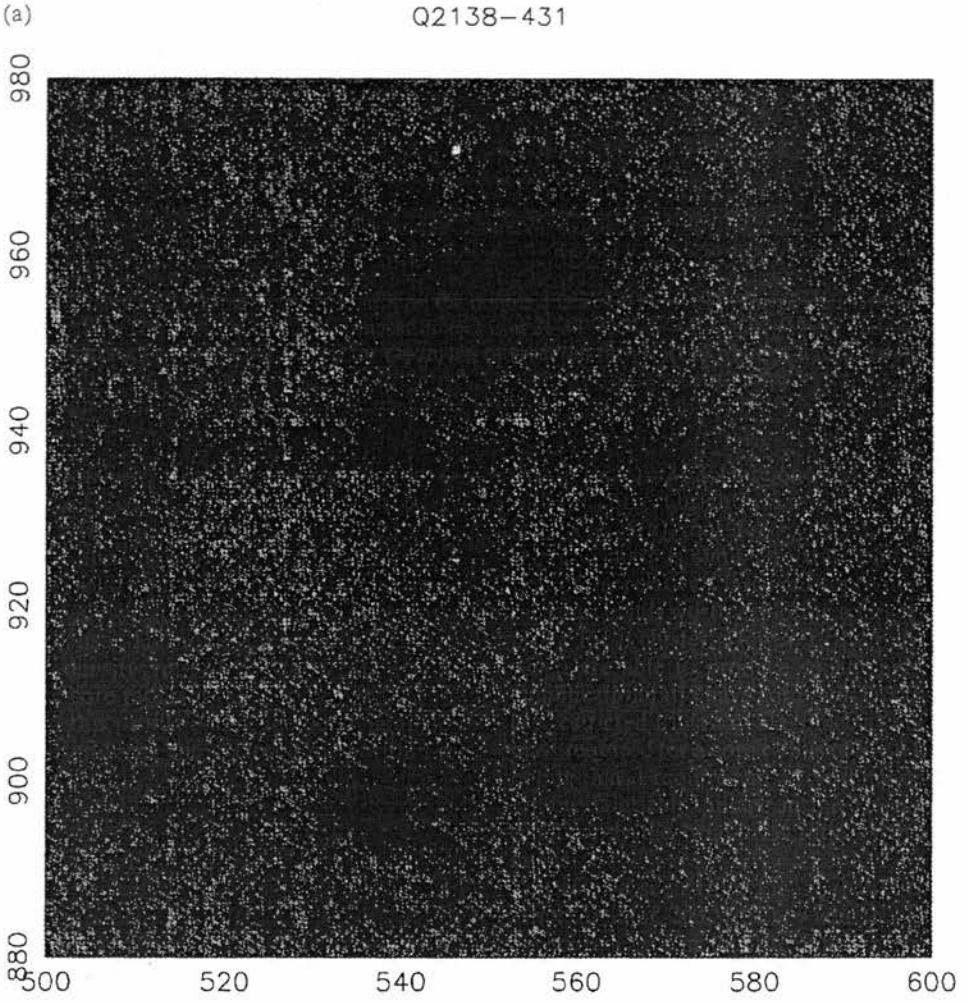

Figure 3. (a) Part of an *R*-band CCD frame of the field around the double quasar Q2138 − 431. The plot is 50 arcsec on a side, and north is up the page, east to the left. The centroid of the two quasar images is at $21^h38^m6^s.66$, $-44°10'50''$ (1950), and they are separated by 4.5 arcsec. The star about 20 arcsec to the south was used for the image subtraction, the effect of which is illustrated in the second panel (b).

It is straightforward to show, from the lensing equations (see, e.g., Schneider, Falco & Ehlers 1992), that $\theta_E = \sqrt{1-f^2}\Delta\theta/2$, where $f \equiv (R+1-\sqrt{4R})/(R-1)$. θ_E is 2.1 arcsec, and the required mass is shown in Fig. 5(a) for two different cosmologies (solid line: Einstein–de Sitter, dashed line: $\Omega_0 = 0.1$). Also shown (dot–dashed) is the mass required in a more realistic Hernquist mass profile (Hernquist 1990), with a density run $\rho(r) = M/[2\pi r_c^2 s(1+s)^3]$, where $s = r/r_c$, and the core radius is taken to be $r_c = 1.7\,h^{-1}$ kpc. An advantage of this profile is that the bending angle may be written in closed form; the enclosed mass within a projected radius rr_c is

$$\frac{M(<rr_c)}{M} = \frac{r^2}{r^2-1} - \frac{r^2}{(r^2-1)^{3/2}}\cos^{-1}\left(\frac{1}{r}\right) \qquad r>1 \qquad (1)$$

$$= \frac{r^2}{r^2-1} - \frac{r^2}{(1-r^2)^{3/2}}\ln\left(\frac{r}{1-\sqrt{1-r^2}}\right) \qquad r<1, \quad (2)$$

with $M(<r_c) = M/3$. Here one needs to search for a solution with the correct brightness ratio and separation, and we see from Fig. 5(a) that for r_c appropriate for galaxies, the required mass is similar to the point-mass calculation. In view of the relatively large masses required if the lens is near the source, it is worth exploring a larger core radius, appropriate for a cluster. However, the only Hernquist profiles which are able to produce split images with the required amplification ratio have core radii less than $7\,h^{-1}$ kpc, so we are restricted to galaxy-like objects (Fig. 5a also shows the mass required for a core radius of $5\,h^{-1}$ kpc). It is also worth noting that it requires an astonishing degree of fine-tuning for the faint third image in the Hernquist model to alter significantly the brightness ratio by merging with another image.

It will be seen from Fig. 5(a) that there is an absolute lower limit of $200\,M_\odot/L_\odot$ when the lens is at a redshift $z = 1.5$ for an Einstein–de Sitter universe, and a slightly lower limit if the Universe is open. In fact, this configuration

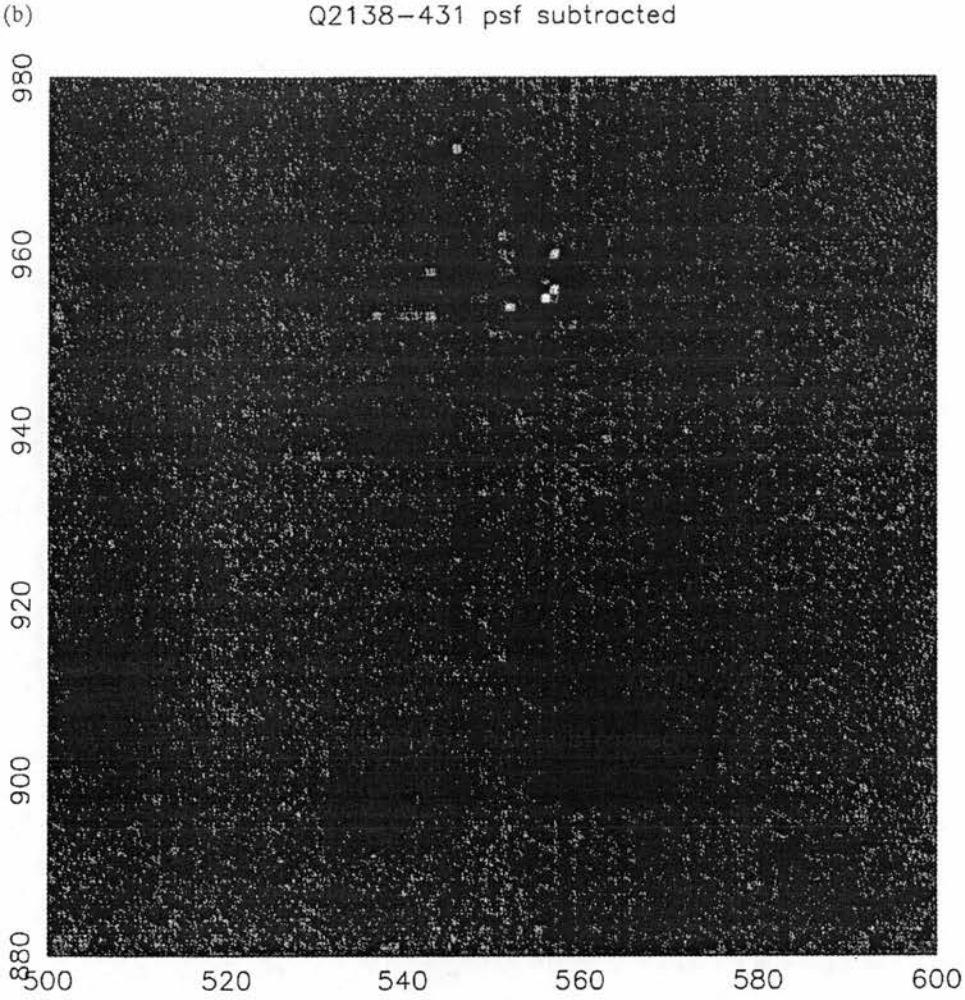

Figure 3 – *continued*

Table 1. CCD photometry for Q2138 – 431AB.

colour	m_A	m_B	f_A/f_B	$m_{gal}>$
B	21.02	19.83	0.33	23.
V	20.85	19.57	0.307	23.5
R	20.43	19.18	0.318	23.8
I	20.12	18.86	0.313	22.8

is highly improbable, and the most likely position for the lens is at around $z=0.5$ (Turner, Ostriker & Gott 1984), implying a minimum mass-to-light ratio of 1000 $M_\odot/L_\odot$. In this case the lensing object would presumably be some form of 'dark galaxy', or perhaps a dark matter galactic halo.

Another approach is to consider the possible effect of shear or convergence produced by a nearby group or cluster of galaxies. This is a model which has been used to describe Q0957 + 561 (Bernstein, Tyson & Kochanek 1993), and also for the wide separation lens Q2345 + 007 (Pelló et al. 1996).

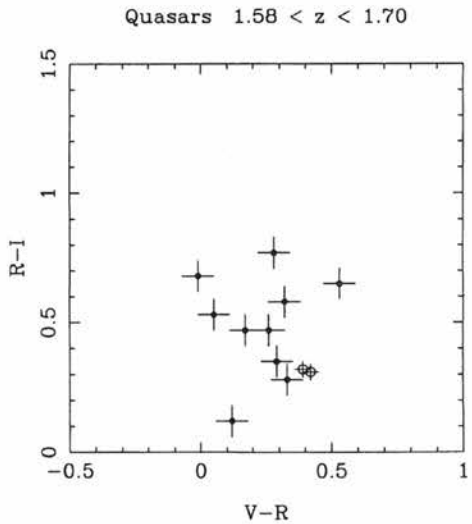

Figure 4. The $V-R$ versus $R-I$ relation for quasars with $z\approx1.64$. The two components of Q2138 – 431 are shown as open circles, and 10 other quasars from the field 287 sample as closed circles.

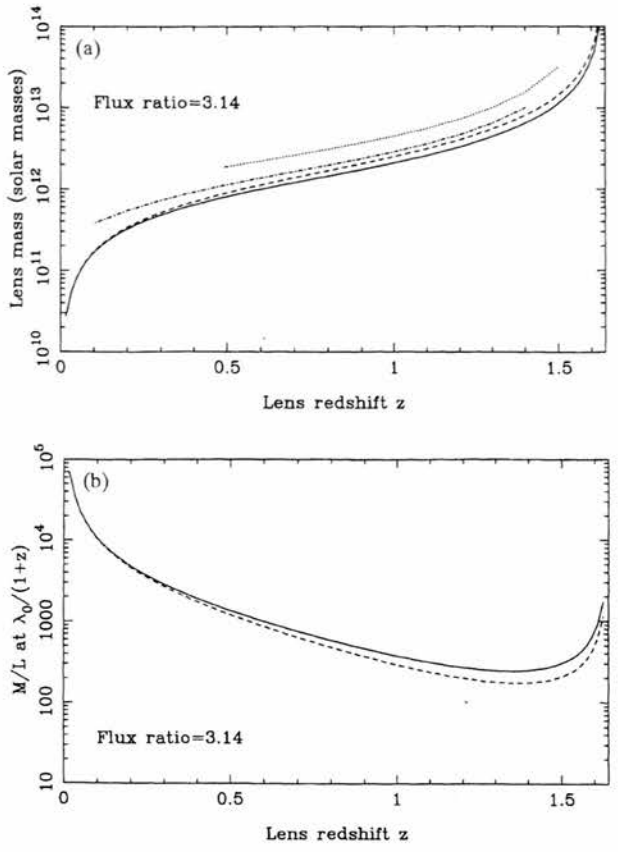

Figure 5. (a) The mass of the postulated lens for the double quasar Q2138 − 431AB as a function of the lens redshift. The solid line assumes a point-mass lens and an Einstein–de Sitter universe; the dotted line assumes that $\Omega_0 = 0.1$ and no vacuum energy. The dot–dashed line shows the required mass if the density distribution follows a Hernquist profile with core radius $1.7h^{-1}$ kpc (corresponding with an effective radius of $3h^{-1}$ kpc), and the dotted line assumes a core radius of $5h^{-1}$ kpc. The last two curves assume $\Omega_0 = 1$. (b) The minimum mass-to-light ratio for a lens for the double quasar Q2138 − 431AB. Lines as in (a).

In both of these cases a group of galaxies is detected close to the quasar images, and the splitting is attributed to the resulting shear field. We are in a much worse position here to model such a situation, as we cannot even establish where the lensing galaxy is (if present). The addition of a uniform screen, representing a smooth cluster, would reduce the mass estimates by a factor $1 - \Sigma/\Sigma_c$, where the critical surface density is $\Sigma_c = c^2 D_{OS}/(4\pi G D_{OL} D_{LS})$. The mass requirement is thus eased if the cluster has a substantial fraction of the critical surface density. Numerical modelling of clusters (Bartelmann & Weiss 1994) indicates that this may be possible, but modelling of observed arcs routinely requires a contribution from a central galaxy (Miralda-Escudé & Babul 1995). Although a significant cluster contribution remains an open possibility, the very small core radius required argues against it, and there is no evidence apparent in the images. Fig. 6 shows an area of approximately 8 arcmin on a side centred on the double quasar. The frame is taken from a digital stack (Hawkins 1994) of 64 UK Schmidt plates in the IIIa-J/GC395 passband with effective wavelength 4500 Å. The limiting magnitude is $B_J \sim 24$, and there is no sign of a cluster within 2 arcmin of the quasar. In fact, judging by the surrounding background, the system lies in a particularly clear region of sky, the nearest cluster being in the top right-hand corner of the field.

3 DISCUSSION

The properties of the double quasar Q2138 − 431AB may be summarized as follows:

Redshift $z = 1.641$.
Velocity difference $\delta v = 0 \pm 115$ km s^{-1}.
Separation = 4.5 arcsec.
B magnitudes: $m_A = 19.8$, $m_B = 21.0$.
Variability amplitudes: $\delta m_A = 1.1$, $\delta m_B = 0.6$.

We now address the question of the underying nature of the system. There seem to be three possibilities:

(1) a chance association of two separate quasars, possibly made more likely by the effects of clustering;
(2) a pair of quasars in a bound orbit, forming a binary system, and
(3) a single quasar gravitationally lensed by a dark galaxy or galactic halo with a mass around 10^{12}–10^{13} $M_\odot$.

The likelihood of a chance coincidence can first be assessed by considering the surface density of the parent population of quasars in the field and asking what is the probability P that two will lie within 4.5 arcsec of each other. The parent population of single quasars with similar characteristics to the lens candidate comprised 310 objects with $U - B < -0.4$ and $B < 21$ in an area of 18.8 deg^2, This gives a surface density of quasars of about 16 per deg^2, which implies a probability of about 1 per cent for any companions within 4.5 arcsec, for the parent sample of $\sim$310 quasars. In practice, one would expect this figure to be modified by clustering, which enhances the probability, and by the redshift information, which reduces it. The small-scale clustering of quasars is poorly constrained, but, assuming that it follows the galaxy correlation function $\xi(r) \simeq (r/r_0)^{-\gamma}$, with $r_0 \simeq 5h^{-1}$ Mpc and $\gamma \simeq 1.8$ (Collins, Nichol & Lumsden 1992; Vogeley et al. 1992), boosted by a relative bias b_Q^2, we can calculate the probability of a pair within $50\ h^{-1}$ kpc (the comoving separation corresponding to 4.5 arcsec at $z = 1.6$ if $\Omega_0 = 1$). Using the comoving number density of $1.7 \times 10^{-5} h^3$ Mpc^{-3} obtained from the redshift distribution in the sample at redshifts around 1 to 1.5, we find this probability to be about 1.5 per cent if $b_Q = 1$ and the clustering does not evolve. This is, however, an underestimate for lensing candidates, since the radial separation can far exceed $50\ h^{-1}$ kpc and still be considered a good lensing candidate. For illustration, a velocity difference of 100 km s^{-1} at a redshift of 1.6 corresponds to a comoving separation of around $600\ h^{-1}$ kpc in an Einstein–de Sitter universe, and this could easily be lost in the uncertainties of redshift determination. If, instead of a radial separation of $50\ h^{-1}$ kpc, we use this larger figure of $600\ h^{-1}$ kpc, the probability would be increased to around 2.5 per cent. Peculiar velocities modify this in a model-dependent manner, reducing the chance of good agreement in the redshifts for virialized systems and increasing it for collapsing systrems, but the point is that the

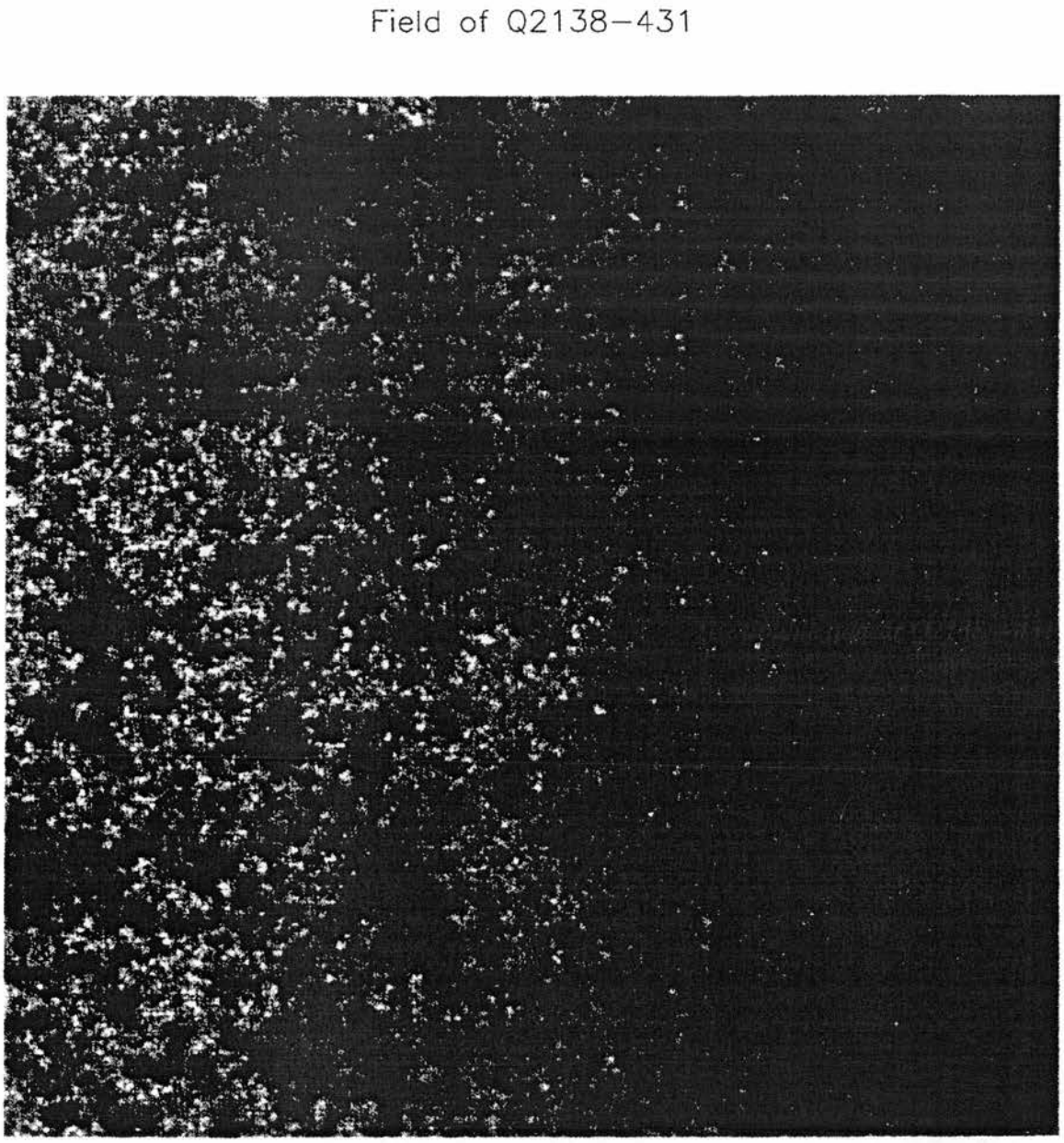

Figure 6. Plot of the area centred on Q2138 – 431. The frame is approximately 8 arcmin^2, and is derived from digitally stacked photographic plates with a limiting magnitude of $B_J \sim 24$. North is up the page, east to the left.

probability of a close separation in angular and redshift terms is small but not negligible.

The idea that the quasars form part of a gravitationally bound binary system is much harder to test, mainly because the circumstances surrounding the formation and evolution of such a system are largely a matter of speculation. There are a number of observations which appear to count against this possibility, such as the extreme similarity of the spectra and colours of the two components and the small differential velocity. It is also clear from the discussion in the previous paragraph that, from a statistical point of view, binary quasars might just be part of a clustering hierarchy. However, none of these arguments is sufficient to rule out the essentially unconstrained concept of binary quasars, and it must remain a possible explanation.

A plausible justification for the binary, or clustered, model is that quasar activity may well be triggered by a close encounter between two galaxies, with a small probability of triggering. The possibility then arises that, in rare cases, quasar activity may be initiated in both galaxies in the encounter. The explanation of the similarity of the spectra, which are not absolutely identical, might then lie in the fact that the quasars would have the same formation epoch, and would be observed at the same time after formation. As part of a common system, their abundances might not significantly differ.

The third possibility, that the system is gravitationally lensed, is well supported by most of the available observations. The similarity of the spectra and colours and the small velocity difference between the two components are to be expected from a gravitationally lensed system. The problem is the failure to find the lensing galaxy. Given the apparent absence of a shear field, this means that to make a case for a gravitationally lensed system one must postulate a dark galaxy as the lens. Although this may seem a radical step, it is, in fact, a position which several other groups have adopted when analysing double quasar systems (e.g. Tyson et al. 1986). An obvious possibility is that the lensing object is a low surface brightness galaxy, which fails not because of the surface brightness limit corresponding with the R limit of 23.8, but rather because known low surface brightness galaxies do not have the very large mass-to-light ratio required (Sprayberry, Bernstein & Impey 1995). We are left with the conclusion that, unpalatable though the idea of dark galaxies may be, it seems to promise the most plausible explanation for the observations.

4 CONCLUSIONS

We have reported the discovery of a new double quasar Q2138 − 431, which we have observed in some detail with a view to establishing whether it is a gravitationally lensed system. It comprises two images with magnitudes $B = 19.8$ and 21.0, separated by 4.5 arcsec. The spectra and colours of the two components are very similar, with a redshift of $z = 1.461$ and velocity diference $\delta v = 0 \pm 115$ km s^{-1}. In spite of an intensive search, we have failed to find a lensing galaxy, which must have a magnitude $R > 23.8$. This has enabled us to put a lower limit on the mass-to-light ratio of any lensing galaxy in the range 200 to 1000 $M_\odot/L_\odot$, depending on its redshift. We have considered three possible interpretations of the system.

(1) Chance coincidence of the two images, which we rule out on statistical ground.

(2) A gravitationally bound binary quasar. The similarity of the two components and the small velocity difference count against this possibility, but we feel that we cannot rule it out.

(3) A gravitational lens. Most of the observations favour this picture, but the lensing object would have to be a dark galaxy or a dark matter halo. This would clearly require a departure from the conventional idea of the galaxy population.

REFERENCES

Bartelmann M., Weiss A., 1994, A&A, 287, 1
Bernstein G. M., Tyson J. A., Kochanek C. S., 1993, AJ, 105, 816
Collins C. A., Nichol R. C., Lumsden S. L., 1992, MNRAS, 254, 295
Hawkins M. R. S., 1994, in MacGillivray H. T., ed., Proc. IAU Symp. 161, Astronomy from Wide-Field Imaging. Kluwer, Dordrecht, p. 177
Hawkins M. R. S., 1996, MNRAS, 278, 787
Hawkins M. R. S., Véron P., 1995, MNRAS, 275, 1102
Hawkins M. R. S., Véron P., 1996, MNRAS, 281, 348
Hernquist L., 1990, ApJ, 356, 359
Miralde-Escudé J., Babul A., 1995, ApJ, 449, 18
Morris S. L., Weymann R. J., Anderson S. F., Hewett P. C., Foltz C. B., Chaffee F. H., Francis P. J., McAlpine G. M., 1991, AJ, 102, 1627
Pelló R., Miralles J. M., Le Borgue J.-F., Picat J.-P., Soucail G., Bruzual G., 1996, A&A, 314, 73
Rafsdal S., 1964, MNRAS, 128, 307
Schneider P., Falco E. E., Ehlers J. L., 1992, Gravitational Lenses. Springer, Berlin
Sprayberry D., Bernstein G. M., Impey C. D., 1995, ApJ, 438, 72
Turner E. L., Ostriker J. P., Gott J. R., 1984, ApJ, 284, 1
Tyson J. A., Seitzer P., Weymann R. J., Foltz C., 1986, AJ, 91, 1274
Vogeley M. S., Park C., Geller M. J., Huchra J. P., 1992, ApJ, 391, L5
Walsh D., Carswell R., Weymann R., 1979, Nat, 279, 381